

Natural System Evaluation and Tool Development - International Collaborations: FY13 Progress Report

Fuel Cycle Research & Development

*Prepared for
U.S. Department of Energy
Used Fuel Disposition
Yifeng Wang, Payton Gardner
Sandia National Laboratories
Paul Reimus, Scott Painter, Nataliia Makedonska,
Ahinoam Pollack
Los Alamos National Laboratory
Jim Houseworth, Jonny Rutqvist, Daisuke
Asahina, Fei Chen, Victor Vilarrasa, H.H. Liu,
Jens Birkholzer
Lawrence Berkeley National Laboratory
James.D. Begg, Mavrik Zavarin, Annie Kersting
Lawrence Livermore National Laboratory
Geon-Young Kim
Korean Atomic Energy Research Institute
December 9, 2013
FCRD-UFD-2013-000628*



DISCLAIMER

This information was prepared as an account of work sponsored by an agency of the U.S. Government. Neither the U.S. Government nor any agency thereof, nor any of their employees, makes any warranty, expressed or implied, or assumes any legal liability or responsibility for the accuracy, completeness, or usefulness, of any information, apparatus, product, or process disclosed, or represents that its use would not infringe privately owned rights. References herein to any specific commercial product, process, or service by trade name, trade mark, manufacturer, or otherwise, does not necessarily constitute or imply its endorsement, recommendation, or favoring by the U.S. Government or any agency thereof. The views and opinions of authors expressed herein do not necessarily state or reflect those of the U.S. Government or any agency thereof.

Natural System Evaluation and Tool Development – International Collaborations: FY13 Progress Report

Executive Summary

Recognizing the benefits of international collaboration in the common goal of safely and efficiently managing the back end of the nuclear fuel cycle, DOE's Office of Nuclear Energy (NE) and its Office of Used Fuel Disposition Research and Development (UFD) have developed a strategic plan to advance cooperation with international partners. Active participation in international R&D is crucial for achieving the UFD long-term goals of conducting "experiments to fill data needs and confirm advanced modeling approaches" (by 2015) and of having a "robust modeling and experimental basis for evaluation of multiple disposal system options" (by 2020). The international collaboration on the natural system evaluation and tool development in FY13 was focused on the following activities: (1) data interpretation of colloid-facilitated transport experiments at Grimsel Test Site, (2) thermal-hydrologic-mechanical (THM) model development and validation for Mont Terri FE-heater test and HG-A test, (3) experimental study of Pu-bentonite interactions, (4) modeling of stable isotope, tritium and CFC-12 transport at the Bedrichov Tunnel site as a part of the DECOVALEX program, (5) KAERI Underground Research Tunnel testing in crystalline rocks, and (6) Swedish Bentonite-Rock Interaction Experiment (BRIE). The major accomplishments include:

- **Colloids Formation and Migration (CFM):** A reactive transport Laplace transform (RELAP) model was developed and used to interpret colloid facilitated transport data collected at the Grimsel Test Site between 2008 and 2012. The model accounts for diffusion between fractures and matrix, as well as linear, first-order reactions in both fractures and matrix. The model was used to fit the conservative tracer extraction breakthrough curves by adjusting the mean residence time and Peclet number in the shear zone as well as the fractional tracer mass participation in each test. The mean residence time, Peclet number and fractional mass participation estimated for the conservative tracers using these matrix diffusion parameters were not significantly different from estimates obtained assuming no matrix diffusion. However, matrix diffusion and sorption were found to be necessary to explain the transport behavior of the reactive solutes that were not strongly associated with colloids, so a small amount of matrix diffusion was allowed. The model was also used to estimate colloid transport parameters (filtration and resuspension rate constants) and reactive solute transport parameters (fracture and matrix adsorption and desorption rate constants for solutes not strongly associated with colloids, and colloid desorption rate constants for solutes strongly associated with colloids). The resulting best-fitting parameters were used as initial parameter estimates in a 2-D numerical model that could account for processes that RELAP does not explicitly account for. The most important of these processes were (1) the variable injection flow rates observed in some of the tests and (2) the simultaneous transport of colloids and reactive solutes (RELAP does not account for interacting

species). RELAP can be used to obtain initial estimates for the more robust numerical model.

- **Mont Terri FE Heater Test:** A new suite of simulations related to the FE test at Mont Terri were conducted, including scoping calculations, benchmarking, and some initial predictive modeling of the real heater test. These include model simulations using 1D axisymmetric, 2D plane strain, and full 3D model geometries. A THM analysis involving the BBM in a full 3D field setting was conducted for modeling the geomechanical behavior of the buffer. Compared to our previous 2D model analysis, this 3D analysis provides a much more accurate estimate of the temperature evolution near the heater and thereby should provide a better prediction of the peak temperature. The peak temperature may become as high as 160°C at the inner parts of the buffer. This prediction strongly depends on the thermal and diffusion properties of the buffer, which are parameters that have presently not been well constrained for this buffer material. THM model simulations were conducted with a simplified buffer mechanical model, whereas a ubiquitous joint model was used for modeling the anisotropic mechanical strength properties of the Opalinus Clay. The analysis shows that some minor failure may occur near the tunnel wall behind the concrete lining after excavation. This failure does not expand much further during the 20-year heating, meaning that the rock mass remains in an elastic mechanical state. Overall, the initial model analyses show that the adopted modeling approach is adequate for modeling the coupled THM processes at the FE heater, including all components of bentonite, concrete lining, and Opalinus Clay.
- **Mont Terri HG-A Test:** The Rigid-Body-Spring-Network (RBSN) model was used to simulate the HG-A test. Two additional model capabilities were developed: (1) a method for computing fracturing under compressive load and (2) a method to treat the anisotropic geomechanical properties of the Opalinus Clay. The use of the Mohr-Coulomb failure criterion led to RBSN model predictions for fracturing under compressive load that roughly follow trends expected for a homogeneous medium. For a layered system, the results were also reasonable in that fracturing followed the stiff layers for high bedding angles but was not controlled by bedding at low bedding angles. Currently, rock failure is modeled using a brittle model in which all strength is lost at failure. However, a more realistic failure response results in a more gradual loss of strength following failure. In addition, contacts along fracture surfaces under compressive loads will lead to friction along fracture planes not currently accounted for in the model. Anisotropic properties for the bulk rock were represented in the RBSN model using layered heterogeneity. While the current approach was successful at producing the desired anisotropic bulk properties and trends for fracture behavior under compressive load, significant differences remain between the RBSN results and observations in the HG-A test, indicating that further model development is needed.
- **Pu-bentonite interactions:** The experiments were designed to develop a mechanistic understanding of Pu interactions with representative mineral substrates under granitic chemical conditions. The sorption/desorption experiments covered a large range of Pu concentrations and were compared to sorption/desorption experiment with montmorillonite. The experiments are being coordinated with the CFM international

project. The work to date indicate that adsorption behavior of Pu(V) on bentonite is similar to montmorillonite, suggesting that our understanding of the simple binary Pu-montmorillonite system can provide insight for the more complex multi-component mineralogy of bentonite clay. The Pu(IV) sorption isotherm for bentonite is broadly linear over a large range in Pu concentration ($[Pu]_{\text{initial}}$ ranging from 10^{-7} mol L⁻¹ to 10^{-16} mol L⁻¹), suggesting that the process controlling sorption at extremely low concentrations is the same as at higher concentrations. The desorption behavior of the bentonite and montmorillonite are very similar, indicating that, as with the adsorption experiments, the same processes are responsible for the desorption of Pu from the two materials.

- DECOVALEX-Bedrichov Tunnel Tests: Lumped parameter models were developed for stable isotope, tritium and CFC-12 transport at the Bedrichov Tunnel site and modeled results were compared to measured data. To account for matrix diffusion in the fractured system at Bedrichov, the effect of matrix diffusion on travel must be investigated. The retention time from matrix diffusion was taken into account using a random walk in time methodology. The lumped parameter models consistently predict heavier isotopic values than those observed at the site, indicating preferential recharge of winter precipitation. The variability in isotopic composition of discharge observed at the site is indicative of short travel times – as modeled isotopic composition with mean travel times over 5 years tend to show no temporal variation. These results are consistent with those from CFC and ³H which indicate travel times of less than 5 years in the Bedrichov tunnel. Using parameters indicative of the Bedrichov Tunnel we show that matrix diffusion is probably not a major process at this site given the very fast transit times. However, this process will have very large effect with longer residence times.
- KAERI Underground Research Tunnel Test: Sandia National Laboratories (SNL) and Korean Atomic Energy Research Institute (KAERI) have developed a multi-year plan for joint field testing and modeling to support the study of high-level nuclear waste disposal in crystalline geologic media. The work currently planned includes three tasks: (1) streaming potential (SP) testing, (2) sharing KURT site characterization data, and (3) technique development for in-situ borehole characterization. For task 1, KAERI has acquired the needed equipment and started experimental setup for laboratory testing. This testing system will be transferred to the underground research laboratory once the new excavation in the KURT is completed. For task 2, KAERI has provided a comprehensive set of geological, hydrological, and geochemical data. These data will be used for the UFD discrete fracture network model development.
- BRIE Project: Refinement and extension of the DFN modeling capability was undertaken to enable representation of the tetrahedral mesh within the DFN mesh. That development work is largely complete and initial computational meshes for the DFN and BRIE boreholes have been generated. The work is continuing in FY2014. The next steps are to apply boundary conditions and perform the flow simulations (Steps 4-6 in Section 7-5). Comparisons to data on moisture content in the bentonite will then be undertaken.

CONTENTS

1.	Objectives and Outline	1
1.1	References	3
2.	Interpretations of Colloid-Facilitated Transport Experiments at the Grimsel Test Site from 2008 through 2012	5
2.1	Introduction	5
2.2	Summary of Tracer Tests 08-01, 10-01, 10-03, and 12-02	6
2.3	Interpretive Modeling Approach	13
2.4	Test Interpretations	19
2.5	Implications for Nuclear Waste Repository Performance Assessments	27
2.6	References	34
Appendix 2-A	Corrections for Uranine Decay in CFM Tracer Test 10-03	35
3.	International Collaboration Involving the FE Heater and HG-A Tests at Mont Terri	43
3.1	Introduction	43
3.2	THM Modeling of FE Experiment	44
3.2.1	FE experiment at the Mont Terri site	44
3.2.2	Modeling approach	48
3.2.3	FE Model Setup	49
3.2.4	3D TH scoping calculations with comparison to 2D results	53
3.2.5	Study of peak temperature considering diffusion	55
3.2.6	3D THM scoping simulation using the BBM	56
3.2.7	1D axisymmetric benchmark calculation	60
3.2.8	Initial 3D TH model prediction of peak temperature	72
3.3	HG-A test	72
3.3.1	Location and description of the HG-A microtunnel test	73
3.3.2	Observations of rock features, EDZ damage, and tunnel convergence	74
3.3.3	Water and gas injection testing	78
3.3.4	Initial analysis of rock failure along the drift wall	80
3.3.5	Implementation of RBSN for modeling the HG-A test	85
3.4	Concluding Remarks	101
3.5	References	103
4.	International Collaboration - Radionuclide Interactions and Transport in Geologic Repository Environments – Pu Interaction with Bentonite	107
4.1	Introduction	107
4.2	Adsorption	107
4.3	Desorption	109
4.4	Summary	110
4.5	References	111
5.	Using Environmental Tracers to Estimate Fracture Network Properties: Bedrichov Tunnel, Czech Republic	113
5.1	Introduction	113
5.2	Lumped Parameter Models	114

5.3	Results	115
5.4	Conclusions	120
6.	KURT Site Characterization Data - Fracture and hydrologic data from deep boreholes in KURT site	121
6.1	Introduction	121
6.2	KURT (KAERI Underground Research Tunnel)	121
6.3	Geology of the KURT site	126
6.4	Deep boreholes in the KURT site	127
6.5	Concluding Remarks	128
6.6	References	130
7.	Status of International Collaboration on Modeling the Bentonite Rock Interaction Experiment (BRIE)	131
7.1	Introduction	131
7.2	Model Development required to support the BRIE Modeling Effort	133
7.3	Scoping Calculations	134
7.4	Model Setup for Hybrid DFN/Bentonite Simulations	137
7.5	Summary and Status of the Work	139
7.6	References	140
8.	Summary	141

1. Objectives and Outline

Recognizing the benefits of international collaboration in the common goal of safely and efficiently managing the back end of the nuclear fuel cycle, DOE's Office of Nuclear Energy (NE) and its Office of Used Fuel Disposition Research and Development (UFD) have developed a strategic plan to advance cooperation with international partners (Birkholzer et al., 2013; UFD, 2012). UFD's strategic plan lays out two interdependent areas of international collaboration. The first area is cooperation with the international nuclear community through participation in international organizations, working groups, committees, and expert panels. Such participation typically involves conference and workshop visits, information exchanges, reviews, and training and education. The second area of international collaboration is active R&D participation of U.S. researchers within international projects or programs (UFD, 2012). By active R&D, it is meant that U.S. researchers work closely together with international scientists on specific R&D projects relevant to both sides. With respect to geologic disposal of radioactive waste, such active collaboration provides direct access to information, data, and expertise on various disposal options and geologic environments that have been collected internationally over the past decades. Many international programs have operating underground research laboratories (URLs) in clay/shale, granite, and salt environments, in which relevant field experiments have been and are being conducted. Depending on the type of collaboration, U.S. researchers can participate in planning, conducting, and interpreting experiments in these URLs, and thereby get early access to field studies without having in situ research facilities in the United States.

UFD considers this second area, active international R&D, to be very beneficial in achieving the program's long-term goals of conducting "experiments to fill data needs and confirm advanced modeling approaches" (by 2015) and of having a "robust modeling and experimental basis for evaluation of multiple disposal system options" (by 2020). Advancing opportunities for active international collaboration with respect to geologic disposal has therefore been the primary focus of UFD's international strategy in the recent year (Birkholzer et al., 2013; Birkholzer, 2012).

This report summarizes work accomplished in FY13 related to international collaborations on natural system evaluation and tool development. The natural system evaluation and tool development work directly supports the following UFD objectives:

- Develop a fundamental understanding of disposal system performance in a range of environments for potential wastes that could arise from future nuclear fuel cycle alternatives through theory, simulation, testing, and experimentation.
- Develop a computational modeling capability for the performance of storage and disposal options for a range of fuel cycle alternatives, evolving from generic models to more robust models of performance assessment.

The natural system is an integral part of a geologic nuclear waste repository. Spatially, it extends from the disturbed rock zone (DRZ) around a disposal room, created by mechanical, thermal and chemical perturbations due to underground excavation or waste emplacement, to the surrounding geologic media, and continues all the way to a specified repository boundary. The natural system evaluation and tool development work package supports all four stages of geologic repository development: site screening, site selection, site characterization, and site suitability study. The information collected in this work package will play a pivotal role in site screening and site selection.

From the well accepted multiple barrier concept for waste repository safety, each barrier is supposed to be utilized for its safety function independently to the optimal extent. In this sense the natural barrier needs to be evaluated and necessary research conducted to ensure its optimal safety function. From a repository design point of view, an appropriate balance must be maintained between the natural system and the engineered barrier system (EBS) in the contribution to the total system performance. In practice, there is a risk to place too much reliance on the engineered barrier while not fully taking credits for the natural system. Such practice often results in an overly conservative, very expensive EBS design. Thus, as one of its main objectives, the natural system evaluation and tool development work package will ensure that sufficient research will be conducted to fully exploit the credits that can be taken for the natural system barrier.

The work documented here addresses the following specific topics identified based on the UFD R&D Implementation Plan (Wang, 2013).

- Topic #S5: Evaluation of state of the art of site characterization techniques
- Topic #S7: Identification of the needs for using underground research laboratory
- Topic #P1: Development of discrete fracture network model
- Topic #P2: Parameter estimation and uncertainty quantification of field testing
- Topic #P10: Better understanding of radionuclide interaction with geomeia
- Topic #P11: New perspective of colloid-facilitated radionuclide transport
- Topic #P14: Technical basis for thermal loading limits
- Topic #P15: Modeling of disturbed rock zone (DRZ) evolution (clay repository).

The international collaboration on the natural system evaluation and tool development in FY13 was focused on the following activities: (1) data interpretation of colloid-facilitated transport experiments at Grimsel Test Site, (2) thermal-hydrologic-mechanical (THM) model development and validation for Mont Terri FE-heater test and HG-A test, (3) experimental study of Pu-bentonite interactions, (4) modeling of stable isotope, tritium and CFC-12 transport at the Bedrichov Tunnel site as a part of the DECOVALEX program, and (5) KAERI Underground Research Tunnel testing in crystalline rocks. The work presented here involves four U.S. national laboratories and one foreign research entity:

- Section 2: Interpretations of Colloid-Facilitated Transport Experiments at the Grimsel Test Site from 2008 through 2012 (LANL)
- Section 3: International Collaboration Involving the FE Heater and HG-A Tests at Mont Terri (LBNL)
- Section 4: International Collaboration - Radionuclide Interactions and Transport in Geologic Repository Environments – Pu Interaction with Bentonite (LLNL)
- Section 5: Using Environmental Tracers to Estimate Fracture Network Properties: Bedrichov Tunnel, Czech Republic (SNL)
- Section 6: KURT Site Characterization Data - Fracture and hydrologic data from deep boreholes in KURT site (KAERI).

1.1 References

- Birkholzer, J.T. (2012). Status of UFD Campaign International Activities in Disposal Research. Report prepared for U.S. Department of Energy Used Fuel Disposition Campaign, FCRD-UFD-2012-000295.
- Birkholzer, J., Asahina, D., Chen, F., Gardner, P., Houseworth, J., Jove-Colon, C., Kersting, A., Nair, P., Nutt, M., Li, L., Liu, H.H., Painter, S., Reimus, P., Rutqvist, J., Steefel, C., Tynan, M., Wang, Y., Zavarin, M. (2013). An overview of US disposal research activities linked to international URLs. Proceedings of the 2013 International High-Level Radioactive Waste Management Conference (IHLRWM), April 28 – May 2, 2013, Albuquerque, New Mexico.
- UFD (2012). Office of Used Fuel Disposition International Program — Strategic Plan (2013) April 2012, U.S. Department of Energy.
- Wang, Y. (2013) Research &Development (R&D) Plan for Used Fuel Disposition Campaign (UFDC) Natural System Evaluation and Tool Development (Rev 1).

2. Interpretations of Colloid-Facilitated Transport Experiments at the Grimsel Test Site from 2008 through 2012

2.1 Introduction

Between 2008 and 2012, four colloid-facilitated transport experiments were conducted in a saturated shear zone at the Grimsel Test Site (GTS) in Switzerland as part of the Colloids Formation and Migration (CFM) project. The shear zone, called the MI shear zone, is a steeply-dipping feature that effectively behaves as a highly-conductive fracture in a very low-permeability granodiorite matrix. It appears as a mineral alteration band that is up to a few cm wide and through which strongly channelized flow is believed to occur. The CFM project is hosted and led by NAGRA (Swiss Nuclear Waste Cooperative), with participants from Germany, Sweden, Finland, United Kingdom, Spain, Japan, South Korea, and the United States. The CFM test bed is schematically illustrated in Fig. 2-1. All of the transport experiments discussed in this report were conducted with injections of tracer solutions into borehole/interval CFM 06.002i2 while water was extracted from the Pinkel surface packer located at the tunnel wall approximately 6.1 m from the injection interval. The tests included three colloid-homologue tracer tests (08-01, 10-01 and 10-03, where the first number indicates the year, and the second number indicates the sequential test for that year) and one test in which several different radionuclides were co-injected with colloids (12-02). The tests were conducted at different extraction flow rates, so they had significantly different transport residence times in the MI shear zone. The homologues included Th(IV), Hf(IV), Eu(III), and Tb(III), which were selected to represent tri- and tetra-valent actinides. The colloids used in all tests were derived from FEBEX

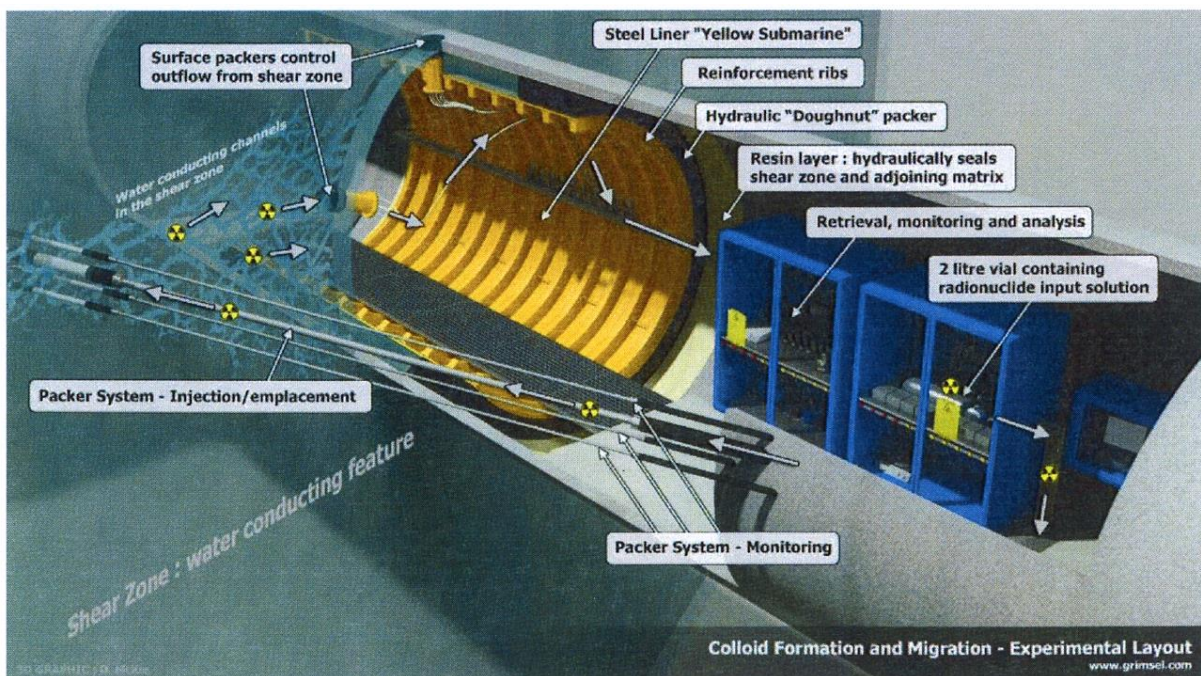


Figure 2-1. Schematic illustration of the CFM field test bed.

bentonite, taken from a mine in Spain. This report summarizes the interpretations and inferences from the four colloid-facilitated transport tests. The FEBEX bentonite will be used in an upcoming experiment in which a radionuclide-doped bentonite plug will be placed into the injection interval of borehole CFM06.002, where it is expected to swell and erode under the influence of shear zone flow, thus serving as a source term for colloid-facilitated transport.

2.2 Summary of Tracer Tests 08-01, 10-01, 10-03, and 12-02

The experimental parameters and test conditions associated with each of the colloid-facilitated transport experiments are summarized in Table 2-1. The normalized tracer breakthrough curves (extraction concentrations divided by injection mass vs. time) from each test are shown in Figures 2-2 through 2-5. The estimated percent recoveries of each tracer are listed in parentheses in the legends of these figures. Additional information about each experiment can be obtained from the Quick-Look reports issued for the tests (Schäfer et al., 2008; Rosli et al., 2010; Schäfer et al., 2010; Achtziger and Kontar, 2011; Schäfer, 2012; Kontar and Gräfe, 2012). These documents and the data from each experiment can be downloaded from the members-only area at www.grimself.com/gts-phase-vi/cfm-section/cfm-documentation (password available to US-DOE participants on request). Several points are worth mentioning regarding the four tracer tests:

1. The concentrations of the conservative dye tracers uranine and amino-G acid (AGA) were measured in the field in both the injection and extraction flows using inline fluorimeters. The concentrations of the homologues Th, Hf, Tb, and Eu and the actinides Pu, Am and Np were measured by ICP-MS at the Karlsruhe Institute of Technology (KIT), Karlsruhe, Germany. The ^{22}Na , ^{137}Cs and ^{133}Ba concentrations in Test 12-02 were measured by gamma spectrometry at both the Paul Scherer Institute (PSI) in Switzerland and at KIT, and the data from the two institutions were found to be in excellent agreement. The bentonite colloid concentrations and size distributions were measured in the field using a mobile laser-induced breakdown detection (LIBD) system operated by KIT personnel, and they were also measured offsite by LIBD at KIT and by single-particle counting (SPC) at PSI. Additionally, colloid concentrations were determined at KIT by background-subtracted ICP-MS measurements of Al (using Al present in the bentonite as a marker). In Test 12-02, the bentonite colloids were labeled with Ni, so ICP-MS measurements of Ni at KIT were also used to determine colloid concentrations. Table 2-1 indicates which colloid data sets were used for each test interpretation.
2. The colloids used in each test were generated from natural FEBEX bentonite (taken from a Spanish mine) by dispersing the bentonite in a synthetic GTS groundwater, collecting the colloidal fraction, ensuring the stability of the colloidal fraction over time, and then diluting the colloids to a target concentration (Möri, 2004). A “cocktail” of tracer solution was then prepared for injection by adding all the tracers to a colloid dispersion prepared in this manner. Thus, all tracers, including the colloids, were injected simultaneously in each test. The fraction of each tracer adsorbed to the colloids at the time of injection was determined by analyzing the supernatant of an ultra-centrifuged sample of the injection cocktail processed at approximately the time of injection.

Table 2-1. Summary of experimental parameters and test conditions in the CFM colloid-facilitated transport tests.

Parameter	Test 08-01	Test 10-01	Test 10-03	Test 12-02
Extraction Flow Rate, mL/min	160-165	48	10	25
Injection Flow Rate, mL/min	10	0.56	0.28	0.33
Injection Interval Volume, mL	4574	2000	3000	3250
Injection Loop Circulation Flow, mL/min	0	45-50	39.5	20
Inj. To Ext. Head Difference, m	0.37-0.675	0.073-0.06	1.16-1.19	0.35
Conservative Tracer Mass Injected, mg	---	5 (Uranine)	9 (Uranine)	3.7 (AGA)
Colloid Mass Injected, mg	15±4.2 (LIBD)	47.2 (LIBD)	~210 (Al)	~220 (Al, Ni)
Th(IV) mass injected, µg	19.8±1.3 (97%)	14.9±1.6 (100%)	49.8±0.9 (99%)	---
Hf(IV) mass injected, µg	23.4±1.4 (98%)	12.8±0.6 (99%)	51.6±0.1 (100%)	---
Tb(III) mass injected, µg	14.3±1.2 (89%)	10.2±0.5 (97%)	45.4±1.1 (99%)	---
Eu(III) mass injected, µg	---	12.0±0.4 (95%)	45.5±0.7 (99%)	---
²⁴² Pu(IV) mass injected, µg	---	---	---	1.6±0.1 (99+%)
²⁴³ Am(III) mass injected, µg	---	---	---	0.035±0.004 (99+%)
²³⁷ Np(V) mass injected, µg	---	---	---	4.8±0.2 (<1%)
²² Na activity injected, MBq	---	---	---	1.17±0.03 (0-3.5%)
¹³³ Ba activity injected, MBq	---	---	---	1.97±0.01 (24-34%)
¹³⁷ Cs activity injected, MBq	---	---	---	0.78±0.02 (97-98%)

Numbers in parentheses, for instance (89%), indicate the percentage of injected tracer mass estimated to be associated with colloids at the time of injection.

- Each test, involved the injection of a relatively large volume of tracer solution into a circulating flow loop running through the borehole injection interval (however, the loop was not circulated in test 08-01). This injection method resulted in an approximate exponential decay of the tracer concentrations vs. time in the injection loop (i.e., a linear plot of log concentration vs. time, which is indicative of slowly flushing a well-mixed volume). The decay in tracer concentrations occurred over time scales that were a significant fraction of the test durations. The resulting injection functions must be properly accounted for in test interpretations to ensure that transport parameters are estimated only for the time that tracers spend in the shear zone, not in the injection loop.

In tests 08-01 and 12-02, the tracer injection from the circulation loop into the shear zone was induced by pumping into the shear zone at a controlled rate (while also circulating in test 12-02, but not circulating in test 08-01), and in tests 10-01 and 10-03, the tracer solution was allowed to passively flow into the shear zone under the influence of the natural flow through the injection interval induced by the hydraulic sink at the tunnel wall (while circulating). The injection rates listed in Table 2-1 for tests 10-01 and 10-03 are the injection flow rates inferred from the concentration decay of the conservative dye tracers in the injection loop.

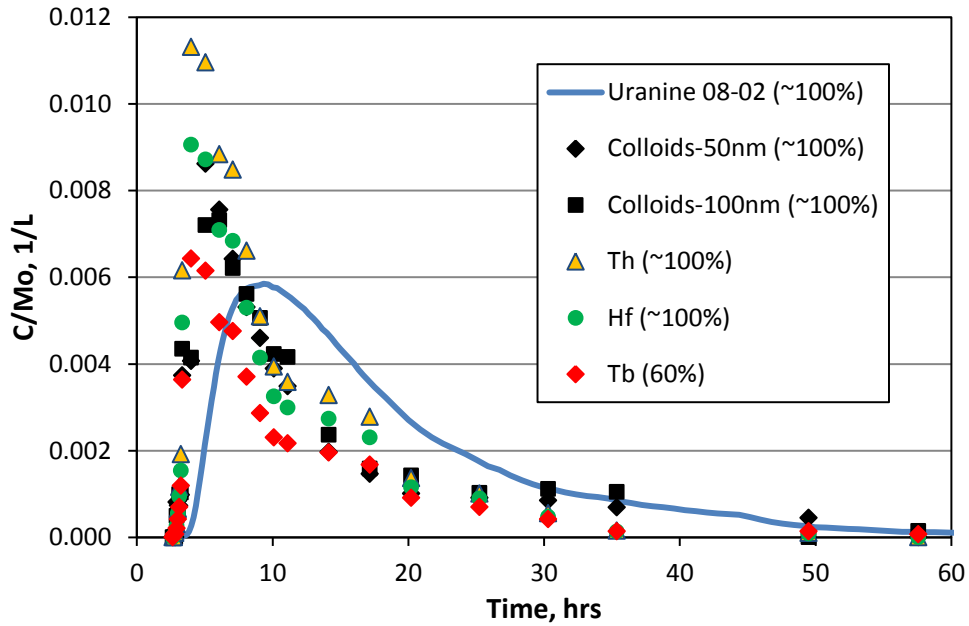


Figure 2-2. Normalized breakthrough curves in test 08-01 (recoveries indicated in parentheses). Colloid breakthrough curves are based on single-particle counting measurements from PSI.

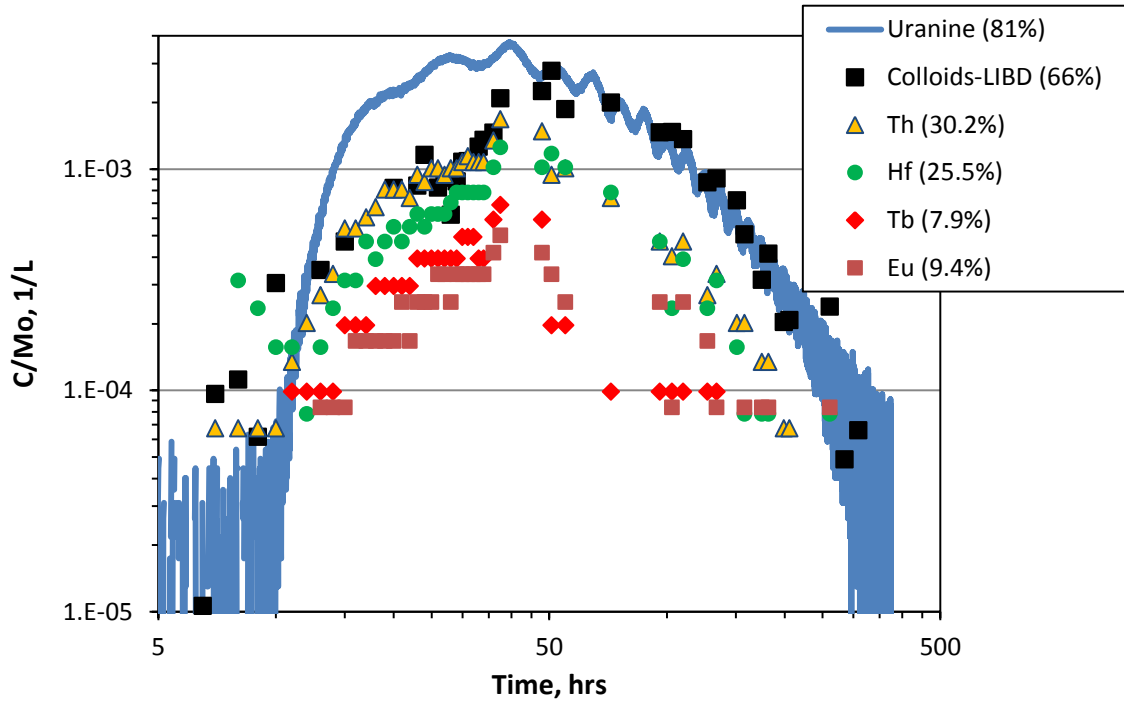


Figure 2-3. Normalized breakthrough curves in test 10-01 (recoveries indicated in parentheses).

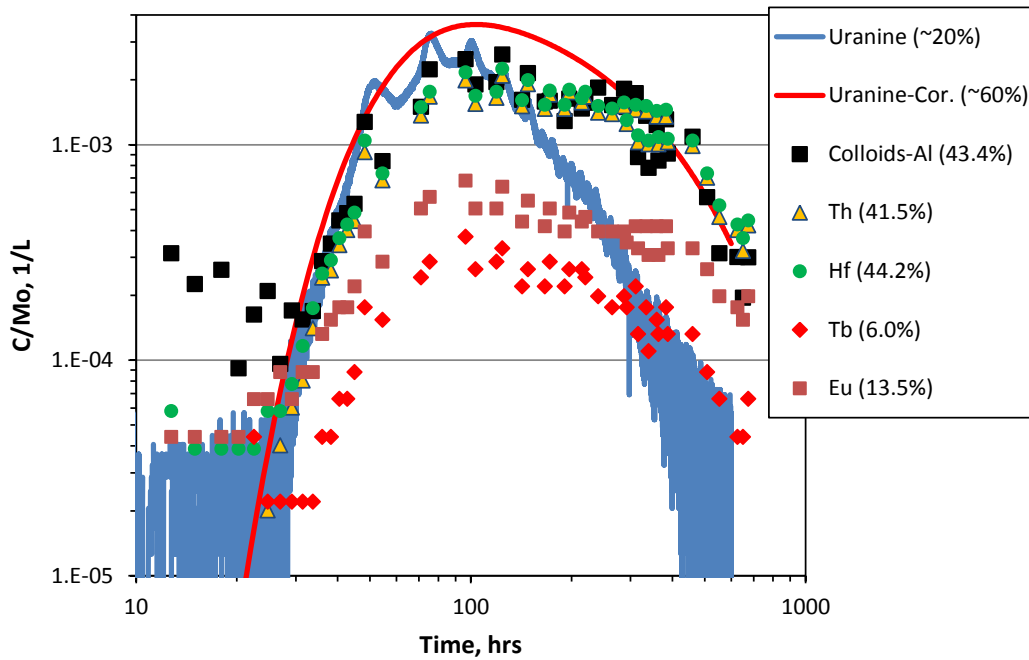


Figure 2-4. Normalized breakthrough curves in test 10-03 (recoveries indicated in parentheses).

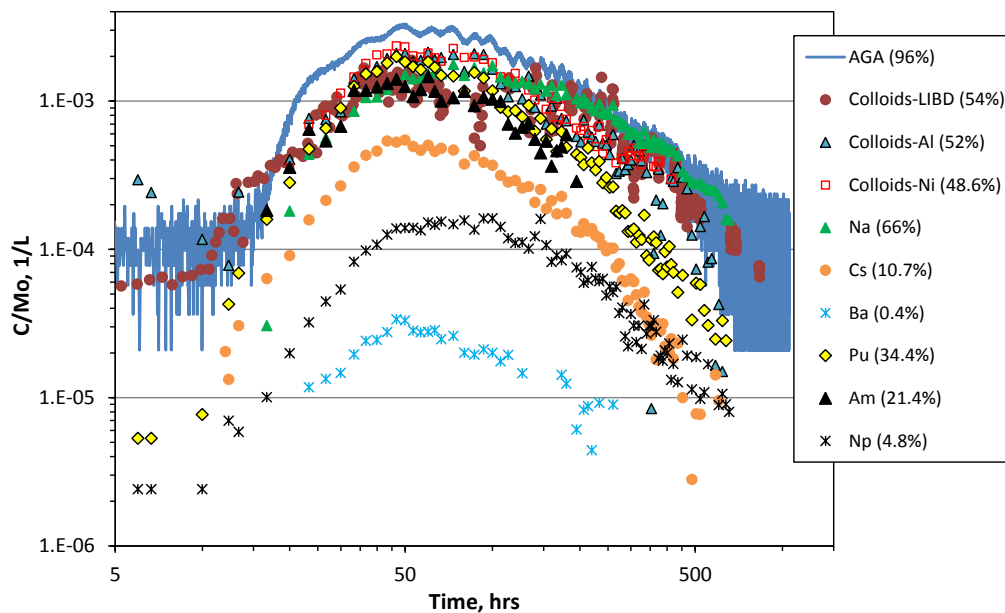


Figure 2-5. Normalized breakthrough curves in test 12-02 (recoveries indicated in parentheses).

4. With the exception of test 08-01, a conservative dye tracer was injected as part of the tracer solution in each test, which allowed colloid and reactive solute transport parameters to be estimated by comparing the breakthrough curves of these tracers with the curves of a simultaneously-injected conservative tracer. A conservative dye tracer was not used in test 08-01, but test 08-02 (Trick and Blechschmidt, 2008) was conducted in the same configuration and at approximately the same flow rates as 08-01 (except that the injection loop in test 08-02 was circulated at ~25 mL/min whereas the loop was not circulated in test 08-01) with the intent of obtaining an applicable conservative tracer breakthrough curve. However, as Figure 2-2 shows, the breakthrough curve of the conservative tracer in 08-02 was inconsistent with the breakthrough curves of test 08-01. This result typifies the general inability to duplicate flow conditions in tests at the GTS because of subtle and uncontrollable variations in barometric pressure, earth tides, and nearby lake levels that clearly affect flow patterns in the shear zone and are believed to result in the zig-zag appearance of the conservative dye tracer breakthrough curves (Figs. 2-3, 2-4, and 2-5). Because the recovery of colloids in test 08-01 was essentially 100% and for the most part earlier than the recovery of the conservative tracer in test 08-02, the colloids were assumed to have transported conservatively in test 08-01.
5. The uranine used as a conservative dye tracer in test 10-03 decayed more rapidly than expected in the injection loop, and its recovery was lower than that of the bentonite colloids, as well as Th and Hf, in this test. It was concluded that some still-unknown process caused decay of the uranine in the injection loop, thus negating the ability to compare its breakthrough curve with that of other tracers to estimate tracer transport parameters in this test. Appendix 2-A describes how a decay-corrected uranine breakthrough curve was estimated for this test to facilitate estimation of colloid transport parameters.

Figure 2-6 shows the extraction-side normalized conservative tracer breakthrough curves in each test multiplied by their respective dilution factors (extraction flow rate divided by injection flow rate) along with the normalized injection concentration histories for each test. Note that the curves for test 10-03 are corrected for the apparent uranine decay in the injection loop (Appendix 2-A). The curves are plotted as a function of volume extracted (instead of time) to facilitate their comparison at the significantly different extraction flow rates. It is apparent from Figure 2-6 that the extraction concentrations very closely follow the injection concentration histories after the extraction concentrations have peaked, which is a clear indication that the tails of the observed extraction breakthrough curves are dictated by the slow decline in concentrations in the injection loops during the tests. Note that the injection function for test 08-01 was estimated assuming a well-mixed injection interval even though the injection interval in this test was not actively circulated (there were no direct measurements of injection interval concentrations in this test because a conservative dye tracer was not used).

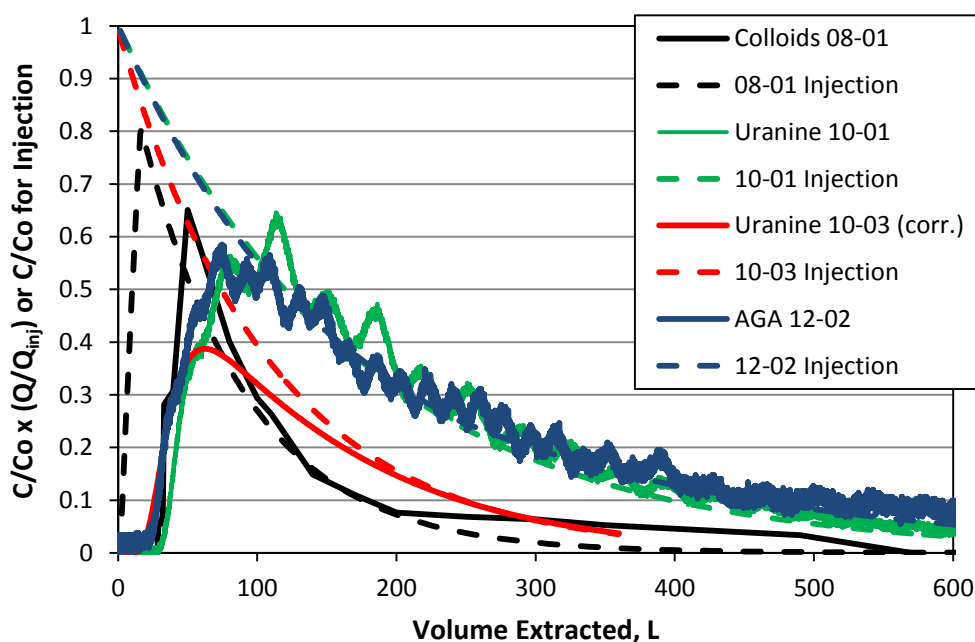


Figure 2-6. Normalized extraction and injection concentration histories in each test plotted as a function of volume extracted. Uranine in test 10-03 is corrected for injection loop decay.

The tracer breakthrough curves corresponding to transport exclusively through the shear zone in each test must be deduced by deconvolving the injection functions from the extraction functions, which is accomplished by matching the extraction functions using an advection-dispersion model while assuming that the observed injection loop concentration histories are the input functions to the shear zone. Figure 2-7 shows the shear-zone-only normalized tracer breakthrough curves as a function of volume eluted for each test obtained from this deconvolution process (see Section 2.3 for modeling approach). The breakthrough curves of this figure were calculated assuming that a 1.5-hr tracer pulse was injected directly into the shear zone (to match the 1.5-hr injection during the 08-01 test), with the normalized concentrations being divided by the extraction flow rate of each test to ensure that the areas under the curves are the same. The shear-zone mean

residence times and Peclet numbers (transport distance divided by longitudinal dispersivity) deduced for each test and used to generate the curves of Figure 2-7 are listed in Table 2-2.

It is apparent from Figure 2-7 that despite the fact that the tests were conducted using the same injection and extraction locations, there was considerable variability in tracer transport through the shear zone in the different tests. Even when the injection and extraction flow rates were the same, as in the 08-01 and 08-02 tests, the breakthrough curves were significantly different. The breakthrough curve of the 08-01 test in Figure 2-7 exhibits essentially no dispersion in the shear zone (perfect plug flow), whereas the 08-02 test has a significantly later arrival and much more dispersion than 08-01. However, the lack of dispersion deduced in test 08-01 is probably an artifact of assuming that the injection interval was well mixed despite the fact that there was no active circulation of the injection loop in this test. The shear zone breakthrough curves for tests 10-01 and 12-02 were the most similar of any pair of tests, even though test 12-02 was conducted after 3 small monitoring boreholes were drilled in the immediate vicinity of CFM06.002i2 (Figure 2-8). Interestingly, these two tests also had similar initial injection flow rates (0.488 vs. 0.556 ml/min) despite the fact that test 10-01 was a passive injection and test 12-02 was actively injected by pumping into the injection interval.

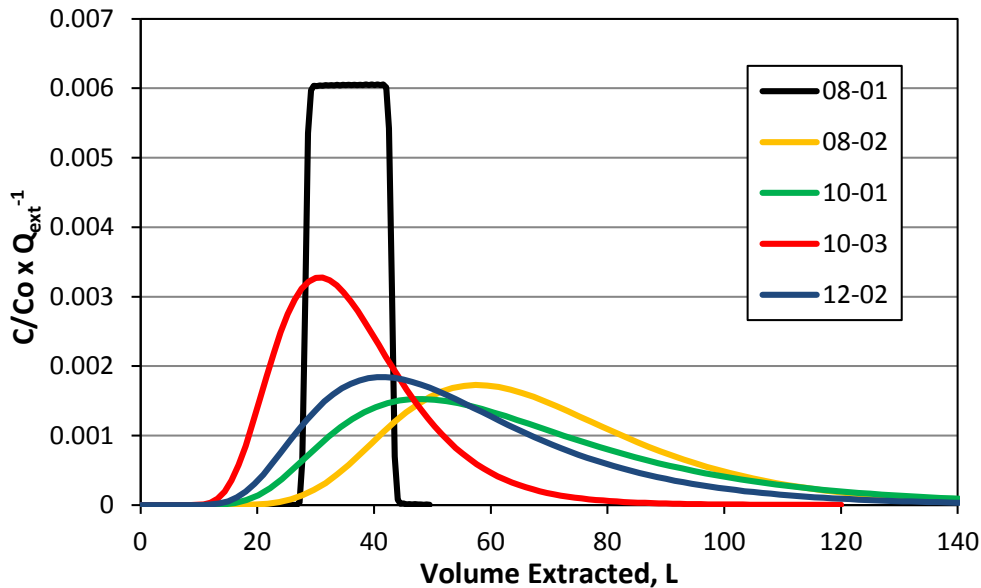


Figure 2-7. Deduced shear-zone-only breakthrough curves in each test.

Table 2-2. Mean residence times and Peclet numbers in shear zone for curves of Figure X-7.

Parameter	Test 08-01	Test 08-02	Test 10-01	Test 10-03	Test 12-02
Mean Residence Time, hr	2.85	6.25	22	60	36
Peclet number	10000	13.5	9	17	10

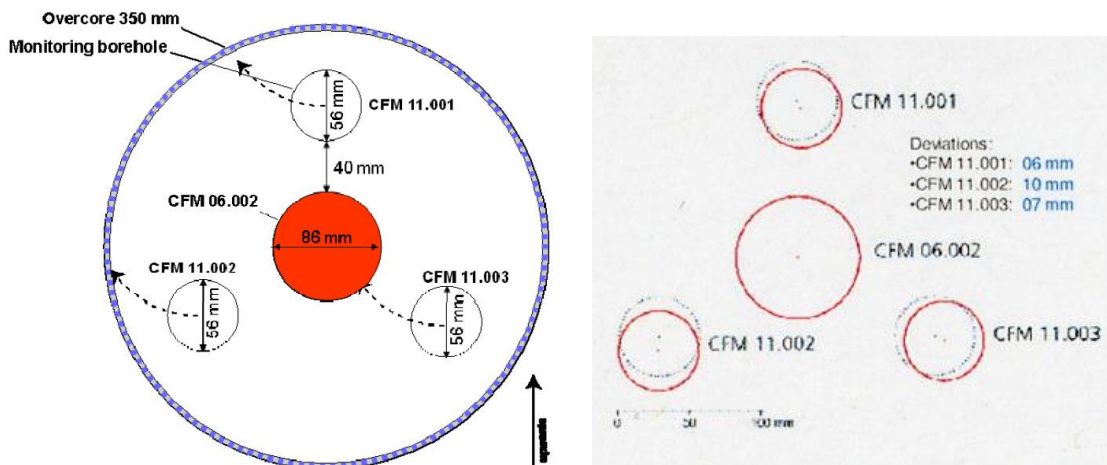


Figure 2-8. Layout of injection borehole (CFM 06.002) and monitoring boreholes (CFM 11.00x) in MI shear zone, with surveyed borehole deviations shown at right.

2.3 Interpretive Modeling Approach

The first step in the interpretation procedure for each test was to estimate the injection flow rate into the shear zone by plotting the log of the conservative tracer concentration in the injection loop vs. time and fitting a straight line to the data. The slope of this line is equal to $-Q/V$, where Q is the flow rate (mL/min) out of the interval and V is the known injection interval volume (mL). In cases where the slope changed during a test, different line segments were fitted to different portions of the data. Examples are provided in Appendix 2-A, which documents the corrections for uranine decay in the injection loop in test 10-03. For test 08-01, a conservative tracer was not used, so an injection flow rate of 10 mL/min was assumed because the flow rate was controlled by a pump and measured in this test. The injection function for each test was taken to be $C = C_0 \exp(-Qt/V)$, where C_0 = initial concentration in injection loop, and t = time.

The RELAP (REactive transport LAPlace transform) model (Reimus et al., 2003) was then used to fit the conservative tracer extraction breakthrough curves by adjusting the mean residence time and Peclet number in the shear zone as well as the fractional tracer mass participation in each test. The exponentially-decaying injection functions were directly input into RELAP to conduct these analyses. RELAP is a semi-analytical model that uses a Fourier transform inversion method to solve the Laplace-domain transport equations in either a single- or a dual-porosity system. The model can account for diffusion between fractures and matrix, as well as linear, first-order reactions in both fractures and matrix. The very rapid execution of the model makes it ideal for the numerous simulations needed for transport parameter estimation. The fractional mass participation in each test was allowed to be an adjustable parameter because some of the tests did not have complete tracer recovery, indicating that some of the tracer mass drifted out of the hydraulic capture zone induced by extraction at the Pinkel surface packer at the tunnel wall. A matrix porosity of 0.02 that extended 1 cm into the matrix from the fracture wall(s) was assumed in the shear zone for all test interpretations (the matrix was assumed to have a porosity of zero at distances greater than 1 cm from the fracture walls), and a solute matrix diffusion coefficient of $1 \times 10^{-6} \text{ cm}^2/\text{sec}$ was also assumed in all interpretations. Also, a fracture

aperture of 2 mm was assumed in all test interpretations. The mean residence time, Peclet number and fractional mass participation estimated for the conservative tracers using these matrix diffusion parameters were not significantly different from estimates obtained assuming no matrix diffusion. However, matrix diffusion and sorption were found to be necessary to explain the transport behavior of the reactive solutes that were not strongly associated with colloids, so a small amount of matrix diffusion was allowed.

In addition to providing estimates of shear-zone transport parameters for the conservative tracers, RELAP was also used to estimate colloid transport parameters (filtration and resuspension rate constants) and reactive solute transport parameters (fracture and matrix adsorption and desorption rate constants for solutes not strongly associated with colloids, and colloid desorption rate constants for solutes strongly associated with colloids). These parameter estimates were obtained by assuming that the mean residence time, Peclet number and fractional mass participation estimated for the conservative tracers also applied to the colloids and reactive solutes, and then the appropriate rate parameters were adjusted to fit the colloid or solute data.

The resulting best-fitting parameters from RELAP were used as initial parameter estimates in a 2-D numerical model that could account for processes that RELAP does not explicitly account for. The most important of these processes were (1) the variable injection flow rates observed in some of the tests and (2) the simultaneous transport of colloids and reactive solutes (RELAP does not account for interacting species). In effect, RELAP was used to obtain initial estimates for the more robust numerical model. This procedure was found to be highly effective for refinement of parameter estimates; only relatively minor adjustments to the RELAP-estimated parameters were necessary, and these adjustments could be made rather quickly by hand. The mean residence times and Peclet numbers of the shear zone in each test listed in Table 2-2 were obtained using this refinement procedure.

The 2-D numerical model simultaneously solves the following equations:

Colloid Transport in Fractures:

$$\text{Mobile: } \frac{\partial C_{col}}{\partial t} + v_f \frac{\partial C_{col}}{\partial x} - D_c \frac{\partial^2 C_{col}}{\partial x^2} + k_{fc} C_{col} - k_{rc} S_{col} + k_{fci} C_{col} - P_{col} = 0 \quad (2-1)$$

$$\text{Immobile: } \frac{\partial S_{col}}{\partial t} - k_{fc} C_{col} + k_{rc} S_{col} - k_{fci} C_{col} = 0 \quad (2-2)$$

Solute Transport in Fractures:

$$\begin{aligned} & \frac{\partial C}{\partial t} + v_f \frac{\partial C}{\partial x} - D_f \frac{\partial^2 C}{\partial x^2} + k_{1f} C C_{col} \left(1 - \frac{C_1}{C_{col} S_1^0}\right) + k_{2f} C C_{col} \left(1 - \frac{C_2}{C_{col} S_2^0}\right) + \\ & \left(\frac{\rho_f}{\eta}\right) k_{fa} C \left(1 - \frac{S_a}{S_a^0}\right) + \left(\frac{\rho_f}{\eta}\right) k_{fb} C \left(1 - \frac{S_b}{S_b^0}\right) + k_{1f} C S_{col} \left(1 - \frac{C_{filt,1}}{S_{col} S_1^0}\right) + k_{2f} C S_{col} \left(1 - \frac{C_{filt,2}}{S_{col} S_2^0}\right) - \\ & k_{1b} C_1 - k_{2r} C_2 - k_{1b} C_{filt,1} - k_{2r} C_{filt,2} - \left(\frac{\rho_f}{\eta}\right) k_{ra} S_a - \left(\frac{\rho_f}{\eta}\right) k_{rb} S_b - \left. \frac{\phi D_m}{b \eta} \frac{\partial C_m}{\partial y} \right|_{y=b} = 0 \end{aligned} \quad (2-3)$$

Solute Transport on mobile colloids (in fractures) while adsorbed to colloid sites 1 and 2:

$$\begin{aligned} & \frac{\partial C_1}{\partial t} + v_f \frac{\partial C_1}{\partial x} - D_c \frac{\partial^2 C_1}{\partial x^2} - k_{1f} C C_{col} \left(1 - \frac{C_1}{C_{col} S_1^0}\right) - k_{rc} C_{filt,1} + \\ & k_{1r} C_1 + k_{fc} C_1 - P_{col} S_a = 0 \end{aligned} \quad (2-4)$$

$$\begin{aligned} & \frac{\partial C_2}{\partial t} + v_f \frac{\partial C_2}{\partial x} - D_c \frac{\partial^2 C_2}{\partial x^2} - k_{2f} C C_{col} \left(1 - \frac{C_2}{C_{col} S_2^0}\right) - k_{rc} C_{filt,2} + \\ & k_{2r} C_2 + k_{fc} C_2 - P_{col} S_b = 0 \end{aligned} \quad (2-5)$$

Solute Transport in Matrix:

$$\begin{aligned} & \frac{\partial C_m}{\partial t} - D_m \frac{\partial^2 C_m}{\partial y^2} + \left(\frac{\rho_b}{\phi}\right) k_{fam} C_m \left(1 - \frac{S_{am}}{S_{am}^0}\right) + \left(\frac{\rho_b}{\phi}\right) k_{fbm} C_m \left(1 - \frac{S_{bm}}{S_{bm}^0}\right) - \\ & \left(\frac{\rho_b}{\phi}\right) k_{ram} S_{am} - \left(\frac{\rho_b}{\phi}\right) k_{rbm} S_{bm} = 0 \end{aligned} \quad (2-6)$$

Immobile Solute in Fractures (sorption sites a and b):

$$\frac{\partial S_a}{\partial t} - k_{fa} C \left(1 - \frac{S_a}{S_a^0}\right) + k_{ra} S_a = 0 \quad (2-7)$$

$$\frac{\partial S_b}{\partial t} - k_{fb} C \left(1 - \frac{S_b}{S_b^0}\right) + k_{rb} S_b = 0 \quad (2-8)$$

Immobile Solute in Matrix (sorption sites a_m and b_m):

$$\frac{\partial S_{am}}{\partial t} - k_{fam} C \left(1 - \frac{S_{am}}{S_{am}^0} \right) + k_{ram} S_{am} = 0 \quad (2-9)$$

$$\frac{\partial S_{bm}}{\partial t} - k_{fbm} C \left(1 - \frac{S_{bm}}{S_{bm}^0} \right) + k_{rbm} S_{bm} = 0 \quad (2-10)$$

Immobile Solute adsorbed onto Immobile Colloids in Fractures (colloid sites 1 and 2):

$$\frac{\partial C_{filt,1}}{\partial t} - k_{1f} C S_{col} \left(1 - \frac{C_{filt,1}}{S_{col} S_1^0} \right) - (k_{fc} + k_{fci}) C_1 + k_{rc} C_{filt,1} + k_{1r} C_{filt,1} = 0 \quad (2-11)$$

$$\frac{\partial C_{filt,2}}{\partial t} - k_{2f} C S_{col} \left(1 - \frac{C_{filt,2}}{S_{col} S_2^0} \right) - (k_{fc} + k_{fci}) C_2 + k_{rc} C_{filt,2} + k_{2r} C_{filt,2} = 0 \quad (2-12)$$

where,

C_{col} = concentration of colloids in solute phase, g/cm³

S_{col} = colloid concentration on fracture surfaces, g/cm³

C = solution concentration of solute in fractures, g/cm³

C_m = solution concentration of solute in matrix, g/cm³

S_a = sorbed concentration of solute on fracture surface site a , g/g

S_b = sorbed concentration of solute on fracture surface site b , g/g

C_1 = concentration of solute sorbed to site 1 on mobile colloids, g/cm³

C_2 = concentration of solute sorbed to site 2 on mobile colloids, g/cm³

$C_{filt,1}$ = concentration of solute sorbed to site 1 on immobile colloids, g/cm³

$C_{filt,2}$ = concentration of Pu on sorbed to site 2 on immobile colloids, g/cm³

S_{am} = sorbed concentration of solute on matrix surface site a_m , g/g

S_{bm} = sorbed concentration of solute on fracture surface site b_m , g/g

P_{col} = colloid production rate in fractures, g/cm³-s

v_f = fluid velocity in fractures, cm/s

D_f = solute dispersion coefficient in fractures, cm²/s

D_c = colloid dispersion coefficient in fractures, cm²/s

D_m = solute molecular diffusion coefficient in matrix, cm²/s

ρ_f = effective bulk density within fractures, g/cm³

ρ_B = bulk density in matrix, g/cm³.

η = porosity within fractures

ϕ = matrix porosity

b = fracture half aperture, cm

k_{fc} = colloid filtration rate constant (1/s) = λv_f , where λ = filtration coefficient (1/cm)

k_{rc} = reverse colloid filtration (detachment) rate constant, 1/s.

k_{fci} = irreversible colloid filtration rate constant, 1/s

k_{fa} = rate constant for sorption of solute onto fracture surface site a , ml/g-s

- k_{ra} = rate constant for desorption of solute from fracture surface site a , 1/s
- k_{fb} = rate constant for sorption of solute onto fracture surface site b , ml/g-s
- k_{rb} = rate constant for desorption of solute from fracture surface site b , 1/s
- k_{fam} = rate constant for sorption of solute onto matrix surface site a_m , ml/g-s
- k_{ram} = rate constant for desorption of solute from matrix surface site a_m , 1/s
- k_{fbm} = rate constant for sorption of solute onto matrix surface site b_m , ml/g-s
- k_{rbm} = rate constant for desorption of solute from matrix surface site b_m , 1/s
- k_{1f} = rate constant for sorption of solute onto colloid surface site 1, ml/g-s
- k_{1r} = rate constant for desorption of solute from colloid surface site 1, 1/s
- k_{2f} = rate constant for sorption of solute onto colloid surface site 2, ml/g-s
- k_{2r} = rate constant for desorption of solute from colloid surface site 2, 1/s
- S_1^0 = maximum solute capacity on colloid sorption site 1, g/g colloid
- S_2^0 = maximum solute capacity on colloid sorption site 2, g/g colloid
- S_a^0 = maximum solute capacity on fracture sorption site a , g/g solid
- S_b^0 = maximum solute capacity on fracture sorption site b , g/g solid
- S_{am}^0 = maximum solute capacity on matrix sorption site a_m , g/g solid
- S_{bm}^0 = maximum solute capacity on matrix sorption site b_m , g/g solid

Equations 2-1 through 2-12 also apply to RELAP, although simplifications are necessary to use the RELAP semi-analytical solution method (Reimus et al., 2003). Figure 2-9 shows the system geometry and boundary conditions assumed in both the numerical model and RELAP. In the numerical model, the parallel-plate fracture domain is one node wide, implying that concentration gradients across the fracture aperture are rapidly leveled by diffusion and/or advective mixing. Solute diffusion between fractures and matrix is assumed to be perpendicular to the fracture flow direction. The matrix nodes in the numerical model can be specified to have variable spacing with different porosities and different solute diffusion coefficients as a function of distance away from the fracture wall. Thus, fracture coatings or gradients in porosity or diffusion coefficients can be simulated.

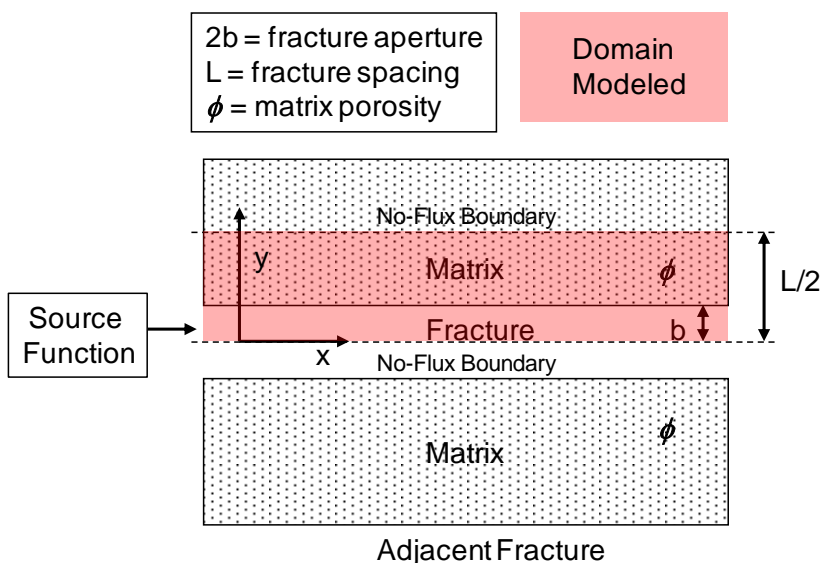


Figure 2-9. System geometry and boundary conditions assumed in the numerical model (also applies to the RELAP model).

The reaction processes accounted for by equations 2-1 through 2-12 are depicted in Figure 2-10 (including diffusion between the fractures and matrix). Solutes can adsorb to and desorb from two different sorption sites that are assumed to be present on (1) fracture surfaces, (2) matrix surfaces, (3) mobile colloid surfaces, and (4) immobile colloid surfaces. The adsorption sites on each surface can be modeled as being irreversible by simply specifying a zero desorption rate constant for that site. Colloids can attach either reversibly or irreversibly to fracture surfaces, but they are not allowed to diffuse into the matrix. When colloids attach or detach, they carry any adsorbed solutes with them, although the solutes can still independently adsorb or desorb from colloids after the colloid transition. Additionally, colloid generation from fracture surfaces is allowed. In this case, the model ensures that a background colloid concentration given by P_{col}/k_{fci} is always maintained in the system, satisfying the steady-state condition that the colloid production rate must be balanced by an irreversible filtration rate (if this were not true either all colloids would disappear from the system or the system would plug with colloids). Each arrowhead in Figure 2-10 has a reaction rate that can be specified by the user (or a diffusion coefficient in the case of diffusion into/from the matrix).

The red-outlined boxes in Figure 2-10 were the only ones that were actually used to model the colloid and solute data from the CFM colloid-homologue and colloid-radionuclide tracer tests. Specifically, only a single type of sorption site was assumed to be present on each of the surfaces present in the system (although the fracture, matrix, and colloid sites were allowed to have different adsorption and desorption rates). It was found that reasonable fits to the tracer data could be obtained without the black-outlined boxes, and it was considered desirable to not complicate the model with additional processes and parameters that did not significantly improve the fits.

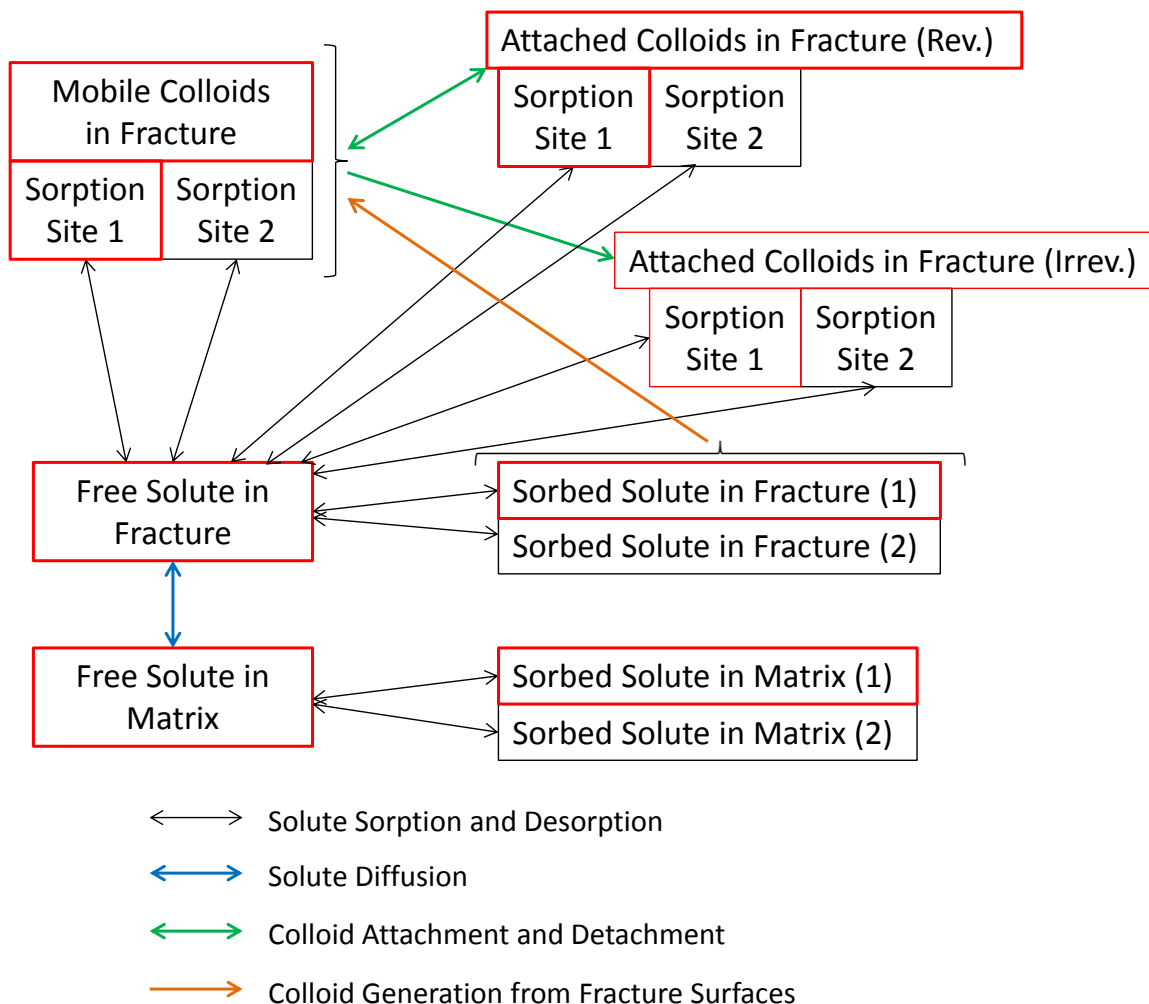


Figure 2-10. Reaction processes accounted for by equations 1-12 and implemented in the numerical transport model. Note that the red-outlined boxes were the only boxes actually used in the interpretation of the colloid-homologue or colloid-radionuclide tracer tests.

2.4 Test Interpretations

The numerical model matches to the breakthrough curves for tests 08-01, 10-01, and 10-03 are shown in Figures 2-11 to 2-13. Note that the uranine data in test 10-03 are corrected for the decay of this tracer in the injection loop in this test (Appendix 2-A), so the data and model match exactly. Also, the zig-zag fluctuations in the uranine breakthrough curves in all the tests are not reproduced by the model. These regular fluctuations are believed to be the result of naturally-occurring cyclic changes to flow patterns in the shear zone as a result of a combination of earth tides and barometric effects. Rather than attempt to model these short-period fluctuations, the models were simply matched to the general long-period trends. The data density for all the tracers except the fluorescent dyes (measured at high frequency with in-line instrumentation) is too low to clearly see the effects of the fluctuations.

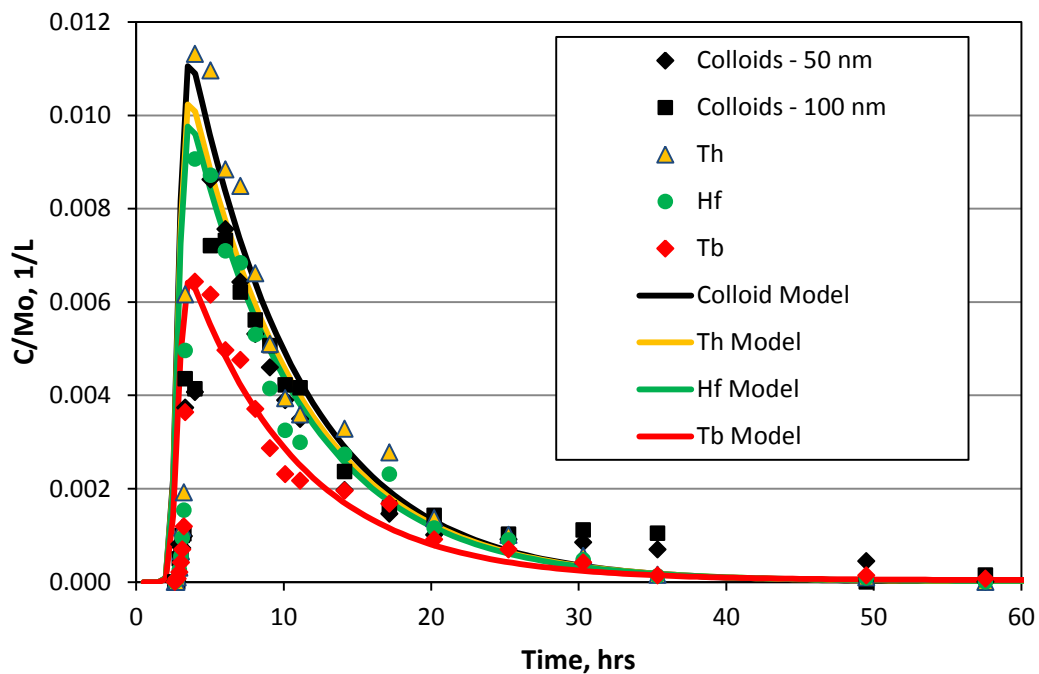


Figure 2-11. Model matches to the extraction breakthrough curves of test 08-01.

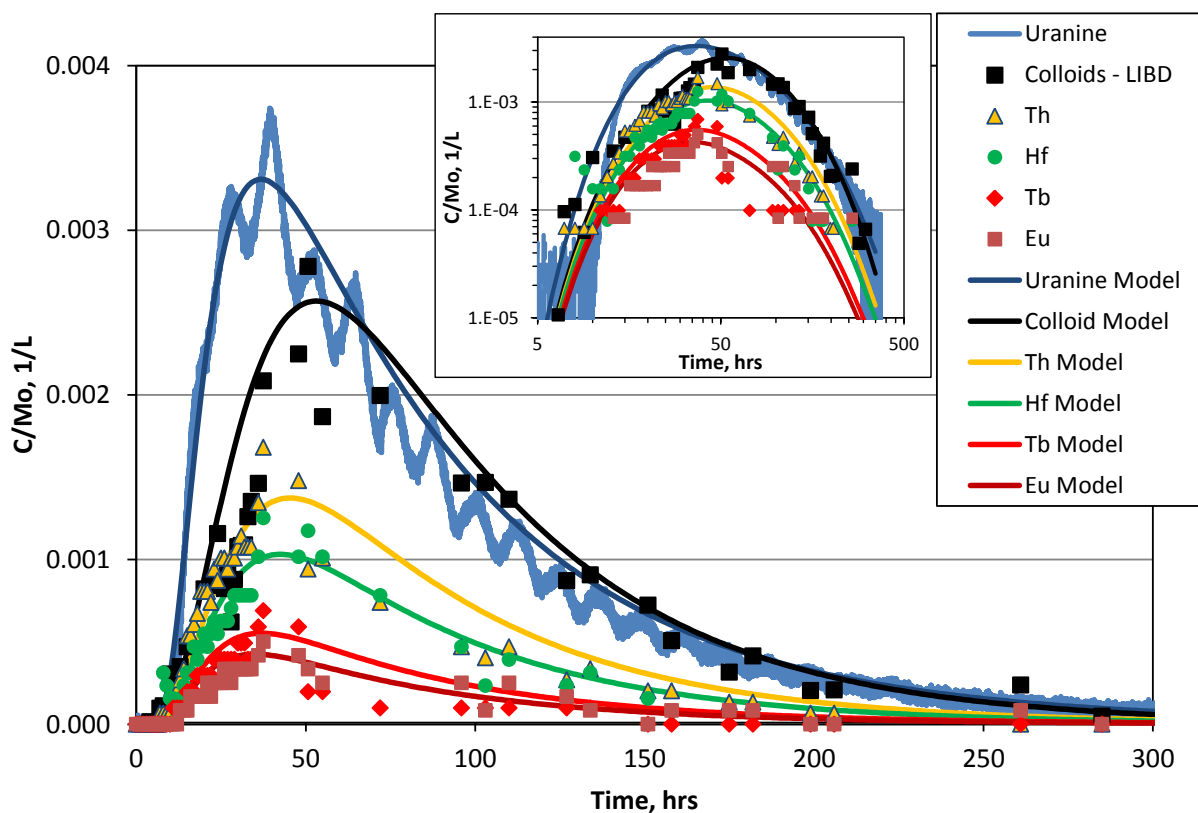


Figure 2-12. Model matches to the extraction breakthrough curves of test 10-01.

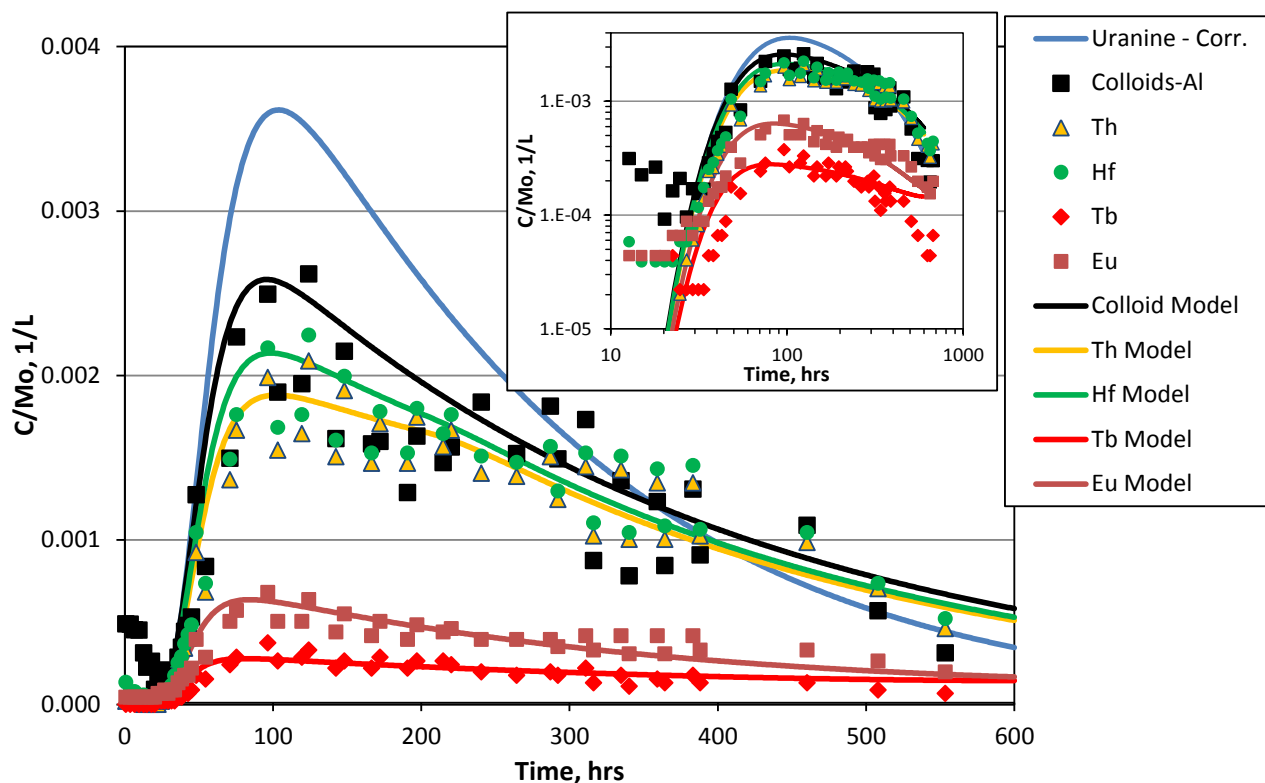


Figure 2-13. Model matches to the extraction breakthrough curves of test 10-01.

Figures 2-14 and 2-15 show the numerical model matches to the 12-02 breakthrough curves, with Figure 2-14 showing the matches to all tracers except Pu and Am, and Figure 2-15 showing the matches to the colloid, Pu and Am breakthrough curves. With the exception of Na, the solutes in Figure 2-14 had relatively low recoveries because they were either not associated with the colloids or their associations with the colloids were relatively weak, but they strongly interacted with shear zone surfaces. Na was very weakly associated with the colloids and its adsorption to other surfaces was relatively weak, so its breakthrough curve is only slightly attenuated relative to the conservative tracer AGA. For the other solutes in Figure 2-14, separate model curves are shown for the colloid-associated and solute contributions to the overall curves. Pu and Am both had strong associations with the bentonite colloids, so their breakthrough curves in Figure 2-15 closely follow the colloids, although some desorption from the colloids is apparent. Note that test 12-02 was the only test in which multiple flow pathways through the shear zone were assumed to achieve a good model match to the conservative tracer breakthrough curve, with 88% of the tracer mass assumed to follow a short-residence time pathway (36 hrs with Peclet number of 10), and 10% of the tracer mass assumed to follow a longer-residence time pathway (200 hrs with Peclet number of 10). Multiple flow pathways were assumed in this test because it was considered important to match the conservative tracer data very well to obtain good estimates of the transport parameters for all the other tracers used in this test.

The bentonite colloid transport parameters resulting in the model matches shown in Figures 2-11 through 2-15 are listed in Table 2-3. It is interesting that the colloids in the different tests

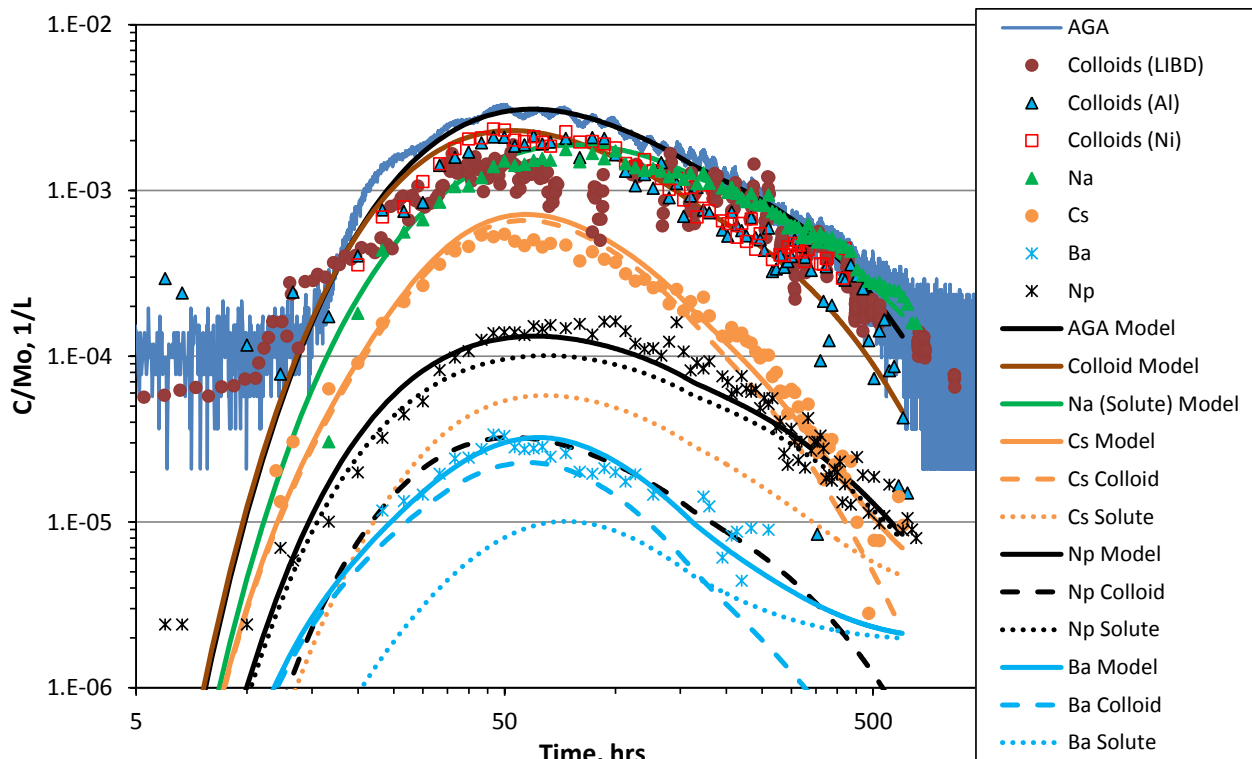


Figure 2-14. Model matches to the AGA, colloid, Na, Cs, Ba and Np breakthrough curves of test 12-02

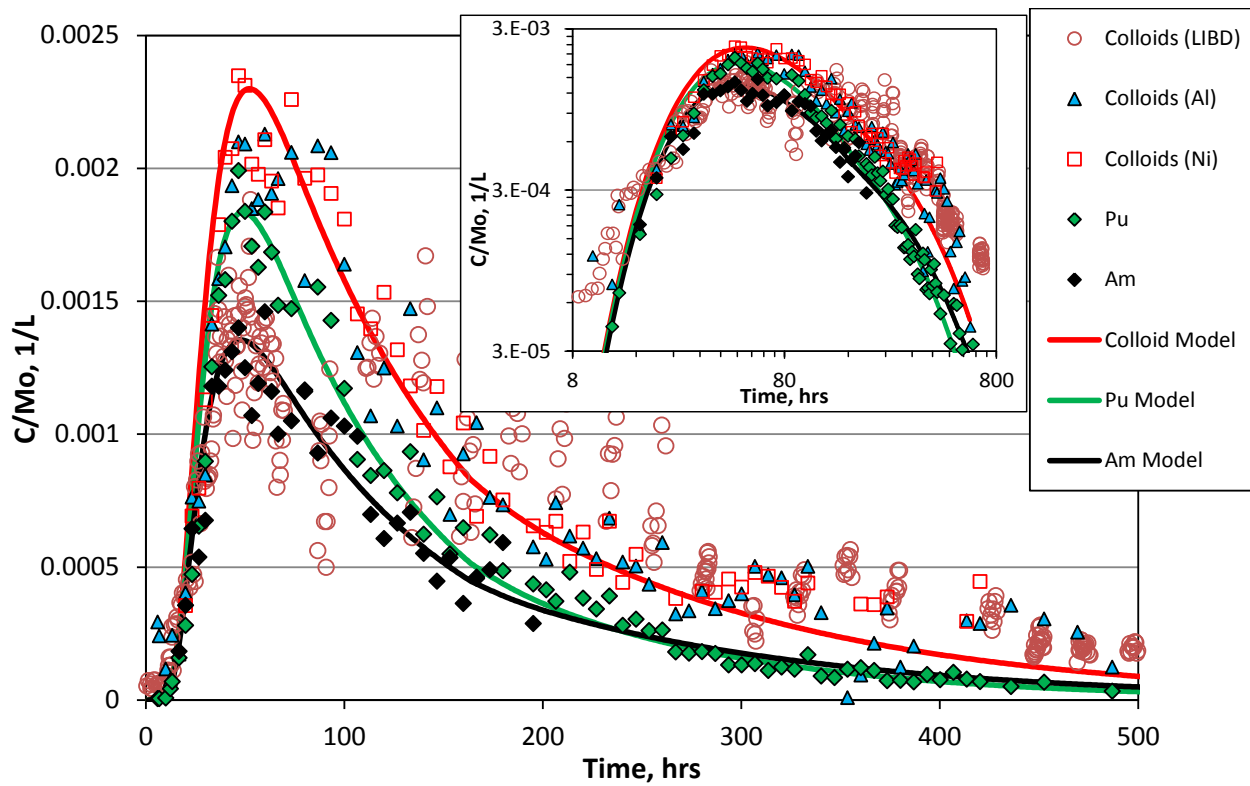


Figure 2-15. Model matches to the colloid, Pu, and Am breakthrough curves of test 12-02

Table 2-3. Apparent colloid transport parameters in the CFM tracer tests.

Test	k_{fci}^* , ml/g-hr	k_{fc}^* , ml/g-hr	k_{rc}^* , 1/hr
08-01	0.015	---	---
10-01	0.0065 (0.01)**	0.2	0.286
10-03	(0.007)**	0.01	0.0042
12-02	0.013	---	---

* k_{fci} = irreversible filtration rate constant; k_{fc} = reversible filtration rate constant; k_{rc} = resuspension rate constant for reversible filtration

**Numbers in parentheses are best estimates of irreversible filtration rate constant if there is no reversible filtration reaction

follow different apparent transport behavior, appearing to be irreversibly filtered in tests 08-01 and 12-02, reversibly filtered in test 10-03, and a combination of reversibly and irreversibly filtered in test 10-01. An explanation for this behavior cannot be offered, although it was apparent that different flow pathways were accessed in the tests (Figure 2-7), so it is certainly plausible that different colloid transport parameters could have been experienced in the different tests. Alternatively, it is possible that subtle differences in the preparation of the colloid dispersions for the different tests resulted in slightly different transport behavior in the tests. It is noteworthy that the two tests exhibiting reversible colloid filtration (10-01 and 10-03) were the two tests with passive injections, whereas the two tests with active injections exhibited only irreversible filtration. This result suggests the possibility that the colloids (and associated homologues) exited the injection loop more slowly than the conservative tracer under the passive injection conditions, resulting in an apparent delay in the arrival of the colloids relative to the conservative tracer at the extraction point. Because all tracers were assumed to follow the same injection function, the models had to account for this delay by invoking a reversible filtration process in the shear zone. The delayed arrival of the colloids relative to the uranine in test 10-01 is quite obvious, and it is interesting that the turbidity in the injection loop in this test showed a slower decay than uranine (Figure 2-A8), suggesting that the colloids exited the loop more slowly than the uranine. Injection loop turbidity histories were not reported in all the colloid tracer tests, so no attempt was made to use different injection functions for the colloids than the solute tracers in any of the tests.

Table 2-4 lists the homologue adsorption and desorption rate constants for tests 08-01, 10-01 and 10-03, as well as the Pu (tetravalent) and Am (trivalent) adsorption and desorption rate constants for test 12-02. Note that although adsorption and desorption rate constants are listed in Table 2-4 for solute interactions with the fracture and matrix surfaces in the shear zone, the model breakthrough curves are quite insensitive to these parameters as long as they reflect strong adsorption to these surfaces. The only parameter that the model curves were very sensitive to for any of these species was the rate constant for desorption from the colloids. The model interpretations indicate that the transport behavior of the homologues, Pu and Am are dictated by how rapidly these solutes desorb from the colloids after entering the shear zone, and once they desorb, they appear to be rapidly and strongly adsorbed to immobile surfaces such that they are effectively removed from the test for the remainder of its duration.

Table 2-4. Tri- and tetravalent solute rate constants in CFM tracer tests (red numbers are desorption rate constants from colloids, the only parameter that the tri- and tetravalent solutes were sensitive to).

Parameter	Test 08-01	Test 10-01	Test 10-03	Test 12-02
X* k _{fa} (ml/g-hr), k _{ra} (1/hr)	10, 0.01	10, 0.01	10, 0.01	10, 0.01
X* k _{fam} (ml/g-hr), k _{ram} (1/hr)	10, 0.01	10, 0.01	10, 0.01	10, 0.01
Th k _{1f} (ml/g-hr), k _{1r} (1/hr)	10, 0.02	10, 0.022	10, 0.0085-0.0001 (0.005)**	
Hf k _{1f} (ml/g-hr), k _{1r} (1/hr)	10, 0.06	10, 0.033	10, 0.005-0.0001 (0.003)**	
Tb k _{1f} (ml/g-hr), k _{1r} (1/hr)	10, 0.2	10, 0.06	10, 0.05-0.002 (0.045)**	
Eu k _{1f} (ml/g-hr), k _{1r} (1/hr)	---	10, 0.072	10, 0.03-0.002 (0.028)**	
Pu k _{1f} (ml/g-hr), k _{1r} (1/hr)				10, 0.005-0.04 (0.01)**
Am k _{1f} (ml/g-hr), k _{1r} (1/hr)				10, 0.018

*X stands for Th, Hf, Tb, Eu, Pu and Am; the sorption and desorption rate constants onto fracture and matrix surfaces for all these species were assumed to be the same (model results were not sensitive to these parameters as long as strong sorption with slow desorption rates were specified).

**First number is initial colloid desorption rate constant and second number is final desorption rate constant. Desorption rate constants varied linearly with time from beginning of test to end of test for Tb, Eu, and Pu; and they varied linearly with time up to 200 hrs for Th and Hf (after 200 hrs they remained constant at 0.0001 hr⁻¹, which is effectively zero, until the end of the test). Numbers in parentheses are the best-fitting time-invariant desorption rate constants.

It was found that significant improvements in the ability of the numerical model to match the homologue breakthrough curves in test 10-03 and the Pu breakthrough curve in test 12-02 could be obtained by assuming that the colloid desorption rate constants for these species varied during these tests rather than remaining constant. The model curves for these species in Figures 2-13 and 2-15 reflect the time-varying rate constants (described in notes of Table 2-4). Figures 2-16 and 2-17 show comparisons of the model curves obtained using the time-varying desorption rate constants and invariant rate constants for these species (numbers in parentheses in Table 2-4). For the homologues in test 10-03, the desorption rate constants were decreased significantly with time to explain the tendency for the differences between the colloid and homologue breakthrough curves to decrease at later times in this test (particularly for Eu and Tb). Conversely, in test 12-02, the Pu desorption rate constant was increased with time to explain the divergence of the Pu and colloid breakthrough curves late in this test. In all other cases, the observed solute breakthrough curves were fit quite well assuming time-invariant rate constants.

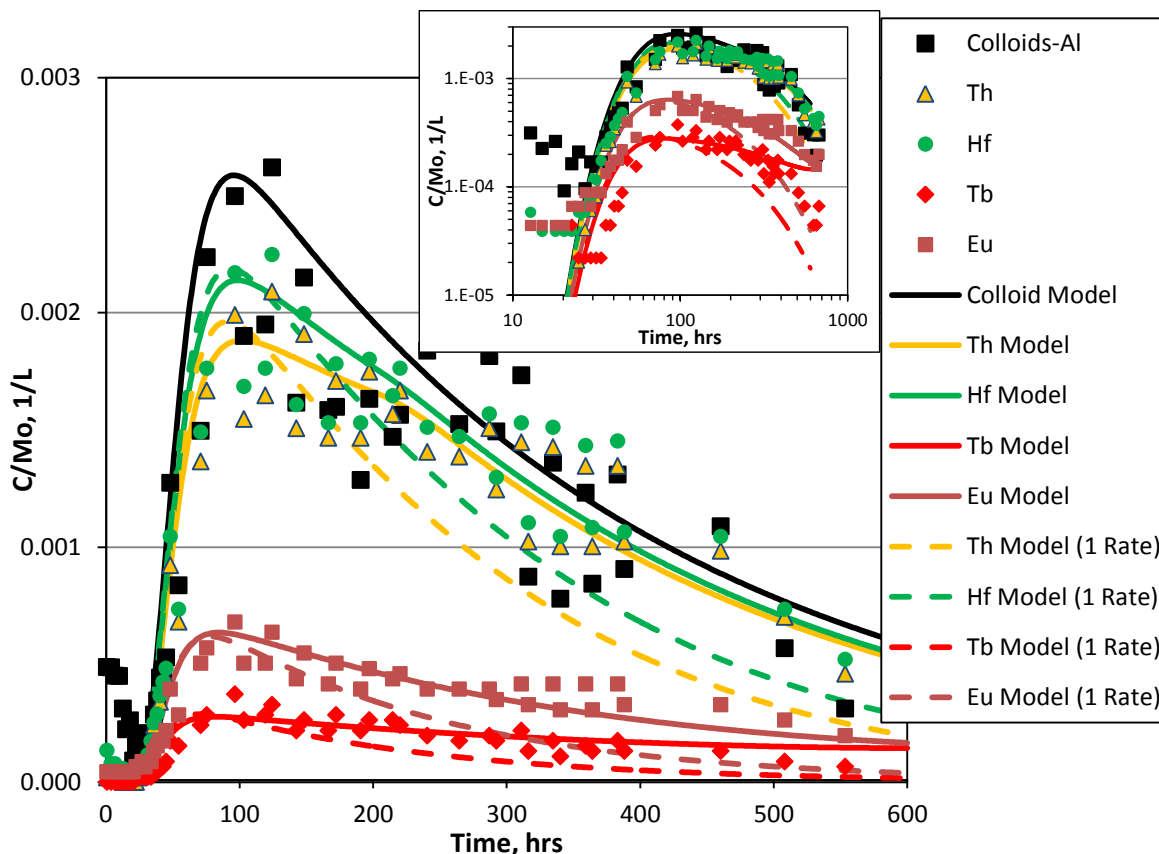


Figure 2-16. Model breakthrough curves for homologues in test 10-03 assuming time-varying (solid curves) and time-invariant (dashed curves) desorption rate constants from colloids.

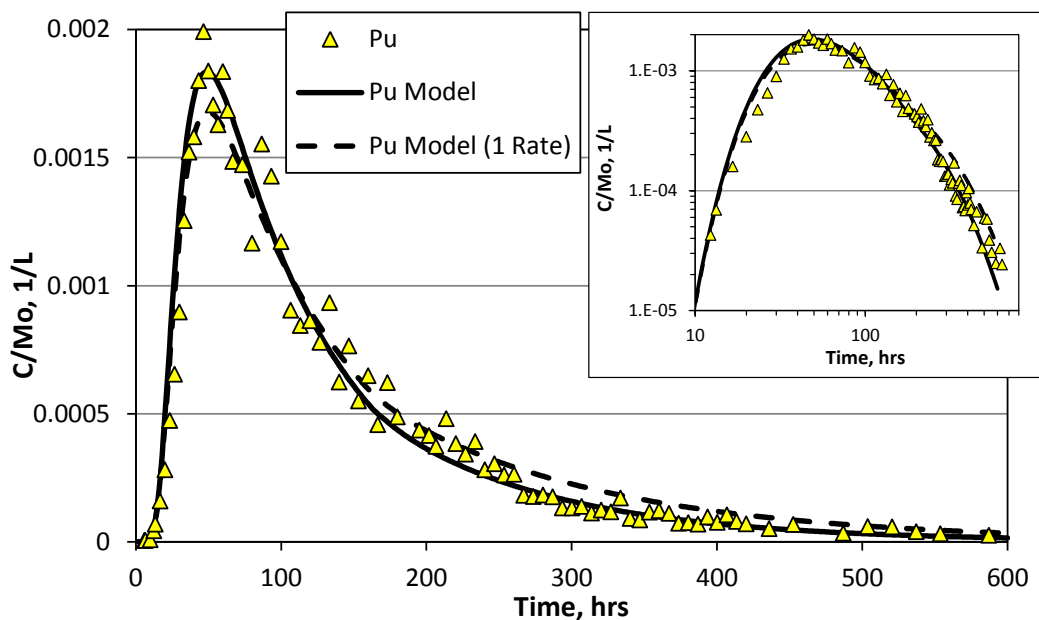


Figure 2-17. Model breakthrough curves for Pu in test 12-02 assuming time-varying (solid curves) and time-invariant (dashed curves) desorption rate constants from colloids.

Although the time-varying desorption rate constants clearly yield better agreement between the models and data, it is difficult to come up with a logical explanation for such behavior. If this behavior is real, one possible explanation is that the colloids tended to travel through different flow pathways late in the tests than early in the tests. In the case of test 10-03, the slower desorption rates of homologues from the colloids and the slower colloid filtration rates (indicated by the apparent reversibility of colloid filtration) late in the test suggest that the flow pathways at late times were more open (i.e., larger apertures) than pathways at early times. In addition to causing less colloid filtration, larger-aperture pathways will have less available surface area per unit volume of flowing water to compete with colloids for homologue adsorption, resulting in smaller apparent desorption rates from colloids. Using this same reasoning, it could be argued that the later flow pathways in test 12-02 were less open (smaller apertures) than the early pathways, resulting in greater desorption of Pu from the colloids late in the test. However, unlike test 10-03, where all the homologues exhibited similar time-varying desorption behavior, Am and other radionuclides associated with colloids in test 12-02 did not exhibit the time-variant desorption that Pu exhibited. This result suggests that either the apparent increase in Pu desorption rate is an artifact of an erroneous trend in the Pu data, or perhaps it is the result of changes in mineralogy of the flow pathways rather than changes in aperture, with the mineralogy changes tending to enhance Pu desorption from the colloids but not the desorption of other radionuclides. Another possible explanation for the apparent time-varying desorption rates from colloids are so-called bond-aging effects (Kaplan and Serkiz, 2004), where sorbed solutes tend to desorb more slowly the longer they remain adsorbed to a surface. However, bond-aging could not explain the apparent increase in Pu desorption rates in test 12-02. Also, the time scales associated with bond-aging are generally thought to be much longer than the differences between the early and late times in the tracer tests, and if bond aging were a valid explanation, it should have affected the homologues in test 10-01 as well as test 10-03. It is also important to note that the tracer cocktails were prepared at KIT a few days prior to injection and then transported to the GTS, so considerable bond aging would have occurred prior to injection, and very little additional bond aging would have occurred between early and late times in the tests. At the present time, we cannot offer a definitive explanation for the apparent time-varying changes in the desorption rate constants observed in some of the tests for some of the solutes.

The solute sorption and desorption parameters yielding the ^{22}Na , ^{137}Cs , ^{133}Ba , and ^{237}Np model curves in Figure 2-14 are listed in Table 2-5. The interpreted transport behavior of the ^{137}Cs and ^{133}Ba is similar to that of the tri- and tetravalent homologues and actinides in that the extraction breakthrough curves of these radionuclides are dominated by colloid-facilitated transport. However, ^{137}Cs and ^{133}Ba are less strongly associated with the bentonite colloids than the higher-valence species, with both nuclides exhibiting greater desorption from the colloids than the homologues, Pu and Am. The behavior of the ^{22}Na is consistent with that of a rapidly and reversibly adsorbing solute that adsorbs weakly in the matrix after diffusing out of fracture flow pathways. This nuclide, more than any other, prompted the implementation of a dual-porosity model with a low but non-zero matrix porosity extending some distance into the fracture walls of the shear zone. The shape of the ^{22}Na breakthrough curve cannot be matched by assuming adsorption strictly within the flowing pathways of the shear zone; some diffusive transport into secondary porosity (i.e., the matrix), coupled with sorption in this secondary porosity must be invoked to match the data. The ^{237}Np transport behavior is peculiar in that it appears to be dominated by a strong adsorption process that is irreversible over the time scale of the test. The very weak (almost nonexistent) adsorption of the ^{237}Np to the colloids seems incompatible with

such strong adsorption to shear zone surfaces, so a logical explanation for the interpreted behavior is that a large fraction of the ^{237}Np was reduced from Np(V) (its oxidation state in the injection solution) to Np(IV) in the shear zone. Np(IV) is known to be much less soluble and much more strongly adsorbing than Np(V), so reduction of the Np would have resulted in what appeared to be a strong adsorption process (which may have been partially precipitation) occurring at a rate that likely reflected the reduction rate.

Table 2-5. Sorption and desorption rate constants for non-trivalent and non-tetravalent solutes in tracer test 12-02 (red numbers indicate parameter values that model matches were most sensitive to).

Solute	Fracture	Matrix	Colloids
	k_{fa} (ml/g-hr), k_{ra} (1/hr)	k_{fam} (ml/g-hr), k_{ram} (1/hr)	k_{1f} (ml/g-hr), k_{1r} (1/hr)
^{22}Na	0, 0		1, 3.76
^{133}Ba	3, 1		5, 0.0025
^{137}Cs	3, 1		5, 0.001
^{237}Np	0.041, 0.00001		4, 5

2.5 Implications for Nuclear Waste Repository Performance Assessments

To assess the implications of the tracer test results for colloid-facilitated radionuclide transport over longer time and distance scales, it is of interest to examine the scaling behavior of both the colloid filtration parameters and the desorption parameters for the tri- and tetravalent homologues or actinides from the colloids in the four tracer tests. Figure 2-18 shows the model-deduced colloid-filtration rate constants as a function of mean conservative tracer residence time in the tests. In this case, the plot shows the best-fitting *irreversible* filtration rate constants, even for the tests in which the colloid transport behavior was better described by partially or fully reversible colloid filtration (10-01 and 10-03). It is apparent that the rate constants tend to decrease with mean residence time in the tests. The numbers next to each data point in Figure 2-18 are the colloid recoveries relative to conservative tracers in the four tests. Extrapolation of the sparse data to significantly longer residence times that are more relevant for performance or risk assessments is very uncertain and likely to be misleading. The time scales of the tests are several orders of magnitude shorter than time scales relevant to performance assessments (100's to 1000's of years or more). A simple linear extrapolation would suggest that filtration rate constants would decrease to near zero (i.e., no filtration, or 100% recovery) after 200 hours of residence time, which is obviously unrealistic. A linear regression of the log-transformed data of Figure 2-18 (see Figure 2-21, $R^2 = 0.57$) suggests that colloid recoveries would drop to about 0.1% after 1500 hrs, or after about 2 months residence time. However, if a log-log extrapolation is done using only the filtration rate constants from tests 10-03 and 12-02 (the two longest residence time tests), then the colloid recoveries would only drop to 1% after about 5000 years. Clearly, there is a very large amount of uncertainty associated with such extrapolations, and it is likely that the reality lies somewhere between these two extremes.

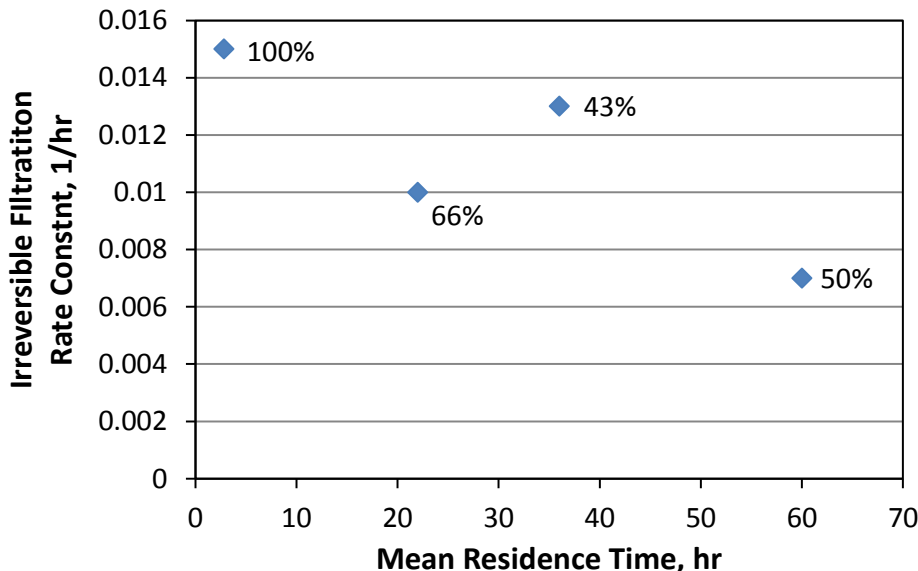


Figure 2-18. Irreversible colloid filtration rate constants vs. time in the four CFM tracer tests. Numbers next to data points are the recoveries of colloids associated with each data point.

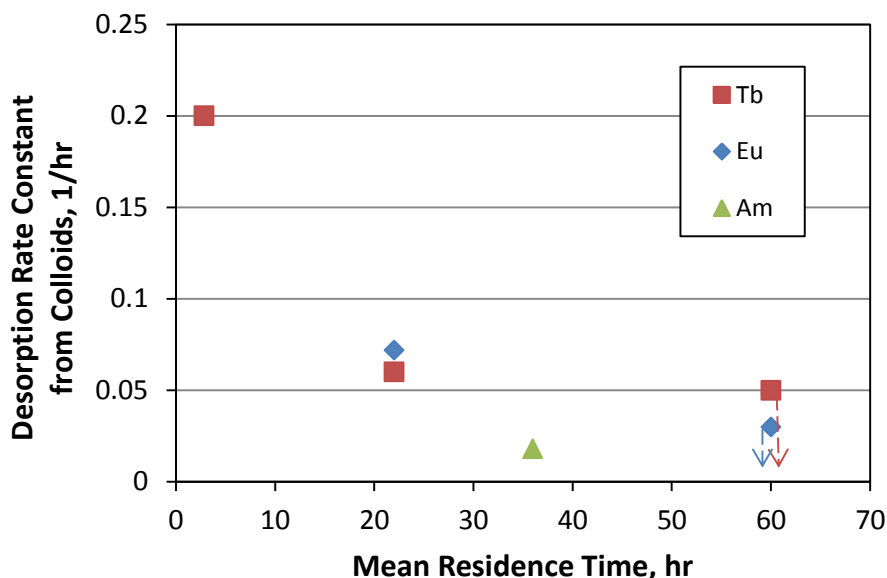


Figure 2-19. Desorption rate constants from colloids vs. time for trivalent homologues and Am in the four CFM tracer tests. Dashed arrows indicate apparent changes at late times.

Figure 2-19 shows desorption rate constants from the colloids for the trivalent homologues and Am as a function of residence time in the shear zone from the four tracer tests, and Figure 2-20 shows an analogous plot for the tetravalent homologues and Pu. The dashed arrows in these figures depict the time-varying trends in the cases where the desorption rates appeared to change with time. In both figures, there is a tendency for the desorption rate constants to decrease with residence time. However, the tetravalent species clearly desorb more slowly than the trivalent species in any given test. Interestingly, the Am and Pu in test 12-02 each have the slowest

desorption rate constants for the tri- and tetravalent species, respectively (if the increase in Pu desorption rate constant at late times is ignored).

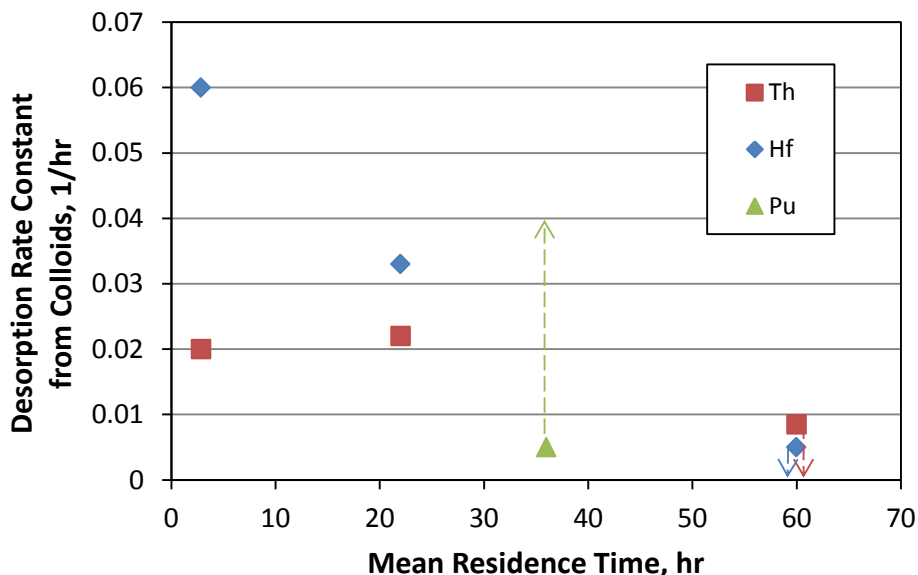


Figure 2-20. Desorption rate constants from colloids vs. time for tetravalent homologues and Am in the four CFM tracer tests. Dashed arrows indicate apparent changes at late times.

Linear regression fits to the log-log transformed data of Figures 2-19 and 2-20 are shown in Figure 2-21, along with the linear regression fit to the log-log transformed colloid filtration data of Figure 2-18. Extrapolation of the desorption rate constant regressions to longer times yields predictions that 99% of the trivalent species will desorb from the colloids after a residence time of about 500 hours and 99% of the tetravalent species will desorb after a residence time of about 1 year. Of course, the uncertainties associated with these extrapolations are quite large, especially for the actinides Am and Pu, which although combined with the tri- and tetravalent homologues for the regressions of Figure 2-21, exhibited smaller desorption rate constants than the respective homologues. The observation of time-dependent desorption rate constants for some of the species in some of the tests casts additional uncertainty on extrapolations of desorption rate constants to longer times. Nonetheless, the tracer test data suggest that the time scales for desorption of the actinides from the colloids should be relatively short compared to time scales for performance assessment, implying negligible colloid-facilitated transport of the actinides over performance assessment time scales of multiple years, even if colloid filtration is minimal. Combined with the extrapolation of colloid filtration rate constants discussed above, the tracer test data would suggest negligible colloid-facilitated transport after relatively short times.

It is of interest to compare the actinide desorption rate constants from colloids in the CFM tracer tests to the rates measured in the laboratory experiments of Huber et al. (2011). Huber et al. (2011) measured desorption rate constants for Am and Pu in the ternary system involving bentonite colloids, fracture fill material from GTS, and a synthetic GTS ground water at two different starting concentrations of the nuclides. Using the Am and Pu injection concentrations in CFM test 12-02 (4.4×10^{-11} mol/L and 2×10^{-9} mol/L, respectively), the desorption rate

constants predicted by the experiments of Huber et al. (2011) would be approximately 0.01 hr^{-1} for Am and 0.002 hr^{-1} for Pu. The desorption rate constants deduced in test 12-02 were approximately twice these values (increasing to about an order of magnitude higher for Pu late in test 12-02). This agreement is considered to be quite good, and the higher rates in the field experiments could just reflect that the shear zone surface area available for competitive sorption with the colloids was somewhat higher in the field test than in the lab experiments.

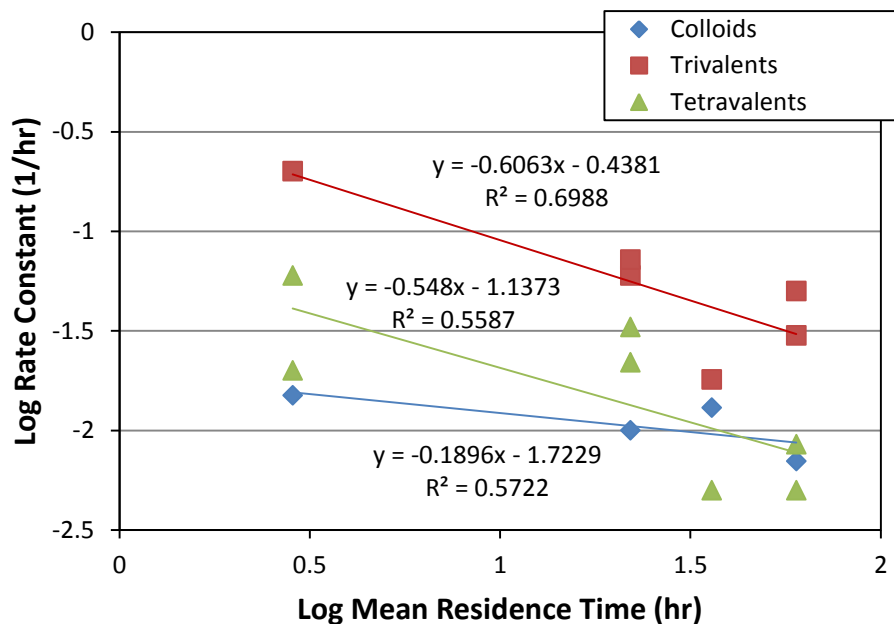


Figure 2-21. Log irreversible filtration rate constant vs. log time (colloids) and log desorption rate constants from colloids vs. log time (trivalent and tetravalent species) in the tracer tests.

The apparent time-scale dependence of the colloid filtration rates and the desorption rate constants in Figures 2-18 through 2-20 are worthy of further discussion. Mechanistically, time-dependent rate constants for specific reactions are not supported by theory or literature data. However, a simple example can illustrate how a small number of reactions or, more accurately, a small number of different types of colloids (with respect to filtration) or different types of sorption sites with different corresponding reaction rates, could result in the observed time-dependent behavior. Figure 2-22 shows the desorption rate constants for the tetravalent species as a function of residence time in the CFM tracer tests (data of Figure 2-20) along with a line generated from a simple calculation of the *apparent* rate constant resulting from a system in which there are 3 types of sorption sites on the colloids, with desorption rate constants of 0.1 hr^{-1} , 0.01 hr^{-1} , and 0.001 hr^{-1} . One-third of the mass of the tetravalent solute was assumed to occupy each of the sites at time zero. Even though each of the sorption sites has a time-invariant desorption rate constant, the overall system exhibits time-dependent desorption rate behavior similar to that observed in the CFM tracer tests. Figure 2-23 shows a similar plot of the CFM colloid filtration rate constants along with a line generated assuming three colloid filtration rate constants (0.03 hr^{-1} , 0.006 hr^{-1} , and 0.002 hr^{-1}), with one-third of the colloids being assigned each of these rate constants at time zero.

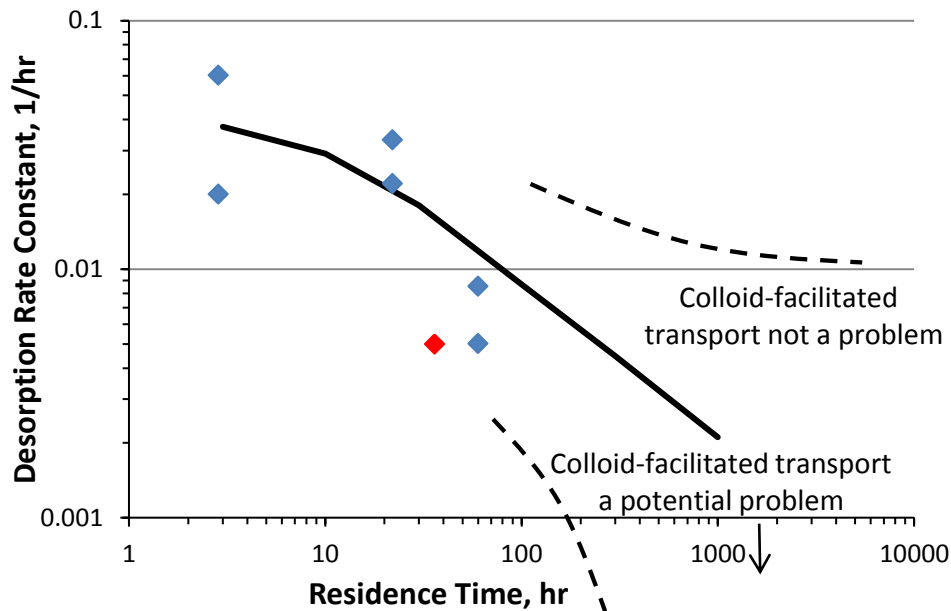


Figure 2-22. Desorption rate constants from colloids for the tetravalent species as a function of residence time in the CFM tracer tests. Red data point is Pu in test 12-02.

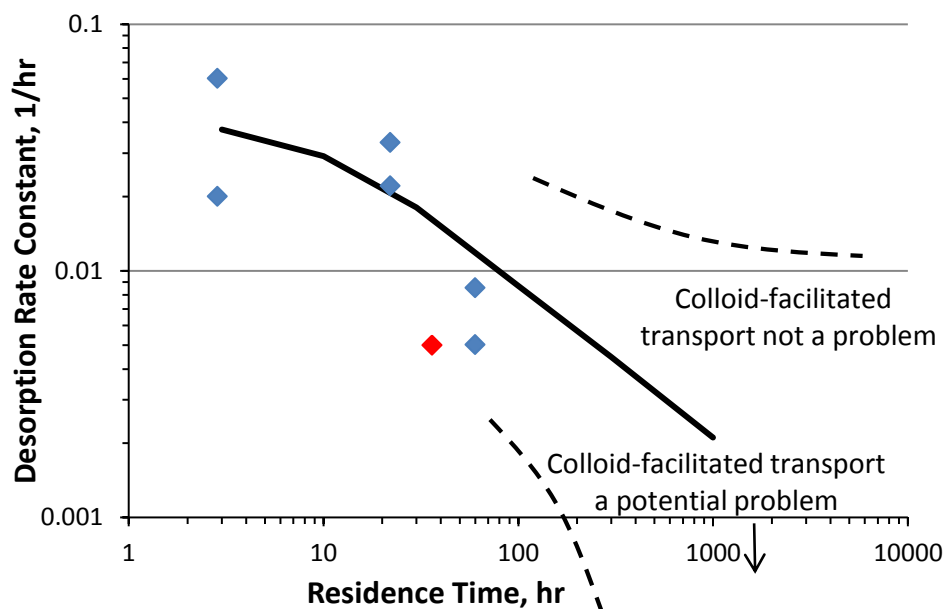


Figure 2-23. Irreversible colloid filtration rate constants as a function of residence time in the CFM tracer tests.

The key point in both Figures 2-22 and 2-23 is that the extrapolation of the CFM tracer test data to longer time scales will critically depend on the presence or absence of colloid filtration rate constants or desorption rate constants that are significantly smaller than the rate constants that can be effectively interrogated in the CFM tests. More specifically, it will depend on the presence or absence of some fraction of sorption sites on colloids that have extremely low

desorption rate constants or some fraction of colloids that have very low filtration rate constants because they possess properties that make them inherently resistant to filtration. Even very small fractions fitting these descriptions could result in significant observable colloid-facilitated transport of an actinide over long time and distance scales. The dashed lines in Figures 2-22 and 2-23 are intended to qualitatively illustrate the range of potential extrapolations that could occur over longer time and distance scales depending on the presence or absence of very small rate constants. If there are no rate constants much smaller than those deduced from the CFM tests, then the extrapolations would flatten out, and colloid-facilitated transport would not be predicted to be a problem over longer time scales. However, if there are significantly smaller rate constants that were not interrogated by the CFM tracer tests, then colloid-facilitated transport might still be a problem over longer time scales.

If we consider the ability to observe either colloid filtration or solute desorption from colloids in the CFM tracer tests to be equivalent to the ability to observe, respectively, a 5% difference between the recoveries of a conservative tracer and the colloids, or a 5% difference between the recoveries of the colloids and the colloid-adsorbed solutes (the breakthrough curve data suggest about a 5% uncertainty), then the *minimum* colloid filtration rate constant or solute desorption rate constant that can be interrogated in the CFM tests is approximately 0.0002 hr^{-1} . This value is calculated from $\ln(0.95)/(-100 \text{ hr})$, where 0.95 corresponds to a 95% recovery (difference of 5%), and 100 hrs is approximately the maximum residence time of the CFM tests. This expression comes from a simple manipulation of the expression for the exponential decay of an initial concentration, C_0 , associated with a first-order reaction with rate constant k :

$$\frac{C}{C_0} = e^{-kt} \quad (2-13)$$

All of the extrapolated mass recoveries vs. time discussed above were based on equation (2-13). Even if the experimental and measurement errors were small enough to observe a 1% difference in recoveries, the minimum observable rate constant would only be $4.4 \times 10^{-5} \text{ hr}^{-1}$, and this rate constant would predict that less than 0.01% of colloids or colloid-associated radionuclides would still remain unfiltered or remain adsorbed to colloids after about 25 years. Using a minimum measureable rate constant of 0.0002 hr^{-1} , corresponding to a 5% observable difference in recoveries, the prediction would be only about 5 years to reach 0.01% of the colloids remaining unfiltered or the solutes remaining adsorbed to colloids. Clearly, with a maximum practical shear zone residence time of around 100 hrs (beyond which recoveries are not guaranteed because of the high ambient flows in the shear zone), the CFM testbed has a limited ability to interrogate the very small rate constants that could mean the difference between significant colloid-facilitated transport or no colloid-facilitated transport over performance assessment time scales. The problem is further compounded by the presence of any colloids that tend to filter rapidly or sorption sites on colloids from which solutes tend to desorb rapidly because these situations will result in observed behavior that completely masks the effects of very slow filtration rates or desorption rates. In effect, if there is any significant observable colloid filtration or solute desorption from colloids over the relatively short time scales of the CFM tracer tests, it will be impossible to see the effects of very slow filtration rates or slow desorption rates that will matter for performance assessments over long time scales.

The results of CFM test 12-02 for the other radionuclides that were used in this test (^{22}Na , ^{137}Cs , ^{133}Ba , and ^{237}Np) suggest that these nuclides, with the possible exception of ^{22}Na (which is really not a relevant nuclide for nuclear waste disposal because of its short half-life and low inventory in nuclear waste), should exhibit negligible transport over long time and distance scales. However, the same caveats apply to the colloid-associated nuclides ^{137}Cs and ^{133}Ba as for the tri- and tetravalent solutes discussed above. Despite the relatively rapid *observable* desorption rates of these radionuclides from colloids in test 12-02, if there are any sorption sites that have very slow characteristic desorption rate constants that were masked by the observed behavior, colloid-facilitated transport of these nuclides could still be an issue over longer time and distance scales. However, the test data suggest that the colloid-facilitated transport of ^{137}Cs and ^{133}Ba (and possibly ^{237}Np) are much less likely to be a problem over long time and distance scales than the colloid-facilitated transport of Am or Pu.

The above discussion is not intended to imply that the CFM test bed is useless for obtaining colloid-facilitated transport information relevant to performance assessment time and distance scales. Rather, it is intended to point out the limitations of directly extrapolating the CFM test data to longer time and distance scales. The discussion also helps to provide insights into how future tests might be conducted to better interrogate the colloid filtration rate constants and solute desorption rate constants that might matter in long-term performance assessments. The transport time scales achievable in the CFM test bed have practical limitations, so suggestions for improvements must necessarily focus on pre-conditioning of the colloids used in the injection cocktails and/or on pre-conditioning of the injection cocktails themselves. Two suggestions are put forward here for consideration, although many variations of these, as well as alternative suggestions, are certainly possible:

- Subject the colloids generated by dispersing bentonite in synthetic GTS water to experiments that tend to eliminate or reduce the number of colloids that are more susceptible to filtration prior to injecting them in a CFM field test. For instance, the dispersed colloids could be run through a large laboratory column containing GTS shear zone material, and only the colloids exiting the column could be used in the field injection cocktail. Based on the column residence time and observed column recovery of the colloids, it will be possible to estimate the maximum effective filtration rate constant of the recovered colloids (although this rate constant won't necessarily strictly apply to the shear zone itself).
- Using the colloids isolated above, adsorb the target homologues or radionuclides onto the colloids and then perform large-scale desorption experiments using shear zone materials in the presence of the colloids to remove homologues or radionuclides that are adsorbed to weaker colloid sorption sites. The maximum effective desorption rate constants associated with homologues or radionuclides that remain adsorbed to the colloids after a certain amount of desorption time could be estimated. The remaining colloids and associated homologues could then be used as part of an injection cocktail in a GTS field tracer test.

One obvious variation of these suggestions would be to perform a large column transport experiment *after* adsorbing the homologues or radionuclides to the dispersed bentonite colloids and effectively isolating both filtration-resistant colloids and the more strongly-adsorbed solutes

in one step. Using an injection cocktail pre-conditioned in these ways in a CFM field test would, in principle, increase the probability of interrogating the small colloid filtration rate constants and small desorption rate constants that will matter over performance assessment time scales.

Acknowledgments: The author (P. Reimus) is grateful to CFM project participants who provided access to the tracer test data as well as descriptions of the conduct of the tracer tests. In particular, special thanks go to Thorsten Schafer (KIT), Bill Lanyon (Fracture Systems, Ltd.), and Ingo Blechschmidt (NAGRA). Funding for this report was provided by the U.S. Department of Energy, Nuclear Energy Office, Fuel Cycle R&D Program, Used Fuel Disposition Campaign.

2.6 References

- Achtziger, P., and Kontar, K. 2011. *GTS Phase VI Homologue Tracer Test Run 10-03*, Quick-Look Report A-1588-25/28, CFM Project, Switzerland.
- Huber, F., Kunze, P., Geckeis, H., and Schäfer, T. 2011. Sorption reversibility kinetics in the ternary system radionuclide-bentonite colloids/nanoparticles-granite fracture filling material, *Appl. Geochem.*, 26, 2226-2237.
- Kaplan, D. I., and Serkiz, S. M., 2004. Quantification of thorium and uranium sorption to contaminated sediments. *J. Radioanal. Nucl. Chem.*, **248**(3), pp. 529-535.
- Kontar, K. and Gräfe, K. 2012. *GTS Phase VI CFM Project Tracer Test Run 12-02*, Quick-Look Report, AN 12-302, CFM Project, Switzerland.
- Möri, A. (Ed.). 2004. The CRR final project report series I: Description of the Field Phase – Methodologies and Raw Data. *Nagra Technical Report NTB 03-01*. Nagra, Wettingen, Switzerland.
- Reimus, P. W., Pohll, G., Mihevc, T., Chapman, J., Papelis, L., Lyles, B., Kosinski, S., Niswonger, R., and Sanders, P., 2003. Testing and parameterizing a conceptual model for radionuclide transport in a fractured granite using multiple tracers in a forced-gradient test, *Water Resour. Res.*, **39**(12), 1350, doi:10.1029/2002WR001597.
- Rösli, U., Achtziger, P., and Kontar, K. 2010. *GTS CFM Homologue Tracer Test Run 10-01*, Quick-Look Report AN 10-271, CFM Project, Switzerland.
- Schäfer, T., Geyer F., Hauser, W., Seher H., Walther, C., Trick, T., Degueldre C., Missana T., Alonso, U., Suzuki, M., Baer, T., and Blechschmidt, I. 2008. *GTS CFM Homologue Tracer Test Run 08-01*, Quick-Look Report A1588-4, CFM Project, Switzerland.
- Schäfer, T., Geyer F., Hauser, W., Heck, S., and Walther, C. 2010. *GTS CFM Homologue Tracer Test Run 10-01, Part II*, Quick-Look Report AN 10-271, CFM Project, Switzerland.
- Schäfer, T., Geyer F., Hauser, W., Heck, S., and Walther, C. 2012. *GTS Phase VI Tracer Test Run 10-03, Part II*, Quick-Look Report, AN 12-182, CFM Project, Switzerland.
- Trick, T. and Blechschmidt, I. 2008. *GTS-CFM Tracer Test Run 08-02*, Quick-Look Report, AN 08-165, CFM Project, Switzerland.

Appendix 2-A. Corrections for Uranine Decay in CFM Tracer Test 10-03

Purpose of the Corrections

Corrections were made for uranine decay in test 10-03 to allow estimates of colloid filtration rate constants in this test. If no correction is made for uranine decay, the colloid recovery is calculated to be greater than the uranine recovery (Fig. 2-A1), which makes it impossible to estimate a meaningful filtration rate constant. Note that it is still possible to estimate desorption rate constants for the homologues from the colloids in test 10-03 without a uranine decay correction because these estimates are based on comparisons of the colloid and homologue breakthrough curves.

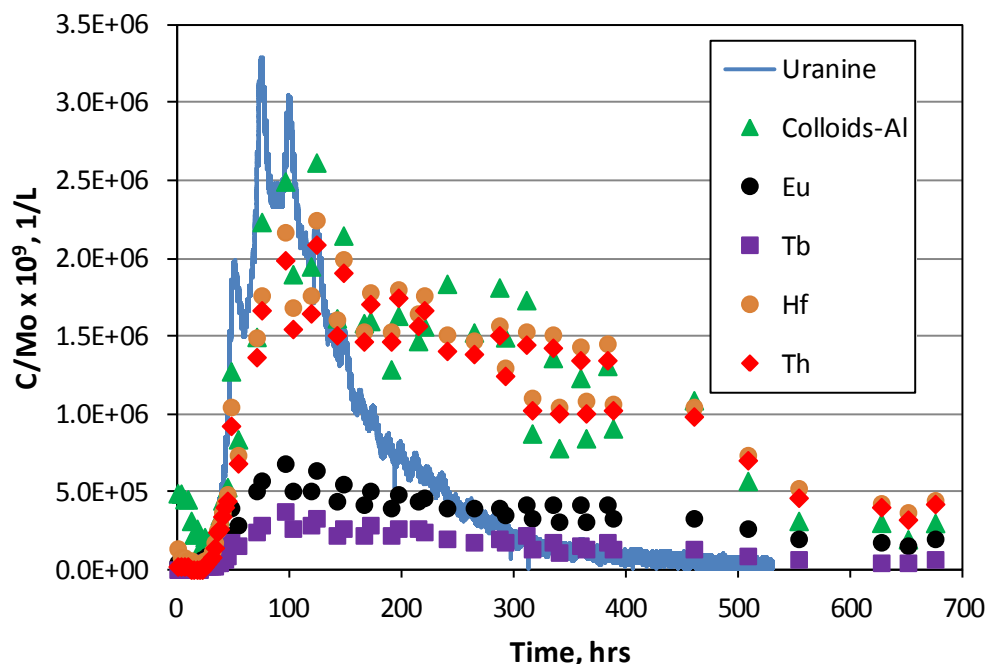


Figure 2-A1. Normalized breakthrough curves of tracers in CFM tracer test 10-03 (concentrations divided by injection mass times 10^9). The bentonite colloid concentrations were determined indirectly by measuring Al and subtracting the background Al concentration. Note the low/short tail of the uranine, which causes the colloids, Hf, and Th to have higher recoveries than the uranine, making it impossible to obtain meaningful estimates of colloid filtration rates.

Assumptions/Approaches

The assumptions used to make corrections for uranine decay in the injection loop in test 10-03 are as follows:

1. Uranine decay occurs only in the injection loop/circuit.

Rationale:

- (1) There was never any evidence of uranine decay in tracer tests prior to 10-03 (nearly complete recovery in most tests), so it seems unlikely that decay would suddenly start occurring in the shear zone in test 10-03.

- (2) Test 11-02 showed an obvious difference in the injection functions of AGA and uranine, and the only possible explanation for such a difference is some sort of uranine decay process that must have occurred in the injection loop.
2. The difference between the AGA and uranine injection functions in test 11-02 can be used to estimate a decay constant for uranine that can also be applied to test 10-03 to make corrections for uranine decay in test 10-03.

Rationale:

- (1) The injection loop in test 11-02 had the same volume and same basic components as the injection loop in test 10-03, so the decay rate of the uranine should have been approximately the same in the two tests. A minor difference between the injection loop in the two tests was that the recirculation rate in 10-03 was 39.5 ml/min, and the recirculation rate in 11-02 was 29 ml/min. It is assumed that this slight difference in recirculation rate did not affect the uranine decay rate. The injection loop pH also differed in the two tests, which is significant because the lower pH of the injection loop in test 10-03 was considered to be a potential explanation for apparent uranine decay (low pH can suppress uranine fluorescence). However, the pH in the injection loop of test 11-02 was significantly higher than in test 10-03 and significant decay was still observed. Also, the pH in the injection loop of test 10-02 (another test with the same injection loop volume and configuration) was lower than in test 10-03, but the uranine recovery was still substantially higher in test 10-02 (~90%) than in test 10-03 (~20%). So it is not apparent that pH is an explanation for uranine decay.
3. As an alternative method to correct for uranine decay, the turbidity injection function in Test 10-03 can be used to estimate the uranine injection function based on the observed differences between the uranine and turbidity injection functions in test 10-01.

Rationale:

- (1) Although the injection loop volumes were different in tests 10-01 and 10-03 (2000 vs. 3000 ml), the recirculation rate in 10-01 was similar to 10-03 (45-50 ml/min vs. 39.5 ml/min in 10-03), so it is reasonable to assume that the ratio of the observed injection decay constants for uranine and turbidity in test 10-01 would also apply to test 10-03. Figs. X-A2 and X-A3 show the uranine and turbidity injection functions in tests 10-01 and 10-03.

Correction using differences between AGA and uranine injection functions in Test 11-02.

Figure 2-A4 shows the injection loop concentrations as a function of time for both AGA and uranine in tracer test 11-02. The log-linear slope analyses of these data indicated that the slopes through the first 289 hours (when a relatively high net injection rate was imposed) were $-0.000868 \text{ hr}^{-1}$ for the AGA and $-0.009694 \text{ hr}^{-1}$ for the uranine. If the slope for the AGA is taken as a reflection of the true flow rate through the injection interval, then the difference between the two slopes (0.00883 hr^{-1}) provides an estimate of the first-order degradation rate constant for the uranine in the injection interval. The fact that the log-linear plot of the uranine concentration is linear implicates a first-order uranine decay process (the plot would have curvature if the process were not first order).

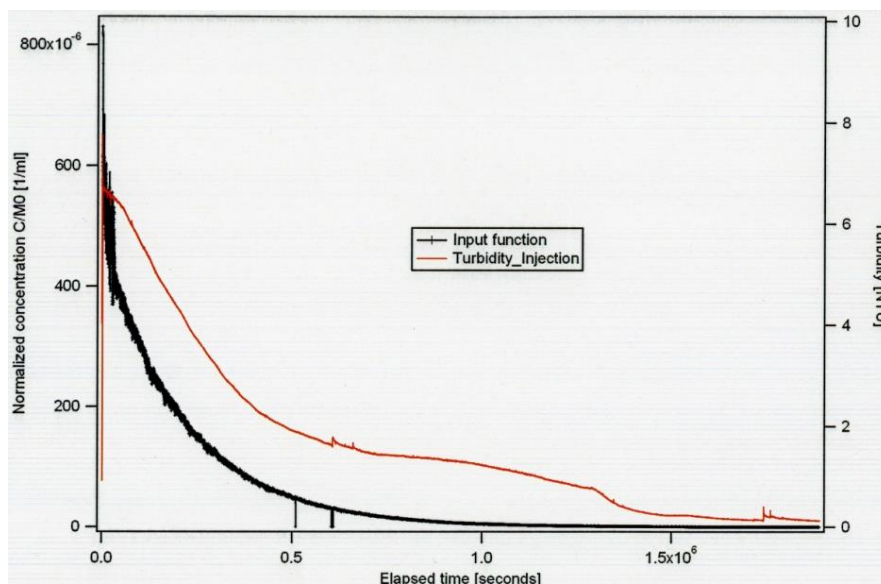


Figure 2-A2. Uranine (black) and turbidity (red) injection functions in Tracer Test 10-01.

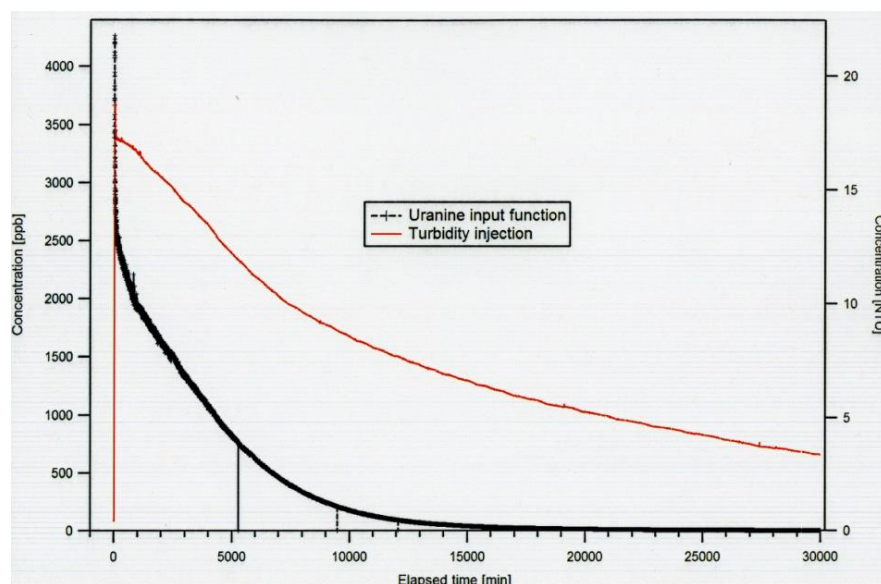


Figure 2-A3. Uranine (black) and turbidity (red) injection functions in Tracer Test 10-03.

The uranine injection function in test 10-03 is shown in Figure 2-A5 along with estimates of the flow rate through the injection interval vs. time based on the observed concentration decline of the uranine. Note that the flow rate was estimated separately for three time periods based on changes in slope of the $\ln(\text{concentration})$ vs. time history, where $\text{slope} = -Q/V$, with Q = volumetric flow rate (ml/min) and V = volume of injection interval (3000 ml). This calculation assumes a well-mixed injection interval. The slopes were -0.0146 hr^{-1} for ~0-130 hr, -0.0184 hr^{-1} for 130-250 hr, and -0.0135 hr^{-1} for 250+ hr. The resulting apparent flow rates through the injection interval are shown in Figure 2-A5. However, the actual flow rates through the injection interval were less than these apparent flow rates because the uranine was decaying in addition to being swept out of the injection interval by flow. The uranine decay constant of 0.00883 hr^{-1} estimated from test 11-02 (see above) translates to an effective flow rate of 0.442 ml/min due to

decay in test 10-03. This effective flow rate due to decay must be subtracted from the observed flow rates to obtain the actual flow rates as a function of time in test 10-03 (alternatively, the decay constant could be added to each of the slopes above and then the flow rates could be calculated from slope = $-Q/V$ to get the same result). The estimated actual flow rates then become 0.289, 0.479, and 0.234 ml/min for the three different time periods in test 10-03, respectively.

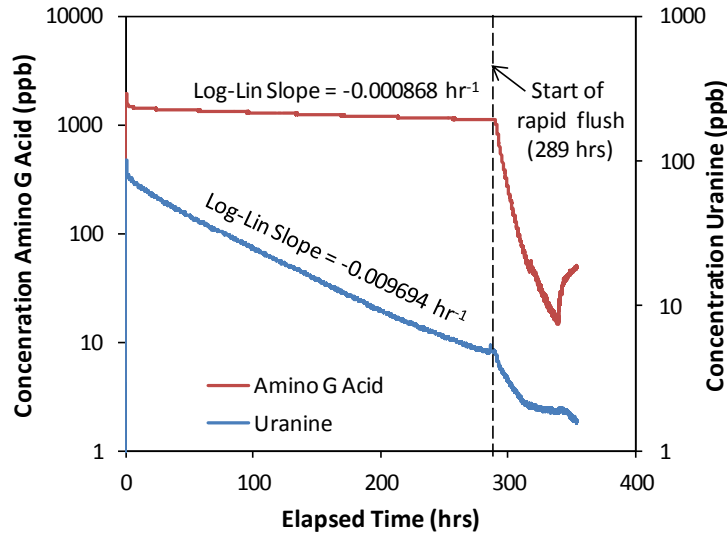


Figure 2-A4. Log AGA and uranine concentrations in the injection loop vs. time in tracer test 11-02.

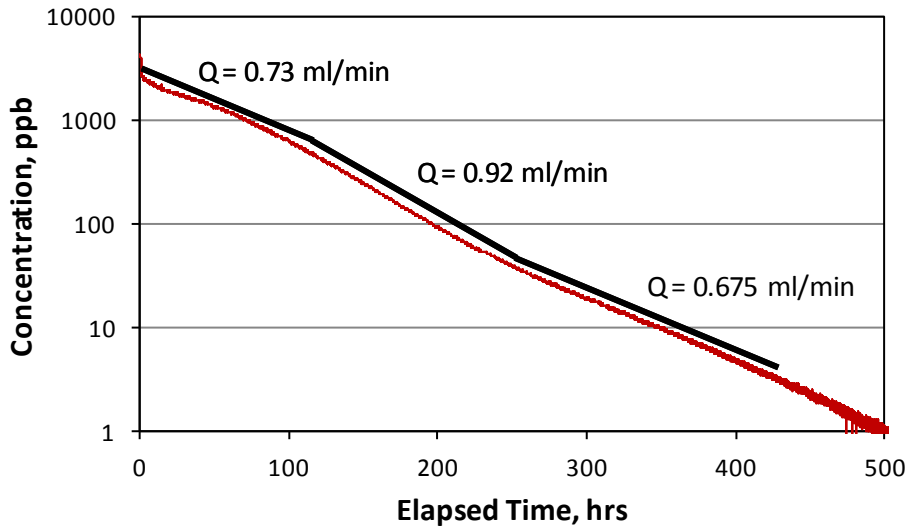


Figure 2-A5. Observed uranine injection function in Test 10-03 (brown line) and linear segments (black lines) showing changes in apparent flow rates out of the injection interval.

The next step in the correction was to match the extraction breakthrough curve of test 10-03 using the observed uranine injection function with the estimates of the actual flow rates through the injection interval, as determined above. This matching process was accomplished as follows. First, the mean residence time and Peclet number (length/dispersivity) in the shear zone were estimated using the RELAP semi-analytical model assuming that the initial apparent injection flow rate in test 10-03 (0.73 ml/min) was the actual injection flow rate throughout the test (RELAP cannot simulate different apparent and actual injection flow rates). The resulting estimates of mean residence time and Peclet number were 64 hrs and 15, respectively, with Figure 2-A6 showing the fit to the observed uranine extraction curve. The uranine recovery based on these calculations was ~19-20% (i.e., the modeled breakthrough curve had to be multiplied by ~0.2 to match the observed breakthrough curve), which is in good agreement with the recovery calculated directly from the observed breakthrough curve.

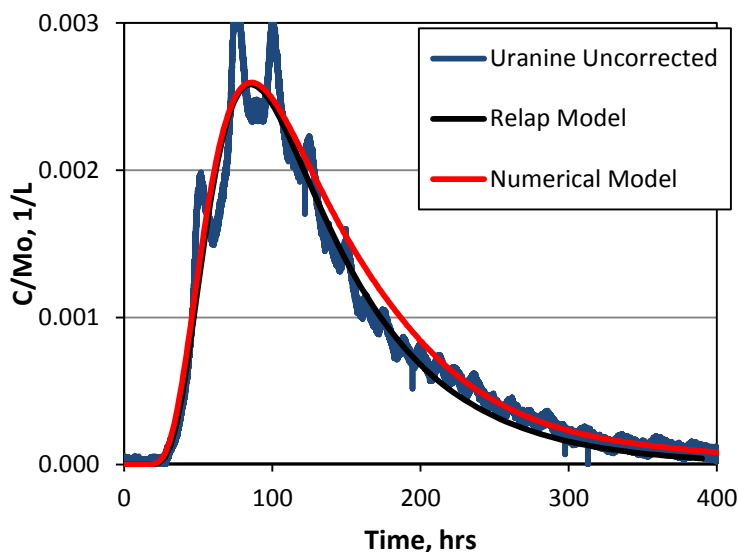


Figure 2-A6. RELAP and numerical model fits to uranine breakthrough curve in tracer test 10-03. Note that the cyclic fluctuations in the data were not fitted. In the RELAP model it was assumed that the injection flow rate was 0.73 mL/min (first flow rate in Figure 2-A5) with the injection concentration history of Figure 2-A5, and in the numerical model it was assumed that the injection flow rate was ~0.29 mL/min with the same injection concentration history.

The RELAP estimates of mean residence time and Peclet number were then used as *initial* estimates in the numerical model described in the main body of this report, with the observed uranine injection function being used as the concentration history in the injection interval and the estimated actual injection flow rate into the shear zone (see above) being used as the simulated injection flow rate. With these assumptions, the best-fitting mean residence time and Peclet number were found to be 60 hrs and 17, respectively. However, it was found that a better match to the observed breakthrough curve could be obtained by assuming that the injection flow rate was a constant 0.289 ml/min (the initial estimated flow rate) instead of the time-varying flow rates deduced in the analysis described above because the deduced increase in the injection flow rate from 0.289 ml/min to 0.479 ml/min at around 110 hours into the test resulted in a significant inflection in the simulated extraction breakthrough curve at around 150 hours that simply was

not observed. This inflection was the result of the significant change in the rate at which tracer was injected into the shear zone at ~110 hours plus the significant change in dilution factor at the extraction location once this higher injection rate took effect. Thus, the mean residence time and Peclet number estimates of 60 hrs and 17 were obtained assuming a constant injection flow rate of 0.289 ml/min throughout the test. The resulting uranine breakthrough curve is shown in Figure 2-A6 as the curve labeled “numerical model”. The estimated mass participation in the test using these assumptions was about 60% (i.e., the simulated breakthrough curve had to be multiplied by 0.6 to match the observed extraction breakthrough curve).

The final step in the correction was to use the numerical model to simulate the uranine breakthrough curve that would have been observed if the uranine had not decayed in the injection loop. This was accomplished by assuming the same initial concentration of uranine in the injection loop as in the decaying case but simulating that the injection concentration declined in accordance with the deduced injection flow rate of 0.289 ml/min instead of the more rapid observed concentration decline. The injection concentration function in this case was $C = C_0 \cdot \exp(-0.289 \cdot 60 \cdot t / 3000)$, where t is time in hours, 60 is the conversion from minutes to hours, and 3000 is the volume of the injection loop in mL. The mean residence time and Peclet number in the shear zone were assumed to be 60 hrs and 17, respectively, the same values obtained by matching the observed extraction function when the observed injection function was assumed as the injection concentration history. The resulting breakthrough curve was multiplied by 0.6 to match the mass participation deduced from the numerical model match to the extraction function using the observed injection function. The resulting corrected extraction function is shown in Figure 2-A7.

Note that the corrected uranine breakthrough curve is considerably higher than the observed colloid breakthrough curve except at late times, and the dip below the colloid data at late times is relatively minor. Using this corrected uranine extraction breakthrough curve, it is possible to obtain reasonable estimates of colloid transport parameters in test 10-03.

Correction using differences between turbidity and uranine injection functions (in test 10-01)

As an alternative analysis, we use the differences in the turbidity and uranine injection functions in tracer test 10-01 as the basis for estimating what the uranine injection function should have looked like in test 10-03. Figure 2-A8 shows the uranine and turbidity injection functions (natural log of concentrations vs. time) in test 10-01 over the first 150 hours of the test, which is when the vast majority of the tracer mass was extracted at the Pinkel extraction point. It is interesting that the injection functions suggest that the uranine flowed out of the injection interval faster than the colloids (assuming that colloid concentrations are linear with turbidity). If we assume that the same ratio of slopes (1.74 times greater slope for the uranine) applies in test 10-03, then we can multiply the slope of the test 10-03 turbidity injection function by 1.74 to obtain an estimate of the uranine injection function for Test 10-03. Figure 2-A9 shows the turbidity injection function for 10-03 (natural log of concentrations vs. time), with a fitted slope of -0.0032 hr^{-1} . If we multiply this slope by 1.74, we get a slope of -0.00556 hr^{-1} for the uranine, which yields an injection flow rate estimate of 0.278 ml/min. This flow rate estimate is in very good agreement with the estimate of 0.289 ml/min at the start of test 10-03 using the uranine decay correction described above. Furthermore, the near-constant slope of the turbidity function suggests that the injection flow rate may have been more constant than the observed uranine

injection function indicated. Perhaps the uranine decay rate in the injection loop fluctuated, which would make it appear that the injection flow rate fluctuated. This may explain why the observed extraction curve could not be matched very well when the injection flow rate was assumed to fluctuate in accordance with the observed uranine injection function in the preceding analysis.

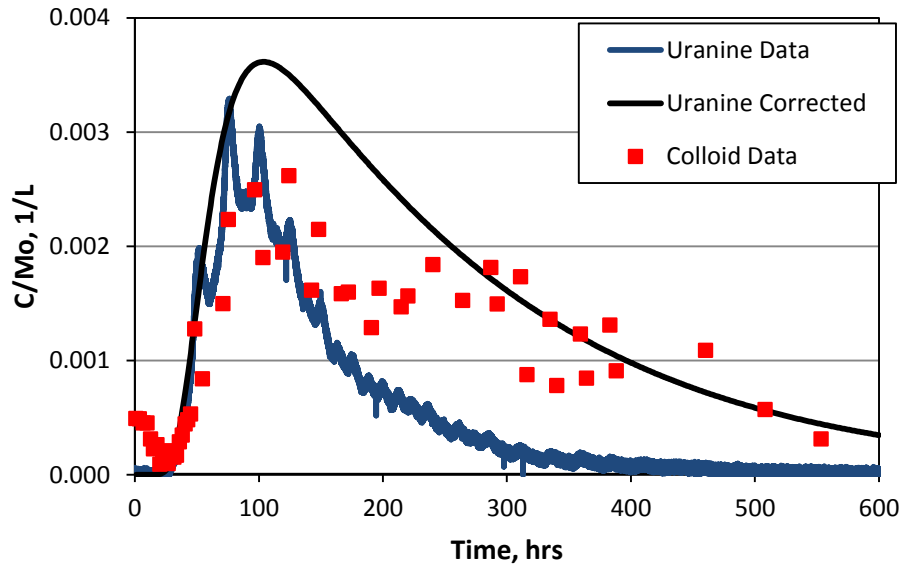


Figure 2A-7. Modeled extraction breakthrough curve in Test 10-03 using the numerical model with corrections for uranine decay.

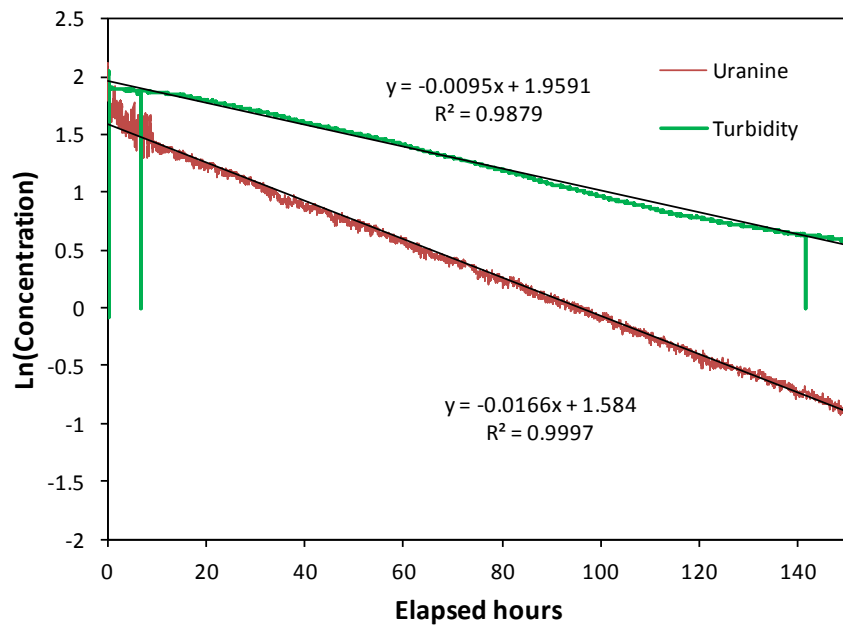


Figure 2-A8. Uranine and turbidity injection functions in Test 10-01, with linear fits to the data.

When an injection flow rate of 0.278 ml/min is used with the observed uranine injection function (decay included), the observed uranine extraction curve can be matched very well assuming a uranine mass participation of ~60% (i.e., essentially identical to the 60% mass participation in

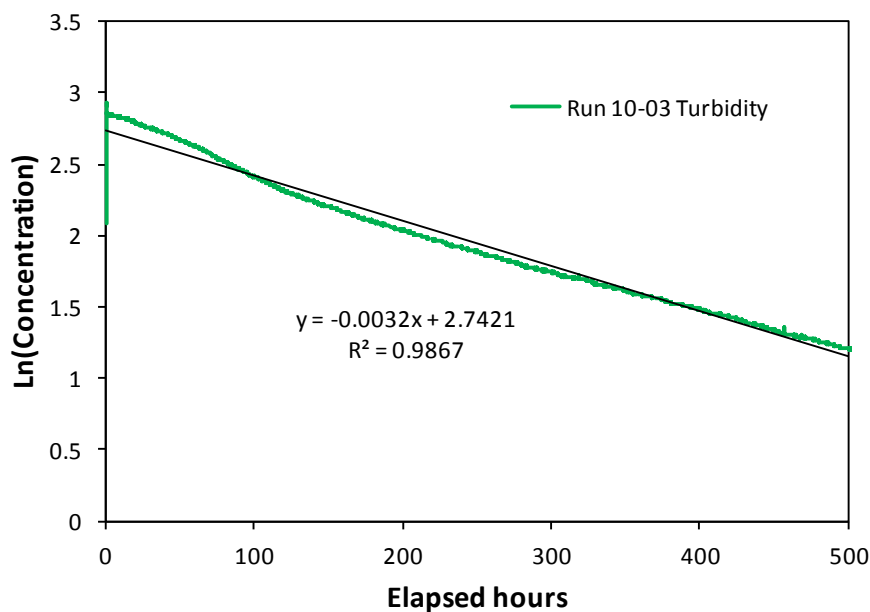


Figure 2-A9. Turbidity injection function in Test 10-03, with linear fit to the data.

the preceding analysis, which is not surprising given that the deduced injection flow rates are very similar). Furthermore, when an uranine injection function that assumes no decay is used in the numerical model with an injection flow rate of 0.278 ml/min, essentially the same corrected uranine extraction function is obtained as in Figure 2-A7. Thus, the turbidity correction and the correction based on the differences in the observed injection functions of uranine and AGA in test 11-02 lead to essentially the same corrected uranine extraction breakthrough curve (the curve of Figure 2-A7). This extraction breakthrough curve and a mass participation of 60% were used as the basis for estimating colloid transport parameters in tracer test 10-03.

Note that the implications of different observed injection functions for colloids and conservative solute tracers in test 10-01 are significant for tracer test interpretations. If these differences are real, and the colloids are in fact flowing out of the injection interval more slowly than conservative solute tracers, it follows that the colloids are transporting more conservatively through the shear zone than test interpretations would suggest. This possibility is not explored or analyzed further here, but it raises the importance of obtaining good quality turbidity and fluorescence injection loop measurements in future tests and also in trying to obtain a few samples from the injection loop to verify the injection functions deduced from the online measurements.

3. International Collaboration Involving the FE Heater and HG-A Tests at Mont Terri

3.1 Introduction

This section summarizes the international activities related to the FE heater and HG-A tests at the Mont Terri URL near St. Ursanne in Switzerland. The objective of the URL is to provide hydrogeological, geochemical and rock mechanical properties of an argillaceous formation to evaluate the potential of argillaceous rock for disposal of high-level nuclear waste (Thurry and Bossart, 1999). The FE heater test is a full-scale long-term heater experiment being planned for the Mont Terri URL. A benchmark analysis using the thermal-hydrological-mechanical (THM) process model, TOUGH-FLAC, is reported here. The benchmark problem considers THM processes associated with excavation of the FE test tunnel followed by heating of the bentonite buffer and argillaceous rock. The benchmark exercise considers the four main stages of the FE heater test: (1) excavation; (2) installation of ground support, (3) emplacement of the heating canister and bentonite buffer; and (4) heating of the cannister. The benchmark is intended to allow comparison of the different THM process-level computer models being used by the participating organizations that are collaborating on the FE heater test and to predict important test results such as peak temperature and buffer resaturation rate. The HG-A test is an ongoing test which provides data on hydromechanical processes associated with the excavation damaged zone (EDZ) surrounding underground waste emplacement tunnels. Modeling of this test is presented here using the THM fracture-damage model, TOUGH-RBSN. RBSN is the Rigid-Body-Spring-Network model, which is a geomechanics and fracture damage model. Key aspects of this analysis are (1) the development of techniques for computing shear fracture; (2) development of techniques for representing anisotropic rock properties; and (3) prediction of fracture damage in the EDZ for the HG-A field test.

The research activities summarized in this section have focused on understanding and modeling EDZ evolution and the associated coupled processes, and impacts of high-temperature on parameters and processes relevant to performance of a clay repository. This report documents results from some of these activities, addressing key Features, Events and Processes (FEPs), that have been ranked in importance from medium to high, as listed in Tables 7 and 8 of the *Used Fuel Disposition Campaign Disposal Research and Development Roadmap* (FCR&D-USED-2011-000065 REV0) (Nutt, 2011). Specifically, they address FEP 2.2.01, Excavation Disturbed Zone, for shale, by investigating how coupled processes affect EDZ evolution; FEP 2.2.05, Flow and Transport Pathways; and FEP 2.2.08, Hydrologic Processes, and FEP 2.2.07, Mechanical Processes. The activities documented in this report also address a number of research topics identified in *Research & Development (R&D) Plan for Used Fuel Disposition Campaign (UFDC) Natural System Evaluation and Tool Development* (Wang, 2011), including Topics S3, Disposal system modeling – Natural system; P1, Development of discrete fracture network (DFN) model; P14, Technical basis for thermal loading limits; and P15 Modeling of disturbed rock zone (DRZ) evolution (clay repository).

3.2 THM Modeling of FE Experiment

Within the framework of participating in the international Mont Terri Project (Thurry and Bossart, 1999), DOE is a partner in the FE Experiment at Mont Terri and supports LBNL to participate as one of several international modeling teams. In this section we present the FE Experiment and the current status of the modeling, including scoping calculations, benchmark simulations, and predictive calculations. To date, we have conducted a number of scoping calculations, have engaged in a comparative benchmarking effort, and have initiated some model predictions for the real experiment. In parallel with these modeling efforts, more data are becoming available on the THM properties of the MX-80 granular bentonite that is used as a backfill material in this experiment. In the modeling results presented in this report, we started with bentonite properties available from a previous experimental study (FEBEX bentonite), whereas we are gradually including material specific MX-80 properties into our analysis when they become available from ongoing laboratory and field experimental studies.

3.2.1 FE experiment at the Mont Terri site

The Full-Scale Emplacement Experiment (FE) at the Mont Terri URL, Switzerland will be one of the largest and longest-duration heater tests worldwide (Figures 3-1 through 3-3). This heater experiment is undertaken by NAGRA and other international partners as an ultimate test for the performance of geologic disposal in Opalinus Clay, with focus on both the EBS components and the host-rock behavior. The experiment will provide data useful for the validation of THM coupling effects regarding the processes in the host rock while correctly accounting for (and examining) the conditions in the emplacement tunnel (temperature, saturation, and swelling pressure). Due to the 1:1 scale of the experiment, it will be possible to achieve realistic temperature, saturation, and stress gradients. It will also be possible to test backfilling technology with granular bentonite, as well as lining technology with shotcrete, anchors, and steel ribs. Processes examined in the test cover many aspects of repository evolution, such as EDZ creation and desaturation of the EDZ during tunnel excavation and operation (including ventilation for about one year), as well as reconsolidation of the EDZ, resaturation, thermal stresses, and thermal pore-pressure increase after backfilling and heating (heating and monitoring period > 10 years).

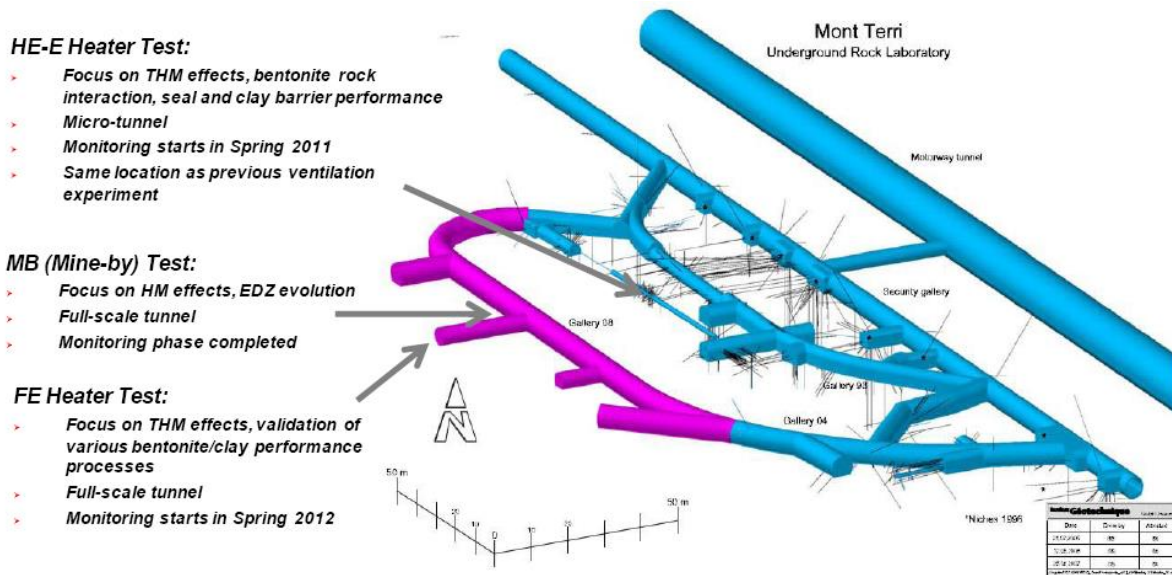


Figure 3-1. Summary schematic of the Mont Terri URL with side galleries and drifts for testing. Three specific experiments of relevance to UFDC are highlighted (based on Garitte and Gens, 2012).

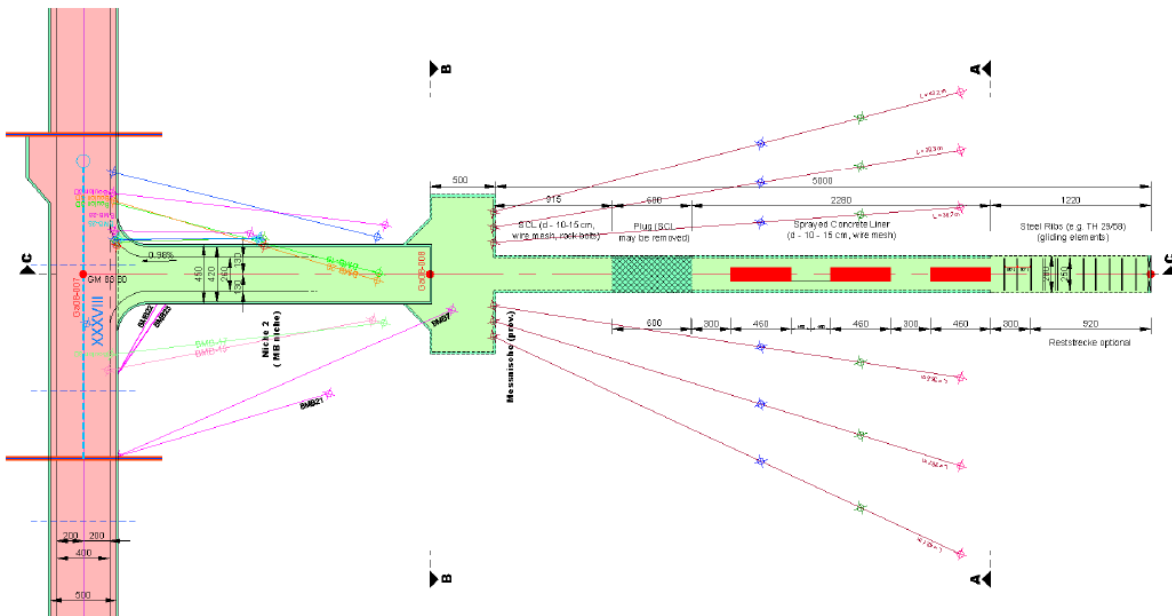


Figure 3-2. Plan view of experiment setup and borehole layout (from Garitte and Gens, 2012).

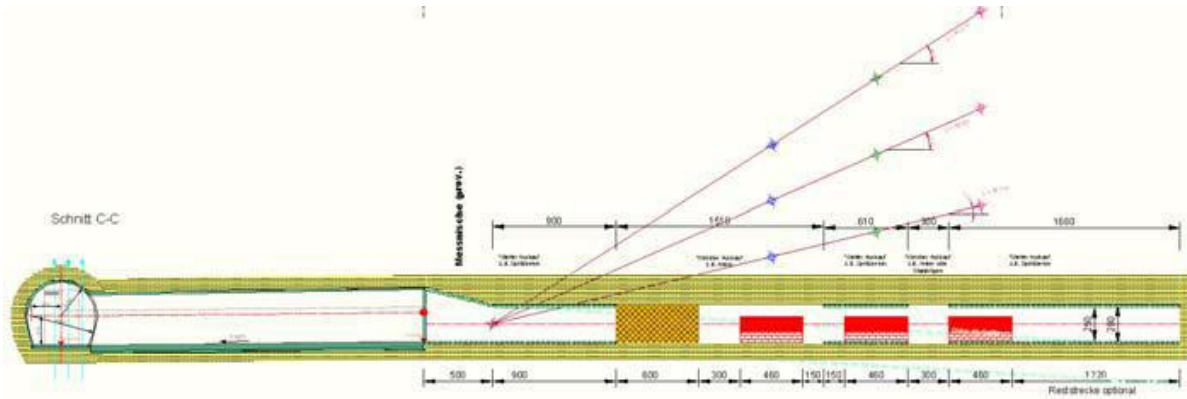


Figure 3-3. Side view of experiment setup and borehole layout (from Garitte and Gens, 2012).

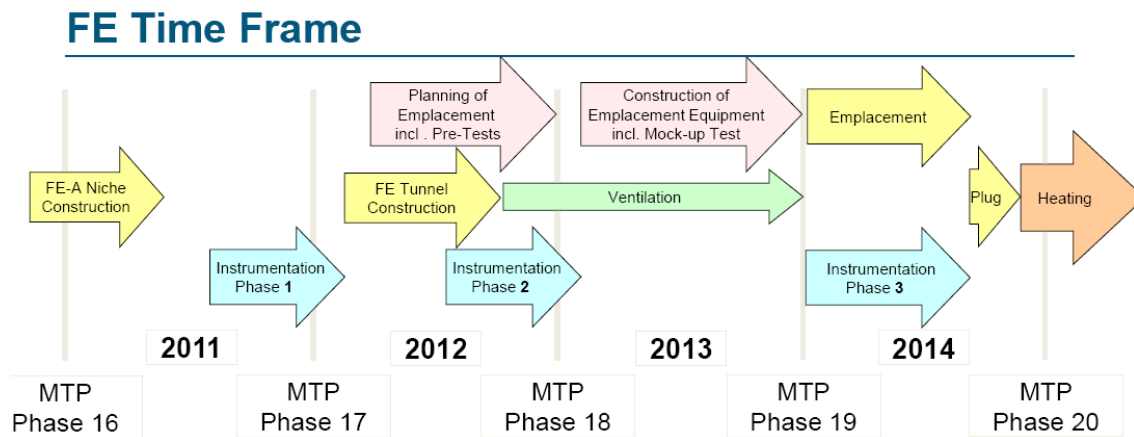


Figure 3-4. FE experiment time frame. Phases 16 to 20 refer to Mont Terri project phases (Viotor, 2012).

As shown in Figures 3-1 through 3-3, the FE experiment will be conducted in a side tunnel at Mont Terri, excavated along the claystone bedding planes for this purpose, extending 50 m in length and about 2.8 m in diameter. Heating from emplaced waste will be simulated by three heat-producing canisters of 1500 W maximum power. A sophisticated monitoring program is planned, including dense pre-instrumentation of the site for *in situ* characterization, dense instrumentation of the bentonite buffer and host rock, and extensive geophysical monitoring (seismic and electric tomography). A THM modeling program will be conducted in parallel with the testing and monitoring activities.

Figure 3-4 shows the FE experiment time frame (Viotor, 2012). A niche in front of the FE tunnel was constructed in 2011, followed by a first phase of instrumentation of the rock mass surrounding the tunnel using boreholes from the niche. The FE tunnel was then excavated by road-header in 2012, and this was followed by another phase of instrumentation. The tunnel is

currently open for a 1-year ventilation period. This will be followed by the emplacement of the heaters, bentonite buffer, and a concrete plug, after which the heating is expected to start at the end of 2014. The heating is then expected to go on for at least 15 years, with continuous monitoring of THM processes in both the bentonite buffer and surrounding rock.

DOE is one of the experimental partners for the FE heater experiment, and LBNL is one of the modeling teams. The plans for the THM modeling program were determined in meetings with the FE modeling teams during 2012. Model simulation tasks for each of the international modeling teams (currently six modeling teams participate) include three types of computations:

- 1) Scoping computations
- 2) Benchmarking
- 3) Predictive simulations

The scoping computations included brainstorming on potential ongoing processes, evaluating their significance and parameter range, comparing simulation results and input parameters derived by each team, and lessons learnt (parameter range, importance, expected response). The benchmarking uses well-defined geometry problems with exact parameter values given to the teams, focusing on process modeling with precise comparison of codes. In the predictive calculations, likely parameters values and the as-built information of the experiment will be defined and then frozen as a starting point for all model teams. The modeling will be used to predict the behavior of the system, and this should be reported prior to heating start (in 2014). Currently, each modeling team develops their own conceptual models and material properties using available literature (papers and reports) on laboratory experiments and previous Mont Terri *in situ* tests etc. Moreover, this is complemented with a restricted benchmark test for code comparison, in which properties and model geometry are set by NAGRA. In the FY2012 NBS report, we presented our first initial 2D modeling of the FE experiment, including a parameter sensitivity study, to evaluate the importance of the different coupled processes and different components of the FE experiment. The following main conclusions were drawn from the FY2012 2D modeling of the FE experiment:

- The canister surface reaches the maximum temperature of 94.5°C after 4.8 years (for 2D model).
- The bentonite buffer resaturates very slowly and will still be unsaturated after 30 years.
- Temperature, water saturation, and pore pressure in the bentonite buffer are largely affected by the bentonite capillary pressure.
- Minor rock failure occurring during excavation does not expand much further during the assumed 20 years heating period, meaning that the rock mass will remain in an elastic mechanical state.

While the 2D analysis is very useful for performing such parameter studies, we also acknowledge that the 2D simplification does not provide an accurate quantitative prediction of the temperature evolution and the peak temperature. Consequently, in FY2013, we have developed a new full 3D model of the FE experiment. Using the 3D model, we conducted simulations, first for a prediction of the thermal-hydrologic evolution and then to predict the

peak temperature. We have also conducted a full-scale 3D THM simulation using the Barcelona Basic Model for the bentonite buffer. Results using the new 3D model were also presented in a recent UFD milestone report (Liu et al., 2013).

3.2.2 Modeling approach

Model simulations of the FE experiment are carried out using the TOUGH-FLAC software (Rutqvist et al. 2002; 2011), which is based on linking the TOUGH2 multiphase flow and heat transport simulator (Pruess et al. 2011) with the FLAC3D geomechanical simulator (Itasca, 2009). The TOUGH-FLAC simulator has in recent years been extended and applied to issues related to nuclear waste disposal in clay host rock within bentonite backfilled tunnels (Rutqvist et al. 2011; 2013a). This includes implementation of the Barcelona Basic model (BBM), for the mechanical behavior of unsaturated soils and applied for modeling of bentonite back-fill behavior (Alonso et al. 1990). Recently, as part of the UFD EBS program, the BBM has been extended to a double structure model, corresponding to the Barcelona Expansive Model (BExM), a model that we also plan to use for advanced modeling of the FE experiment. For the modeling of the FE experiment, we have developed an initial conceptual model and modeling approach based on experiences from recent design scoping calculations conducted by teams contracted by NAGRA, to help with the experimental design:

- 1) Pöyry (Engineering and Consulting): Modeling for excavation design using FLAC3D with ubiquitous joint model (anisotropic plasticity with different shear strength along bedding planes). This modeling approach was used to analyze the ground support design (Nater, 2012).
- 2) CIEMAT and UPC of Spain conducted scoping calculations for thermal and monitoring design using the CODE-Bright FEM code, and they used the BBM for modeling bentonite mechanical behavior (Garitte and Gens, 2012).
- 3) The INTERA Switzerland performed 3D TOUGH2 model simulations with anisotropic properties and inclined mesh. Their modeling was limited to thermal-hydrological processes (no mechanics) and done for thermal and monitoring design (Ewing and Senger, 2011).

Our modeling approach contains important components from these three models. The host rock is modeled using TOUGH-FLAC with anisotropic properties considering bedding planes of the Opalinus Clay. The bedding planes across the FE tunnel can be seen in Figure 3-5. These bedding planes are oriented with its strike along the tunnel axis, and dipping about 45°. To accurately model anisotropic thermal and hydrological behavior, we created an inclined TOUGH2 mesh, the same way as done by the INTERA team. Anisotropic mechanical material behavior is simulated using the FLAC3D ubiquitous joint model, with initial properties of those derived from the excavation design analysis by the Pöyry team (Nater, 2012). For the bentonite, we started with the BBM model as applied by the CIEMAT and UPC (Garitte and Gens, 2012), and derived specific input material parameters for the MX-80 bentonite pellets that will be used as emplacing bentonite buffer around the heaters. With this modeling approach, we are able to simulate THM processes in both the bentonite and host rock, as well as their interactions.



Figure 3-5. View of FE tunnel face from the FE niche showing beddings dipping 45° (Vieter, 2012).

3.2.3 FE Model Setup

Figure 3-6 presents the new 3D numerical grid that has been developed as an extension of the previous 2D grid. This model grid includes all vital material components for the modeling of the FE experiment, including layered Opalinus Clay host rock, excavation disturbed zone, tunnel, three heaters, bentonite buffer, concrete liner, and concrete plug. The initial conditions for the model simulation are 2 MPa in pore fluid pressure and 15°C in temperature for the host rock. The 2 MPa of pore pressure is not under hydrostatic conditions, and the process is affected by the existing tunnel system at the site. In our simulations, we first run a simulation with an open tunnel at the atmospheric pressure for 1 year, creating a pressure drop and hydraulic gradient around the tunnel. Potential desaturation caused by ventilation effects will be considered in future simulations. Thereafter, we assume instantaneous emplacement of the heater and buffer, and start our heating simulation.

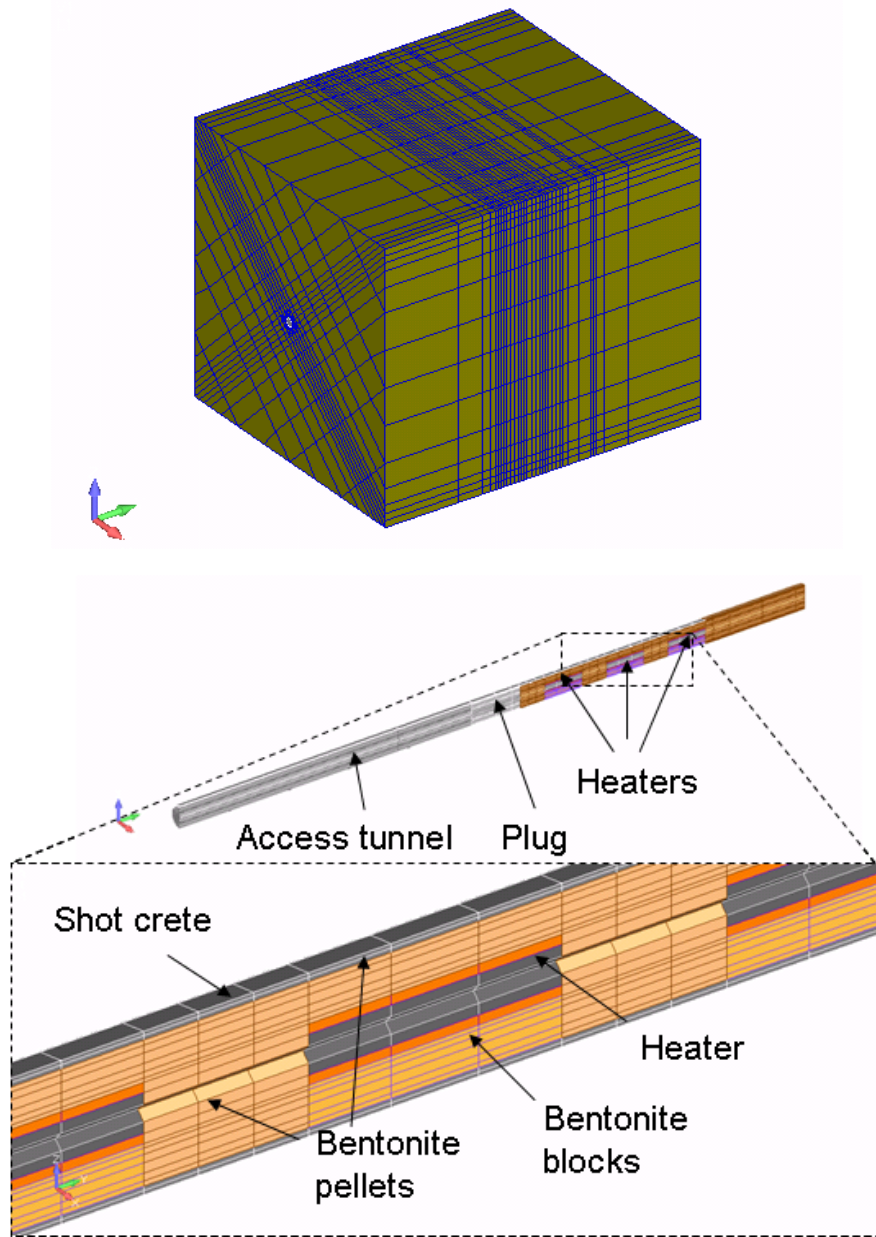


Figure 3-6. TOUGH-FLAC 3D numerical grid of the FE experiment (Rutqvist et al., 2013b).

Heating is assumed to occur for 20 years, according to the specifications set by NAGRA. The output from each of the heaters will be approximately 1500 W, and this is the heat power assumed in the current model. However, the heater power may be regulated to achieve a desired temperature evolution. For example, the targeted maximum temperature at the heater/bentonite interface is 125 to 135°C. On the other hand, a preliminary model simulation by the UPC team indicates that the temperature might not exceed 110°C, if the initial bentonite saturation is about 20 to 25%. A much higher peak temperature was calculated by the INTERA when assuming an initial saturation of 1%. Since buffer thermal conductivity depends on water saturation, the 1% initial saturation leads to a lower thermal conductivity in the buffer, which in turn results in a

relatively high temperature at the heater/bentonite interface. A 1% saturation is reasonable for the pellets being deposited into the tunnel during buffer emplacement. However, experience from the ongoing HE-E heater test at Mont Terri shows that the bentonite pellets quickly draw moisture from the air and equilibrate with air relative humidity. Therefore, the initial buffer saturation of 18% is a reasonable value for the modeling.

Table 3-1. Parameters for the Opalinus and Bentonite clay used in the scoping calculation

Properties	Parameters	Symbol	Opalinus Clay	Bentonite	Unit
Physical	Grain density	ρ_g	2.7×10^3	2.7×10^3	kg/m ³
	Porosity	\emptyset	0.15	0.389	-
	Pore compressibility	B	1.0×10^{-9}	5.0×10^{-8}	Pa ⁻¹
Hydraulic	Intrinsic permeability	K	5.0×10^{-20}	2.0×10^{-21}	m ²
	Liquid relative permeability	N	-	3	-
	Capillary curve	P_0	1.47×10^7	2.00×10^7	Pa
	Capillary curve	λ	0.595	0.51	-
	Capillary curve	S_{ls}	1.0	1.0	-
	Capillary curve	S_{lr}	0.01	0.00	-
Thermal	Thermal conductivity (wet)	λ_{sat}	2.0	1.3	W/m-K
	Thermal conductivity (dry)	λ_{dry}	2.0	0.3	W/m-K
	Grain specific heat	C	900	800	J/kg-K
Mechanical	Bulk modulus	K	4170	-	MPa
	Shear modulus	G	1920	-	MPa
	Cohesion	C	5	-	MPa
	Friction angle	ϕ	25	-	°
	Thermal exp. coeff.	α_T	1.0×10^{-5}	1.5×10^{-4}	1/°C
	Dilation angle	D	10	-	°
	Tensile strength	T	1.0	-	MPa
	Joint cohesion	C_J	2.2	-	MPa
	Joint friction	ϕ_J	23	-	°
	Joint tensile strength	T_J	0.5	-	MPa
	Joint dilation angle	d_J	10	-	°

The basic thermal and hydraulic material parameters are presented in Table 3-1. These are equivalent to the material parameters used in our previous 2D model analysis of the FE experiment. The properties for the Opalinus Clay are derived from Gens et al. (2007). We started with bentonite properties, including the thermal and hydraulic properties, derived from laboratory experiments and *in situ* tests related to the FEBEX experiment at Grimsel, Switzerland (Rutqvist et al., 2011). We then modified some of the properties to represent a bentonite buffer composed of MX-80 pellets. In our initial modeling we also consider the water-retention curves for the bentonite and Opalinus Clay as important parameters for the behavior. The capillary curves used in the model are shown in Figure 3-7. We use the van Genuchten formulation to describe the water-retention characteristic curves (van Genuchten, 1980):

$$P_c = -P_0 \left[\left(\frac{S_l - S_{lr}}{S_{ls} - S_{lr}} \right)^{-1/\lambda} - 1 \right]^{1-\lambda} \tag{3-1}$$

where P_0 is the air entry pressure, S_l is water saturation, the subscripts ls and lr refer to the fully saturated and residual conditions, respectively, and λ is a curve fitting parameter. These values are presented in Table 3-1. Those for the Opalinus Clay are taken from the previous simulation and fit against a series of laboratory and *in situ* measurements (Garitte et al., 2013), and those for bentonite clay are adjusted to match an *in situ* measurement of the initial state at the Mont Terri site (approximately 100 MPa at water saturation of 20%).

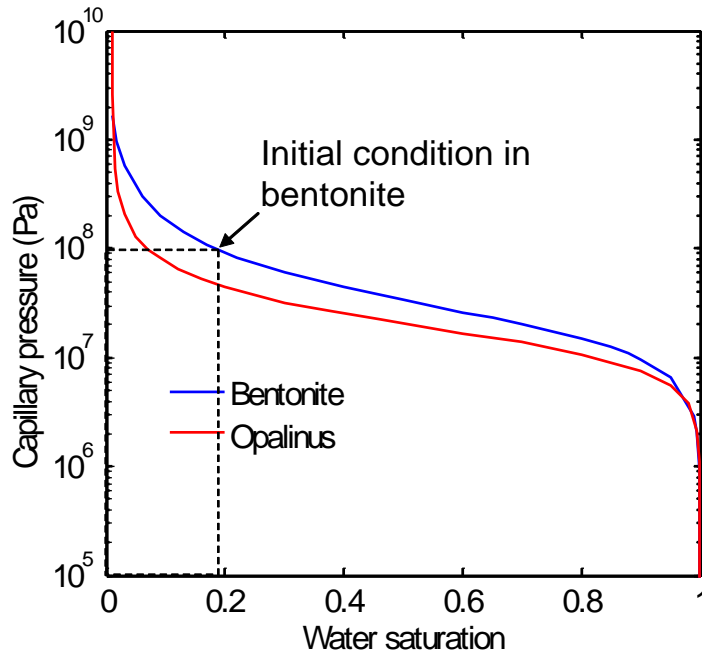


Figure 3-7. Capillary curves for Bentonite and Opalinus clays

3.2.4 3D TH scoping calculations with comparison to 2D results

Figure 3-8 shows the TH results from the new 3D analysis, and in Figure 2-9 we compare the results of the new 3D and the previous 2D analyses, where the 2D model domain is a cross section orthogonal to the tunnel axis. The monitoring points in the 3D model are located at the middle of the center heater at different radial distances from the tunnel axis. In the new 3D simulation, the peak temperature in the bentonite near the heater surface (0.55 m) is higher than in the 2D analysis; it is about 120°C (Figure 2-8(a)). Similar to the 2D analysis, the buffer is not fully saturated after 30 years (Figure 2-8(b)). At the buffer and concrete interface (1.18 m), the temperature peaks at about 67°C after 20 years, i.e., slightly lower than in the 2D analysis. Consistent with the previous 2D analysis, as soon as the bentonite buffer is installed, liquid water is pulled from the host rock due to the strong capillary pressure at an initial saturation of 18%. Water saturation near the bentonite buffer and concrete liner interface (1.18 m) increases immediately after the installation; correspondingly, a slight desaturation is observed in the host rock. The resaturation process is quite slow due to the low permeability of the host rock and bentonite buffer. The water saturation near the canister is approximately 68% after 30 years.

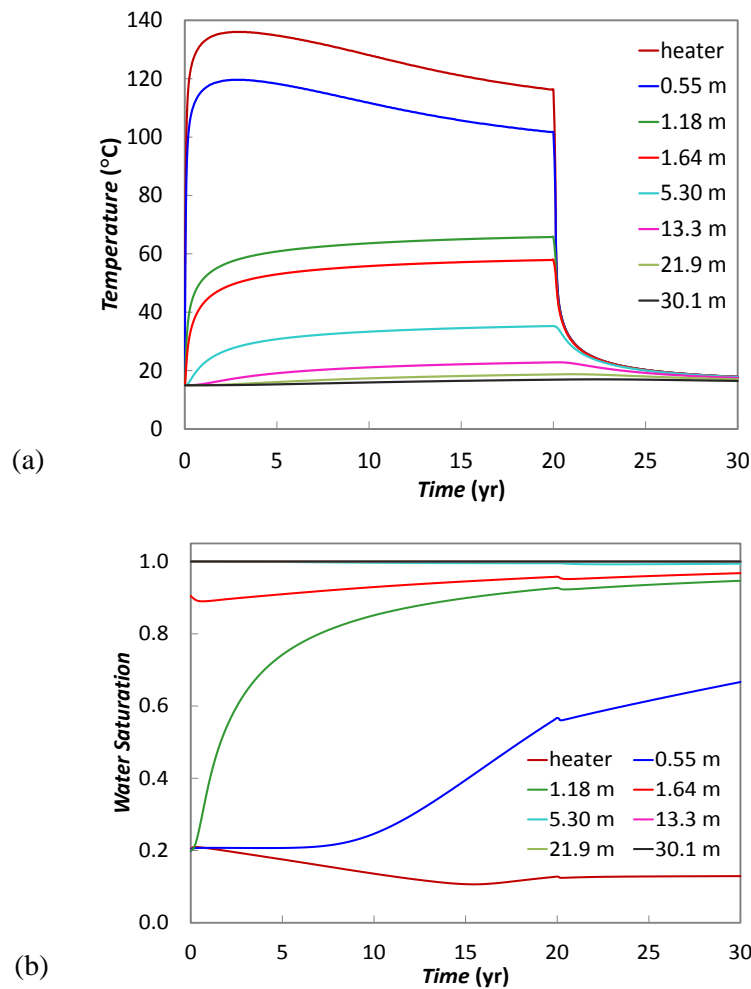


Figure 3-8. 3D simulation results related to the evolution of TH processes in the buffer and host rock: (a) temperature, (b) liquid saturation. Monitoring points are located at the middle of the center heater at different radial distances from the tunnel axis.

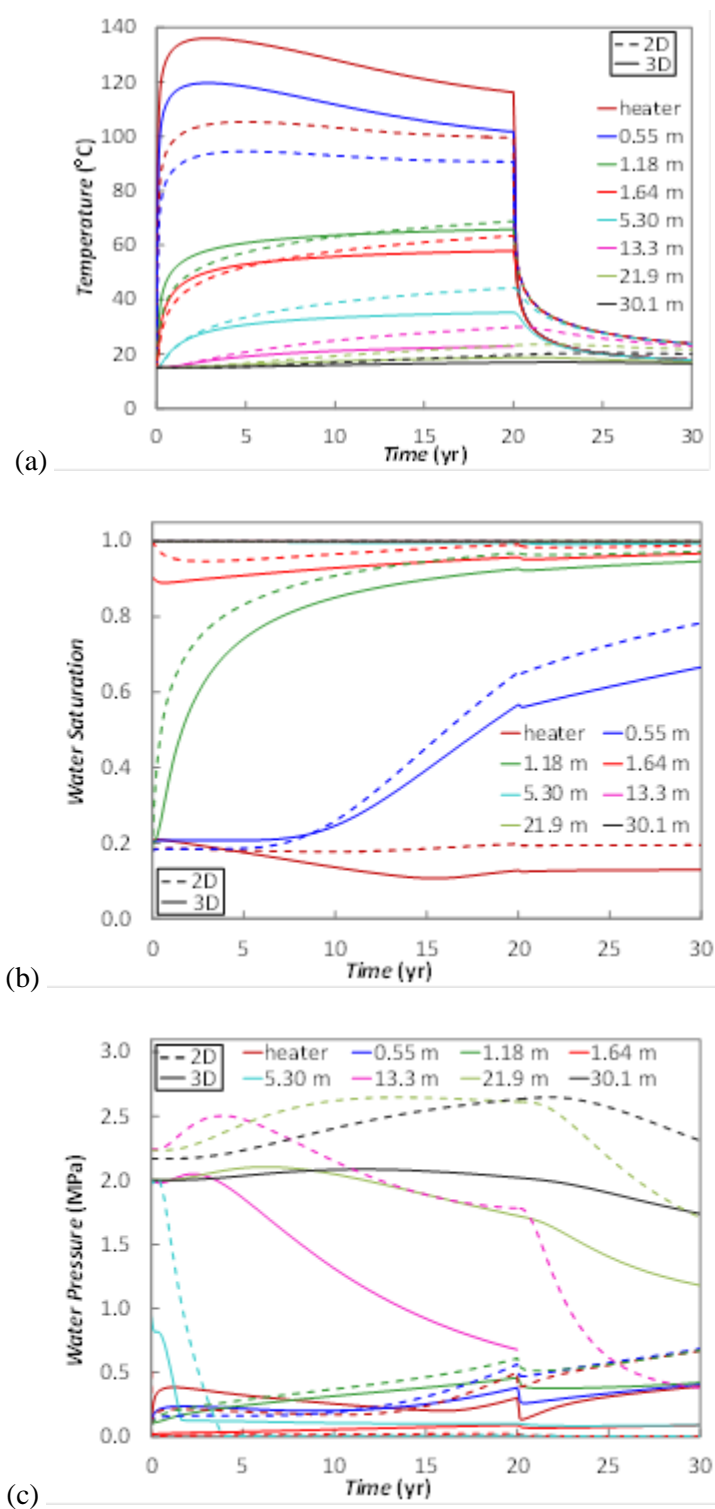


Figure 3-9. Comparison of previous 2D and new 3D simulation results: (a) temperature, (b) liquid saturation, (c) fluid pressure.

The pore-pressure evolution is rather complex in the buffer and rock system around the FE experiment, but these are all responses that can be explained by the coupled TH processes. The pressure increases gradually in the bentonite buffer along with the resaturation of the buffer. The host rock near the concrete/Opalinus interface experiences a sudden depressurization after the installation of the bentonite buffer. Because the rock is unsaturated, the pore pressure remains low during the 20 years of heating. However, the deep host rock (>13.3 m away from canister) is pressurized owing to the increase in temperature in the first few years, whereupon the pressure declines again as a result of suction from the bentonite-filled tunnel.

In the comparison of the new 3D versus the previous 2D analysis, we can observe that the most significant difference occurs in the temperature evolution close to the heater and in the pressure evolution in the Opalinus Clay at some distance away from the tunnel (Figure 3-9). The 3D analysis predicts a higher peak temperature at the heater; this is expected, because in the 2D analysis the heat load was based on an average line thermal load of 197 W/m, taking into account the spacing between individual heaters. The 3D analysis is more accurate for calculating the peak temperature at the mid-heater surface; this was about 120°C compared to 94°C for the 2D analysis. The fluid pressure in the host rock away from the tunnel is different in terms of magnitude of thermal pressurization, which is significantly higher in the case of the 2D model analysis. In the 2D analysis, an incremental pressure increase of about 0.5 MPa can be observed (e.g., black dashed line in Figure 3-9(c)), whereas the maximum pressure increase is about 0.1 MPa in the 3D analysis (e.g., black solid line in Figure 3-9(c)). The thermal pressurization is lower in the case of the 3D analysis, because the pressure can escape in the third dimension, whereas in the 2D analysis, the pressure is confined within the 2D model.

3.2.5 Study of peak temperature considering diffusion

In the previous simulation, we had neglected diffusion of water vapor, which is an important process for capturing early time drying of the bentonite buffer near the heater. We therefore conducted another simulation in which we assigned a diffusion coefficient of $1.73e-5 \text{ m}^2/\text{s}$. Figure 3-10 presents the evolution of temperature and saturation in the case where the thermal diffusion causes drying and a decrease in saturation near the heater. This reduction in liquid saturation results in a lower buffer thermal conductivity and (consequently) a higher peak temperature of 130°C. We note that the evolution of the liquid saturation in the buffer is important for the peak temperature, and that 130°C is right within the targeted 125 to 135°C temperature range. However, further analysis should be made once the accurate thermal properties have been determined for the MX-80 granular bentonite to be used in the actual experiment. For example, in our first predictive analysis presented in Section 2.7, we used parameters that are likely to be more representative of the MX-80 granular bentonite, and in that case a substantially higher peak temperature is predicted.

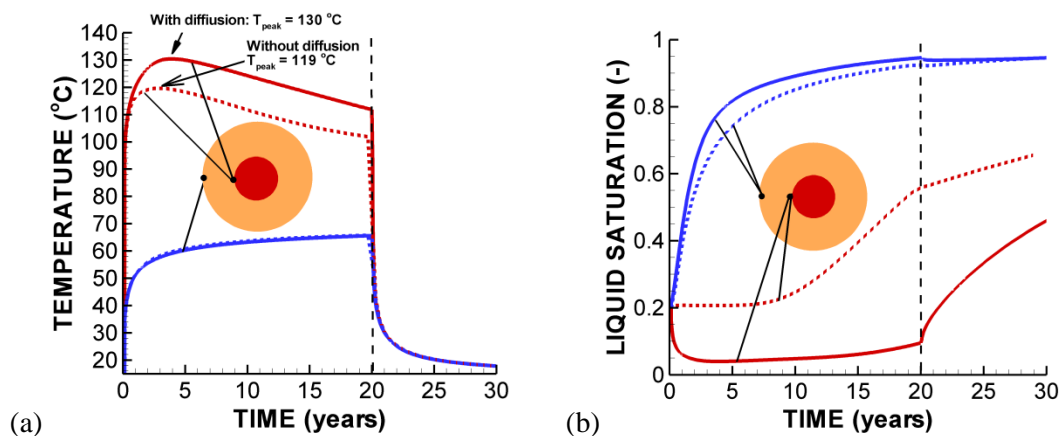


Figure 3-10. Simulation results considering drying induced by diffusion of water vapor within the buffer: (a) temperature, (b) liquid saturation.

3.2.6 3D THM scoping simulation using the BBM

We have conducted new modeling simulations using (for the first time) the BBM in a full 3D setting. The BBM (Alonso et al., 1990) has been implemented into TOUGH-FLAC as part of the UFD EBS program. BBM is a constitutive model for elasto-plastic mechanical behavior of unsaturated soil, which has been applied for modeling of bentonite-buffer behavior (Gens et al., 2009). It includes important coupled hydraulic and mechanical features such as strengthening and stiffening with drying. In this model simulation, we are using the same TH properties, which are given in Table 3-1. In addition, we now add the material parameters for the BBM, which are given in Table 3-2. The parameters for the BBM used in this initial 3D THM model simulation are those derived for FEBEX bentonite by Gens et al. (2009), and also applied in Rutqvist et al. (2013a) for the modeling of THM processes around a generic nuclear waste repository. A large number of material parameters are required to describe the THM material behavior, and those given in Table 3-2 have been determined from laboratory experiments. As mentioned, for the rock-mass behavior, we used a ubiquitous joint model (anisotropic plasticity with different shear strength along bedding planes) consistent with the previous ground-support design analysis (Nater, 2012). The rock mechanical properties for the Opalinus Clay were taken from Corkum and Martin (2007).

A significant number of measurements using different procedures (borehole slotter, undercoring, and hydraulic fracturing) of the in situ stress have been made at Mont Terri. A synthesis of these is given in Garitte et al. (2013):

- Major principal stress is subvertical and corresponds approximately with overburden weight (about 7MPa)
- The magnitude of the intermediate principal stress obtained from the undercoring technique is consistent with the results from hydraulic fracture tests (about 5MPa)

- The value of the minor principal stress is quite low and probably controlled by the presence of a deep valley to the SW of the laboratory. A low value of the minor principal stress is consistent with the small number of breakouts observed in vertical boreholes (about 2MPa).

In our modeling we then set the vertical stress to 7 MPa, whereas the maximum horizontal stress perpendicular to the tunnel is set to 5 MPa.

Figure 3-11 shows the simulated stress evolution in the buffer; Figure 3-12 shows the evolution of the mean effective stress and bulk modulus in the buffer. The compressive stress increases along with the resaturation of the buffer, which first takes place at the tunnel wall. The maximum stress at the end of heating (20 years) is about -2.5 MPa (compressive stress), with highest maximum occurring at the tunnel wall, i.e., at the buffer and concrete lining interface. After 20 years, there is a sudden drop in compressive stress as a result of the temperature drop once the heater is turned off. This drop in buffer stress, caused by the cooling shrinkage, results in a substantial stress drop because the buffer is relatively stiff at that time (Figure 2-12). The radial compressive stress in the buffer is quite uniform (similar to the magnitude at the heater and concrete lining) and is about -1.7 MPa at the end of this simulation. This compressive stress is applied on the concrete lining and supports the rock wall.

The rock stress evolution is shown in Figure 3-13. The initial stress is quite anisotropic at the tunnel wall, with a relatively high tangential stress, while the radial stress is small as a result of the free rock surface. However, the concrete lining provides some support, so the radial stress is not zero, but rather a few MPa. During the heating of the rock, and as a result of the buffer swelling, the stress changes with time (as expected). At 20 years, the stress at the tunnel wall is about -3.3 MPa, which is higher than initial, as the swelling pressure from the buffer provides some support to the rock wall. Note that in our FY2012 report, we presented 2D results for stress evolution using a simple swell model for the buffer and achieved a higher swelling stress in the buffer. The magnitude of this swelling stress depends on the parameter input governing the swelling in both the simple swell model and the BBM. However, the higher swelling pressure in our previous model simulation resulted in more substantial effects on the rock stress near the tunnel wall, making the stress more isotropic than was achieved in the current 3D model simulation. A detailed back analysis of swelling stress parameters will be made for the MX-80 granular bentonite material to be used in the FE experiment.

Table 2-2. BBM material parameter values for the bentonite buffer (Gens et al., 2009)

Parameter	Value
Compressibility parameter for stress-induced elastic strain, κ_{PS0} [-]	0.05
Compressibility parameter for suction-induced elastic strain, κ_{SP0} [-]	0.25
Shear modulus, G [MPa]	NA
Poisson's ratio, ν [-]	0.4
Parameter for suction induced elastic strain, α_{SS} [-]	0
Parameter for stress-induced strain α_{PS} [MPa ⁻¹]	-0.003
Parameter for stress-induced strain, α_{SP} [-]	-0.161
Reference stress state for relating elastic compressibility to suction, P_{ref} [MPa]	0.5
Parameters that relate elastic volumetric strain and temperature changes, α_0 [°C ⁻¹]	1.5e-4
Compressibility parameter in virgin soil states at zero suction, λ_{PS0} [-]	0.15
Parameter defining soil stiffness associated with loading collapse yield, r_λ [-]	0.925
Parameter for the increase of soil stiffness with suction, β_λ [MPa ⁻¹]	0.1
Parameter that relates cohesion to temperature, ρ_s [°C ⁻¹]	0
Parameter describing the increase of cohesion with suction, k_s [-]	0.1
Tensile strength at saturated conditions, P_{S0} [MPa]	0
A reference stress state for compressibility relation in virgin states, P^C [MPa]	0.5
Slope of the critical state line, M [-]	1
Nonassociativity parameter in the plasticity flow rule, α_a [-]	0.53
Specific volume at reference stress states P^C in virgin states, v^c [-]	1.937
Net mean yield stress for saturated conditions at reference temperature, P_{OT}^* [MPa]	12.0

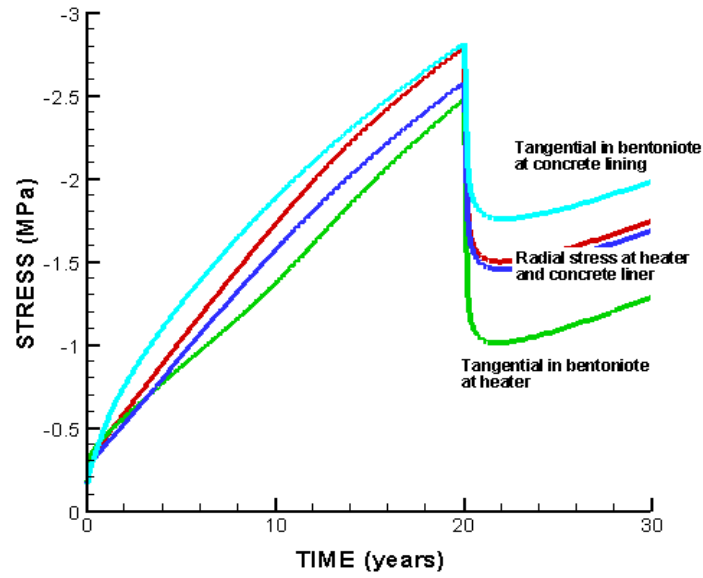


Figure 3-11. Simulated stress evolution within the bentonite buffer.

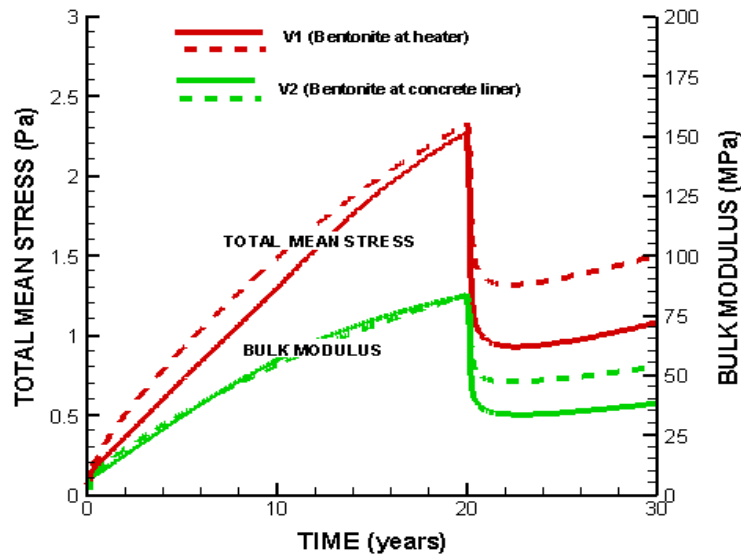


Figure 3-12. Simulated evolution of mean stress and bulk modulus within the buffer.

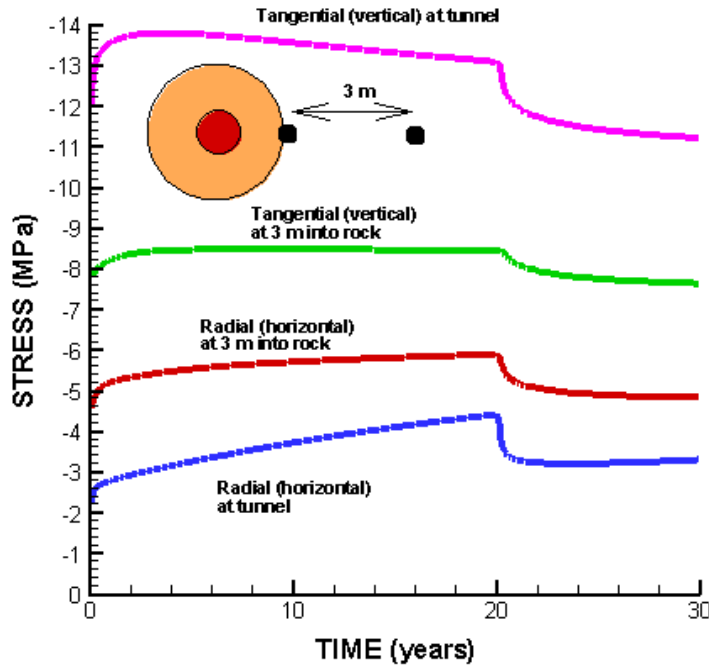


Figure 3-13. Simulated stress evolution within the Opalinus Clay.

3.2.7 1D axisymmetric benchmark calculation

A benchmark calculation has been defined by NAGRA aiming at validating the different models used for the THM analysis of the FE experiment (Garitte, 2013). The models developed for this benchmark aim at reproducing the THM response of the backfill material and the rock considering the simplest possible approach. The model results will thus not be representative of the response expected in the real FE experiment. Our approach was to first conduct a TOUGH2 simulation to calculate TH responses, uncoupled from geomechanics. Then, we conducted a full TOUGH-FLAC simulation to add geomechanical processes to the analysis.

Definition of the Benchmark

The modeling of the benchmark involves simulation of initial conditions, tunnel excavation, emplacement of shotcrete, emplacement of backfill and finally heating. The geometry and initial and boundary conditions for each of these steps are shown in Figure 3-14 and summarized in Table 2-3. The model domain shown in Figure 3-14 represents a 1D slice of Opalinus Clay of 30 m radial extension with:

- an axisymmetric axis on the left boundary and
- a temperature of 15°C, a pore water pressure of 2 MPa and 5 MPa normal stress on the right boundary. The right boundary condition will remain in this state throughout the simulation.

Before tunnel excavation, Opalinus Clay is considered saturated, with a pore water pressure of 2 MPa and isotropic stress state of 5 MPa, and an initial temperature of 15°C (Figure 3-14a).

The tunnel excavation is simulated by removing instantaneously 1.5 m of Opalinus Clay at the centre of the model. The new left boundary condition is characterized by 0 normal stresses, a pore-water pressure of 0 MPa and a temperature of 15°C (Figure 3-14b).

The shotcrete is emplaced one day after the tunnel excavation (Figure 3-14c). The shotcrete is initially saturated, with 0 MPa of pore water pressure, a temperature of 15°C and the initial stress state is 0 MPa. The new left boundary condition is characterized by 0 normal stresses, a pore-water pressure of -20 MPa and a temperature of 15°C.

The backfill material is emplaced 668 days after the shotcrete (Figure 3-14d). As a consequence of the 1D assumption no difference can be made between the bentonite blocks and the bentonite pellets mixture. The initial conditions of the bentonite are:

- Degree of saturation of 18.5% and dry density of 1.45.
- Pore water pressure: according to retention curve (see parameters section)
- Temperature of 15°C
- 0 MPa stresses

The new left boundary condition is characterized by zero displacement, no water, and no heat flux.

Heating is turned on 1 day after the bentonite has been emplaced. A constant heat flux of 325 W/m is applied on the left boundary. This heat flux was determined as 1500 W (heat output of one heating device) divided by the length of a heating device.

The material parameters were strictly defined by NAGRA, but may have to be adjusted depending on the specific numerical model used by a modeling team. We discuss how the material parameters were input to the TOUGH2 TH model later in this section.

Table 3-3. Summary of the initial and boundary conditions. Start of each action is referenced to the start of heating

Action	Start (Days)	Left boundary condition				Initial conditions new material			
		Position	T	H	M	Material	T	H	M
Excavation	-670	1.5m	15°C	0MPa	0MPa	Opa.	15°C	2MPa	5MPa
Shotcrete emplacement	-669	1.35m	15°C	-20MPa	0MPa	Shotcrete	15°C	0MPa	0MPa
Bentonite emplacement	-1	0.525m	0W/m	0 flux	0 displ.	Bentonite	15°C	Sr=18.5%	0MPa
Heating	0	0.525m	325W/m	0 flux	0 displ.	-	-	-	-

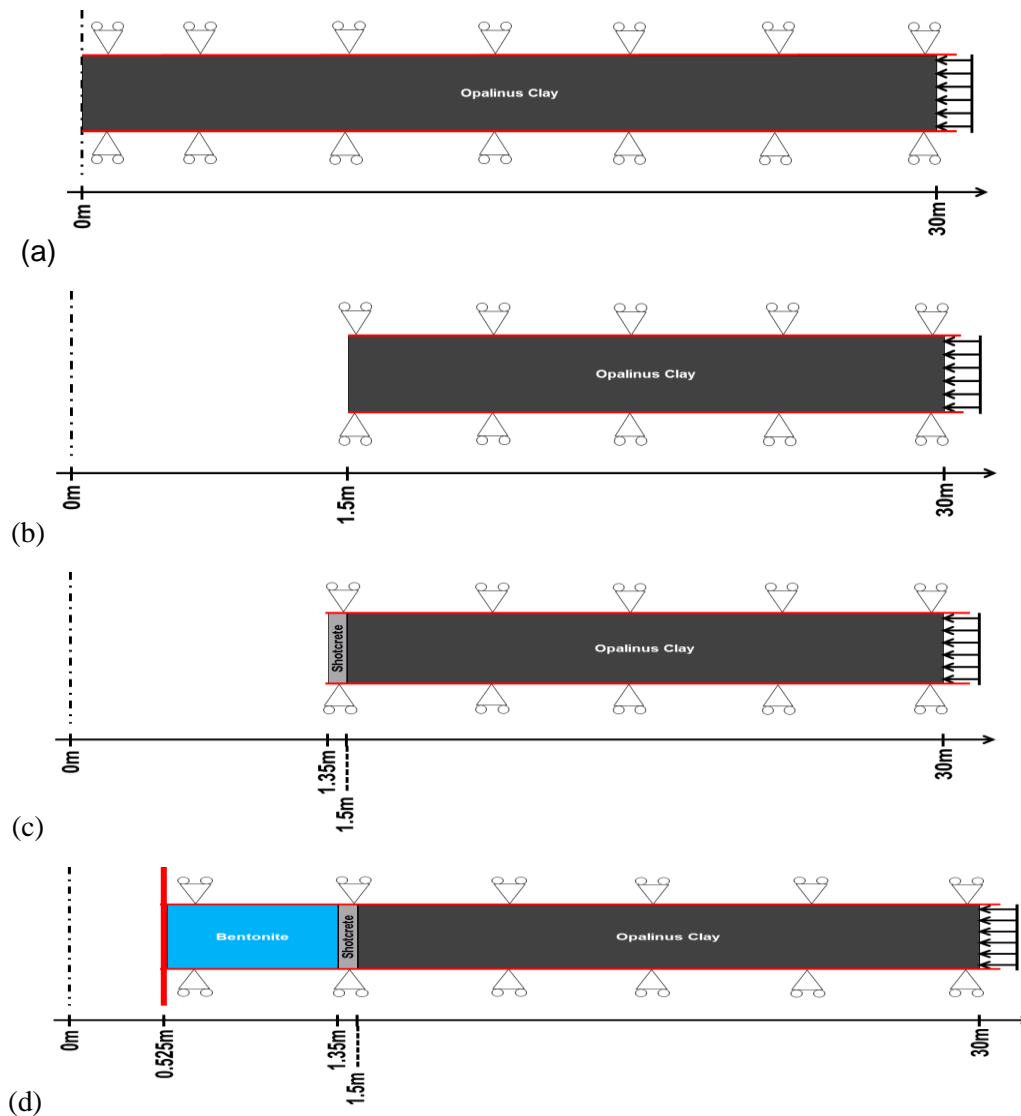


Figure 3-14. Model geometry and boundary conditions at (a) initial state, (b) after excavation, (c) after shotcrete emplacement, and (d) after emplacement of backfill material (Garitte, 2013)

Setup of a TOUGH2 model for TH analysis

The system is a one-dimensional, radial slice of the buffer and rock out of an infinitely long cylinder (Figure 3-15). The origin of the radial coordinate system is at the center of the waste package and extends out to 30 m. The system is modeled in stages starting with tunnel excavation, followed by shotcrete emplacement, followed by buffer emplacement, and then by heating from the waste package. The model domain was discretized into 323 cells with the radial dimensions given in Table 3-4. The cell thickness is a constant 1 m. A large-volume cell is also included at the end of the rock section to maintain constant thermodynamic conditions at the rock boundary.

Table 3-4. TOUGH2 numerical discretization of the 1D BMT

Component	Number of cells	Cell size (m)
Buffer	1	0.005
Buffer	82	0.01
Shotcrete	15	0.01
Rock	50	0.01
Rock	50	0.1
Rock	115	0.2

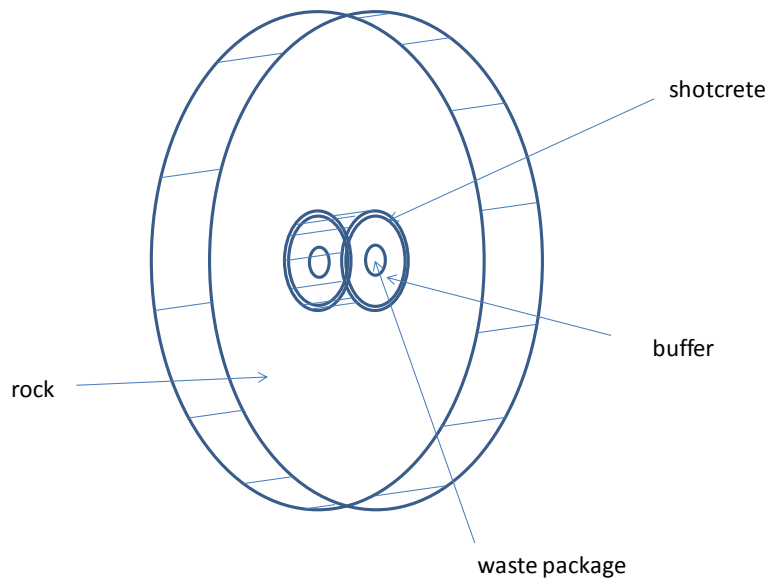


Figure 3-15. Three-dimensional view of overall problem domain

In the TOUGH2 simulation of this problem, the model domain changes for the different stages according to the benchmark description, and the exact initial and boundary conditions used in the model are presented in Figure 3-16. Stages 1 to 3 are simulated to provide correct initial conditions for the heating in Stage 4. The heat flux for Stage 4 was applied at the inner buffer radius into a cell representing the heater. As mentioned before, according to the benchmark definition, heat flux was applied at a constant rate of 325 W/m.

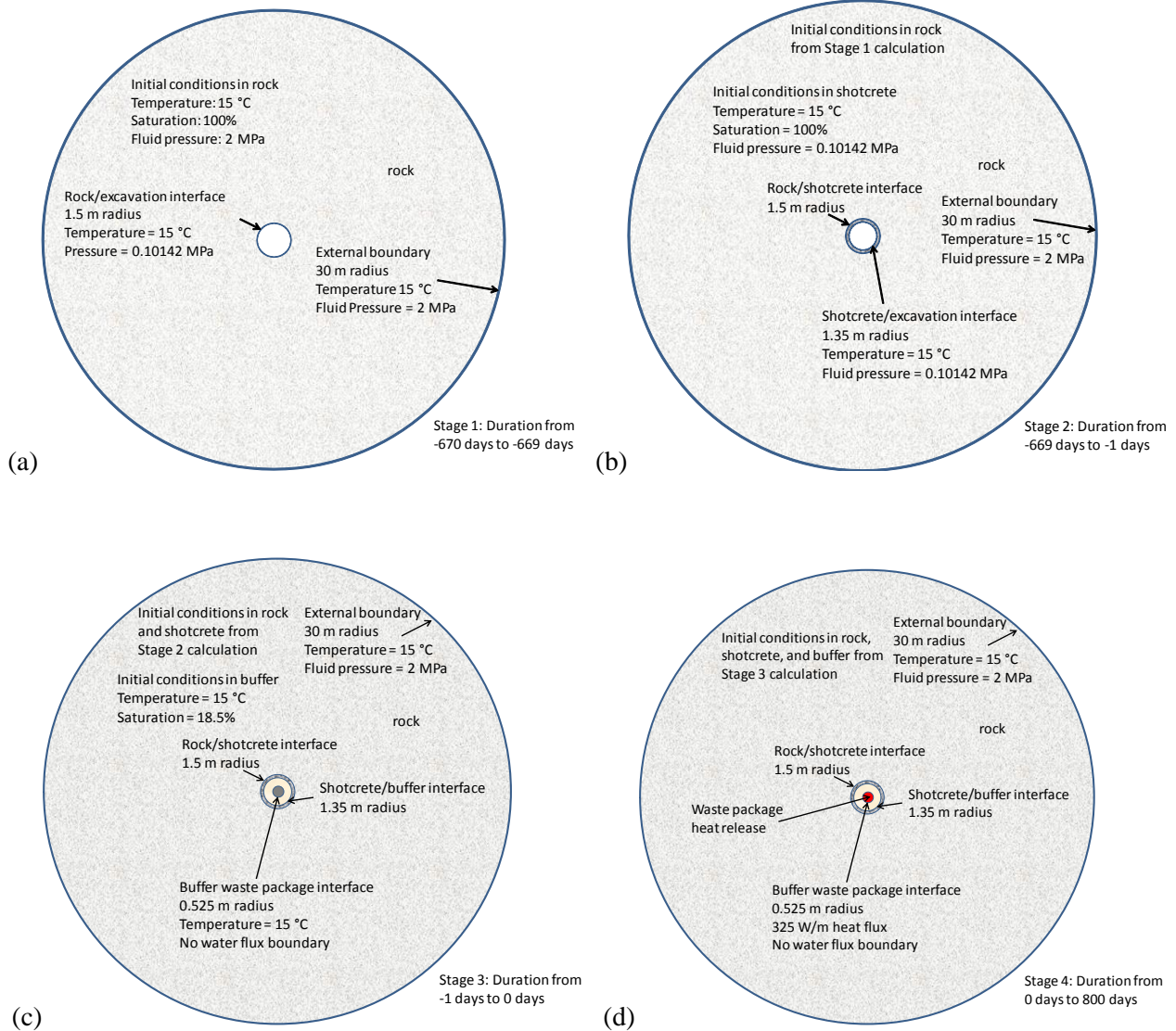


Figure 2-16. TOUGH2 model conditions during (a) Stage 1 (-670 to -669 days), (b) Stage 2 (-669 to -1 day), (c) stage 3 (-1 to 0 days), and (d) stage 4 (0 to 800 days)

The parameters used in the TOUGH2 model are those defined in the task description and given in Table 3-5. Note that there are differences in values of some of these parameters compared to those used in the previous scoping calculation. Most significantly, the thermal conductivity of the both the buffer and the rock are lower than those used in the scoping calculation.

Table 2-5. Parameters for FE 1-D benchmark

	Overpack	Buffer	Shotcrete	Rock
Solids density (kg/m ³)	8000.	2700.	2700.	2700.
Porosity	0.46	0.46	0.15	0.15
Permeability (m ²)	5 x 10 ⁻⁵² (3,4)* 5 x 10 ⁻¹¹ (1,2)*	3.5 x 10 ⁻²¹	3.5 x 10 ⁻²¹	3.5 x 10 ⁻²⁰
Thermal conductivity (saturated) (W/m-K)	20.	1.	1.7	1.7
Specific heat (solids) J/kg-°C	490.	950.	800.	800.
Thermal conductivity (desaturated) (W/m-K)	20.	0.3	1.06	1.06
Tortuosity	10 ⁻¹¹ (3,4)* NA (1,2)*	1.	1.	1.
Water relative permeability parameter A, (Equation (2-2))	1.3	5	NA	NA
Water relative permeability residual saturation, S _r (Equation (2-2))	0.	0.	NA	NA
Water relative permeability maximum saturation, S _m (Equation (2-2))	1.	1.	NA	NA
Water relative permeability parameter m, (Equation (2-3))	NA	NA	0.52	0.52
Water relative permeability residual saturation, S _r (Equation (2-3))	NA	NA	0.0071	0.0071
Water relative permeability maximum saturation, S _m (Equation (2-3))	NA	NA	1.	1.
Capillary pressure parameter, α (Pa ⁻¹) (Equation (2-4))	10 ⁻⁷	10 ⁻⁷	9.091 x 10 ⁻⁸	9.091 x 10 ⁻⁸
Capillary pressure parameter, m, (Equation (2-4))	0.4	0.4	0.29	0.29
Capillary pressure residual saturation, S _r (Equation (2-4))	0.	0.	0.0071	0.0071
Capillary pressure maximum saturation, S _m (Equation (2-4))	1.	1.	1.	1.
Vapor and air diffusion coefficients (D in Equation (2-6)) (m ² /s)	2.68 x 10 ⁻⁵	2.68 x 10 ⁻⁵	2.68 x 10 ⁻⁵	2.68 x 10 ⁻⁵
Vapor and air diffusion temperature exponents, (n in Equation (2-6))	2.3	2.3	2.3	2.3

*The numbers in parentheses indicate to which of the four stages the parameter applies (tunnel excavation is 1, shotcrete emplacement is 2, bentonite emplacement is 3, and heating is 4).

NA = not applicable

The water relative permeability in the buffer is a power-law relationship given by

$$k_{rw}(S_w) = \left(\frac{S_w - S_r}{S_m - S_r} \right)^A \quad (3-2)$$

The water relative permeability in the shotcrete and rock is given by the van Genuchten relationship

$$k_{rw}(S_w) = \left(\frac{S_w - S_r}{S_m - S_r} \right)^{1/2} \left[1 - \left\{ 1 - \left(\frac{S_w - S_r}{S_m - S_r} \right)^{1/m} \right\}^m \right]^2 \quad (3-3)$$

Capillary pressure in the buffer, shotcrete, and rock are given by the van Genuchten relationship:

$$\psi(S_w) = \frac{1}{\alpha} \left\{ \left(\frac{S_w - S_r}{S_m - S_r} \right)^{-1/m} - 1 \right\}^{1-m} \quad (3-4)$$

The relative permeability to gas for the buffer is set to a constant value of 1. The relative permeability to gas in the shotcrete and rock is:

$$k_{rg}(S_w) = 1 - k_{rw}(S_w). \quad (3-5)$$

Variations in thermal conductivity and specific heat with water saturation are assumed to be linear between the defined end points. The vapor and air diffusion coefficients are a function of temperature and gas saturation defined by:

$$D_g^w = \tau S_g D \frac{P_{g0}(273.15+T)^n}{P_g(273.15)^n} \quad (3-6)$$

The problem was solved using TOUGH2 with the EOS4 equation-of-state module. From the simulations of this benchmark test, we discovered some numerical instability in the water saturation when the relatively high diffusion coefficient listed in Table 3-5 was used. One remedy to avoid such numerical instability was to change diffusion driving force in TOUGH2 from the mass fraction gradient times the phase density to the density gradient of the diffusing component. If the phase density is constant, these two methods give the same result. However, we also found that if a high intrinsic gas permeability was used numerical instability in water saturation did not occur. It is known from numerous laboratory and field experiments that intrinsic permeability to gas flow can be high, and a difference of about six order of magnitude between intrinsic gas and water permeability has been observed (Olivella and Gens, 2000). In TOUGH2 we simulated this high gas permeability through the Klinkenberg parameter according to:

$$K_g = K_l(1+b/P) \quad (3-7)$$

where K_g is intrinsic permeability for gas flow, K_l is intrinsic permeability for water flow, b is the Klinkenberg parameter, and P is pressure. In this case we assigned a high value, 2.5×10^{11}

Pa^{-1} , for the Klinkenberg parameter. For a near atmospheric pressure, i.e. 0.1×10^6 Pa as assumed initially in the buffer, b/P would be 2.5×10^6 , that is, intrinsic permeability for gas flow would be about 6 orders of magnitude higher than the intrinsic permeability for water flow.

TOUGH2 TH benchmark simulation results

TOUGH2 simulation results are given in Figures 3-17, 3-18, and 3-19 for temperature, water saturation, and pore-water pressure, respectively. The waste package-buffer interface is at $x = 0.525$ m, the buffer-shotcrete interface is at $x = 1.35$ m, shotcrete-rock interface is at 1.5 m, and the far boundary is at 30 m. Time histories are given in Figure 2-20 for water saturation and temperature at the heater ($r = 0.525$ m) and near the outer edge of the buffer ($r = 1.275$ m). The simulation results show that the buffer remains dry near the heater whereas water infiltrates from the rock and saturates the buffer near its interface with the rock. The temperature increases substantially near the heater with a peak temperature exceeding 200°C . Note, though, that the temperature will be overestimated compared to what will be expected in the field because of the simplified 1D model geometry and the assumed heat load.

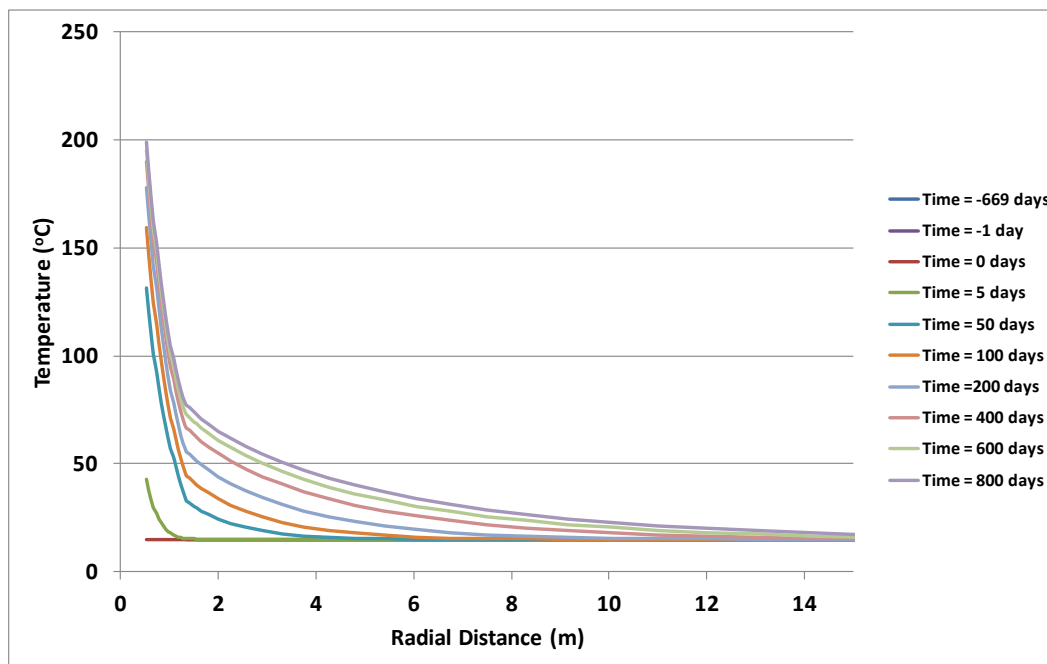


Figure 3-17. Temperature profiles

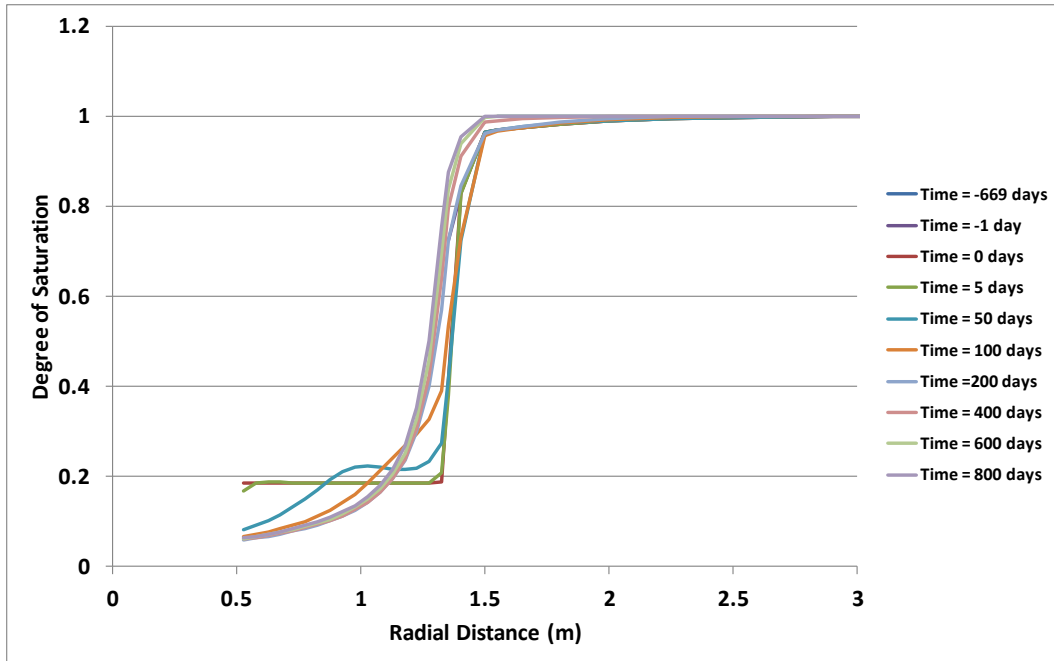


Figure 3-18. Degree of saturation profiles

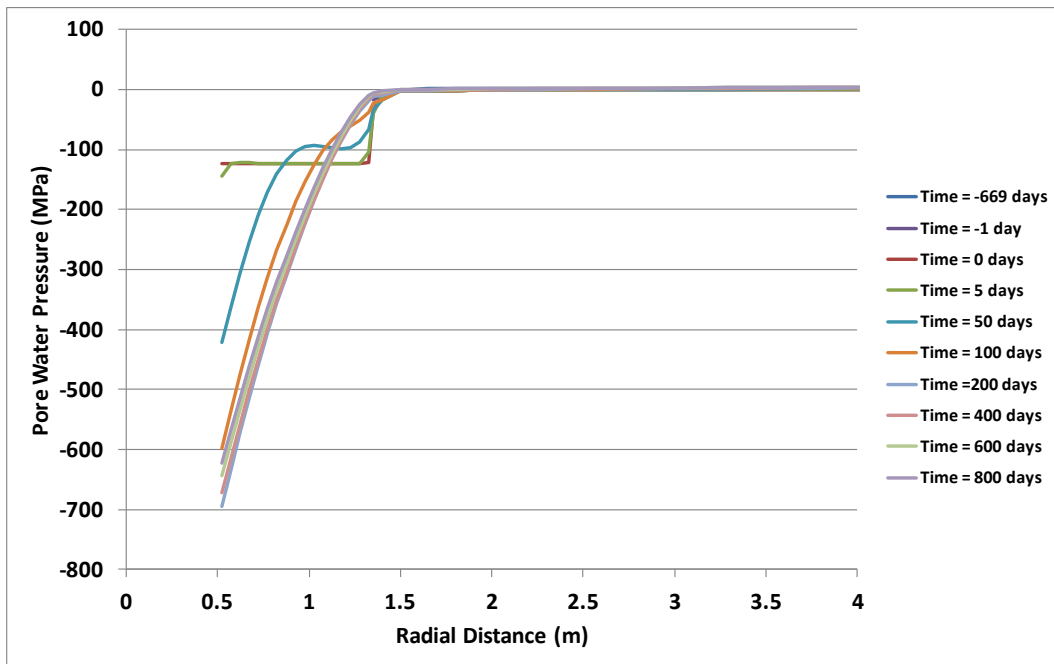


Figure 3-19. Water pressure profiles

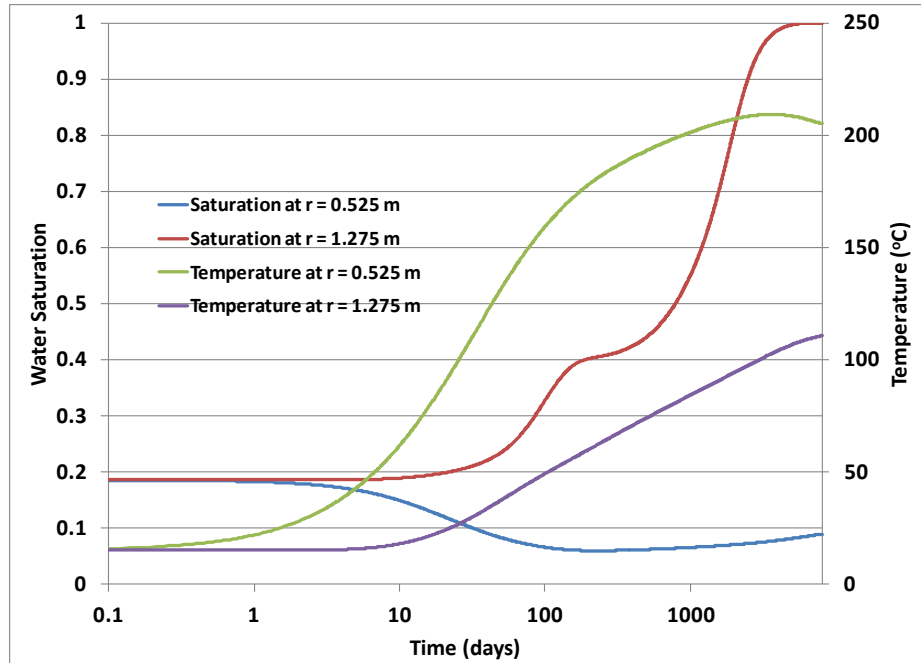


Figure 3-20. Time histories for saturation and temperature at two locations in the buffer

TOUGH-FLAC THM benchmark simulation results

We conducted an initial THM model simulation of the benchmark example using TOUGH-FLAC. The THM simulation was conducted over the same modeling stages including tunnel excavation, shotcrete projection, canister and bentonite placement and heating induced by the nuclear waste. In this case we make use of axisymmetry and model only 10° of the cylinder for the FLAC3D part of the TOUGH-FLAC model. The mechanical properties used in the THM model are summarized in Table 3-6. From recent experiments conducted on laboratory samples of MX-80 granular bentonite, the swelling stress developed when going from about 18.5% to 100% liquid saturation is about 7 MPa (Rizzi et al., 2011). In this model simulation, and as defined in the benchmark, a simple elastic model is used to simulate the mechanical behavior of the bentonite with a Young's modulus fixed at 300 MPa. We used a linear elastic swelling model (Rutqvist et al., 2011), in which the volumetric swelling and the swelling stress depends on the changes in water saturation, ΔS_l , according to:

$$\Delta\sigma'_{sw} = 3K\Delta\varepsilon_{sw} = K\Delta S_l\beta_{sw} \quad (3-8)$$

where $\Delta\sigma'_{sw}$ is the induced swelling stress (an effective stress), K is the bulk modulus, and β_{sw} is a model input parameters can be determined analytically to achieve a desired maximum swelling stress of 7 MPa. For the given Young's modulus and Poisson's ratio the bulk modulus would be 200 MPa, and then the appropriate moisture swelling coefficient can be calculated using Equation (2-9) as:

$$\beta_{sw} = \frac{\Delta\sigma'_{sw}}{3K\Delta S_l} = \frac{7 \cdot 10^6}{3 \cdot 200 \cdot 10^6 \cdot (1.0 - 0.185)} = 0.0143 \quad (3-9)$$

The results of stress profiles are shown in Figure 3-21. The highest stress occurs in the shotcrete as longitudinal and tangential stress with maximums of 75 and 40 MPa, respectively. These are thermal stresses as these can be very high as a result of the relatively high Young's modulus and high thermal expansion coefficient in the shotcrete. The tangential and longitudinal stresses in the Opalinus Clay peak at about 25 to 30 MPa just outside the shotcrete and is also a result of thermally induced stress. In the bentonite buffer, the stress is less than 2 MPa and is affected by both thermally induced stress and moisture swelling induced stress. Tangential and longitudinal stress is low near the heater due to drying shrinkage in that area, whereas it is higher near the interface of the buffer with the shotcrete. However, overall the buffer stays quite dry throughout the 800 days of simulations and therefore the stress in the buffer is relatively low till the end of the simulation.

Table 3-6. FLAC3D Mechanical parameters for FE 1-D benchmark.

	Overpack	Buffer	Shotcrete	Rock
Young's modulus (MPa)	200x10 ³	300	30x10 ³	6x10 ³
Poisson ratio (-)	0.3	0.25	0.25	0.25
Thermal expansion coefficient (°C ⁻¹)	1.5x10 ⁻⁵	1.5x10 ⁻⁵	3.5x10 ⁻⁵	3.5x10 ⁻⁵
Swelling coefficient	0	0.0143	0	0

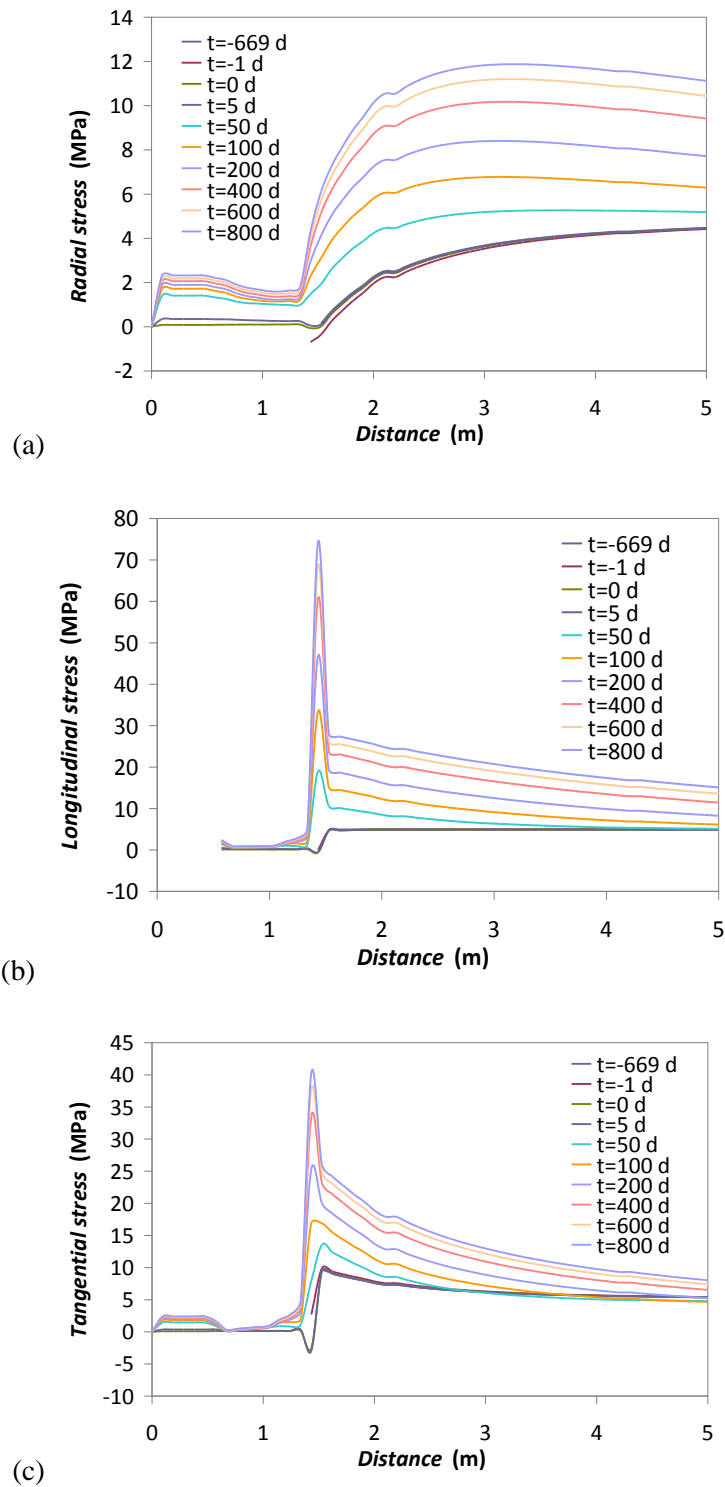


Figure 3-21. Profiles of (a) radial, (b) longitudinal, and (c) tangential stress

3.2.8 Initial 3D TH model prediction of peak temperature

In this section we present an initial model prediction of temperature evolution during the FE Experiment using the current best estimate of TH properties. These properties are equivalent to those given in the benchmark definition. With regard to predicting the peak temperature, some of the most significant differences compared to the scoping calculation in Section 3.2.4 is the properties are the thermal conductivity of the buffer and the Opalinus Clay as well as water diffusivity. The results of the 3D TOUGH2 simulation are presented in Figure 2-22. The most striking result is that the peak temperature at the buffer now is about 160°C, i.e., considerably higher than the targeted 125 to 135°C. The temperature at the outer edge of the buffer is up from 68 to 74°C, which is a result of the slightly lower thermal conductivity of the host rock in this case. The substantially higher peak temperature at the canister surface is caused by the combined effects of lower thermal conductivity of the buffer and the rock as well as the high diffusion coefficient that keep the buffer dry around the heater. We consider this an initial predictive modeling result as there are still uncertainties related to the thermal conductivity and diffusion coefficient to be applied for this type of bentonite material.

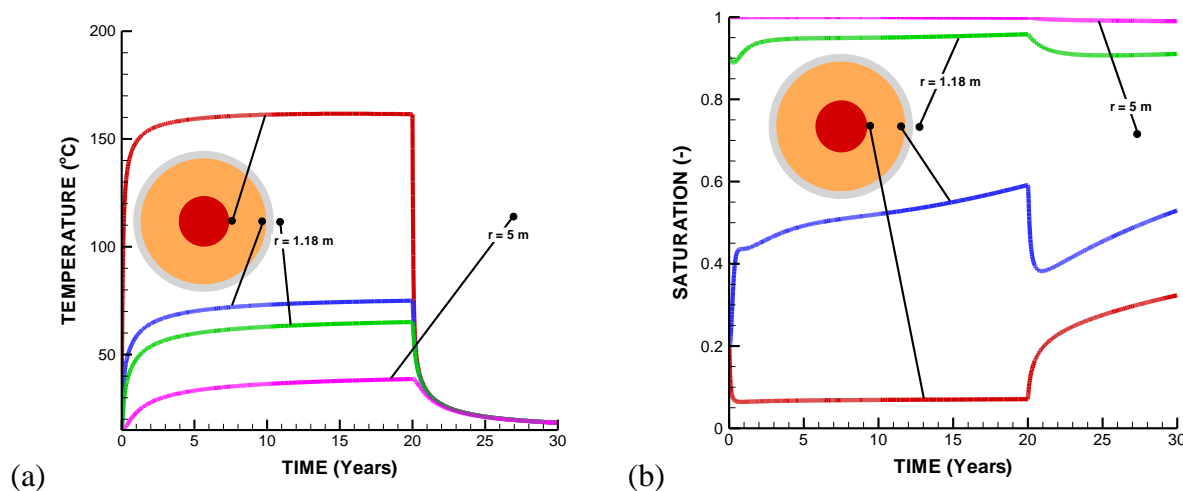


Figure 3-22. Initial model prediction using parameters defined in the benchmark simulation: (a) temperature and (b) liquid saturation.

3.3 HG-A test

The HG-A test is being conducted in the Opalinus Clay at the Mont Terri underground research laboratory (URL) near Saint-Ursanne, Switzerland. The HG-A test is intended to provide data on the geomechanical and hydrogeologic effects of the excavation damage zone (EDZ). The test is specifically targeted to observe how fluids injected into a test section sealed by a packer penetrate both into the rock and within the EDZ (Marschall et al., 2006).

In this section, we describe the test, discuss some of the test attributes and observations, apply an analytical model for rock failure around the tunnel, and then use a coupled hydro-mechanical fracture damage model, TOUGH-RBSN, to investigate the development of fractures around the

tunnel in greater detail. The development of the TOUGH-RBSN model is documented in Liu et al. (2013). The goal of this activity is to use the Mont Terri test data to help build confidence in the TOUGH-RBSN model for predicting various facets of fracture development and evolution within the EDZ.

3.3.1 Location and description of the HG-A microtunnel test

Figure 3-23 shows the general location of the HG-A test within the Mont Terri URL. This test is being conducted in a 13-m long, 1 m diameter microtunnel located off Gallery 04. The tunnel was excavated in February 2005 over a period of about 3 weeks. Steel liner was installed in the first 6 m, and the mid-section where the packer is installed was coated with an epoxy resin (Meier et al., 2005). The test section is supported by a wire mesh and is backfilled with sand. A retaining wall to hold the gravel backfill is grouted in place between the packer and the test section (Lanyon et al., 2009). Finally, the packer seals the test section from the front end of the microtunnel and Gallery 04.

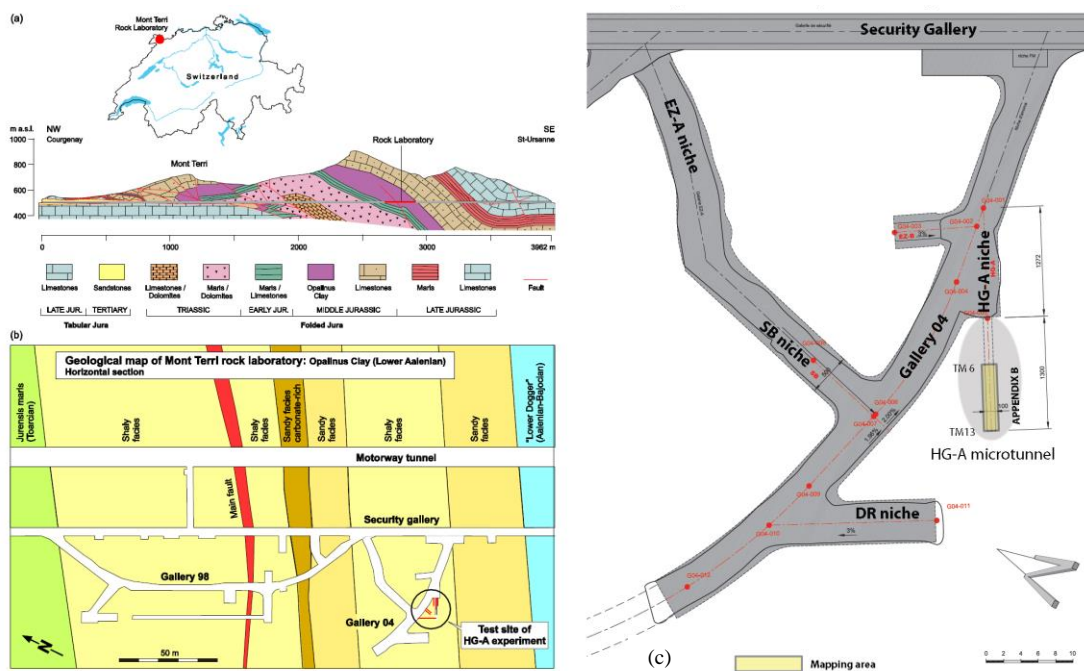


Figure 3-23. The Mont Terri underground rock laboratory: (a) geological profile of the site after Freivogel and Huggenberger (2003), (b) site map showing the underground facilities of the laboratory. The HG-A microtunnel is located in the New Gallery 04. (source: Marschall et al., 2006), (c) map view of the HG-A microtunnel and adjacent excavations; structural map of tunnel surface shown in Figure 3-3 is the area highlighted in yellow (source: Nussbaum and Bossart, 2006).

The HG-A test configuration is shown in Figure 3-2. Instrumented boreholes emanate from the nearby gallery and from the face of the HG-A niche into the rock surrounding the tunnel. The instrumentation outside the tunnel includes piezometers for monitoring water pressure, stressmeters for rock stress, and chain deflectometers for deflection of tunnel axis. The region

inside and adjacent to the tunnel is instrumented with piezometers, total pressure cells along the packer for radial stress, time-domain reflectometers for water saturation, strain gauges measuring tangential movement, and extensometers for radial movement. The locations of some of these instruments are shown in Figure 3-24.

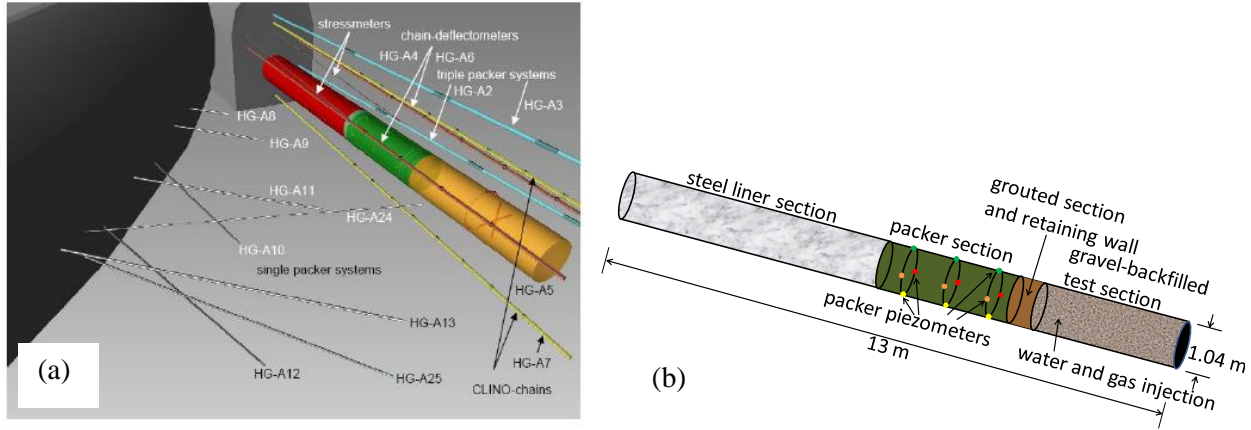
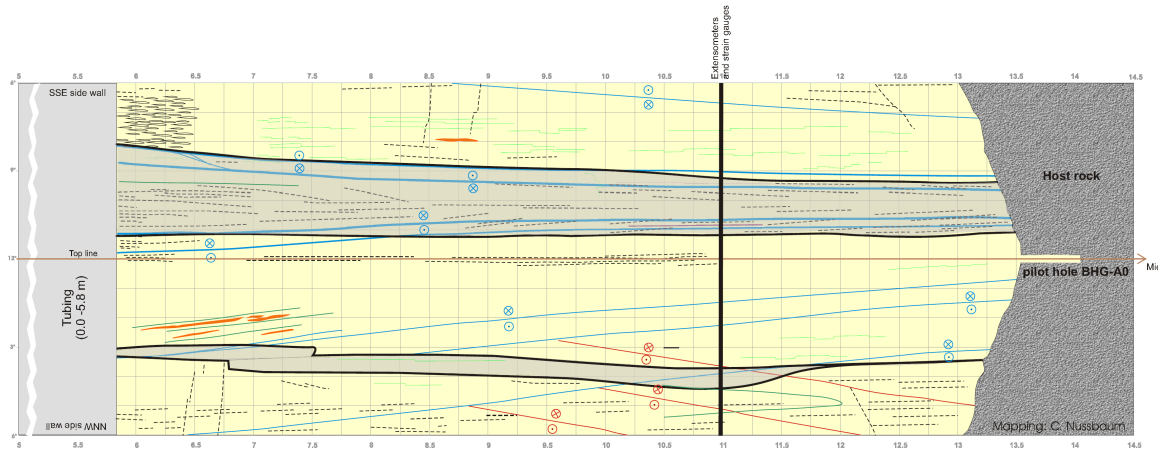


Figure 3-24. HG-A test configuration: (a) schematic drawing of the microtunnel and the site instrumentation. Color coding refers to the steel liner (red), the packer seat (green) and the backfilled test section (orange) (source: Marschall et al., 2008); (b) detail of tunnel showing packer piezometers and test section for fluid injection.

3.3.2 Observations of rock features, EDZ damage, and tunnel convergence

The HG-A microtunnel was mapped to identify natural structural features and any induced fracturing or damage. The tunnel map is shown in Figure 3-25. The natural features include bedding planes and tectonic-related fractures and faults. The rock is relatively homogeneous on the meter scale but pronounced bedding was mapped at finer scales (Marschall et al., 2006). The rock is highly fractured with fracture frequencies ranging from 0.3 to 1 m, although fracture permeability is not significant indicating that fractures are mainly closed under natural stress conditions (Marschall et al., 2006; 2008). There are two main fault orientations: (1) an SSE-dipping system subparallel to the bedding planes and (2) a low-angle S to SW dipping system. The microtunnel is oriented along the bedding strike, and the bedding planes dip at 48° SSE, such that the bedding planes are tangent to the tunnel surface at about 3 to 5 o'clock and 9 to 11 o'clock (see also Figure 3-26) (Marschall et al., 2006).

Extensional and shear brittle fracturing, tunnel wall breakouts, and reactivation of bedding and fault planes are features related to the excavation damage zone. These features are mapped in Figure 3-25 and can be seen to be quite non-uniform around the tunnel.



Legend

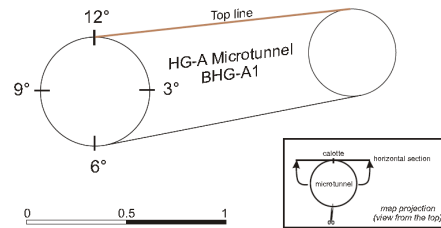
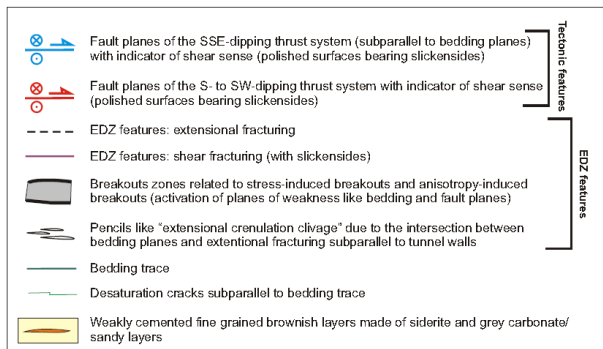


Figure 3-25. Structural Mapping of the HG-A microtunnel (source: Nussbaum and Bossart, 2006)

Excavation resulted in some visible damage along the microtunnel walls as shown in Figure 3-26(a). A conceptual model for the occurrence of damage is given in Figure 3-26(b), which attributes most of the damage to anisotropic strength characteristics of the rock and anisotropic stresses. Rock strength is found to be a function of orientation relative to the bedding (Bock, 2001). The damage is not uniform around the tunnel as shown above, a result of the relative weakness of the rock orthogonal to the bedding planes and as a result of weakness near faults intercepting the tunnel.

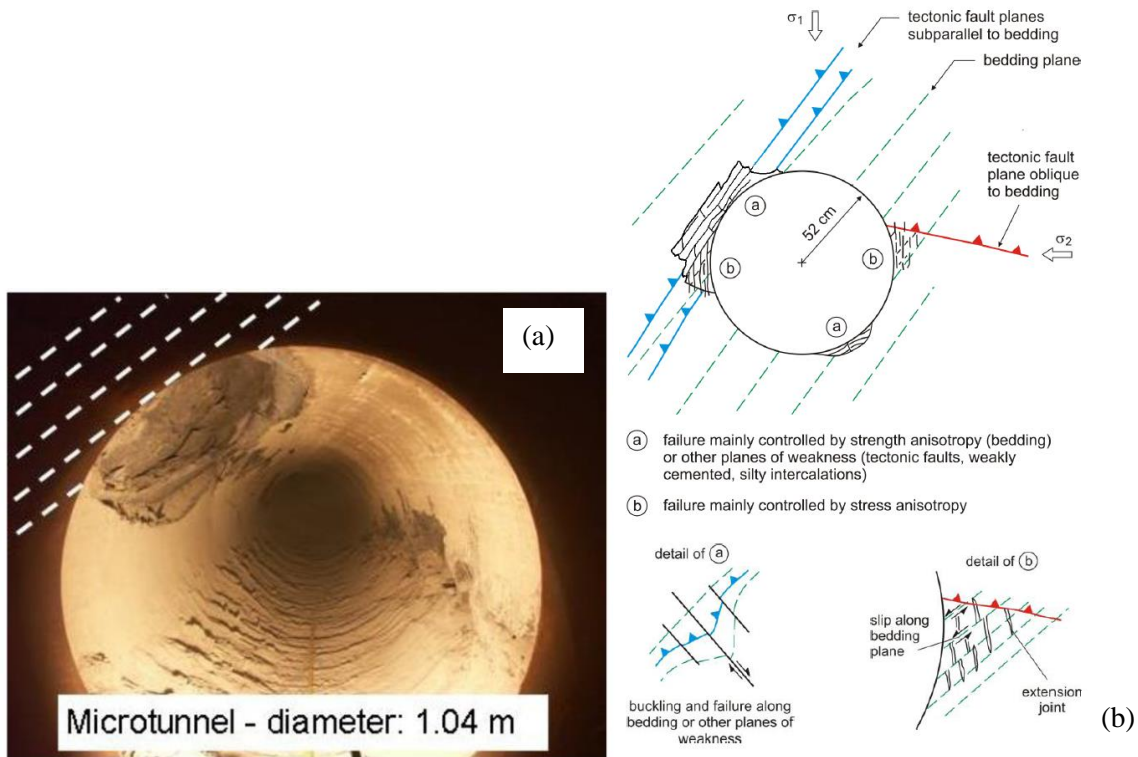


Figure 3-26. Excavation damage. (a) Breakouts along microtunnel walls, with an orientation looking from the HG-A Niche towards back end of microtunnel (source: Marschall et al., 2006); (b) Conceptual diagram of the damage zone with the same orientation as in (a). (source: Lanyon et al., 2009; Marschall et al., 2006)

Horizontal and vertical extensometers in the test section of the tunnel (at about 11 m from the tunnel entrance) provide data on the rate of tunnel convergence. Figure 3-27 shows the horizontal and vertical convergence rates. Over a five-year period, the tunnel diameter decreased about 3 mm in the horizontal direction and about 0.3 mm in the vertical direction. Most of the horizontal convergence occurred during the first year, whereas the slower vertical convergence continued over the entire 5 years. Shorter-term variations in convergence are also seen. These are in response to changes in the megapacker pressure and fluid injection (Lanyon et al., 2009) discussed in the next section.

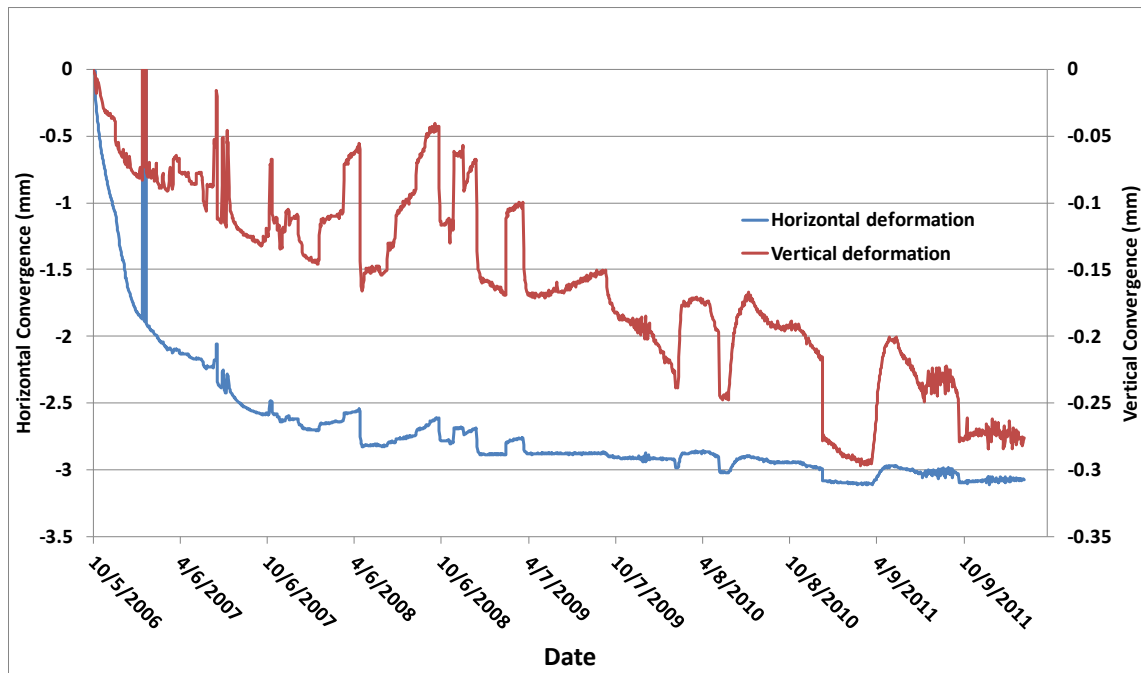


Figure 3-27. Tunnel convergence over a 5-year period

Figure 3-28 plots convergence over the last 2.5 years with the horizontal and vertical axes at the same scale. The figure shows that for this time period, convergence in the horizontal and vertical directions have been similar, about -0.05 to -0.08 mm/year.

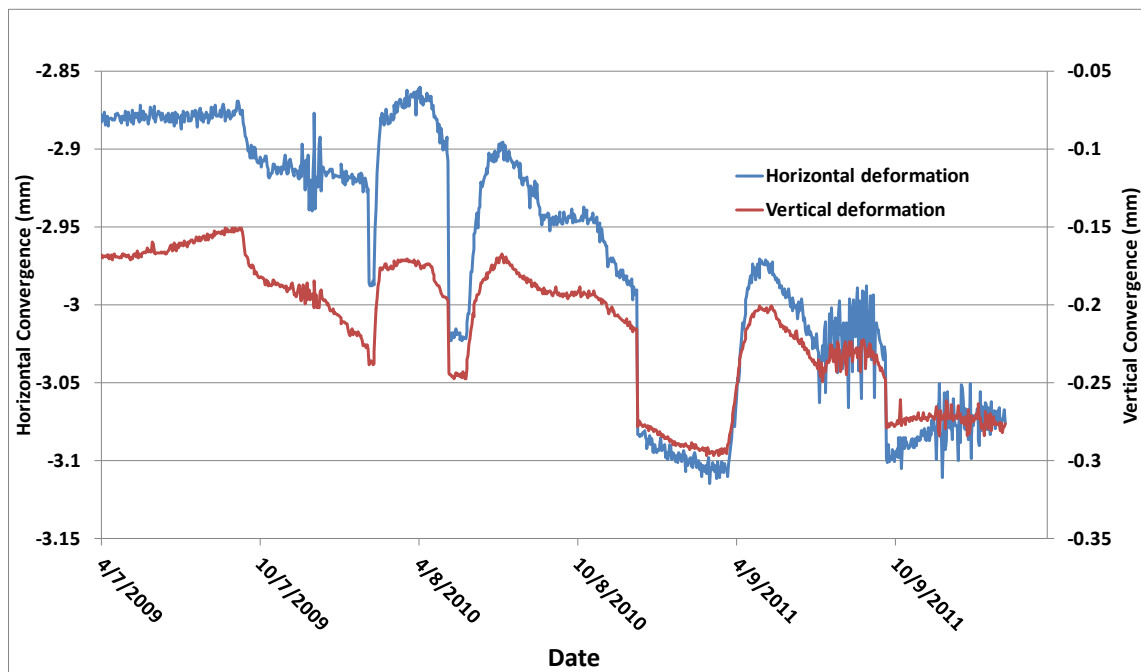


Figure 3-28. Tunnel convergence over the last 2.5 years

3.3.3 Water and gas injection testing

Water was injected into the test section at a variety of rates from 2007 to February 2010, followed by three periods of gas injection until September 2011. Pressure signals from piezometers along the packer (see Figure 3-24(b)) are shown in Figure 3-29. Figure 3-29(a) is for the piezometer ring furthest from the test section, Figure 3-29(c) is for the piezometer ring nearest to the test section, and Figure 3-29(b) is for the intermediate piezometer ring. As can be seen, pressure response is most vigorous and ubiquitous in Figure 3-29(c); moving away from the test section, pressure response dies out in several locations in Figures 3-29(b) and 3-29(a). However, the “3 o’clock position” still shows significant pressure response to the injected fluid pressure in the test section, signifying a high-permeability connection several meters from the packer. The testing has also shown indirect evidence of fracture self-sealing, where injection rate and/or pressure behavior is consistent with an increasing resistance to fluid injection into the test section. The increased resistance to injected fluids, presumably in the EDZ fractures, is identified by the sealing index, S , introduced by Lanyon et al. (2009), where $S = \frac{Q}{P-100}$ and Q is the flow rate (mL/min) and P is the pressure in (kPa), with self-sealing indicated by S decreasing with time, as shown in Figure 3-30.

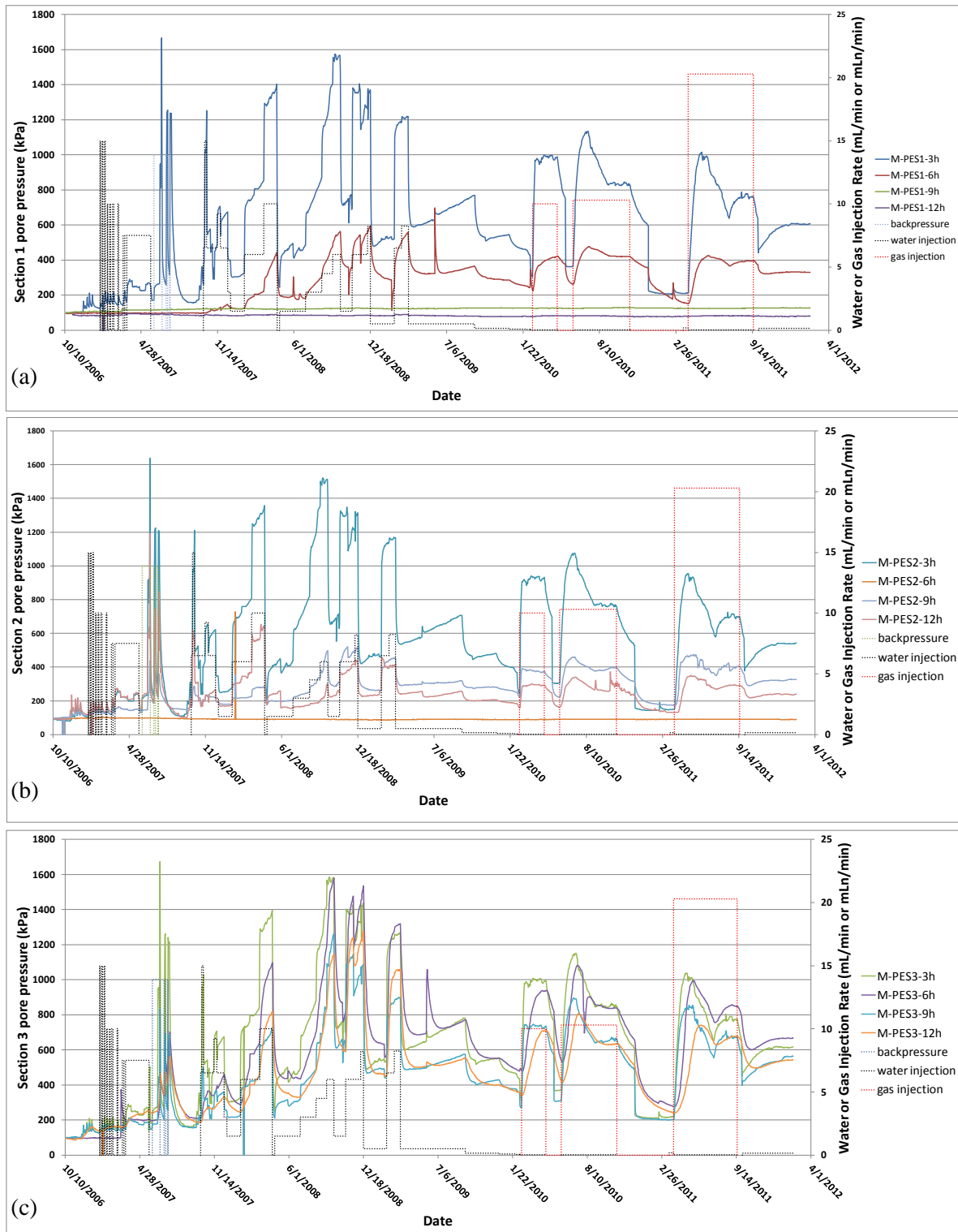


Figure 3-29. Fluid pressure response along packer section; (a) piezometer ring furthest from test section; (b) intermediate piezometer ring; (c) piezometer ring nearest to test section.

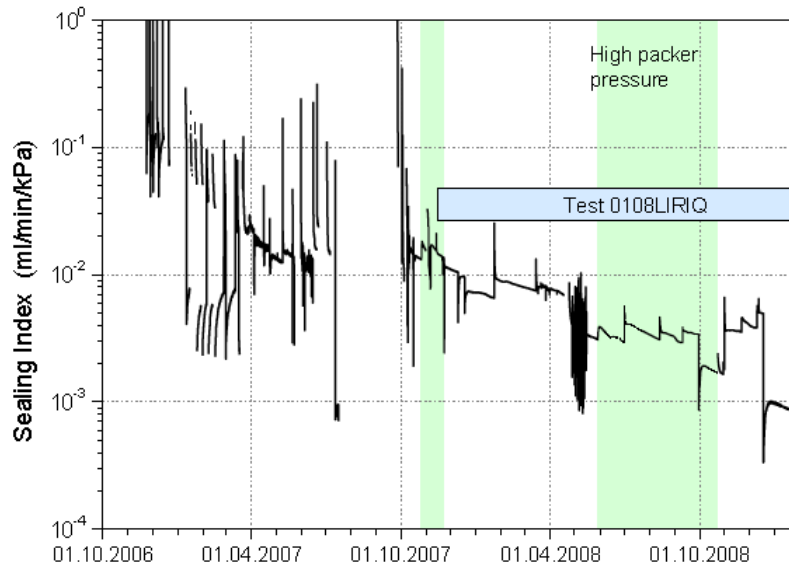


Figure 3-30. Sealing index as a function of time over a 2-year period. (source: Lanyon et al., 2009)

Packer pressure was also varied during the test over a range of 1 to 3 MPa. The effects of packer pressure on EDZ appeared to be consistent with the idea that fracture permeability decreased with increased packer pressure (Lanyon et al., 2009).

3.3.4 Initial analysis of rock failure along the drift wall

An initial analysis has been performed to investigate failure mechanisms along the tunnel wall. Failure is computed by first computing the stress around an open drift using an analytical solution for this problem derived by Kirsch (1898). The Kirsch solution is limited to a homogeneous rock mass, therefore, the effects of faults are not included. The solution also requires that the rock be treated as isotropic in terms of the elasticity parameters, Young's modulus and Poisson's ratio, but can accommodate anisotropic stress conditions at the far boundaries. The elasticity parameters for the Opalinus Clay are known to be anisotropic for measurements parallel and orthogonal to bedding (Bock, 2001). However, the assumption that these parameters are isotropic does not significantly impact the computed stress field around the tunnel if the far field can be treated as a constant stress boundary (Tonon and Amadei, 2003). It should be pointed out that displacements in response to the stress field are not accurately predicted using isotropic elastic parameters (Tonon and Amadei, 2003), but the present analysis is not evaluating displacements. Once the stress field is known, the anisotropic rock strength parameters may be used to evaluate whether tensile or shear failure is expected. Tensile failure is simply evaluated by comparing the effective normal stresses with the corresponding tensile strength. Shear failure is evaluated using a Mohr-Coulomb failure approach.

The solution for the mechanical stress, σ_{rr}^m , $\sigma_{\theta\theta}^m$, and $\sigma_{r\theta}^m$ is given by Pollard and Fletcher (2005, p. 236):

$$\sigma_{rr}^m = \left(1 - \frac{a^2}{r^2}\right) \left(\frac{\sigma_h + \sigma_H}{2}\right) - \left(1 - 4\frac{a^2}{r^2} + 3\frac{a^4}{r^4}\right) \left(\frac{\sigma_h - \sigma_H}{2}\right) \cos(2\theta) \quad (3-10)$$

$$\sigma_{\theta\theta}^m = \left(1 + \frac{a^2}{r^2}\right) \left(\frac{\sigma_h + \sigma_H}{2}\right) + \left(1 + 3\frac{a^4}{r^4}\right) \left(\frac{\sigma_h - \sigma_H}{2}\right) \cos(2\theta) \quad (3-11)$$

$$\sigma_{r\theta}^m = \left(1 + 2\frac{a^2}{r^2} - 3\frac{a^4}{r^4}\right) \left(\frac{\sigma_h - \sigma_H}{2}\right) \sin(2\theta) \quad (3-12)$$

where r is the radial coordinate (radially outward positive), θ is the angular coordinate (counterclockwise positive), a is the tunnel radius, p is the fluid pressure, σ_H is the minimum far-field stress (which is horizontal in this case), and σ_h is the maximum far-field stress (which is vertical in this case) (Figure 3-31). The stresses are defined here such that compression is positive.

The effective stresses accounting for fluid pore pressure are:

$$\sigma_{rr}^e = \sigma_{rr}^m - p \quad (3-13)$$

$$\sigma_{\theta\theta}^e = \sigma_{\theta\theta}^m - p \quad (3-14)$$

$$\sigma_{r\theta}^e = \sigma_{r\theta}^m \quad (3-15)$$

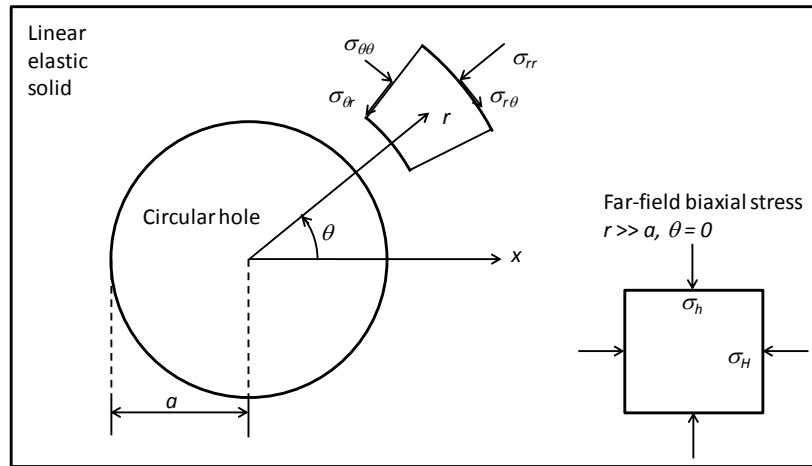


Figure 3-31. Definition diagram for plane stress around a circular hole

First consider damage at the tunnel wall, where $r = a$. The stress Equations (3-10) through (3-12) simplify to:

$$\sigma_{rr}^e = -p \quad (3-16)$$

$$\sigma_{\theta\theta}^e = (\sigma_h + \sigma_H) + 2(\sigma_h - \sigma_H)\cos(2\theta) - p \quad (3-17)$$

$$\sigma_{r\theta}^e = 0 \quad (3-18)$$

Tensile failure occurs if either of the effective normal stresses fall below the negative of the tensile strength, $-T_r(\theta)$ in the radial direction, and $-T_\theta(\theta)$ in the circumferential direction, because of the anisotropic nature of the Opalinus Clay rock strength:

$$\sigma_{rr}^e = -p < -T_r(\theta) \quad (3-19)$$

$$\sigma_{\theta\theta}^e = (\sigma_h + \sigma_H) + 2(\sigma_h - \sigma_H)\cos(2\theta) - p < -T_\theta(\theta) \quad (3-20)$$

Shear failure occurs if the stress state of the system touches the Mohr-Coulomb failure curve,

$$\tau_m \geq \sigma_m \sin(\phi) + c(\theta) \cos(\phi) \quad (3-21)$$

Where

$$\tau_m = \frac{|\sigma_{rr} - \sigma_{\theta\theta}|}{2} \quad (3-22)$$

And

$$\sigma_m = \frac{\sigma_{rr} + \sigma_{\theta\theta}}{2} \quad (3-23)$$

The cohesive strength, $c(\theta)$, is also a function of angle because of the anisotropic nature of the Opalinus Clay rock strength, and the friction angle, ϕ .

Far-field, natural, stress conditions in the Opalinus Clay are approximated by $\sigma_h = 6.5$ MPa and $\sigma_H = 4.5$ MPa, and pore pressure is approximated by, $p = 1.5$ MPa (Martin and Lanyon, 2003, p. 1085 and 1087). Tensile strength is characterized by values parallel and normal to bedding, $T_p = 2$ MPa and $T_n = 1$ MPa, respectively (Bossart, 2012, Annex 4-21). Similarly, cohesive strength is also characterized by values parallel and normal to bedding, $c_p = 5.5$ MPa and $c_n = 2.2$ MPa (Bossart, 2012, Annex 4-22). The friction angle ranges from 24° to 26° is adequately characterized by the value 25° (Bossart, 2012, Annex 4-22).

The radial tensile strength is represented as a function of angle through the following:

$$T_r(\theta) = T_p \cos^2(\theta - \theta_b) + T_n \sin^2(\theta - \theta_b) \quad (3-24)$$

where θ_b is the angle of the bedding, previously identified to be 48° . The circumferential tensile strength is given by

$$T_\theta(\theta) = T_p \sin^2(\theta - \theta_b) + T_n \cos^2(\theta - \theta_b) \quad (3-25)$$

The cohesive strength is given by

$$c(\theta) = c_p \cos^2(\theta - \theta_b) + c_n \sin^2(\theta - \theta_b) \quad (3-26)$$

Calculations done for effective stress and the negative of tensile strength around a tunnel are shown in Figure 3-32. When radial or circumferential stress falls below the negative of tensile strength, tensile failure occurs. As seen in Figure 3-33, tensile failure only occurs for some positions in the radial direction.

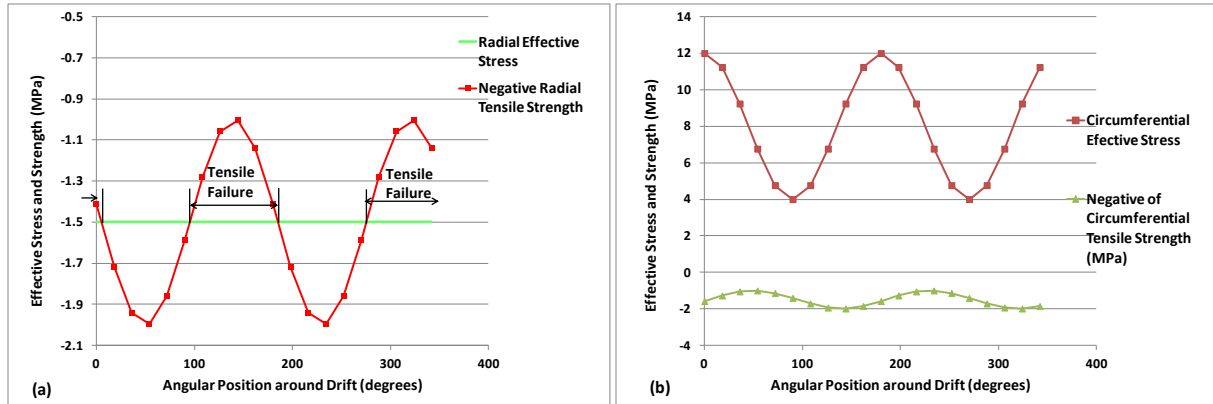


Figure 3-32. Comparison of effective stress and tensile strength to identify tensile failure: (a) radial direction; (b) circumferential direction.

Calculations for shear failure using Equation (3-12) are shown in Figure 3-11. When the ordinate in Figure 3-11 exceeds zero, shear failure occurs.

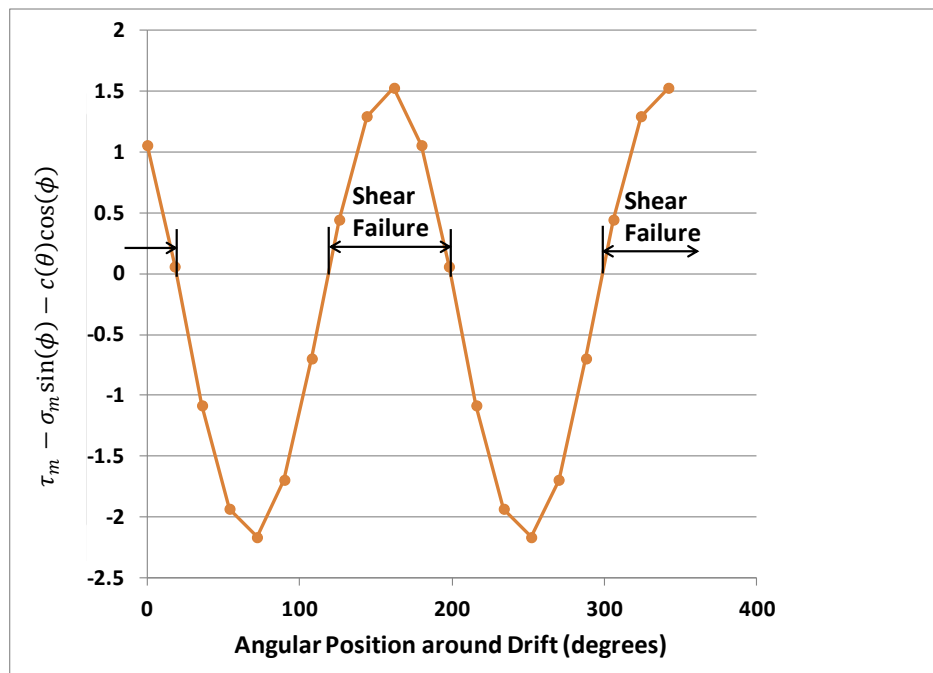


Figure 3-33. Results for shear failure

The failure analyses results are summarized in Figure 3-34. This shows that both shear and tensile failure occur along the NNW side of the drift wall roughly between 3 and 5 o'clock, with shear failure only at 2:30 o'clock and tensile failure at 5:30 o'clock. Along the SSE side, both shear and tensile failure occur roughly between 9 and 11 o'clock, with shear failure at 8:30 o'clock and tensile failure at 11:30 o'clock. This is in qualitative agreement with the observations of failure, although the observed failure (Figure 3-25), especially on the NNW side, is restricted to a narrower region than predicted here.

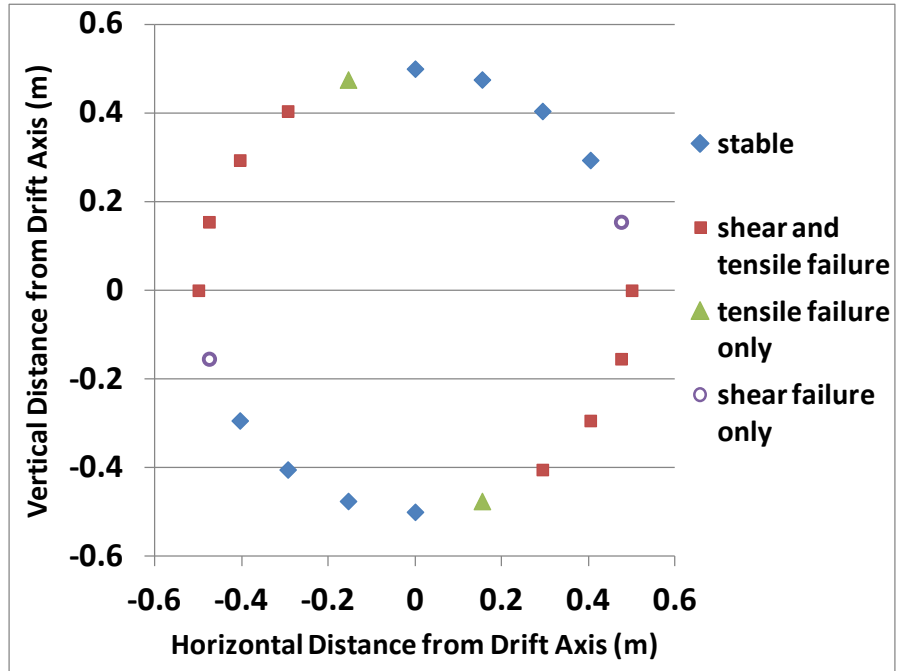


Figure 3-34. Results for failure analysis, with an orientation looking from the HG-A Niche towards the back end of microtunnel

Failure analysis at radii greater than 0.5 m (the radius of the drift) suggests that damage is confined to a narrow region around the drift. Tensile failure is found to be limited to only 3 to 4 cm into the drift wall, while shear failure is limited to about 10 cm into the drift wall.

The analysis can be extended to determine the extent of rock failure into the drift wall. The results are shown in Figure 3-35, which indicates that damage lies within 0.1 m of the drift wall. The other observation is that the failure mode changes from “shear and tensile failure” at a number of locations along the drift wall to “shear failure only” as the radial coordinate increases. At radial distances less than 0.1 m from the drift wall, the rock condition becomes “stable” at all orientations. This analysis demonstrates that shear failure may be expected to play an important role in the development of fractures in the EDZ.

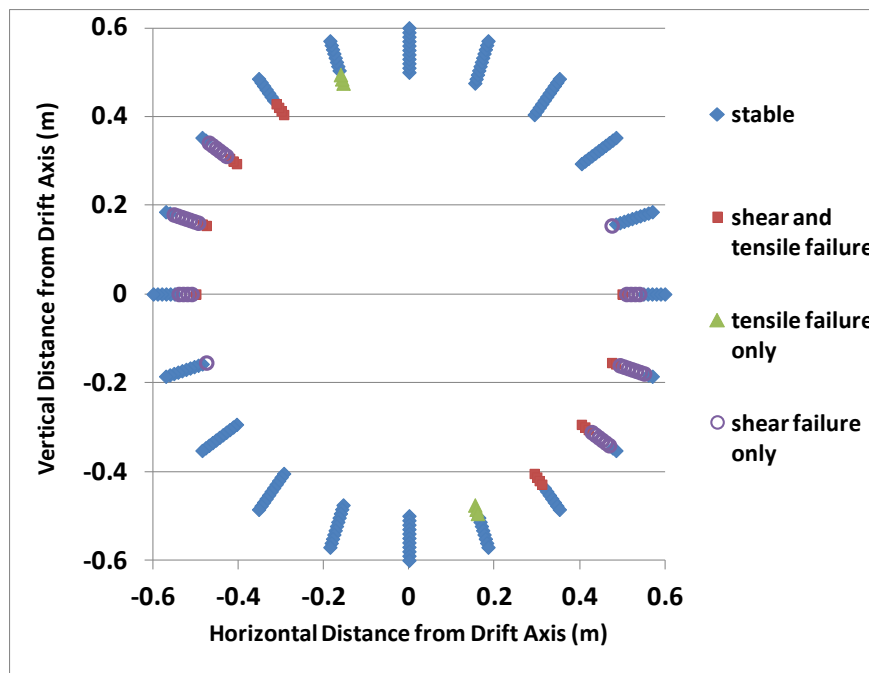


Figure 3-35. Results for failure analysis as a function of depth into the drift wall, with an orientation looking from the HG-A Niche towards back end of microtunnel.

3.3.5 Implementation of RBSN for modeling the HG-A test

This section presents work to date on the implementation of RBSN to model the HG-A test. The initial focus of the work is not on the injecting testing, which requires a three-dimensional model, but to first look at geomechanical behavior including fracture development in the EDZ with a two-dimensional model. The problem has been further simplified for the present analysis by assuming a constant uniform pore pressure such that the geomechanical and fracture damage calculations may be performed using RBSN as a stand-alone model, i.e., without coupling to TOUGH2 for hydrogeologic processes. This approximation is accurate up until rock failure leads to fracturing and a rapid loss of pore pressure (Liu et al., 2013).

Previous applications of the RBSN model have mainly focused on fracturing under tensile stress conditions. However, as discussed in Section 3.3.4, shear failure under compressive stress conditions also plays an important role in the development of fractures in the EDZ for the HG-A test. This section presents the development and testing of compressive behavior and failure using the RBSN model.

Background and model formulation

Discrete models have become popular as computational tools for studying the heterogeneous characteristics of geomaterials. This category includes the Rigid-Body-Spring network (RBSN), in which system behavior is represented by primitive two-node elements interconnected on a set of nodal points. The approach considered here is based on the Rigid-Body-Spring concept of

Kawai (1978). To provide a basic understanding of this modeling approach, an overview is given here. Details regarding the RBSN are given elsewhere (Bolander and Saito, 1998; Asahina et al., 2011).

Geometry of the RBSN is defined by the dual Delaunay tessellation of the nodal points. The basic unit of RBSN is a 1D lattice element consisting of a zero-size spring set located at the centroid of the Voronoi boundary (Fig. 3-36). Each node has six degrees of freedom for the 3D case. The spring set is formed from three axial springs and three rotational springs (referenced to local coordinate axes n-s-t) as shown in Figure 3-36 (the rotational springs have been omitted for clarity). The local spring coefficients are assigned according to

$$k_s = k_t = \beta_1 k_n = \beta_1 \beta_2 E \frac{A_{ij}}{h_{ij}} \tag{3-27}$$

in which E is the Young’s modulus and A_{ij} is the area of the Voronoi boundary common to nodes i and j . By adjusting β_1 and β_2 in accordance with experimental results, macroscopic modeling of both elastic constants (E and Poisson ratio,) is possible. The Voronoi scaling of the spring constants, A_{ij}/h_{ij} , enables the method to be elastically homogeneous under uniform modes of straining. Such Voronoi scaling also results in energy conserving, grid-size-insensitive representations of tensile fracture.

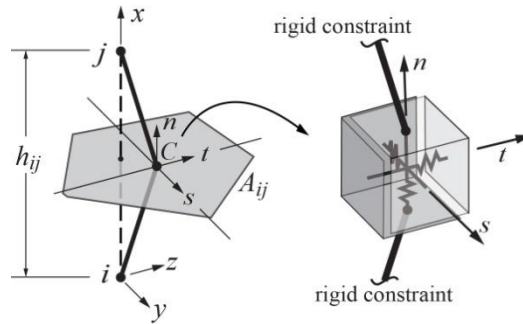


Figure 3-36. Typical lattice element ij with a zero-size spring set located at centroid C of facet area A_{ij} . Note that A_{ij} is the Voronoi facet or cell boundary, and i and j are the neighboring Voronoi cell nodes (matrix nodes).

In this study, the strength properties of the RBSN elements are defined by a Mohr-Coulomb criterion as shown in Fig. 3-37. The fracture line is defined by three parameters: the angle of internal friction φ (surface inclination with respect to the σ_n axis), surface intersection c with the shear axis; and the tensile strength, f_n , of the material. Axial stresses are measured as $\sigma_I = F_I/A_{ij}$, where F is axial spring force and I indicate corresponding each of the n - s - t local axes, respectively. The stress condition at each element is measured as $\rho = OP/OP_o$, where OP_o is the point at which $OP = \sqrt{\sigma_n^2 + \sigma_s^2 + \sigma_t^2}$ intersects the fracture surface. Element breaking occurs when $\rho = 1$. The most critical element undergoes fracture in a brittle manner, which entails a complete reduction of its elastic stiffness and an associated release of element forces.

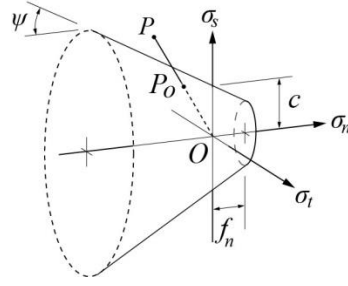


Figure 3-37. Mohr-Coulomb surface with tension cut-off

Anisotropy in the RBSN model

As discussed in Section 3.3.2 the Opalinus Clay presents strong anisotropy as shown by comparing a number of properties measured parallel or perpendicular to the bedding planes. In terms of the rock elastic mechanical behavior, anisotropy is found in Young's modulus, shear modulus, and Poisson's ratio (Bossart, 2012). Anisotropy is also found for tensile and cohesive strength, however, friction angle is close to isotropic (Bossart, 2012). Because the RBSN model is a mechanical analogue to the continuum equations for rock mechanics, methodologies to match continuum properties using the RBSN model must be developed. Methods for matching isotropic values of Young's modulus and Poisson's ratio have been discussed previously (Liu et al., 2013). Here we discuss one methodology using a layered system which leads to anisotropic bulk elastic and strength properties in the RBSN model. This in fact mimics the physical system because bedding is the feature in the Opalinus Clay that drives anisotropy. As we will show, using alternating soft and stiff layers can produce the desired bulk anisotropic behavior.

Anisotropic elastic properties: Qualitatively, it is clear that a system built from layers that are individually homogenous and isotropic but have properties that vary from layer to layer will result in effective bulk anisotropy. Consider a system with two layers of equal thickness, one with a low Young's modulus and one with a high Young's modulus. If force is applied orthogonal to the layers, the soft layer will dominate the resulting strain of the system. However, if force is applied parallel to the layers, the stiff layer will dominate the resulting strain of system. The exact linkage for elastic properties (Young's modulus, shear modulus, and Poisson's ratio) between layer properties and the bulk rock properties has been derived (Salamon, 1968), so the effective bulk rock properties may be computed from known layer properties. Young's modulus for the Opalinus Clay is characterized by different values parallel and normal to bedding, $E_p = 15.5$ GPa and $E_n = 9.5$ GPa, respectively (Bossart, 2012). The relationships between the bulk and layer Young's modulus are,

$$E_p = \phi_1 E_1 + \phi_2 E_2 \quad (3-28)$$

$$E_n = 1 / \left(\frac{\phi_1}{E_1} + \frac{\phi_2}{E_2} \right) \quad (3-29)$$

where ϕ_i is the volume fraction and E_i is Young's modulus for each layer i .

For alternating layers of equal thickness, there is a unique pair of individual layer properties that will produce a given pair of anisotropic bulk rock properties. For such conditions, Young's

modulus for two layers, E_1 and E_2 , can be calculated to be 25.1 GPa and 5.8 GPa, respectively. The exact nature of the layering that exists in the Opalinus Clay has not been investigated in detail and individual layer characteristics are not known. However, the formation is known to be finely bedded and numerous measurements have been made of the bulk rock geomechanical properties. So our approach is to use alternating layers of equal thickness and assign layer properties such that the correct bulk rock behavior is obtained. Although not addressed in the current study, it should be pointed out that layering is also a potential avenue to represent anisotropic hydrogeological properties. While hydrogeological anisotropy in permeability using TOUGH2 can be implemented directly for a structured grid oriented along the principal axes, modeling permeability anisotropy for a general unstructured grid is a subject of current research.

Anisotropic strength properties: Anisotropic strength behavior is also found for the Opalinus Clay as discussed in Section 3.3.4. This anisotropy is represented in the RBSN through alternating stiff and soft layers as presented in the previous section for elastic properties. The basis for evaluating the individual layer properties is shown in Figure 3-38.

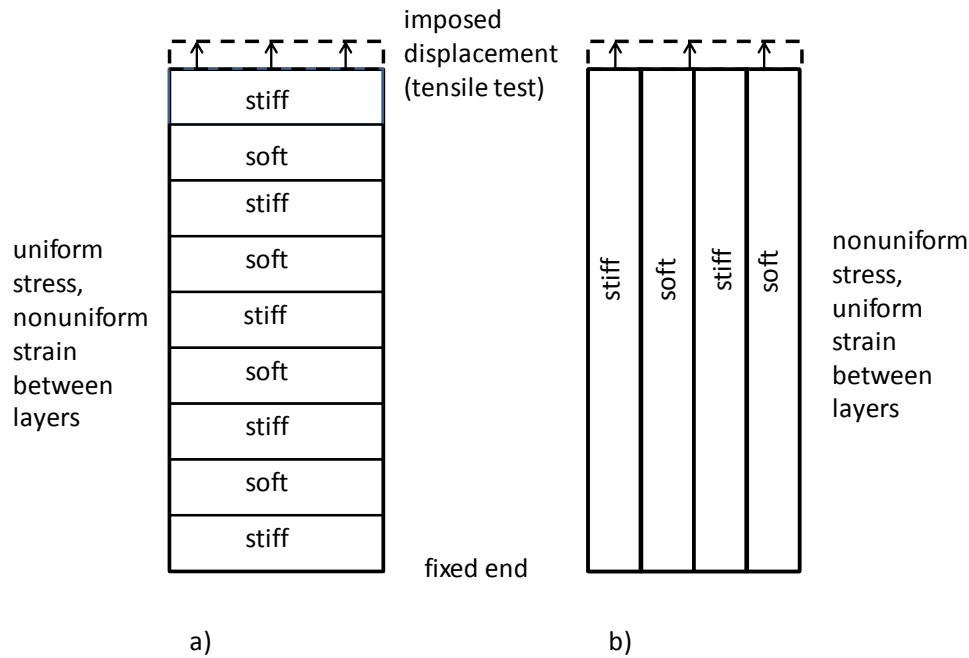


Figure 3-38. Tensile strength test for layered rock. a) strength perpendicular to the layers; b) strength parallel to the layers

A uniaxial tensile strength test causes different responses when the imposed displacement is parallel or perpendicular to the layering. In Figure 3-38a), the displacement is perpendicular to the layers. For this orientation, a uniform displacement of the top end of the sample (with the other end held motionless) results in a uniform stress across the material with different strains within the stiff and soft layers. Because stress is uniform, it is clear that the tensile strength of the layered rock will be equal to the value in the soft layer because it will fail at lower stress. For displacement parallel to bedding shown in Figure 3-38b), the strain, ϵ , will be uniform across the sample, however, stress will vary between the stiff and soft layers. The bulk stress, σ_B , is equal to the total force divided by the bulk area, A_B . The total force, F_T , is the sum of the forces for the soft and stiff layers,

$$F_T = \varepsilon(A_1E_1 + A_2E_2) \quad (3-30)$$

Where A_1 is the total area of stiff layers, A_2 is the total area of soft layers, E_1 is Young's modulus for the stiff layer, and E_2 is Young's modulus for the soft layer. Because the stiff and soft layers have equal area, this becomes

$$F_T = A_B \varepsilon \left(\frac{E_1 + E_2}{2} \right) = A_B \bar{E} \varepsilon \quad (3-31)$$

where $\bar{E} = \frac{E_1 + E_2}{2}$. Then the bulk stress is given by

$$\frac{F_T}{A_B} = \sigma_B = \bar{E} \varepsilon \quad (3-32)$$

To obtain the tensile strength of the strong layer, T_1 , such that tensile failure occurs when the bulk stress reaches the tensile strength of the bulk rock parallel to the layering, T_{BP} , the strain is

$$\varepsilon = \frac{T_{BP}}{\bar{E}}. \quad (3-33)$$

Then the stress in the strong layer associated with this strain is the tensile strength of the stiff layer,

$$T_1 = \frac{E_S}{\bar{E}} T_{BP}. \quad (3-34)$$

If, instead of tensile loading the sample is placed under compressive loading the results are similar. For compressive loading, the displacement of the top of the material is reversed to move downward in Figure 3-38. For compressive loading oriented perpendicular to the layering, the stress is uniform and failure will occur at the same stress as for the soft layer. Therefore, the bulk rock cohesive strength perpendicular to the layering equals the cohesive strength of the soft layer. For displacement parallel to the layering, the relationships remain as for the tensile case. That is, the magnitude of the maximum (vertical) normal stress required to achieve failure in the stiff layer, σ_1 , is equal to

$$\sigma_1 = \frac{E_1}{\bar{E}} \sigma_{BP} \quad (3-35)$$

where σ_{BP} is the maximum normal stress parallel to bedding required for failure of the bulk rock. Figure 3-39 shows a schematic diagram of the Mohr-Coulomb failure envelopes for the bulk rock and for the stiff layer (the diagram is schematic only – it does not correspond quantitatively with parameter values for the Opalinus Clay). The envelopes are parallel because, according to Bossart (2012), the friction angle, φ , is approximately isotropic and equals 25° . Therefore, there is only one friction angle for the individual layers and for the layered rock. As shown in Figure 3-39, the cohesive strength scales the same as the maximum normal stress on Mohr's circle such that

$$c_1 = \frac{E_1}{\bar{E}} c_{BP}, \quad (3-36)$$

where c_s is the cohesive strength of the stiff layer and c_{BP} is the bulk cohesive strength of the layered system parallel to the bedding.

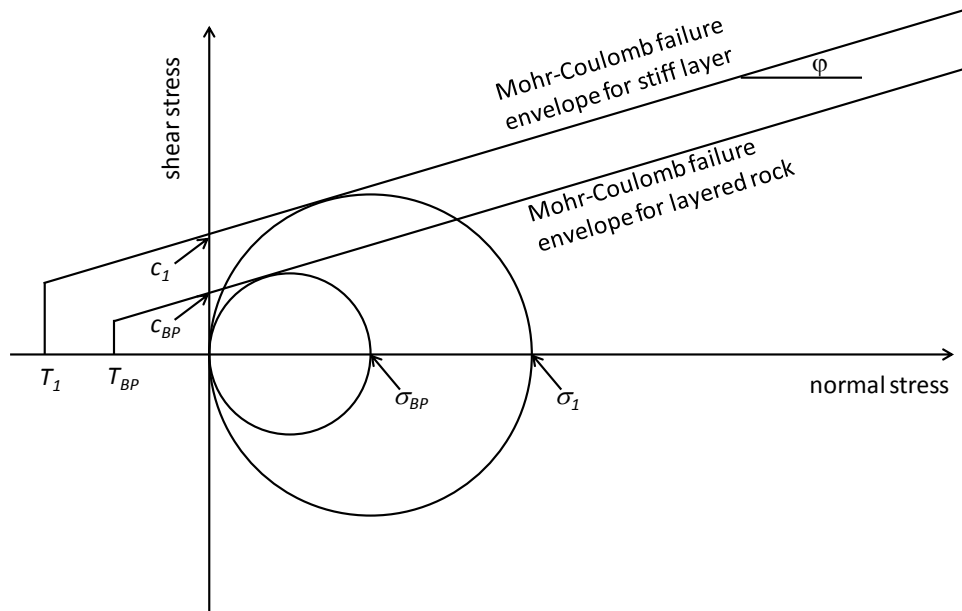


Figure 3-39. Schematic of the Mohr-Coulomb failure diagram for the layered rock and the strong layer.

The Young’s moduli for the strong and weak layers are 5 and 25 GPa, respectively, as presented in the previous section. Therefore, $\frac{E_1}{E} = 5/3$. The bulk rock tensile and cohesive strengths and the stiff and soft layer values are given in Table 3-7.

Table 3-7. Tensile and cohesive strengths of layered rock and individual layers

	tensile strength perpendicular to layers (MPa)	tensile strength parallel to layers (MPa)	cohesive strength perpendicular to layers (MPa)	cohesive strength parallel to layers (MPa)
layered rock	1	2	2.2	5.5
	tensile strength (isotropic) (MPa)		cohesive strength (isotropic) (MPa)	
stiff layer	3.33		9.17	
soft layer	1		2.2	

Note: source for layered rock values is Bossart (2012).

Voronoi discretization of transversely isotropic rock: Voronoi discretization is an effective approach for partitioning a computational domain containing a set of nodal points within a set of spatial regions or cells. Each cell is associated with an individual nodal point such that all locations within the cell lie closer to the given nodal point than to any other nodal point. The Voronoi grid is computed from the nodal point set by first constructing the Delaunay tessellation, which is then used to construct the dual Voronoi tessellation (Asahina and Bolander, 2011).

Here, the Voronoi grid is used to represent transversely isotropic rock. The bedding configuration is directly mapped onto Voronoi cells and the boundaries of layer are identified by the edges of a polygon. Figure 3-40 shows a reference geometry of transversely isotropic material and its approximation by a collection of Voronoi cells. With reference to the 2-D case, a transversely isotropic specimen is discretized as follows:

- Discretize rock matrix based on an irregular Voronoi grid (Fig. 3-40(a)).
- Overlay the reference layers onto the Voronoi grid (Fig. 3-40(b)).
- Select node for each reference layer. The corresponding Voronoi cells represent the reference layers (Fig. 3-40(c)).

By automating this approach, layered materials can be effectively generated. Figure 3-41 shows the discretized two phase transversely isotropic material for equal volume fraction with different angles.

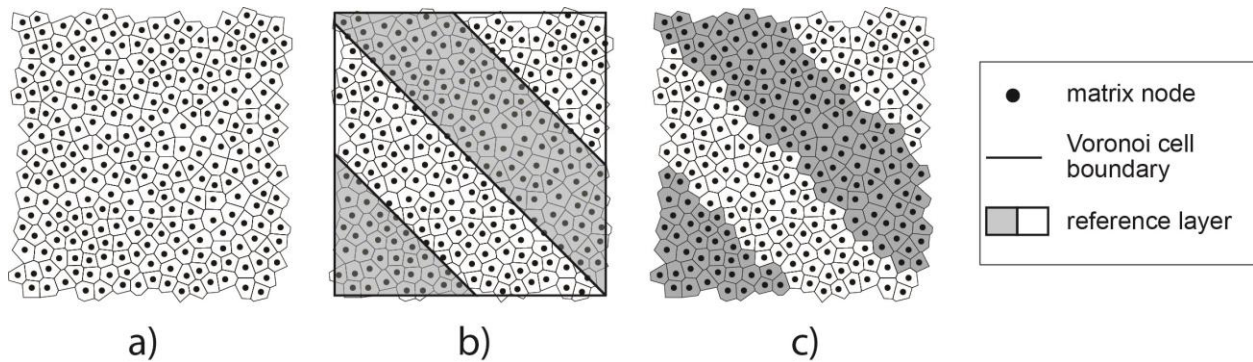


Figure 3-40. (a) An irregular 2-D Voronoi grid, (b) Voronoi grid with overlay transverse isotropic layer, and (c) Voronoi grid representation of transversely isotropic material.

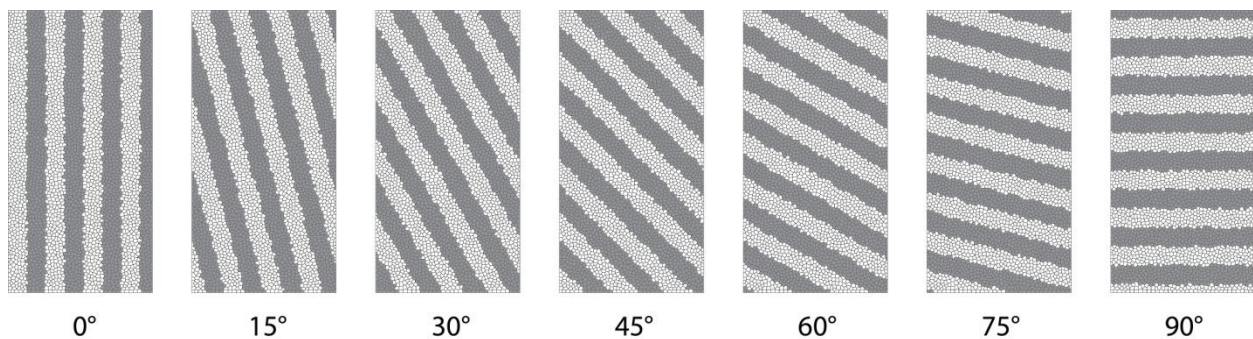


Figure 3-41. 2-D Voronoi discretization of transversely isotropic materials with 7 different bedding angles.

Modeling compression failure with RBSN

Failure in compression is more complex than failure in tension because combined modes of failure (tension and shear) are possible. Identification of compressive behavior and failure characteristics such as specific fracture energy and local failure mechanisms is difficult. Furthermore, heterogeneous composition and anisotropy found in many geomaterials lead to complications in determining the elastic properties of the continuum. To accurately model compressive behavior and failure processes of heterogeneous and anisotropic materials one needs to:

- Introduce heterogeneity in the model to capture the fracture processes and strength characterization.
- Select fracture criteria and the associated parameters. For example, cohesion and friction angle are inputs for a Mohr-Coulomb fracture criterion.

Several approaches have been applied to include the effect of heterogeneity in fracture-damage models such as, random assignment of different element properties based on spatial heterogeneous distribution (Tang, 1997), random geometry of mesh with equal properties for the elements (Garboczi and Day, 1995), mapping micro/meso structure onto regular/irregular mesh (Schlangen and Van Mier, 1992; Asahina et al., 2011), random geometry of mesh and associated grain structure (Cusatis et al., 2003), and statistical approach with a Weibull distribution (Tang, 1997). Although it is possible in the RBSN model to simulate heterogeneity of a rock, in this study the focus is on anisotropic behavior as discussed in the previous section.

Numerical example: uniaxial compression for two homogeneous rocks: Prior to modeling transversely isotropic materials, homogeneous specimens are considered here to demonstrate the basic simulation capability of RBSN model under uniaxial compression loading. Consider a 2-D section of cylindrical core sample which is subjected to unconfined uniaxial compression as shown in Fig. 3-42(a). The model is discretized with about 10,000 lattice elements and 3,800 nodes. The top and bottom cells, represented with darker cells in Fig. 3-42(a), are restrained while others are free to move. Incremental loads are applied along top layer by displacement control and load rate/duration effects are not considered. Two Young's moduli, 25.1 GPa and 5.8 GPa, obtained in section "Anisotropic elastic properties" above are used to represent two homogeneous specimens. Fracture is based on a multi-component vectorial measure of stress, limited by a Mohr-Coulomb surface with a tension cut-off (Figure 3-37). The cohesive strength, and the internal friction angle is set to 3.5 MPa, and 25°, respectively, reported as best approximation of the Opalinus Clay in the literature (Bossart, 2012). The tensile strength is set to 1.5 MPa which is the mean value of uniaxial tensile strength of normal to bedding, 1 MPa, and parallel to bedding, 2 MPa, of the Opalinus Clay.

As can be seen in the axial stress and strain curves in Fig. 3-43, the model shows brittle behavior. After the first element breakage neighboring elements undergo fracture even without increasing the load point displacement. After many of the elements have broken, the fracture process stabilizes in the sense that small load steps no longer produce bursts of element failures. Young's moduli obtained by the stress-strain curve agree with their elemental values. Figure 3-42(b)-(d) shows simulated fracture processes under uniaxial compressive loading. The broken line in Fig. 3-42 (b) indicates the angle of 57.5° which is based on the critical plane angle $\phi/2 + 45^\circ$. As

indicated, the angle of shear failure in early stage of fracture development roughly captures this theoretical angle.

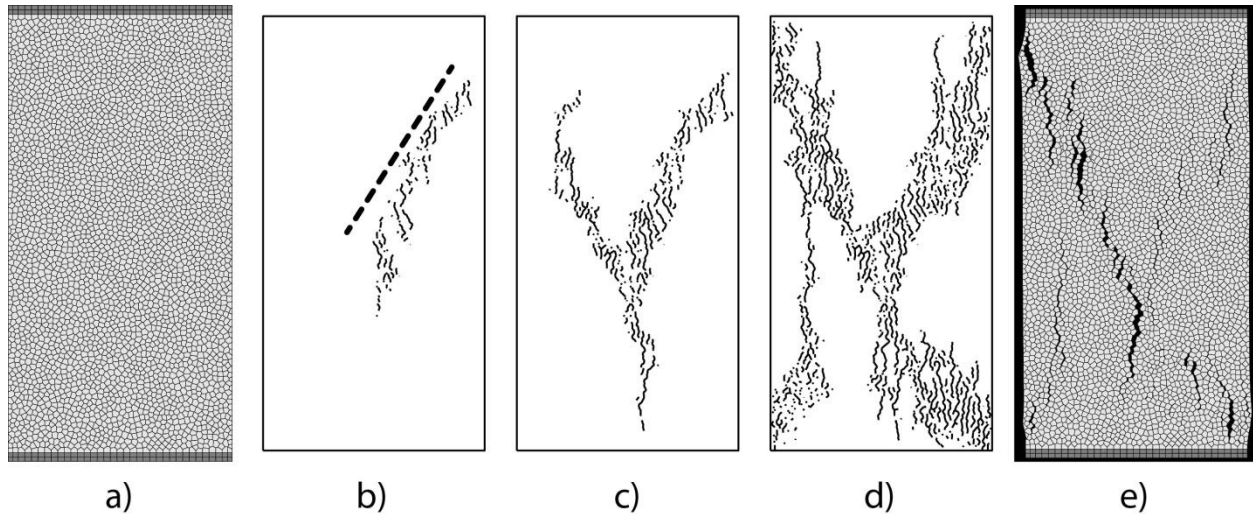


Figure 3-42. 2-D specimen under uniaxial compression loading: a) Voronoi discretization, (b), (c), (d) fracture processes in early, intermediate, and late stages, and (e) failure patterns in late stage.

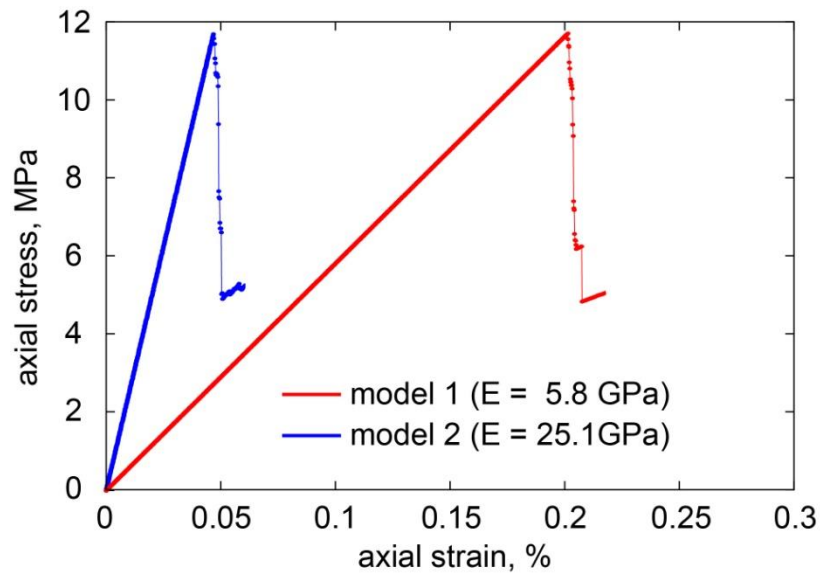


Figure 3-43. Axial stress-strain curve of two homogeneous rock models under uniaxial compression loading

Numerical example: uniaxial compression for transversely isotropic rock: Compressive behavior and failure of the transversely isotropic rocks are simulated using the RBSN modeling. Figure 3-D4 shows the Voronoi discretization of 2-D specimens with seven different angles. The same loading boundary conditions used for the homogeneous materials are considered. As discussed in Section “Anisotropic strength properties” above, the stiff and soft phases are alternatively layered, and each layer is assumed to be a homogeneous. The bulk Young’s modulus with different bedding angle can be obtained by (Pariseau, 2006):

$$\frac{1}{E} = \frac{\cos^2(\beta)}{E_p} + \left(\frac{1}{G_{12}} - \frac{2\nu_{12}}{E_p} \right) \sin^2(\beta) \cos^2(\beta) + \frac{\sin^4(\beta)}{E_n} \quad (3-37)$$

where β is the angle between the normal to the bedding plane and axial load, G_{12} is shear modulus, and ν_{12} is Poisson’s ratio. When Poisson’s ratio is set to zero and equal volume fraction for the stiff and soft phases is used, G_{12} can be expressed as:

$$G_{12} = \frac{1}{\left(\frac{1}{E_p} + \frac{1}{E_n} \right)} \quad (3-38)$$

Figure 3-44 compares the results of Eq 3-37 and simulated bulk Young’s modulus with three different layer thicknesses, $d/5$, $d/7.5$, and $d/15$, where d is the diameter (width in 2-D model) of the sample. The variation in elastic modulus is found to be nearly independent of layer thickness. The numerical results for bulk Young’s modulus using at bedding angles of $\beta = 0^\circ$ and 90° show good agreement with measured values from the Opalinus Clay for these orientations, $E_p = 15.5$ GPa and $E_n = 9.5$ GPa, respectively (Bossart, 2012). Agreement for other bedding angles ($\beta = 15^\circ, 30^\circ, 45^\circ, 60^\circ, 75^\circ$) can be viewed as predictions. The numerical model results roughly agree with the analytical values.

Figures 3-45 through 3-51 show fracture developments of transversely isotropic rock for each bedding angle. Although Young’s modulus is varied between stiff and soft layers, for the simulations in Figures 3-46 through 3-52, cohesive and tensile strength are the same in both stiff and soft layers. The light- and dark-shaded regions represent stiff and soft phase, respectively. For most cases, many fractures occur within one loading step.

In Figure 3-45, the bedding is parallel to the loading direction resulting in a bedding angle of 0° . Layering is seen to dominate both fracture orientation and distribution. Failure is found to occur first in the stiff layers (Figure 3-45 b) and c)), which is consistent with the conceptual arguments given in Section “Anisotropic strength properties” above. However, as fractures develop, failure spreads into the soft layers as well (Figure 3-45 d)). Similar trends are also found when bedding is at a 15° angle to the loading direction in Figure 3-46.

The fracture pattern begins to change when the bedding angle reaches 30° , as shown in Figure 3-47. Although the initial fracture orientation still follows the bedding angle, the fractures are initially formed preferentially in the soft layers rather than the stiff layers. This occurs because there is now sufficient stress across the layers such that the load is not supported as much by the stiff layers. As fracturing continues (Figure 3-47 c) and d)), there is some loss of the orientation of the fracturing along bedding. The pattern is roughly similar for the case with a bedding angle

of 45°, but the orientation of fractures along the bedding angle deteriorates further, as shown in Figure 3-48. At later stages (Figure 3-48c and d), a secondary overall fracture orientation appears. The orientation of the secondary fracture pattern is associated with the friction angle of the material rather than the bedding angle.

At the highest bedding angles in Figures 3-49, 3-50, and 3-51, the orientation of the general fracture pattern departs from the bedding angle and begins to follow an orientation associated with the friction angle of the material. As for a homogeneous material (Figure 3-42), the general fracture pattern shows two orientations. Furthermore, fracturing is not focused in the stiff or soft layers because at high bedding angles there is a more uniform stress distribution across layers as discussed in Section “Anisotropic strength properties”. Therefore, fracturing should be reasonably equivalent in the different layers, given uniform cohesive and tensile strength across layers.

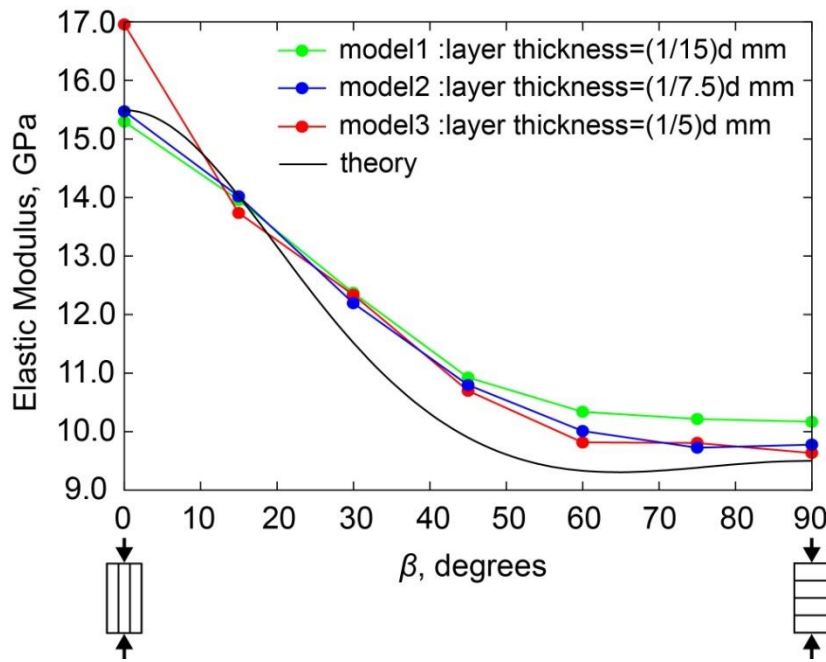


Figure 3-44. Variation of elastic modulus with the angle β between the bedding plane and the loading (vertical) direction.

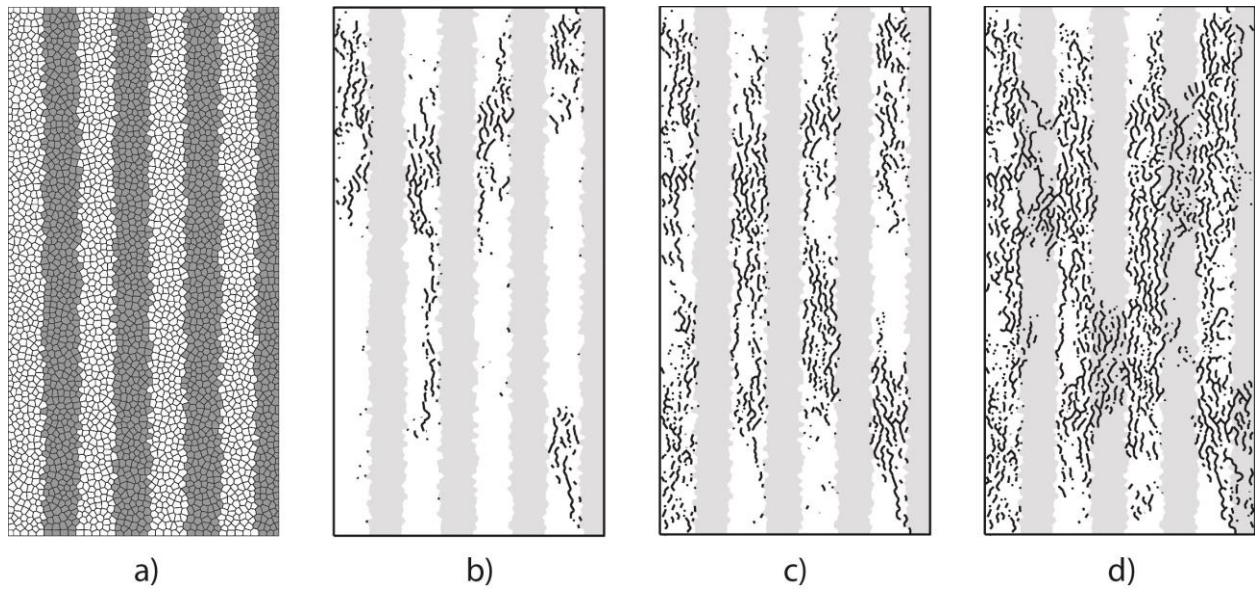


Figure 3-45. Transversely isotropic rock with bedding angle $\beta=0^\circ$: (a) Voronoi discretization, (b), (c), (d) numerical results of fracture processes under uniaxial compression loading (early, intermediate and late stages).

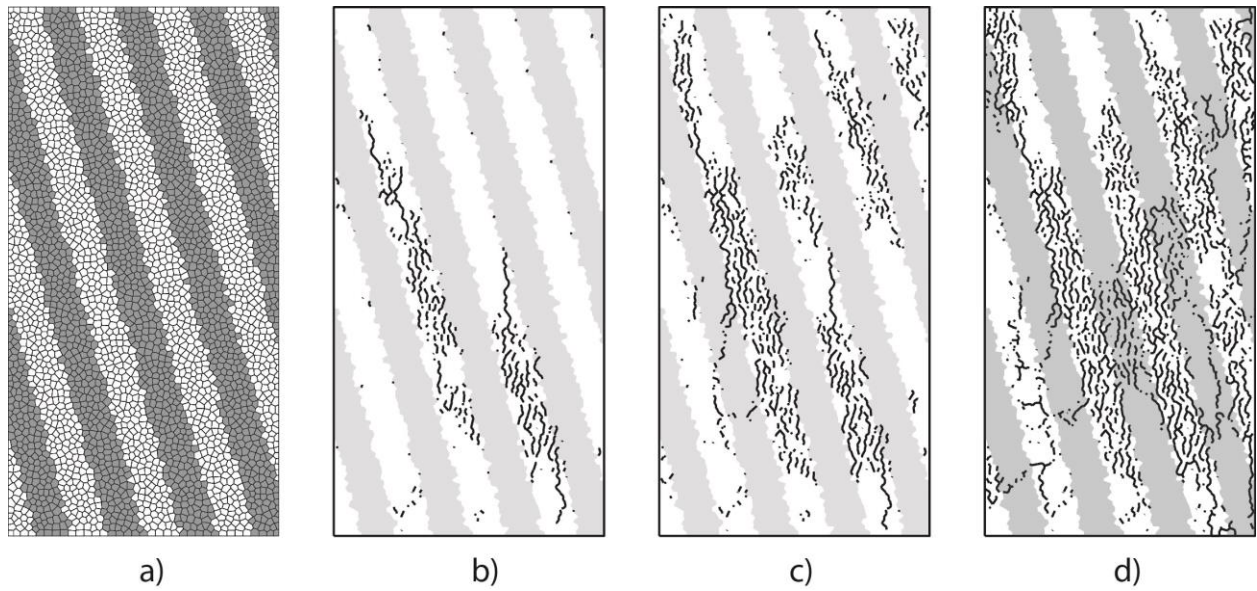


Figure 3-46. Transversely isotropic rock with bedding angle $\beta=15^\circ$: (a) Voronoi discretization, (b), (c), (d) numerical results of fracture processes under uniaxial compression loading (early, intermediate and late stages).

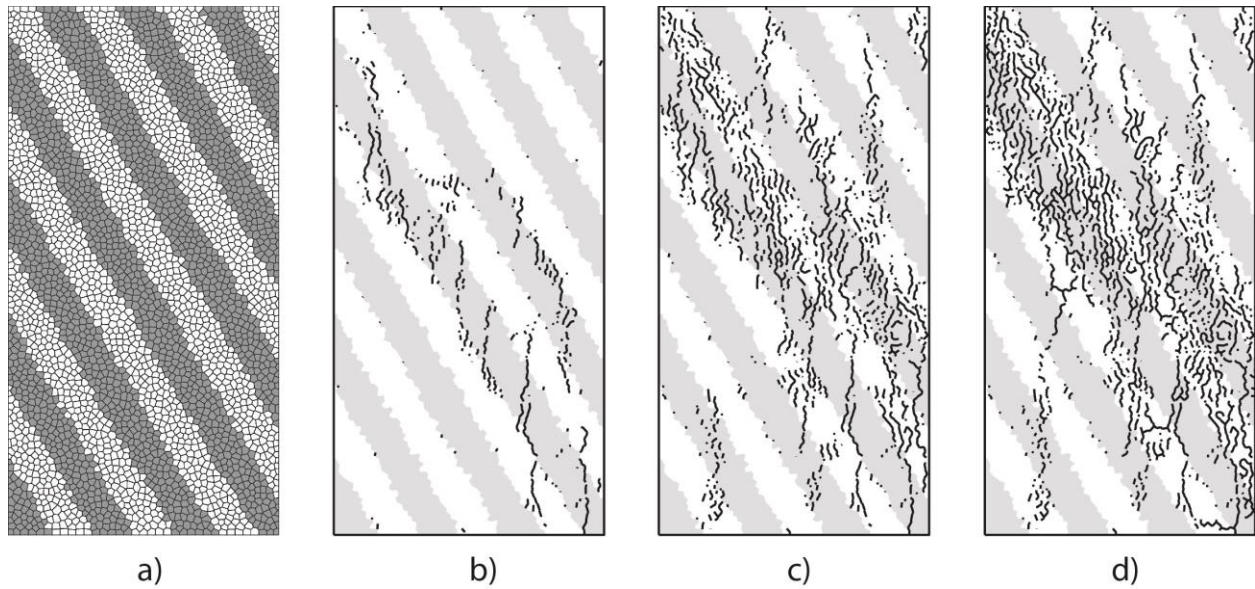


Figure 3-47. Transversely isotropic rock with bedding angle $\beta=30^\circ$: (a) Voronoi discretization, (b), (c), (d) numerical results of fracture processes under uniaxial compression loading (early, intermediate and late stages).

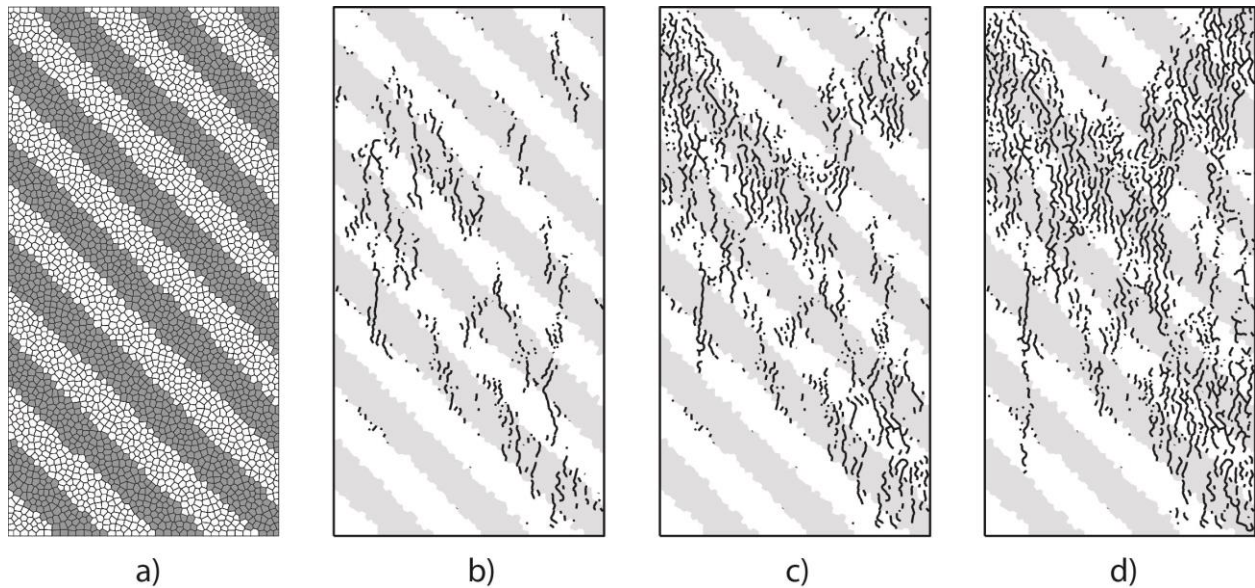


Figure 3-48. Transversely isotropic rock with bedding angle $\beta=45^\circ$: (a) Voronoi discretization, (b), (c), (d) numerical results of fracture processes under uniaxial compression loading (early, intermediate and late stages).

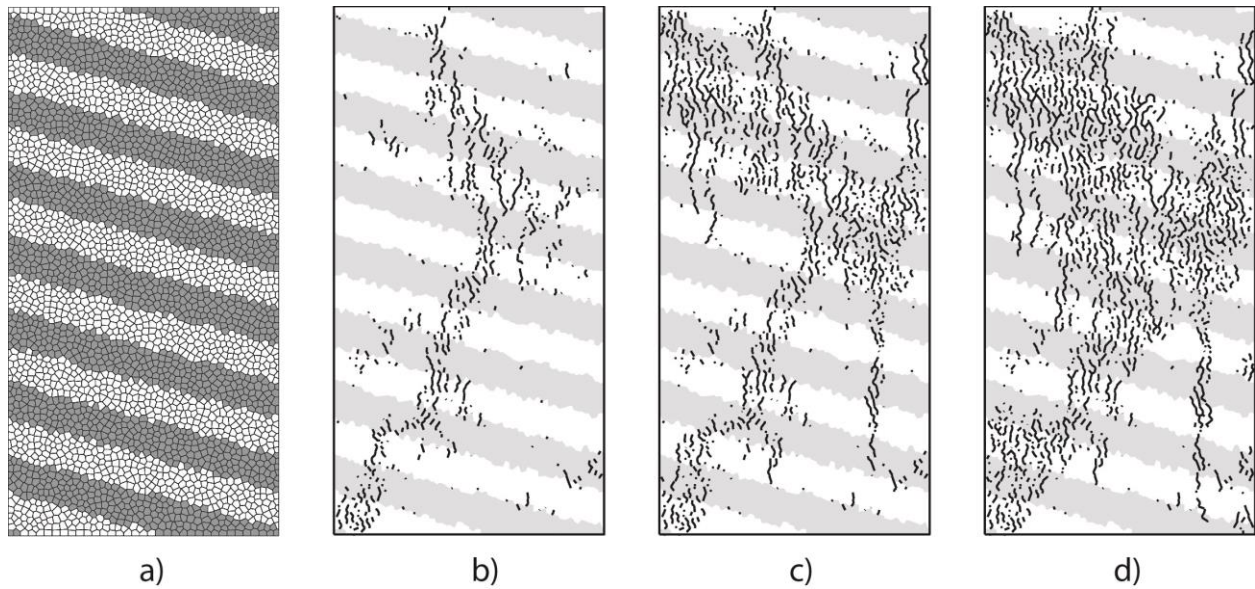


Figure 3-49. Transversely isotropic rock with bedding angle $\beta=60^\circ$: (a) Voronoi discretization, (b), (c), (d) numerical results of fracture processes under uniaxial compression loading (early, intermediate and late stages).

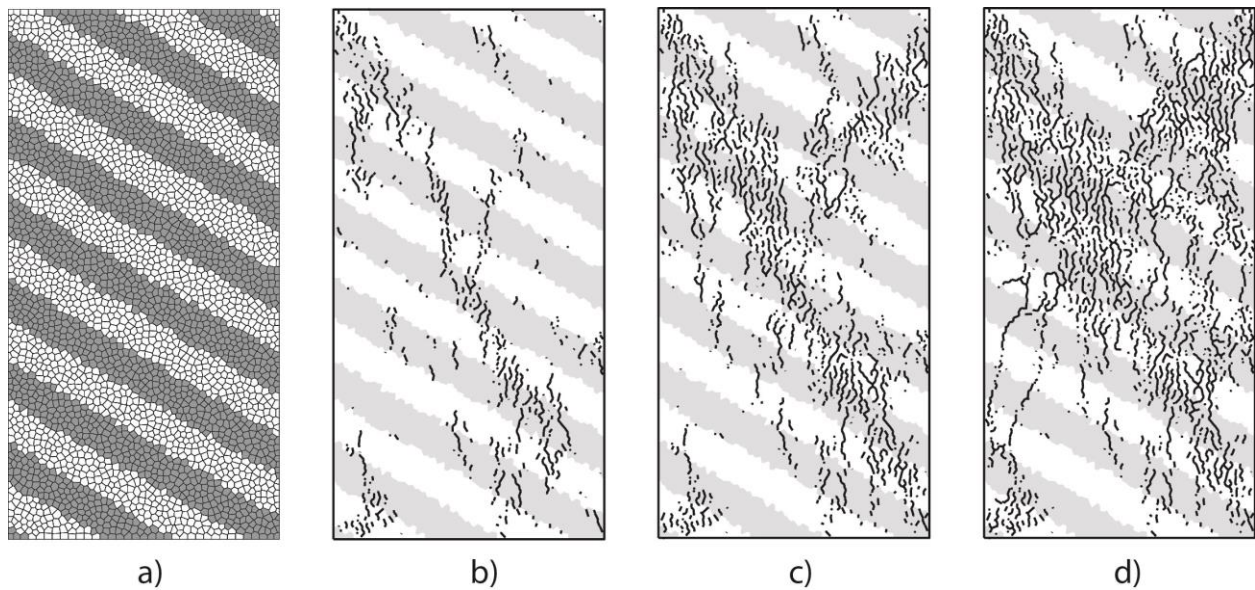


Figure 3-50. Transversely isotropic rock with bedding angle $\beta=75^\circ$: (a) Voronoi discretization, (b), (c), (d) numerical results of fracture processes under uniaxial compression loading (early, intermediate and late stages).

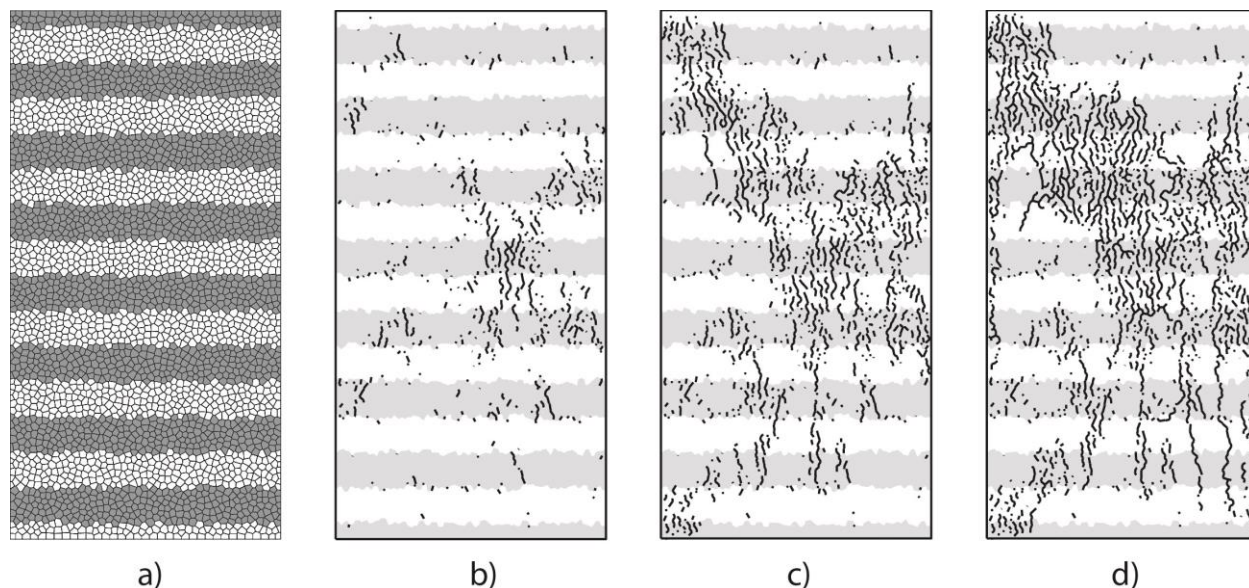


Figure 3-51. Transversely isotropic rock with bedding angle $\beta=90^\circ$: (a) Voronoi discretization, (b), (c), (d) numerical results of fracture processes under uniaxial compression loading (early, intermediate and late stages).

Fracture damage modeling of the HG-A test

In this section we present the initial simulation of the Opalinus Clay's geomechanical and fracture damage response in the vicinity of the 1-m diameter HG-A microtunnel using the RBSN model. This simulation uses the modeling methodologies described in Section "Background and model formulation" above for shear fracture and in Section "Anisotropy in the RBSN Model" above for representing anisotropic properties of the Opalinus Clay.

First, the basic stress profiles around the microtunnel under compressive stress condition are simulated using the RBSN model. Figure 3-52 (a) shows the 2D computational domain, which is $10\text{m}\times 10\text{m}$ with a circular opening (having a radius of 0.5 m) at the center, and is subjected to a far-field compressive stresses of 4.5 MPa in the horizontal direction and 6.5 MPa in the vertical direction. The model is considered as a homogeneous and isotropic material, whose elastic modulus and the Poisson's ratio are 15.5 GPa and 0.3, respectively. Figure 3-52(a) shows a discretization of the computational domain and the boundary conditions. The areal density of nodal points (or Voronoi grid size) can be controlled by changing a minimum allowable distance between nodes as a function of spatial coordinates (Asahina and Bolander, 2011). This problem may also be solved analytically using the Kirsch (1898) solution presented in Section 3.3.4. Figure 3-52(b) shows the RBSN simulation results and analytical model results for the stress profiles versus distance from the center of the domain. The RBSN model results closely match the analytical model results.

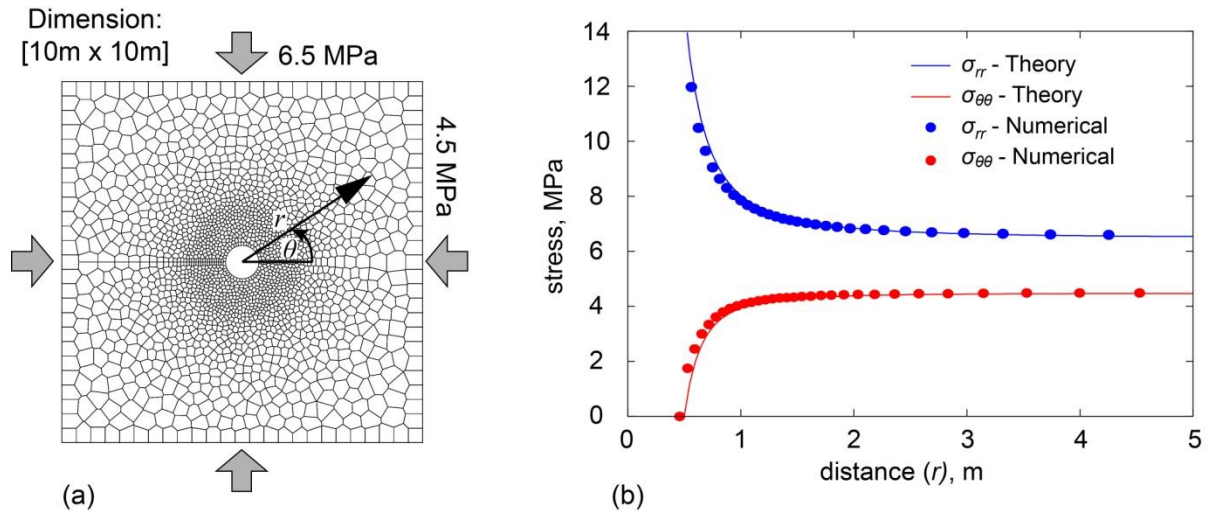


Figure 3-52. (a) Computational grid used for the RBSN simulator (2044 nodes), and (b) simulation results of radial and tangential stress for $\theta=0^\circ$ versus the distance from the center of the domain.

Next, transverse isotropy is generated around the microtunnel with higher nodal density as shown in Figure 3-53. The layered system is discretized within a 1.5 m radius around the microtunnel to keep a manageable computational cost associated with the number of nodes. Beyond the 1.5 m radius, the rock matrix is represented as homogeneous and isotropic. The material properties for each phase used in the RBSN model are summarized in Table 3-8. Figure 3-53(c) shows fracture patterns around the microtunnel. The fractured regions are affected by the material anisotropy and are not symmetric. Non-uniform damage has also been observed around the tunnel in the HG-A test as shown in Figure 3-26. Marschall et al. (2006) observed two types of failure that are postulated to be a result of strength anisotropy and stress anisotropy. Fracturing shown in Figure 3-53(c) is also not distributed symmetrically around the tunnel. Fracturing is focused in the soft layers, which is expected based on the reduced material strength in the soft layer. However, the failure mechanism around the microtunnel is not simple because of interactions with the anisotropic strength and stress field and with pre-existing tectonic structures. As shown in Figure 3-26, most of the observed damage at the tunnel wall is associated with pre-existing faults. Nevertheless, the differences in damage distribution relative to the orientation of bedding between Figures 3-53(c) and 3-26 needs to be investigated in future studies.

Table 3-8. Material properties for the Opalinus Clay

	Stiff layer	Soft layer	Matrix (r > 1.5m)
Young's modulus (GPa)	25.1	5.8	15.5
Poisson's ratio	0.3	0.3	0.3
Tensile strength (MPa)	3.3	1.0	2.2
Internal friction angle (degree)	25	25	25
Cohesion (MPa)	9.17	2.2	4.8

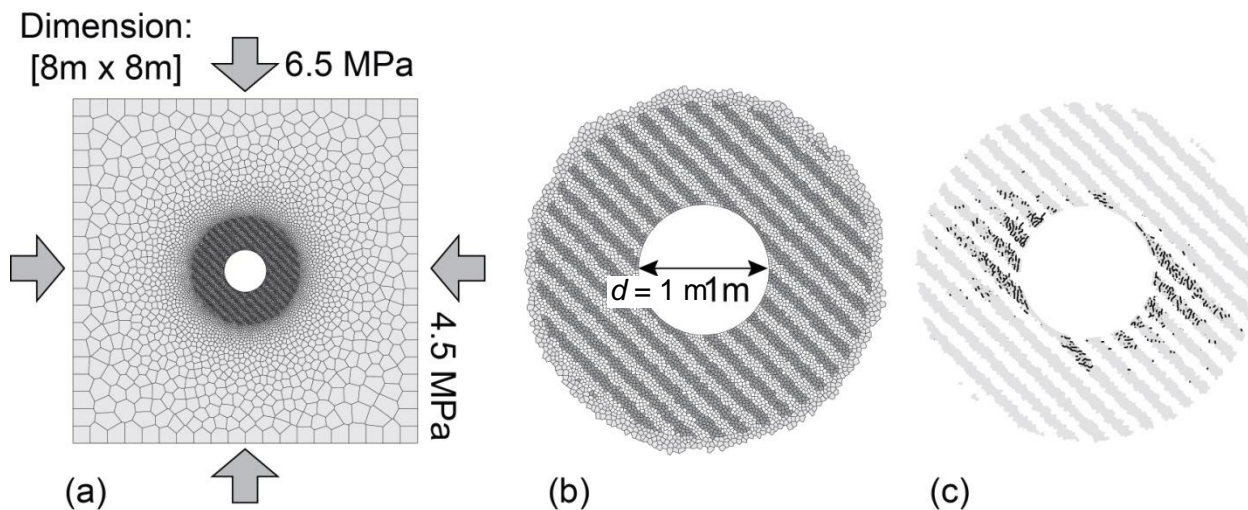


Figure 3-53. (a) Computational grid used for the RBSN simulator (10248 nodes), (b) enlarged view around the borehole, and (c) simulated fracture pattern.

3.4 Concluding Remarks

This section has addressed the following items for testing being conducted at the Mont Terri URL, Switzerland: (1) development and validation of a THM model for FE heater test (Section 2); and (2) development and validation of a hydro-mechanical fracture-damage model for the HG-A test (Section 3). The results of these efforts are summarized here:

FE Heater Test

We conducted new suite of simulations related to the FE test at Mont Terri, including scoping calculations, benchmarking, and some initial predictive modeling of the real heater test. These include model simulations using 1D axisymmetric, 2D plane strain, and full 3D model geometries. We conducted (for the first time) a THM analysis involving the BBM in a full 3D field setting for modeling the geomechanical behavior of the buffer. Compared to our previous 2D model analysis, this 3D analysis provides a much more accurate estimate of the temperature evolution near the heater and thereby should provide a better prediction of the peak temperature. Our current understanding is that the peak temperature may become as high as 160°C at the inner parts of the buffer. However, this prediction strongly depends on the thermal and diffusion properties of the buffer, which are parameters that have presently not been well constrained for this buffer material.

Our THM model simulation was conducted with a simplified buffer mechanical model, whereas a ubiquitous joint model was used for modeling the anisotropic mechanical strength properties of the Opalinus Clay. The analysis showed that some minor failure may occur near the tunnel wall

behind the concrete lining after excavation. This failure does not expand much further during the 20-year heating, meaning that the rock mass remains in an elastic mechanical state.

Overall, the initial model analyses showed that our adopted modeling approach is adequate for modeling the coupled THM processes at the FE heater, including all components of bentonite, concrete lining, and Opalinus Clay. We managed to discretize the 3D model using the inclined mesh in both TOUGH2 and FLAC3D, and the modeling results are reasonable.

Our next steps will be (1) to compare our benchmarking simulation results with those of the other international modeling teams, (2) to model newly available laboratory experiments for constraining THM parameters of the MX-80 granular bentonite, and (3) provide a final prediction of FE heater experiment (should be completed and reported before start of heating).

HG-A Test

Use of the RBSN model for the HG-A test requires development of two additional model capabilities: (1) a method for computing fracturing under compressive load and (2) a method to treat the anisotropic geomechanical properties of the Opalinus Clay. The use of the Mohr-Coulomb failure criterion led to RBSN model predictions for fracturing under compressive load that roughly follow trends expected for a homogeneous medium. For a layered system, the results were also reasonable in that fracturing followed the stiff layers for high bedding angles but was not controlled by bedding at low bedding angles. Currently, rock failure is modeled using a brittle model in which all strength is lost at failure. However, a more realistic failure response results in a more gradual loss of strength following failure. In addition, contacts along fracture surfaces under compressive loads will lead to friction along fracture planes not currently accounted for in the model. Anisotropic properties for the bulk rock were represented in the RBSN model using layered heterogeneity. While the current approach was successful at producing the desired anisotropic bulk properties and trends for fracture behavior under compressive load, significant differences remain between the RBSN results and observations in the HG-A test, indicating that further model development is needed. The results and test observations suggest that:

1. Either finer layering or a different approach may be needed for modeling anisotropic behavior.
2. Additional mechanisms need to be investigated for fracture under compressive load.
3. The geomechanical characteristics of existing fault features in the rock need to be incorporated.

Future work will also address:

1. Coupling of the hydro-mechanical response for post-excavation dryout and fracture formation and the associated dynamic pore-pressure response.
2. Development of a three-dimensional model capable of representing the HG-A fluid injection tests.

3.5 References

- Alonso, E.E., Gens, A., Josa, A. (1990). A constitutive model for partially saturated soils, *Géotechnique*, 40(3), 405-430.
- Asahina, D., Bolander, J.E. (2011). Voronoi-based Discretizations for Fracture Analysis of Particulate Materials, *Powder Technology*, 213, 92-99.
- Asahina, D., Landis, E.N., Bolander, J.E. (2011). Modeling of phase interfaces during pre-critical crack growth in concrete, *Cement & Concrete Composites*, 33, 966-977.
- Bock, H. (2001). RA Experiment Rock Mechanics Analyses and Synthesis: Data Report on Rock Mechanics, Mont Terri Project, Technical Report 2000-02.
- Bolander, J.E., Saito, S. (1998). Fracture analyses using spring networks with random geometry, *Eng Fract Mech*, 61, 569-91.
- Bossart, P. (2012). Characteristics of the Opalinus Clay at Mont Terri, http://www.mont-terri.ch/internet/mont-terri/en/home/geology/key_characteristics.parsys.49924.DownloadFile.tmp/characteristic_sofopa.pdf
- Corkum, A.G., Martin, C.D. (2007). The Mechanical Behaviour of Weak Mudstone (Opalinus Clay) at Low Stresses, *International Journal of Rock Mechanics and Mining Sciences*, 44, 196-209.
- Cusatis, G., Bažant, Z.P., Cedolin, L. (2003). Confinement-shear lattice model for concrete damage in tension and compression: I. Theory, *Journal of Engineering Mechanics*, 129 (12), 1439-1448.
- Ewing, J., Senger, R. (2011). Evolution of Temperature, Pressure and Saturation in the Bentonite Buffer: Scoping Calculations in Support of the Design of the Full-Scale Emplacement Experiment at the Mont Terri URL. NAGRA NAB 10-38, September 2011.
- Freivogel, M., Huggenberger, P. (2003). Modellierung bilanzierter Profile im Gebiet Mont Terri - La Croix (Kanton Jura), in: *Geology, Paleohydrology and Stress Field*, Heitzmann & Tripet (eds.), Reports of the Federal Office for Water and Geology (FOWG), Geology Series 4, Switzerland.
- Garboczi, E.J., Day, A.R. (1995). An algorithm for computing the effective linear elastic properties of heterogeneous material: 3D results for composites with equal Poisson ratios, *J. Mech. Phys. Solids*, 43, 1349-1362.
- Garitte, B. (2013). FMT FE-Experiment: 1D Benchmark definition for the modelling groups. Aktennotiz AN 13-300, NAGRA, Wettingen, Switzerland.
- Garitte, B., Gens, A. (2012). TH and THM Scoping computations for the definition of an optimal instrumentation layout in the Full-scale Emplacement (FE). experiment NAGRA NIB 10-34, March 2012.
- Garitte, B., Gens, A., Vaunat, J., Armand, G. (2013). Thermal Conductivity of Argillaceous Rocks: Determination Methodology Using In Situ Heating Tests, *Rock Mechanics and Rock Engineering* DOI 10.1007/s00603-012-0335-x.
- Gens, A., Garitte B., Wileveau Y. (2007). In situ Behaviour of a Stiff Layered Clay Subject to Thermal Loading: Observations and Interpretation, *Geotechnique*, 57, 207-228.
- Gens, A., Sanchez, M., Guimaraes, L.D.N., Alonso, E.E., Lloret, A., Olivella, S., Villar, M.V., Huertas, F. (2009). A full-scale in situ heating test for high-level nuclear waste disposal: observations, analysis and interpretation, *Geotechnique* 59, 377-399.
- Itasca (2009). FLAC3D V4.0, Fast Lagrangian Analysis of Continua in 3 Dimensions, User's Guide. Itasca Consulting Group, Minneapolis, Minnesota.

- Kawai, T. (1978). New Discrete Models and their Application to Seismic Response Analysis of Structures, *Nuclear Engineering and Design*, 48, 207-229.
- Kirsch, G. (1898). Die Theorie der Elastizität und die Bedürfnisse der Festigkeitslehre, *Zeitschrift des Vereines deutscher Ingenieure*, 42, 797-807.
- Lanyon, G.W., Marschall, P., Trick, T., de La Vaissière, R., Shao, H., Leung, H. (2009). Hydromechanical Evolution and Self-Sealing of Damage Zones around a Microtunnel in a Claystone Formation of the Swiss Jura Mountains, American Rock Mechanics Association, ARMA 09-333.
- Liu, H.H., Houseworth, J., Rutqvist, J., Zheng, L., Asahina, D., Li, L., Vilarrasa, V., Chen, F., Nakagawa, S., Finsterle, S., Doughty, C., Kneafsey, T., Birkholzer, J. (2013). Report on THMC modeling of the near field evolution of a generic clay repository: Model validation and demonstration. (FCRD-UFD-2013-000244), U.S. DOE Used Fuel Disposition Campaign.
- Marschall, P., Distinguin, M., Shao, H., Bossart, P., Enachescu, C., Trick, T. (2006). Creation and Evolution of Damage Zones Around a Microtunnel in a Claystone Formation of the Swiss Jura Mountains, *Society of Petroleum Engineers*, SPE-98537-PP.
- Marschall, P., Trick, T., Lanyon, G.W., Delay, J., Shao, H. (2008). Hydro-Mechanical Evolution of Damaged Zones around a Microtunnel in a Claystone Formation of the Swiss Jura Mountains. American Rock Mechanics Association, ARMA 08-193.
- Martin, C.D., Lanyon, G.W. (2003). Measurement of In-Situ Stress in Weak Rocks at Mont Terri Rock Laboratory, Switzerland, *International Journal of Rock Mechanics & Mining Sciences*, 40, 1077-1088.
- Meier, O., Nussbaum, C., Bossart, P. (2005). HG-A experiment: Drilling of the microtunnel (BHG-A0 and BHG-A1), Mont Terri Project, TN 2005-55.
- Nater, P. (2012). Mont Terri / FE-Experiment Geomechanische Modellierung des Vortriebs. NAGRA AN 12-184.
- Nussbaum, C., Bossart P. (2006). HG-A experiment: Mapping of new breakouts developed in the HG-A microtunnel about 11 months after the excavation, Mont Terri Project, TN 2006-31.
- Nutt, M. (2011). Used Fuel Disposition Campaign Disposal Research and Development Roadmap (FCRD&D-USED-2011-000065 REV0), U.S. DOE Used Fuel Disposition Campaign.
- Olivella, S., Gens A. (2000). Vapour transport in low permeability unsaturated soils with capillary effects, *Transport in Porous Media*, 40, 219–241.
- Pariseau, W.G. (2006). Design Analysis in Rock Mechanics. London ; New York: Taylor & Francis.
- Pollard, D.D., Fletcher, R.C. (2005). Fundamentals of Structural Geology, Cambridge University Press, Cambridge, U.K.
- Pruess, K., Oldenburg, C.M., Moridis, G. (2011). TOUGH2 User's Guide, Version 2.1, LBNL-43134(revised), Lawrence Berkeley National Laboratory, Berkeley, California.
- Rizzi, M., Seiphoori, A., Ferrari, A., Ceresetti, D., Laloui, L. (2011). Analysis of the Behaviour of the Granular MX-80 bentonite in THM-processes; Orders No 7'928 and 5'160; Swiss Federal Institute of Technology: Lausanne, 2011.
- Rutqvist J., Wu Y.-S., Tsang C.-F., Bodvarsson G. (2002). A modeling approach for analysis of coupled multiphase fluid flow, heat transfer, and deformation in fractured porous rock, *International Journal of Rock Mechanics and Mining Sciences*, 39, 429-442.

- Rutqvist, J., Ijiri, Y., Yamamoto, H. (2011). Implementation of the Barcelona Basic Model into TOUGH-FLAC for simulations of the geomechanical behavior of unsaturated soils, *Computers & Geosciences*, 37, 751-762.
- Rutqvist, J., Zheng, L., Chen, F., Liu, H.-H., Birkholzer, J. (2013a). Modeling of Coupled Thermo-Hydro-Mechanical Processes with Links to Geochemistry Associated with Bentonite-Backfilled Repository Tunnels in Clay Formations. *Rock Mechanics and Rock Engineering*, (In Press, January 2013).
- Rutqvist, J., Chen, F., Birkholzer, J., Liu, H.-H., Müller, H., Garitte, B., Vietor, T. (2013b). Modeling of coupled thermo-hydro-mechanical processes at Mont Terri heater experiment in Opalinus Clay, using TOUGH-FLAC. Proceedings of the 2013 International High-Level Radioactive Conference (IHLRWM), April 28 – May 2, 2013.
- Salamon, M.D.G. (1968). Elastic Moduli of a Stratified Rock Mass, *Int. J. Rock Mech. Min. Sci.*, 5, 519-527.
- Shlangen, E., Van Mier, J.G.M. (1992). Experimental and numerical analysis of micromechanism of fracture of cement-based composites, *Cement and Concrete Composites*, 14, 105-118.
- Tang, C.A. (1997). Numerical simulation of progressive rock failure and associated seismicity, *Int. J. Rock Mech. Min. Sci.*, 34, 249-262.
- Thury, M., Bossart, P. (1999). The Mont Terri Rock Laboratory, a New International Research Project in a Mesozoic Shale Formation, in Switzerland, *Engineering Geology*, 52, 347-359.
- Tonon, F., Amadei, B. (2003). Stresses in anisotropic rock masses: an engineering perspective building on geological knowledge, *International Journal of Rock Mechanics & Mining Sciences*, 40, 1099-1120.
- van Genuchten, M.T. (1980). A closed-form equation for predicting the hydraulic conductivity of unsaturated soils, *Soil Sci Soc Am J*, 44, 892-898.
- Vietor, T. (2012). Mont Terri Project - FE Experiment Modelling Kick-off Meeting. February 9, 2012, Mont Terri, Switzerland. NAGRA Technical Discussion TD-217.
- Wang, Y. (2011). Research & Development (R&D). Plan for Used Fuel Disposition Campaign (UFDC). Natural System Evaluation and Tool Development, U.S. DOE Used Fuel Disposition Campaign.

4. International Collaboration - Radionuclide Interactions and Transport in Geologic Repository Environments – Pu Interaction with Bentonite

4.1 Introduction

The focus of this collaboration is to investigate radionuclide interactions with natural and engineered materials, specifically the mineral bentonite that will be used in EU repositories and possibly in US high-level waste repository designs. These experiments are designed to develop a mechanistic understanding of Pu interactions with representative mineral substrates under granitic chemical conditions. The sorption/desorption experiments cover a large range of Pu concentrations and will be compared to sorption/desorption experiment with montmorillonite. The experiments are being coordinated with the Colloid Formation and Migration (CFM) international project led by Karlsruhe Institute of Technology and located at the Grimsel Test Site underground research laboratory in Switzerland. Experiments will be completed by 8/15/2014. Milestone M4FT-13LL0807071 is a progress report on this effort. The research is addressing the following FEPs/needs identified in the R&D Roadmap: 2.2.09.05 - radionuclide speciation and solubility in host rock; 2.2.09.55 - sorption of dissolved radionuclides in host rock; 2.2.09.59 - colloidal transport in host rock.

The bentonite clay used in these experiments was FEBEX bentonite received from the National Cooperative for the Disposal of Radioactive Waste (Nagra), Switzerland that plans to use the clay as a backfill material in its nuclear waste repositories. This clay has been characterized previously and comprised 93±3% montmorillonite, 2±0.5% quartz, 2±1% potassium feldspars, 1±0.7% plagioclase, 2±0.2% cristobalite, 1±0.7% calcite and 1.5±0.1% rhyodacitic rock (Sánchez et al., 2006). Prior to use the clay was Na-homoionized, lightly ground in a mortar and pestle and the resulting material sieved (size fraction <63 µm). The surface area of the clay as used in these experiments was 25.2±1.0 m² g⁻¹. In order to ensure consistency with previous montmorillonite adsorption work, experiments were performed in 0.7 mM NaHCO₃, 5 mM NaCl buffer solution with a solid: solution ratio of 1 g L⁻¹. All experiments were performed under ambient atmospheric conditions.

4.2 Adsorption

To compare the rate of adsorption of Pu(V) on bentonite to the rate of Pu(V) adsorption on montmorillonite at pH 8, a time series experiment was performed in triplicate with an initial concentration of 10⁻¹⁰ mol L⁻¹ Pu(V). The results of this experiment are shown in Figure 4-1. Here the adsorption of Pu to bentonite is plotted as a function of time along with previously published data for the adsorption of Pu(V) to montmorillonite (Begg et al., 2013). The log surface area normalized apparent rate of sorption for bentonite was -3.4 L m⁻² h⁻¹ as compared to the value of -2.8 L m⁻² h⁻¹ for montmorillonite. This similarity in the rate of Pu(V) adsorption to both clays suggests that the large component of montmorillonite in the bentonite clay is primarily responsible for the uptake of Pu(V) from the aqueous phase.

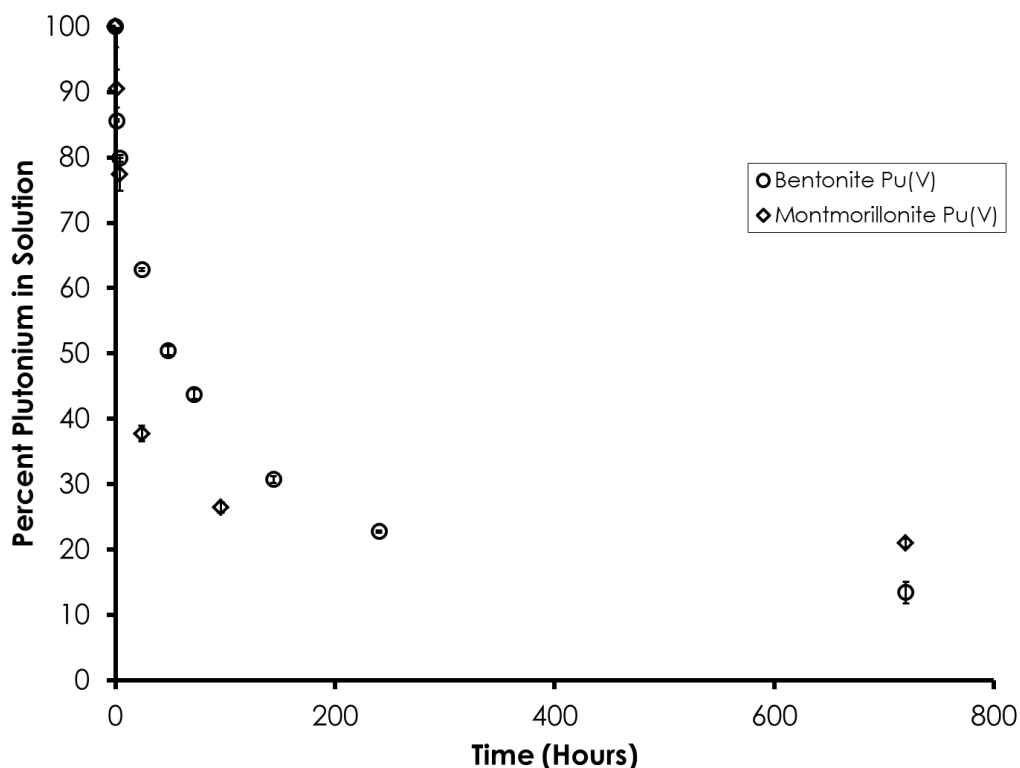


Figure 4-1. Sorption of Pu(V) to FEBEX bentonite (circles) and SWy-1 Na-montmorillonite (diamonds) plotted as percentage of Pu removed from solution vs. time. Initial Pu concentrations were 10^{-10} M for bentonite and 10^{-9} M for montmorillonite. Error bars for bentonite are 1σ of triplicate experiments and are 1σ values calculated from parallel quadruplicate experiments for montmorillonite.

A Pu(IV) adsorption isotherm was performed with bentonite at pH 8. Previous work with Pu(IV) and Pu(V) adsorption to montmorillonite has shown that Pu(V) adsorption behavior will converge with that of Pu(IV) over sufficient timescales (Zavarin et al., 2012; Begg et al., 2013). The Pu adsorption experiment was performed with initial Pu(IV) concentrations ($[Pu]_{\text{initial}}$) ranging from 10^{-7} – 10^{-16} mol L $^{-1}$. As previous work has highlighted the need for long equilibration periods when performing Pu adsorption studies, Pu(IV) was equilibrated for 120 days in these experiments (Powell et al., 2006; Begg et al., 2013). Pu in solution was measured using liquid scintillation counting (LSC) for experiments with $[Pu]_{\text{initial}}$ 10^{-7} – 10^{-11} mol L $^{-1}$ and at the Center for Accelerator Mass Spectrometry (CAMS) at LLNL for experiments with $[Pu]_{\text{initial}}$ 10^{-11} – 10^{-16} mol L $^{-1}$.

The Pu(IV) sorption isotherm is shown in Figure 4-2. Pu(IV) sorption was broadly linear at $[Pu]_{\text{initial}}$ ranging from 10^{-7} mol L $^{-1}$ to 10^{-16} mol L $^{-1}$ after 120 days' equilibration. The slope of the plot of $\log[Pu]$ in solution against $\log[Pu]$ on solid was 1.06 (R^2 0.998). The K_d values ranged from 21000 – 79000 mL g $^{-1}$. Also plotted in Figure 2 is the equivalent Pu(IV) montmorillonite adsorption isotherm for $[Pu]_{\text{initial}}$ 10^{-7} mol L $^{-1}$ – 10^{-13} mol L $^{-1}$ following 30 days' equilibration. The slope of the plot of $\log[Pu]$ in solution against $\log[Pu]$ on solid for montmorillonite was 1.04 (R^2 0.997) while K_d values ranged from 8900 – 27000 mL g $^{-1}$. The similarity of the Pu(IV)

bentonite and montmorillonite isotherms further suggests that the montmorillonite in the bentonite is largely responsible for controlling the adsorption of Pu in these experiments.

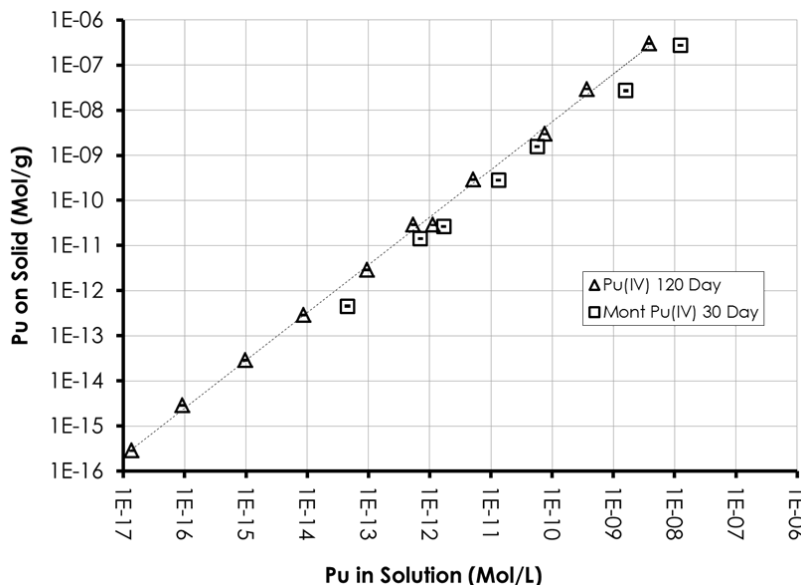


Figure 4-2. 120 day Pu(IV) sorption isotherm for FEBEX bentonite (1 g L^{-1} ; triangles) and 30 day Pu(IV) sorption isotherm for Na-montmorillonite (1 g L^{-1} ; squares) in 0.7 mM NaHCO_3 , 5 mM NaCl buffer solution at pH 8.

4.3 Desorption

A flow-cell experiment was used to characterize Pu(IV) desorption from bentonite and to compare it with previously determined Pu(IV) – montmorillonite desorption behavior. Prior to the desorption step, Pu(IV) was equilibrated with bentonite at pH 8 for 21 days. Desorption experiments were performed in a 20 mL stirred cell fitted with a 100 nm filter and a stir bar to ensure ideal mixing conditions. An aliquot of adsorption suspension was placed in the flow cell and atmosphere-equilibrated Pu-free 0.7 mM NaHCO_3 , 5 mM NaCl buffer solution at pH 8 flowed through the cell at an initial rate of 0.4 mL/min (average retention time of ~ 50 minutes). Effluent fractions were collected over time, acidified with 2% HNO_3 and Pu concentration determined via LSC. In order to evaluate the kinetics of the desorption process, the flow rate was changed approximately every 10 pore volumes to flow rates of 0.2 , 0.04 , and 0.02 mL min^{-1} .

The results from both the bentonite and the montmorillonite flow cell experiments at pH 8 are shown in Figure 4-3. The results show that there is measurable desorption of Pu from bentonite over the duration of the flow cell experiment. In the first flow regime (0.4 mL min^{-1}), differences between the two systems are likely due to poor mixing in the bentonite cell caused by a non-rotational stir bar. This was rectified after 1.8 pore volumes. Further divergence between the two systems is also seen towards the end of the flow cell experiment (0.04 mL min^{-1}). Nonetheless,

the desorption profiles for bentonite and montmorillonite are very similar, indicating that, as with the adsorption experiments, the same processes are responsible for the desorption of Pu from the two clays.

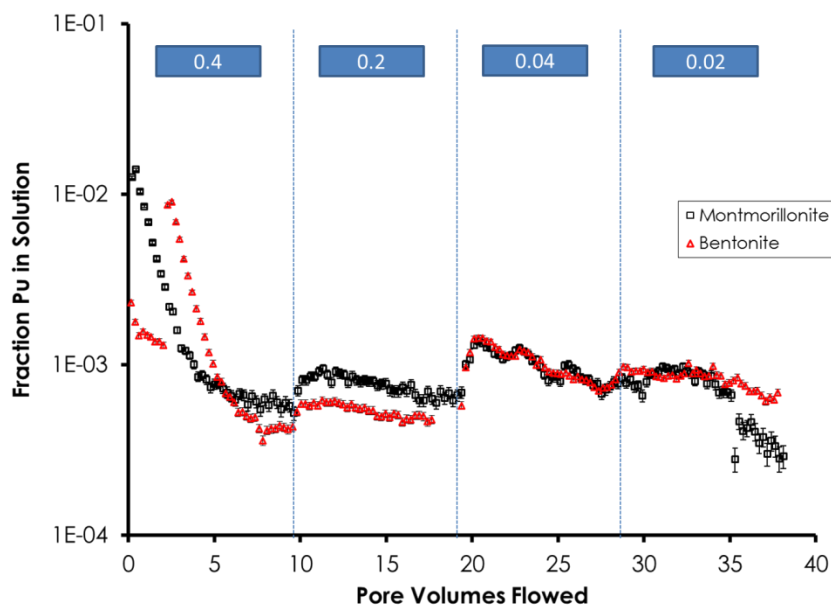


Figure 4-3. Results from Pu(IV) - montmorillonite (squares) and Pu(IV) - bentonite (triangles) desorption flow-cell experiments. Data points represent the fraction of the total system Pu in the collected effluent. Experiments performed in a 20 mL cell with 1 g L⁻¹ clay at pH 8. Montmorillonite experiments were spiked with [Pu]_{initial} 1 × 10⁻¹⁰ M, bentonite experiments spiked with [Pu]_{initial} 3 × 10⁻¹⁰ M. Influent solution was Pu-free 0.7 mM NaHCO₃, 5 mM NaCl buffer. Influent flow rates were 0.4, 0.2, 0.04 and 0.02 ml min⁻¹ and are shown on the plot. Changes in flow rate are denoted by vertical dashed lines. Error bars based on propagation of % 2s liquid scintillation counting uncertainties.

4.4 Summary

From our work to date we can conclude that:

- Adsorption behavior of Pu(V) on bentonite is similar to montmorillonite suggesting that our understanding of the simple binary Pu-montmorillonite system can provide insight for the more complex multi-component mineralogy of bentonite clay.
- The Pu(IV) sorption isotherm for bentonite is broadly linear over a large range in Pu concentration ([Pu]_{initial} ranging from 10⁻⁷ mol L⁻¹ to 10⁻¹⁶ mol L⁻¹) suggesting that the process controlling sorption at extremely low concentrations is the same as at higher concentrations.
- The desorption behavior of the bentonite and montmorillonite are very similar, indicating that, as with the adsorption experiments, the same processes are responsible for the desorption of Pu from the two materials.

4.5 References

- Begg, J. D.; Zavarin, M.; Zhao, P.; Tumey, S. J.; Powell, B.; Kersting, A. B., Pu(V) and Pu(IV) Sorption to Montmorillonite. *Environ Sci Technol* **2013**, *47*, (10), 5146-5153.
- Powell, B. A.; Duff, M. C.; Kaplan, D. I.; Fjeld, R. A.; Newville, M.; Hunter, D. B.; Bertsch, P. M.; Coates, J. T.; Eng, P.; Rivers, M. L.; Sutton, S. R.; Triay, I. R.; Vaniman, D. T., Plutonium oxidation and subsequent reduction by Mn(IV) minerals in Yucca Mountain tuff. *Environ Sci Technol* **2006**, *40*, (11), 3508-3514.
- Sánchez, L.; Cuevas, J.; Ramírez, S.; Riuiz De León, D.; Fernández, R.; Vigil Dela Villa, R.; Leguey, S., Reaction kinetics of FEBEX bentonite in hyperalkaline conditions resembling the cement–bentonite interface. *Applied Clay Science* **2006**, *33*, (2), 125-141.
- Zavarin, M.; Powell, B. A.; Bourbin, M.; Zhao, P. H.; Kersting, A. B., Np(V) and Pu(V) ion exchange and surface-mediated reduction mechanisms on montmorillonite. *Environ Sci Technol* **2012**, *46*, (5), 2692-2698.

5. Using Environmental Tracers to Estimate Fracture Network Properties: Bedrichov Tunnel, Czech Republic

5.1 Introduction

Environmental tracers are non-applied chemical species present in precipitation with known concentration histories and known decay and production rates in the subsurface. These tracers provide information on the transport characteristics of groundwater systems over a wide range of time scales. The primary goal of this study is to use environmental tracer data from the Bedrichov tunnel experiment to help characterize fracture transport characteristics. Cutting-edge transport theory and computational power are being used to incorporate environmental tracer information in estimating fracture network capabilities. The primary activities accomplished during FY-2013 include attending the DECOVALEX-2012 meetings in Leipzig Germany and Jeju Island Korea, and the development of lumped parameter for the simulation of environmental tracer concentrations discharging in the Bedrichov Tunnel.

Interpretation of environmental tracers has proven useful for the conceptualization and parameterization of fracture flow systems. Simplified analytic solutions to the 1-D advection-diffusion models have been used to estimate recharge and fracture spacing (Cook and Robinson, 2002), and 1-D numerical models have been used to show the effect of matrix diffusion on environmental tracer concentration and groundwater age distribution using parallel fracture networks (Cook et al., 2005). However, higher dimensional modeling and or more sophisticated fracture networks have not been used.

Fracture network transport of applied tracers is an area of active research (e.g. Painter and Cvetkovic, 2005; Painter et al., 2008). However, these studies are concerned with the movement of applied tracers and/or released contamination. Applied tracers have a very limited time range of applicability and even the longest term tracer experiments would be on the order of 10's of years, while travel times in large fracture networks can be over 10⁵ years. Making predictions of long term transport over the latter time scale will be highly uncertain using only observations on the former. Improving the interpretation of environmental tracers which can provide information on transport up to 10⁸ years will clearly aid when making predictions on the at time scale.

Task C2 of the DECOVALEX workgroup is centered around a dataset of environmental tracers and discharge in Bedrichov Tunnel located in the Bohemian Massif of the Czech Republic. The tunnel is around 1 km in length with a max depth of 200m and cuts through fractured granite. The dataset includes stable isotopes of water, tritium, tritiogenic ³He and other noble gases, and dissolved chlorofluorocarbons (CFC's) measured in fracture discharge. It leverages an existing data collection point for stable isotopes and tritium measured in precipitation near the study site. The goal of Task C2 is to model groundwater flow and transport of environmental tracers in the fractured system surrounding the Bedrichov Tunnel, and utilize this data to constraint fracture network parameters.

Methods:

In FY13 we developed lumped parameter models and numerical models which simulate tracer transport to the Bedrichov Tunnel. Existing lumped parameter conceptual models and a newly developed conceptual model which includes matrix diffusion were used to provide a initial first order interpretation of the tracer data. Subsequently 3-d models of groundwater flow and isotope tracer transport were developed using the PFLOTRAN flow and transport code. These models are simplified and will be used as the building blocks for more advanced simulation and interpretation in the future.

5.2 Lumped Parameter Models

The concentration of a tracer at a sampling point is a function of the distribution of groundwater age ($g(\tau)$) given by the convolution integral:

$$C(t) = \int_0^{\infty} C_{in}(t - \tau)g(\tau)e^{-\lambda\tau}d\tau \quad (5-1)$$

where C_{in} is the input function for the tracer and λ is the decay constant for the tracer of interest. Age distributions have been developed for a variety of simple aquifer type and flow systems (e.g. Cook and Herczeg, 2000). The models used in this study include commonly used dispersion and exponential model as well as a newly developed model which includes matrix diffusion in fractured systems. For the exponential model:

$$g(\tau) = \frac{1}{\tau} * e^{-\frac{t-\tau}{\tau}} \quad (5-2)$$

and for the dispersion model:

$$g(\tau) = \left(\frac{4\pi(t-\tau)^3}{Pe\tau}\right)^{1/2} \exp\left(-1 - \frac{t-\tau}{\tau}\right)^{2\tau Pe(t-\tau)} \quad (5-3)$$

where Pe is the pecelet number for transport. In order to account for matrix diffusion we use the random walk in time method after (Painter et al., 2008). Here the retarded travel time distribution is given by:

$$g(t_{tr}) = \int_0^{\infty} \int_0^{\infty} g_{ret}(t_{tr} - \tau|\beta)g_{\beta|\tau}(\beta|\tau)g(\tau) d\tau d\beta \quad (5-4)$$

where τ is the non-retarded advective travel time, β is the transport resistance parameter and t_{tr} is the total travel time include retention. The retention time distribution can be derived for a variety of processes including unlimited matrix diffusion which is given by (Painter et al., 2008):

$$g_{ret} = H(t_{ret})\kappa\beta/2\sqrt{\pi t_{ret}}\exp(-\kappa^2\beta^2/4t_{ret}) \quad (5-5)$$

where:

$$\kappa = \theta_{im}\sqrt{DR_{im}} \quad (5-6)$$

is a function of the immobile porosity θ_{im} , effective diffusion coefficient and immobile retardation factor R_{im} . We incorporate matrix diffusion via the random walk in time methodology after Painter et al. (2009) by sampling an advective travel from travel time distributions of a dispersive and exponential age distribution, then sample the resistance parameter given the travel time, then sample from the retention time distribution give the resistance parameter to calculate a total travel time. The total travel time distribution is then reconstructed from these samples.

Observation of isotopes at the Bedrichov tunnel were then used to constrain the mean age of the lumped parameter models. For a given conceptual model, lumped parameter models were run with different mean groundwater age (τ) and the resulting modeled isotope concentrations compared with observed concentrations.

5.3 Results

The main activities in this fiscal year were workshop attendance and model development. At this point only preliminary results for the lumped parameter and PFLOTRAN numerical modeling are available. More sophisticated forward modeling and parameter estimation will be included in future work.

Lumped Parameter Modeling:

Modeled stable δD composition in the Bedrichov tunnel at sampling point V6 for an exponential age distribution with mean ages of 1, 2.5, 5 and 10 years is show in Figure 5-1. The exponential model is incapable of fitting the observed data for any age distribution and shows a bias toward heavy isotopes. Models stable δD composition in the Bedrichov tunnel at sampling point V6 for a dispersion age distribution with mean ages of 1, 2.5, 5 and 10 years is shown in Figure 5-2. The dispersion model fits the observed data slightly better, but as in the case of the exponential model, the dispersion model produces consistently heavy isotopic signals for all ages modeled. A similar bias is modeled results was observed for all other sample locations. This bias is an effect of preferential seasonal recharge of winter snow melt. However, it can be noted that temporal variation in modeled isotopes essentially disappears for all mean ages over 5 years, thus the fact that the observed isotopic composition does vary indicates a short residence time of 5 years or less in Bedrichov tunnel waters. Future work will include developing a seasonally weighted input function which will allow a more quantitative comparison.

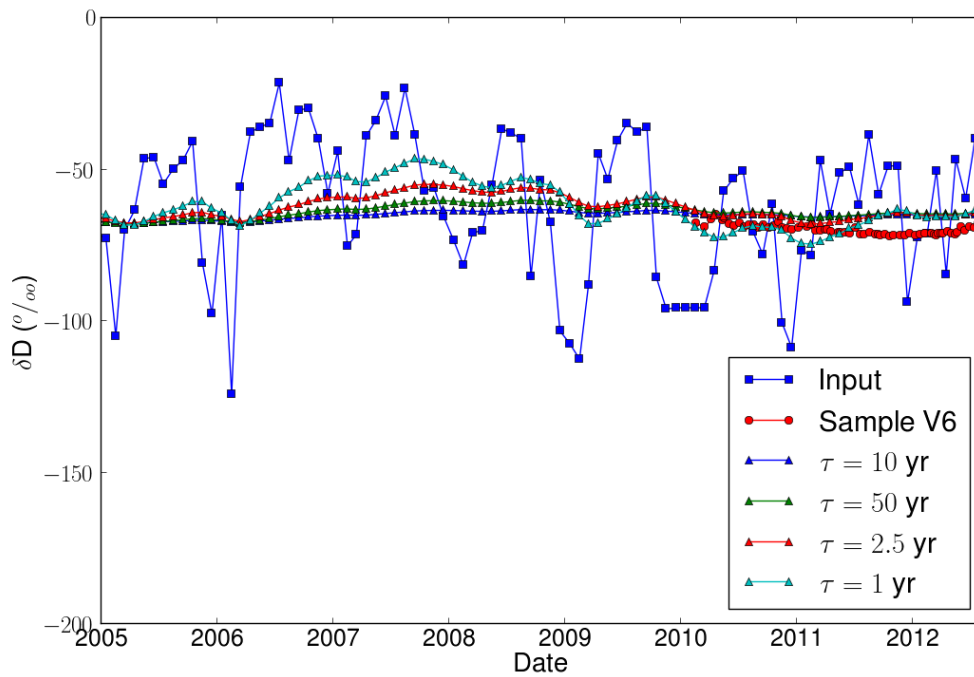


Figure 5-1. Measured and modeled stable isotope composition for the Bedrichov sample V6 using the exponential age distribution

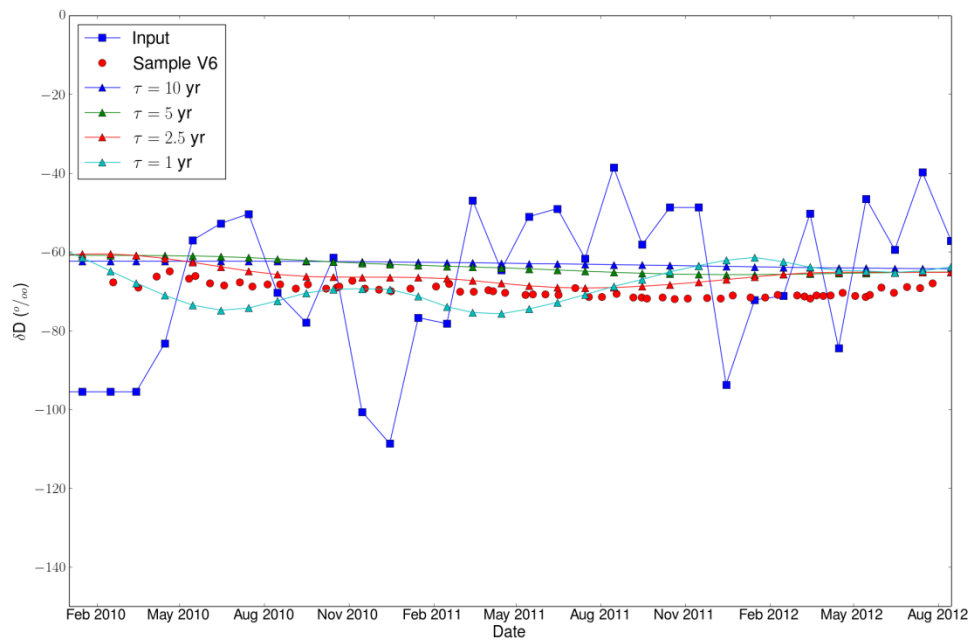


Figure 5-2. Measured and modeled stable isotope composition for the Bedrichov sample V6 using the dispersive age distribution

A tracer plot of tritium versus CFC-12 is shown in Figure 5-3. Tritium in Bedrichov precipitation was created using an inverse distance weighted average of surrounding records including Vienna, Prague, and Uhlirska. The expected concentration measured in 2012 for increasing mean age is plotted in the dashed red line. Black dots indicate 5 year intervals in mean age. From Figures 5-3 and 5-4 it is apparent that waters discharging the Bedrichov tunnel are generally less than 5 years in age. This is the case regardless of the age distribution chosen. Thus, we conclude that fluid flow in the Bedrichov fractures rapid and groundwater ages are less 5 years for almost all samples.

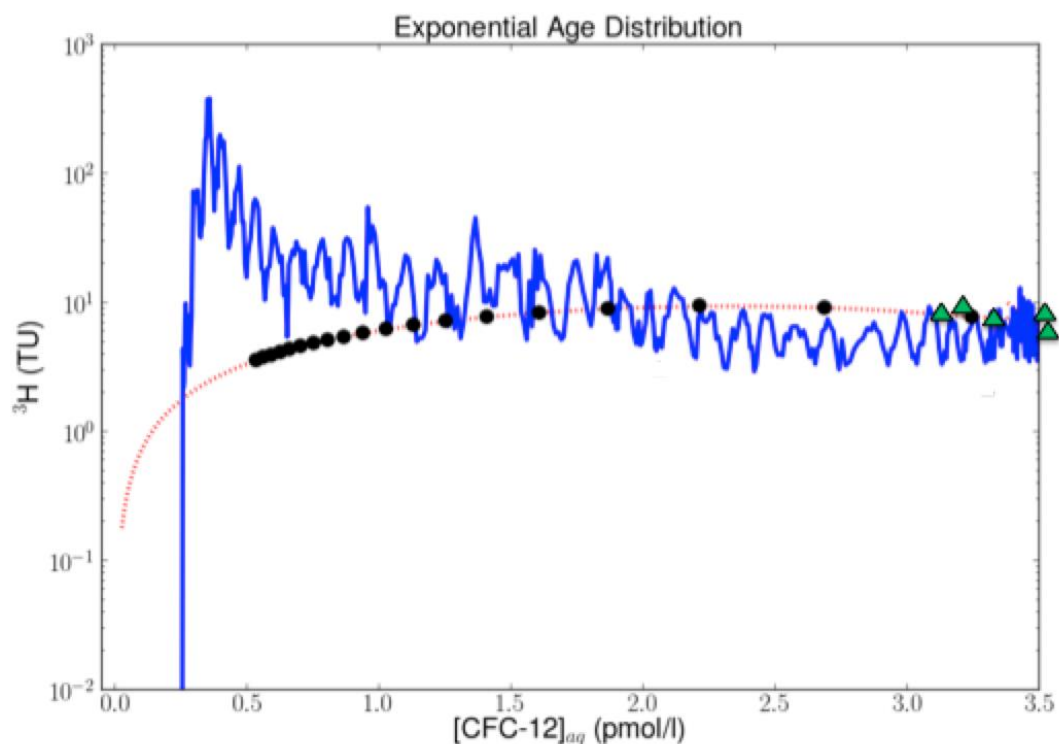


Figure 5-3. Tracer plot of ^3H vs CFC-12 for precipitation (blue line) at Bedrichov, measured samples (green triangles) and expected concentration for the year 2012 given an exponential age distribution as a function of increasing mean age. Black circles are the expected concentration for every 5 year interval of mean age

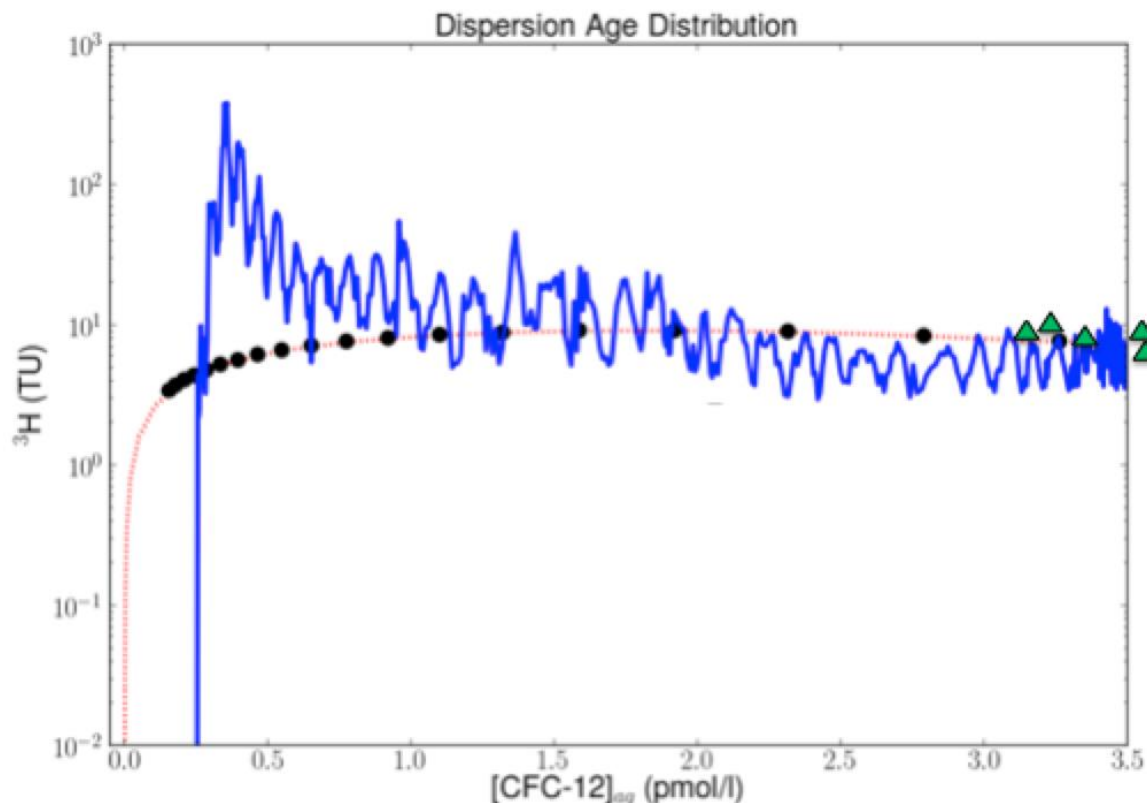


Figure 5-4. Tracer plot of ^3H vs CFC-12 for precipitation (blue line) at Bedrichov, measured samples (green triangles) and expected concentration for the year 2012 given a dispersion age distribution as a function of increasing mean age. Black circles are the expected concentration for every 5 year interval of mean age

Matrix Diffusion:

We explored the effect of matrix diffusion at the Bedrichov site using our random walk in time method. Figure 5-5 shows the expected travel times for dispersion only and for dispersion and retention assuming infinite matrix diffusion. Here we assume matrix diffusion parameters representative of the Bedrichov site, and assign a mean advective travel time was 2 years, matrix porosity of 1% and fracture diameter of 0.2 mm. We observe no difference in the age distribution in Figure 5-5 and find that the mean total travel time including retention is indistinguishable from the mean travel time considering advection alone. Figure 5-6 shows the advective and total travel time distributions for a system with a mean advective travel time of 100 years, 10% matrix porosity and fracture width of 0.2 mm. There is a clear effect of matrix diffusion in Figure 5-6 and the mean total travel time of 5000 years is significantly different than that of purely advection alone.

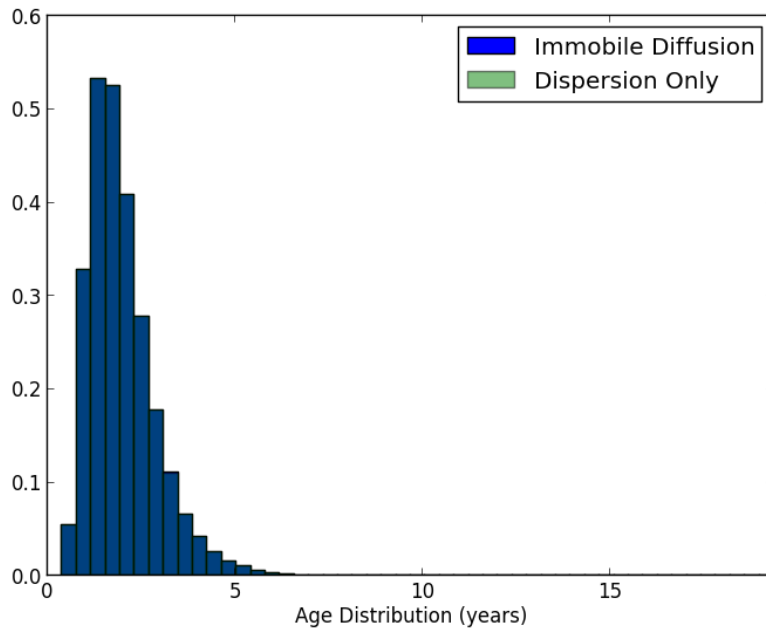


Figure 5-5. Expected age distributions for a dispersion model only and a dispersion model which includes retention time from infinite matrix diffusion for a mean advective travel time of 2 years, a matrix porosity of 1% and a fracture diameter of 0.2mm

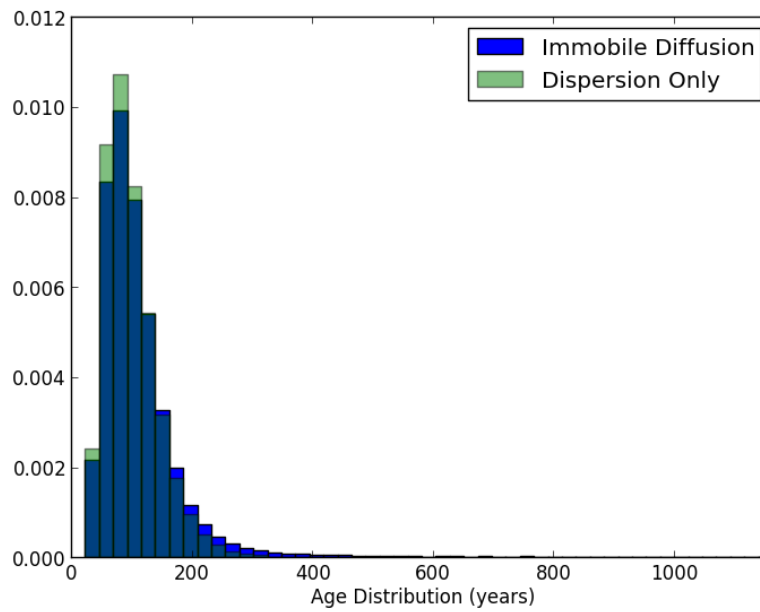


Figure 5-6. Expected age distributions for a dispersion model only and a dispersion model which includes retention time from infinite matrix diffusion for a mean advective travel time of 100 years, a matrix porosity of 10% and a fracture diameter of 0.2mm

5.4 Conclusions

We have developed lumped parameter models of stable isotope, tritium and CFC-12 transport at the Bedrichov Tunnel site and compared modeled results to measured data. To account for matrix diffusion in the fractured system at Bedrichov, the effect of matrix diffusion on travel must be investigated. Here we account for the retention time from matrix diffusion using a random walk in time methodology. Our lumped parameter models consistently predict heavier isotopic values than those observed at the site, indicating preferential recharge of winter precipitation. The variability in isotopic composition of discharge observed at the site is indicative of short travel times – as modeled isotopic composition with mean travel times over 5 years tend to show no temporal variation. These results are consistent with those from CFC and ^3H which indicate travel times of less than 5 years in the Bedrichov tunnel. Using parameters indicative of the Bedrichov Tunnel we show that matrix diffusion is probably not a major process at this site given the very fast transit times. However, this process will have very large effect with longer residence times.

5.5 References

- Cook, P.G., Herczeg A. L. (2000) Environmental Tracers in Subsurface Hydrology. Kluwer, Boston, 529p.
- Cook, P. G., Love, A. J., Robinson, N. I., Simmons, C. T. (2005) Groundwater ages in fractured rock aquifers. *J. Hydrology* 308(1-4), 284-301.
- Cook, P.G., Robinson, N.I. (2002) Estimating groundwater recharge in fractured rock from environmental ^3H and ^{36}Cl ; Clare Valley, South Australia. *Water Resources Research* 10.1029/2001WR000772.
- Painter, S. Cvetkovic, V. (2005) Upscaling discrete fracture network simulations: An alternative to continuum transport model. *Water Resour. Res.* 41, W02002.
- Painter, S., Cvetkovic, V., Pensado, O. (2008) Time-domain random-walk algorithms for simulating radionuclide transport in fractured porous rock. *Nuclear technology* 163 (1), 129-136

6. KURT Site Characterization Data - Fracture and hydrologic data from deep boreholes in KURT site

6.1 Introduction

Korea Atomic Energy Research Institute (KAERI) was engaged, on behalf of the Sandia National Laboratories (SNL), to conduct three tasks including sharing KURT site characterization data, technique development for in-situ borehole characterization and streaming potential (SP) testing, to support the study of high-level nuclear waste disposal in crystalline geologic media. This section documents a deliverable for the task of sharing KURT site characterization data. In this task, KAERI provides SNL with fracture and hydrologic data from the deep borehole DB-1 (500m), DB-2 (1,000m), YS-1 (500m) and YS-6 (500m) and hydrochemical data from the deep borehole DB-1 and YS-1 around the KURT (Table 6-1).

6.2 KURT (KAERI Underground Research Tunnel)

History and current status of KURT:

KURT is a generic underground research laboratory, and it intends to obtain information on the geological environment and behavior and performance of engineered barriers under repository conditions. For an investigation into the feasibility, stability, and safety of the proposed HLW disposal concept in Korea, it was necessary to experimentally investigate the disposal system in underground conditions. The Planning Committee for the Korean Nuclear Energy R&D Program decided to construct a small-scale underground research laboratory at KAERI to test the disposal concept in 2003. Site characterization and a detailed design for the construction of KURT were completed in 2004. In November 2004, KAERI received a construction license from the municipal local governments of Daejeon city and Yuseong district, as well as from the Ministry of Science and Technology (MOST). Construction started in March 2005 and was completed in November 2006.

KURT has a total length of 255 m with a 180 m long access tunnel and two research modules with a total length of 75 m. The maximum depth of the tunnel is 90-100 m from the peak of a mountain that locates over the site. The horseshoe-shaped tunnel section is 6 m wide and 6 m high (Figure 6-1). The host rock is granite, which is one of the potential host rock types for an HLW disposal repository in Korea. The utilization of radioactive material in KURT is not allowed.

The design requirements for KURT were as follows (Cho et al., 2008):

- The long-term stability of the tunnel should be ensured with minimum rock support.
- Damage to the host rock from an excavation should be minimized.
- The access tunnel should be linear to obtain the maximum overburden of the research modules with the minimum length of the access tunnel.
- The research modules should be located at the rock mass with good quality.
- The research modules should be located in a fresh bed rock with the minimum thickness of 50 m.
- Construction should be economical as possible.

Table 6-1. Data list for the task of sharing KURT site characterization data

		Data	Detail	Format	
	Background information about KURT			MS Word	
Geology	General geology	Geological description		MS Word	
		Lineaments (local)	Orientation, Length	Excel	A1
		Topography	Digital elevation map	Cad	A2
	Deep borehole data <u>DB-1 : 500m (length)</u> <u>DB-2 : 1,000m (length)</u> <u>YS-1 : 500m (Core, fracture) only</u> <u>YS-6 : 500m</u>	Core data	Core mapping	Cad/PDF	A3
		Logging data	Image by Acoustic televiewer	PDF and Excel	A4
			Image by BIPS	PDF	A4
		Geophysical logging data	Natural gamma	Excel	A5
			Full-wave sonic	Excel	A5
			SP	Excel	A5
			Electronic conductivity	Excel	A5
Fractures	Temp	Excel	A6		
	Deterministic fracture zones	Orientation, Width, Length	Excel	A7	
	Background faults/large fractures	Frequency	Excel	A8	
	Fracture set	Fracture set	Excel	A9	
Hydrogeology	Hydrogeological properties	Permeability	K	Excel	A10
			T	Excel	A10
	Storage	S	Excel	A10	
	Effective porosity	n	Excel	A10	
Geochemistry	Geochemical properties. <u>DB-1 : 500m</u> <u>YS-1 : 500m</u>	Major ion	Cation, Anion	Excel	A11
		Minor ion	trace element	Excel	A11
		In-situ data	pH, DO, EC, Temp	Excel	A11
		Rock/Fracture minerals	Chemistry, mineralogy	Excel	A12

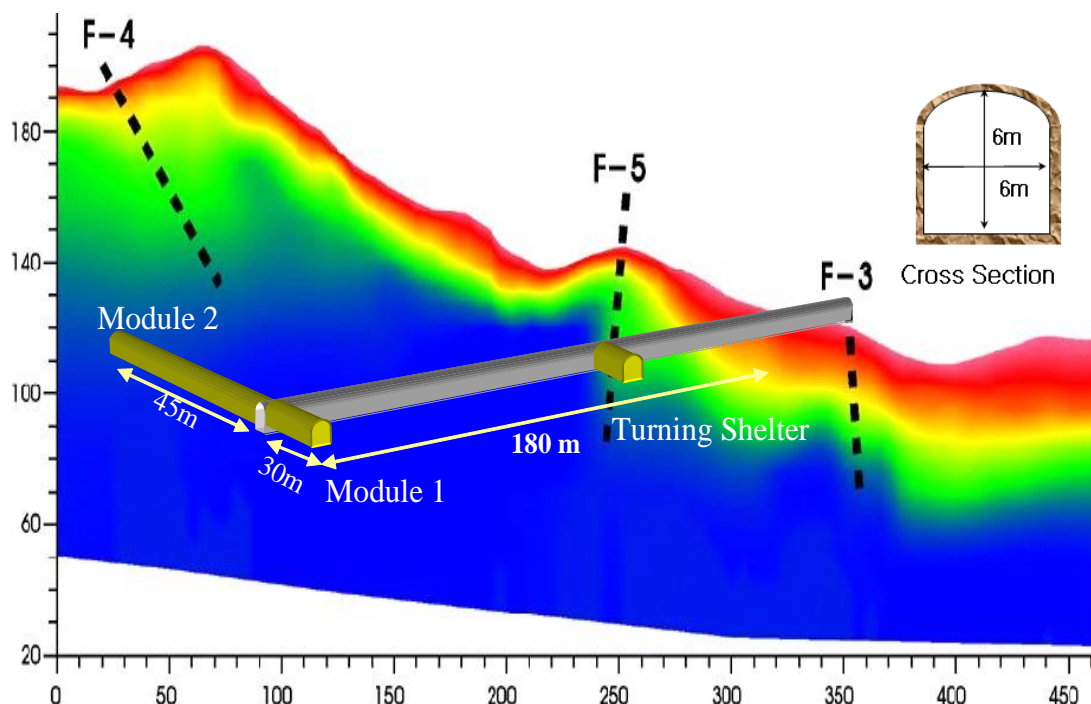


Figure 6-1. Current layout of the KURT

The drill and blasting method was applied to make a horseshoe shaped access tunnel and research modules. A careful blasting to minimize the blasting impact on the research reactor and other neighboring buildings at KAERI was required. Daily excavation was advanced about 1–3 m depending on the rock quality. The tunnel was supported mainly by using rock bolts and shotcrete in some zones of the tunnel. Lattice girders were installed at weak zones around the tunnel entrance and the fracture zones (Cho et al., 2008).

Data collected from geological investigations provided important information for the design and safety assessment of a repository system. Geological investigations at the KURT site were progressing, including developing site descriptive models and collecting geological, hydrological, and geochemical baseline datasets.

KURT has also played a significant role in developing and demonstrating a repository disposal system as well as the technologies needed for its construction and closure. The research experience gained at KURT has provided important information to validate the safety and feasibility of a disposal system and has made important contributions toward the successful implementation of a future commercial geological repository program.

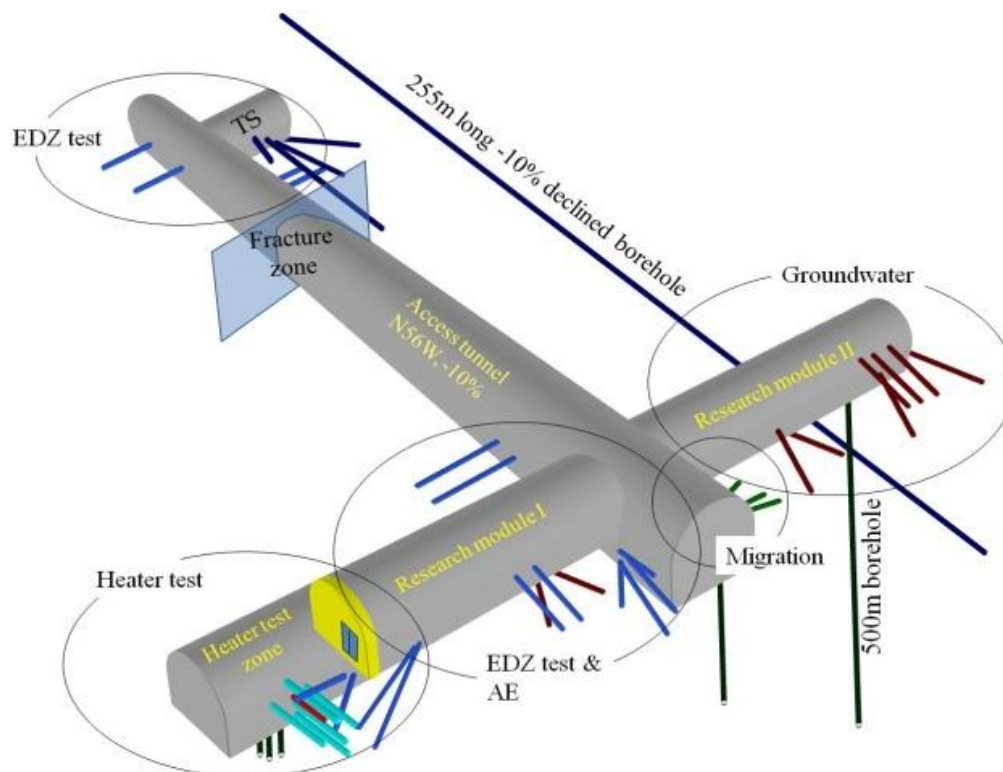


Figure 6-2. Location of in situ tests and experiments with related boreholes at KURT

Test and experiments in KURT:

During phase I (2006~2011), the following in situ tests and experiments were carried out after the successful completion of construction in Nov. 2006. Figure 6-2 shows the location of in situ tests and experiments and the associated boreholes.

- Single hole heater test: A 5 kw heater was installed in a heater hole, and about 100 temperature sensors were installed inside the rock surrounding the heater. The heater temperature was controlled to be increased step by step to 90°C. The power input, heater, air and rock temperatures, rock displacement, and rock stress were measured to investigate thermo-mechanical responses of the rock mass during the heating phase.
- EDZ characterization: Rock mass properties were measured to determine the characteristics of EDZ. Rock cores collected before and after excavation were investigated to evaluate thermal and mechanical property changes. Different geophysical tests were also applied to determine the size of EDZ.
- Solute migration experiments: Solute retardation by filling minerals in rock fractures was investigated to improve understanding of transport and retention of solute/colloid in a fractured rock mass.
- Development of site investigation techniques: Deep geological survey techniques, as well as QA procedures for various borehole tests, were developed to improve data quality.

- Long-term corrosion experiment: Estimation of long-term corrosion rate of disposal canister materials and the effect of dissolved oxygen (DO), Eh, and pH on the corrosion behavior.
- Hydrogeological and geochemical studies: Comprehensive data of hydrogeological and geochemical conditions were collected in regular term. Long-term monitoring of hydrogeological and geochemical parameters and the site descriptive hydro-structural modeling have been carried out.
- International collaboration project with SNL: KAERI investigated the influence of groundwater pressure on fracture aperture size, which controls the fracture transmissivity. Another research, i.e., a streaming potential (SP) experiment, is in progress to determine the hydraulic properties and behavior of the 3D subsurface volume of saturated fractured rock using a hydraulic head and streaming potential data.

Future plan:

During phase II (2012–2016), intensive experiments on hydrogeological characterization of MWCF and in situ long-term performance tests on a 1/3 scale engineered barrier system are major experimental research items to be executed at the KURT facility. The current dimensions of the research modules are limited, and thus the KURT facility needs to be extended for the execution of the planned tests and experiments during phase II. The design of the tunnel layout and construction method was optimized by March 2013. Fig. 6-3 shows an example of the potential tunnel layouts, which could be modified depending on the results from site investigations. The tunnel and additional utilities will be constructed from 2013 to 2014.

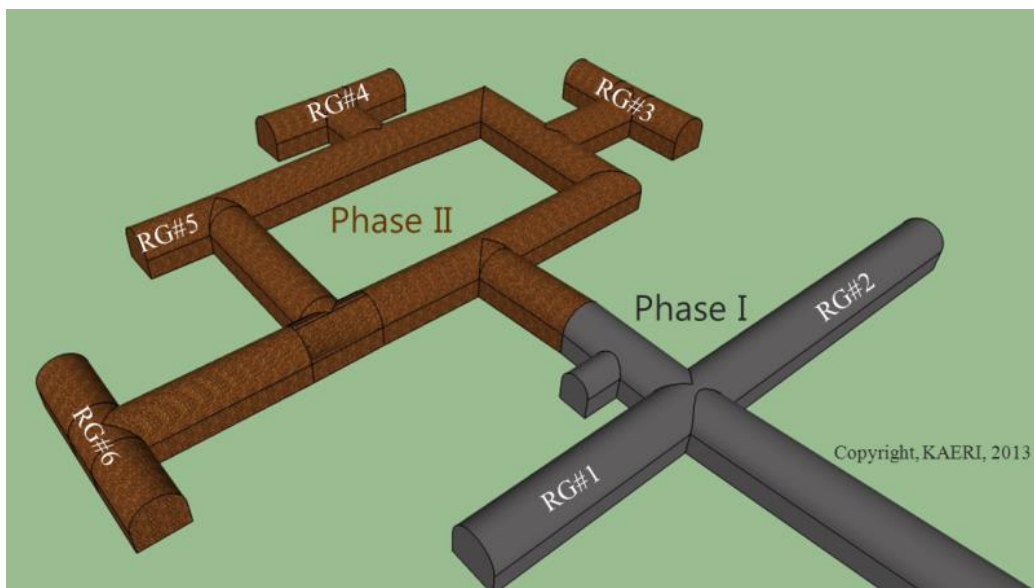


Figure 6-3. An alternative layout for tunnel extension of KURT

Two-mica granite with discernible foliation is a major rock type in cored rock samples at the KURT site. Under the microscopic observation of drill cores, the two mica granite consisted mainly of quartz, plagioclase, orthoclase, biotite, and muscovite, along with small amounts of chlorite, rutile, zircon, and apatite as accessory minerals. The two-mica granite often showed as biotitic granite and schistose biotitic granite in some biotite-concentrated areas. Sericitization was commonly observed along the twin or grain boundaries of the plagioclase, and chloritization was seen along the cleavages in the biotite. Some iron oxides existed as a glassy vein along the micro-fractures. The results of the modal analysis from fresh host rocks collected from the deep boreholes (YS-1 and DB-1) illustrate the existence of a classified table of plutonic rock, which was mostly distributed in the granite region. The plagioclase of the fresh two-mica granite had an albite to oligoclase composition, and the biotite had an Al-depleted composition.

Whole-rock analyses of the major and trace elements suggested that the two mica granite was I-type and peraluminous granite and was formed by a differentiation of the calc-alkaline series. The SiO₂ content varied from 66.4 to 75.0%. The content of TiO₂, Al₂O₃, MgO, FeO_T, CaO, and P₂O₅ tended to have negative correlations with SiO₂, whereas K₂O had a positive correlation with SiO₂, which are the usual tendencies of granite (Kim et. al., 2004)

The mineralogy of fracture filling mineral were investigated from the borehole core samples. Most of the fractures were characterized by the existence of mineral coatings on the fracture surfaces. The fracture filling minerals are intergrown with each other. Illite, laumontite, calcite, chlorite, epidote, and montmorillonite were identified as fracture filling minerals. Laumontite (zeolite mineral) was very widely produced among the fracture-filling minerals. While a large amount of illite was not generated, it had the highest frequency of occurrence. The frequency of calcite was lower than that of the other fracture-filling minerals. Chlorite was mainly produced as an altered mineral on the fracture surfaces. The production of laumontite, epidote, and pyrite, in particular, suggest that the KURT site was influenced by hydrothermal alteration. According to observations using a scanning electron microscope (SEM), laumontite of a typical columnar crystal type and the illite and kaolinite of plate-type crystals were identified. In addition, chlorite and montmorillonite were produced as in a typical plate-type crystalline aggregation and typical honeycomb-type structure, respectively. Other fracture filling minerals identified in the cores include kaolinite, clinozoisite, pyrite, and iron oxides.

6.4 Deep boreholes in the KURT site

During an earlier stage, BH and YS series boreholes were drilled for a field-scale investigation. The depth of these boreholes ranged from 100 to 500 m. Among them, YS-1 and YS-6 boreholes were drilled at a depth of 500 m. KP-1 and KP-2 boreholes were investigated for the design of the KURT facility in particular prior to construction. During the KURT operation phase, DB-1 borehole was drilled at a depth of 500 m inside the tunnel to investigate deep geological environment. Recently, DB-2 borehole was drilled to a depth of 1,000 m outside of the tunnel to evaluate a main water conducting feature, which was identified during the DB-1 borehole investigation (Figure 6-5).

The lithological, mineralogical, rock mechanical, hydrogeological, and hydrogeochemical characteristics were investigated in these boreholes. A long-term monitoring of the groundwater pressure and chemical variations using a multi-packer system in DB-1 (SolExperts system,

Switzerland) and YS-1 (Westbay system, Canada) boreholes was carried out. However, hydrochemical monitoring of YS-1 borehole has been stopped since 2006 due to the problem of MP system and grouting effect. The hydrochemical differences of YS-1 borehole were mainly resulted from the grouting activity, which carried out before MP installation on the fracture zone around GL-115m with Portland cement, where the borehole was collapsed after the drilling and hydraulic testing.

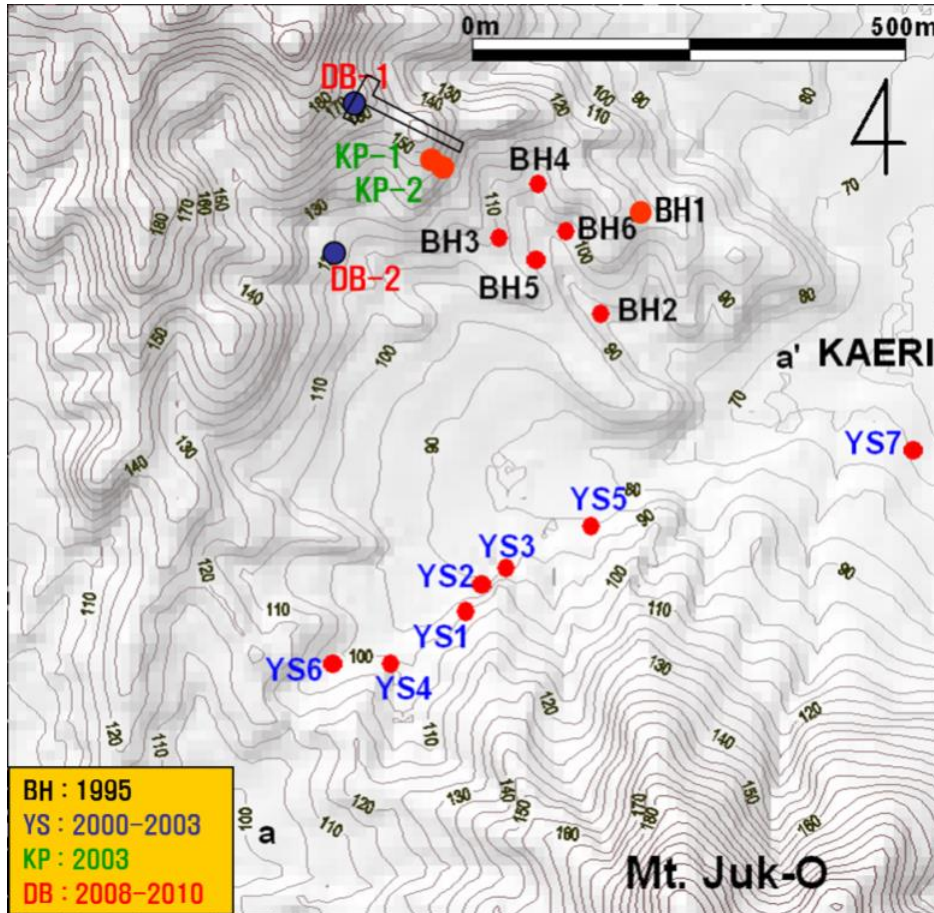


Figure 6-5. Location of boreholes around KURT.

During the operation of the KURT, additional geophysical surveys inside and outside of the tunnel, hydrogeological investigations (hydraulic testing and groundwater sampling), geophysical loggings, and VSP explorations in DB-1 and DB-2 boreholes were performed for developing geological model of the KURT site. These results were used to evaluate a conceptual hydrogeological model and a groundwater flow simulation.

6.5. Concluding Remarks

Sandia National Laboratories (SNL) and Korean Atomic Energy Research Institute (KAERI) have developed a multi-year plan for joint field testing and modeling to support the study of

high-level nuclear waste disposal in crystalline geologic media, by leveraging the existing KAERI Underground Research Tunnel (KURT) (Wang, 2012). The work currently planned includes three tasks:

1. Streaming potential (SP) testing: This testing will use the existing experimental setup in the KURT to obtain a mechanistic understanding of the coupling of electrochemical processes with hydrologic flows in a fractured rock and develop a modeling capability for fusing SP signal with hydrologic measurements. This testing will directly support the Used Fuel Disposition (UFD) effort on developing advanced methods for characterizing an excavation-disturbed zone (EDZ). KAERI will be responsible for instrumentation, field testing and data acquisition. SNL and KAERI will work jointly on experimental design and data interpretation. The work will be reported as a part of UFD milestone reports on flow characterization and modeling and international collaborations.
2. Sharing KURT site characterization data: The UFD Campaign is developing a discrete fracture network (DFN) model for modeling water flow and transport in fractured geologic media. Over the years, KAERI has performed extensive site characterization in KURT and its adjacent area. The data obtained from this effort will be valuable for DFN model validation and demonstration. In this task, KAERI will provide SNL with detailed fracture maps and hydrologic data around the KURT.
3. Technique development for in-situ borehole characterization: SNL and KAERI will develop a roadmap for the technique development and demonstration for in-situ borehole measurements. A key technique will be identified and the preliminary demonstration will be initiated using the DB-2 borehole.

For task 1, KAERI has acquired the needed equipment and started experimental setup for laboratory testing. This testing system will be transferred to the underground research laboratory once the new excavation in the KURT is completed. For task 2, KAERI has provided the following set of geological, hydrological, and geochemical data:

- A1: Lineament around KURT
- A2: Lineament index and DEM file
- A3: Core logging data of deep boreholes in KURT site
- A4: BHTV data of deep boreholes in KURT site
- A5: BIPS data of deep boreholes in KURT site
- A6: Geophysical logging data of deep boreholes in KURT site
- A7: Fracture zone data of deep boreholes in KURT site
- A8: Fracture frequency data of deep boreholes in KURT site
- A9: Summary of fracture set in KURT site
- A10: Hydrological properties of KURT site
- A11: Hydrochemical properties of water samples from the YS-1 and DB-1 boreholes.
- A12: Geochemical properties of rock and minerals in KURT

These data will be used for the UFD discrete fracture network model development. Because of a large quantity of data involved, these data are available upon request (ywang@sandia.gov).

6.6 References

- Cho, W. J., Kwon, S. K., Park, J. H. (2008). "KURT, a small-scale underground research laboratory for the research on a high-level waste disposal," *Annals of Nuclear Energy* 35, pp.132-140.
- Kim, G. Y., Koh, Y. K., Bae, D. S., and Kim, C. S. (2004). "Mineralogical characteristics of fracture-filling minerals from the deep borehole in the Yuseong area for the radioactive waste disposal project." *J. Miner. Soc. Korea*, 17(1), 99-114.
- Ryu, J.-H., Koh, Y. K., Park, S. W., Kim, G. Y. and Choi, J.-W. (2012). "Geochemical Characterization of Deep Groundwater in KURT Using Geochemical Modeling" *J. Env. Eng.*, March, 2012, 351-359.
- Wang Y. (2012) "Work Plan for UFD R&D Tests at KAERI Underground Research Tunnel (KURT) Site" DOE-NE UFD FCRD-UFD-2012-000212.

7. Status of International Collaboration on Modeling the Bentonite Rock Interaction Experiment (BRIE)

7.1 Introduction

As part of the Crystalline Rock Disposal R&D work package in the Used Fuel Disposition Campaign (UFDC), Los Alamos National Laboratory is developing a new discrete fracture network (DFN) modeling capability (Painter et al., 2012; Hyman et al., 2013). DFN models depict the rock mass as an interconnected network of explicitly represented fractures. The approach is in the reductionist tradition, implicitly assuming that detailed statistical descriptions of small observable features will, once combined in numerical simulations, lead to understanding of the system as a whole. Networks of fractures are first stochastically generated using a stochastic model derived from site data. A computational mesh is placed on each fracture plane usually ensuring that the mesh on each of a pair of intersecting fractures matches along the intersection. Groundwater flow equations are then solved using this computational mesh. The final step is then to simulate radionuclide transport using the computed flow field, usually by particle tracking. DFN simulations were introduced first in theoretical studies; feasibility of detailed site-specific applications has also been clearly demonstrated (e.g. Cvetkovic et al. 2004, Svensk Kärnbränslehantering 2011).

The Swedish Nuclear Fuel and Waste Management Company (SKB) is currently conducting a multiyear flow experiment in the fractured crystalline rock at the Äspö Hard Rock Laboratory (Äspö HRL). The Bentonite Rock Interaction Experiment (BRIE, www.chalmers.se/en/projects/Pages/brie.aspx, Bockgård et al., 2010) is focused on the interaction between rock and bentonite in a borehole similar to those planned for emplacement of waste in the KBS concept for disposal in crystalline rock. The main objectives of the BRIE are better understanding of the movement of water across the bentonite-rock interface, better prediction of wetting of the bentonite, and better characterization methods for emplacement boreholes. The site selected for BRIE is located at 420 m depth in the TASO-tunnel of Äspö HRL.

Details of the BRIE can be found elsewhere (Bockgård et al., 2010). The main part of the experiment comprises two bentonite-filled boreholes that are monitored as water flows from the surrounding fracture network into the bentonite. The experiment involved several phases: characterization of the site, drawdown of the water table near the two emplacement boreholes, emplacement of the bentonite, wetting of the bentonite, and post-experiment recover and analyses of the bentonite. Tunnel and borehole geometry in the vicinity of the BRIE is shown in Figure 1. The two arrows indicate the positions of the boreholes in which bentonite was placed. Five pilot boreholes shown in Figure 7-1 were first drilled in the bottom of the tunnel. These boreholes and the nearby tunnels made it possible to infer the position of three major fractures, which are shown in Figure 7-2. The pilot boreholes were then pumped to draw down the water table. Two emplacement boreholes were then drilled to a diameter of 30 cm and the bentonite emplaced. The bentonite contained relative humidity sensors to allow the saturation of the bentonite to be monitored.

This section summarizes the status of the UFDC's efforts to model the BRIE experiment using the new DFN modeling capability. The main objective of the work is to trial and refine the DFN

modeling capability using the BRIE site as a relatively well characterized demonstration site. This work is part of SKB's Task Force on Groundwater Flow and Transport Modeling (Bockgård et al., 2010, www.skb.se/templates/SKBPage____37222.aspx), which involves modeling teams from several countries.

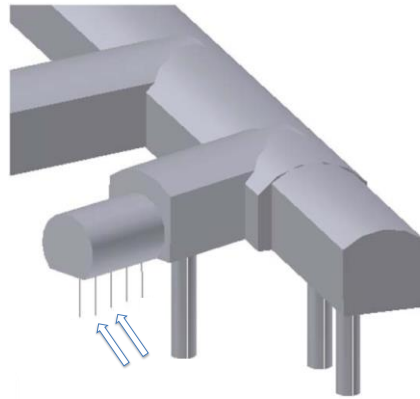


Figure 7-1. Tunnel geometry in the vicinity of the BRIE. The two arrows indicate the positions of the bentonite boreholes. Modified from Bockgård et al. (2010).

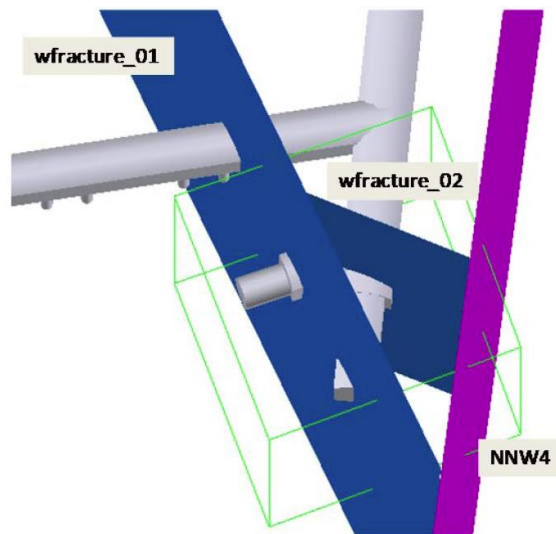


Figure 7-2. Location of known fractures near the BRIE. The green box shows the location of the modeling domain. Modified from Bockgård et al (2010).

7.2 Model Development Required to Support the BRIE Modeling Effort

The scope of the modeling task is to model wetting of the bentonite in the emplacement boreholes. This requires that flow in the fracture network near the boreholes also be modeled. The DFN grids are locally two-dimensional whereas the emplaced bentonite requires a conventional three-dimensional space-filling grid. As preliminary step in the BRIE modeling, the UFDC’s DFN modeling capability needed to be extended to allow for hybrid DFN/volume grids.

The procedure used to create hybrid DFN/volume meshes is illustrated in Figure 3. In this example, the interior of a cylinder is to be meshed and merged with a DFN grid in the nearby rock volume. A DFN is first generated using the procedures described previously (Painter et al. 2012, Hyman et al. 2013). The generated DFN ignores the volume to be meshed. However, before the DFN is meshed, interfaces between fractures and the cylinder to be meshed are identified. A two-dimensional mesh is then created on each fracture in a way that conforms to the fracture intersections and to the fracture-volume interfaces (Figure 7-3a). The fracture grids are then merged, as described previously and in Hyman et al. (2013). In the second step, nodes on the fractures within the volume to be meshed are removed (Figure 7-3b). A tetrahedral mesh that conforms to the fracture intersection is then created within the cylinder. In the final step, the tetrahedral mesh and the DFN mesh are merged and duplicate nodes removed (Figure 7-3c). The LaGriT software (Los Alamos Grid Toolbox, 2013) was used to execute the meshing calculations.

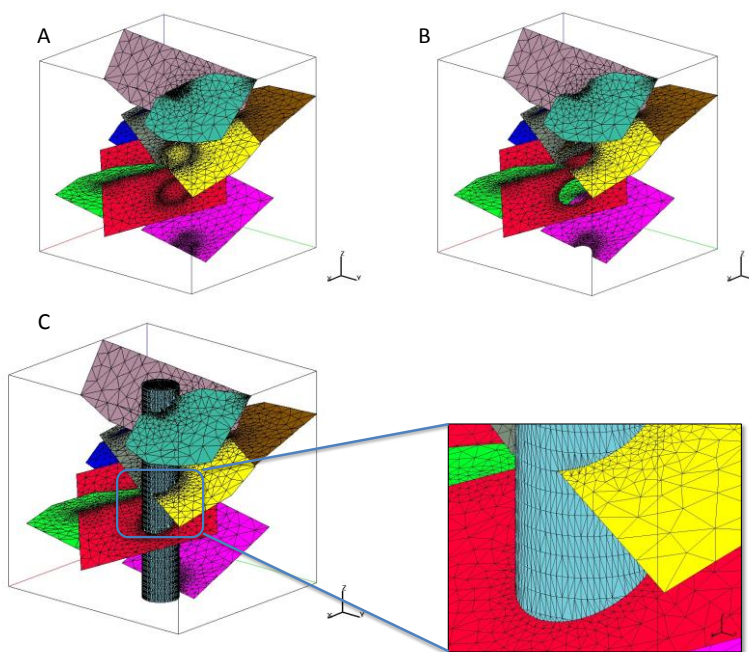


Figure 7-3. Example showing the creation of a hybrid tetrahedral/DFN mesh. Such hybrid meshes were required to model the rewetting of bentonite in the BRIE.

7.3 Scoping Calculations

A set of scoping calculations were first performed to test the capability to solve for flow in hybrid tetrahedral/DFN grids. Those scoping calculations used a single fracture intersecting the bentonite volume. The FEHM software was used (Zyvolosky, 2007). FEHM has an option for defining the same node multiple times. It then imposes a constraint that the unknowns be the same for a multiply defined node. That capability simplifies the construction of the mesh because it avoids having to merge control volumes at the interface between the three-dimensional and two-dimensional meshes, which would create issues with property assignments at the merged control volumes.

The van Genuchten model (van Genuchten, 1980) was used for both the bentonite and the rock fracture. In the van Genuchten model, liquid saturation s_l is related to capillary pressure as

$$s_l = \frac{1}{1 + \frac{C}{\lambda} \left(\frac{P_g - P_l}{P_0} \right)^{\frac{1}{\lambda}}} \quad (7-1)$$

where P_g is gas pressure, P_l is liquid pressure, and P_0 and λ are empirical parameters. The reference case parameters used for the fracture and bentonite are provided in Table 7-1. The initial saturation of the bentonite was specified as 36%. The fracture was initially saturated with water. The boundary conditions on the fracture edges were specified at 2 MPa. Richards model was used for the reference case.

Table 7-1. Parameter Values Used in the Scoping Calculations (Bockgård et al., 2010)

Parameter	Bentonite	Fracture
van Genuchten pressure parameter P_0 [MPa]	9.23	1.74
van Genuchten shape parameter λ [-]	0.3	0.6
Hydraulic conductivity [m/s]	6.4×10^{-14}	Not applicable
Porosity [-]	0.44	Not applicable
Transmissivity [m ² /s]	Not applicable	5×10^{-10}
Fracture Aperture [m]	Not applicable	10^{-4}

Results for the reference case at 10 days, 6 months and 1 year are shown in Figure 7-4. The top row of images shows the liquid saturation in three-dimensional view. The bottom row shows the saturation at a horizontal cut at the fracture plane. After about 1 year, enough water has been imbibed into the bentonite to raise the saturation in the bentonite at the location of the fracture to approximately 65%. Water is also starting to migrate upward in the bentonite.

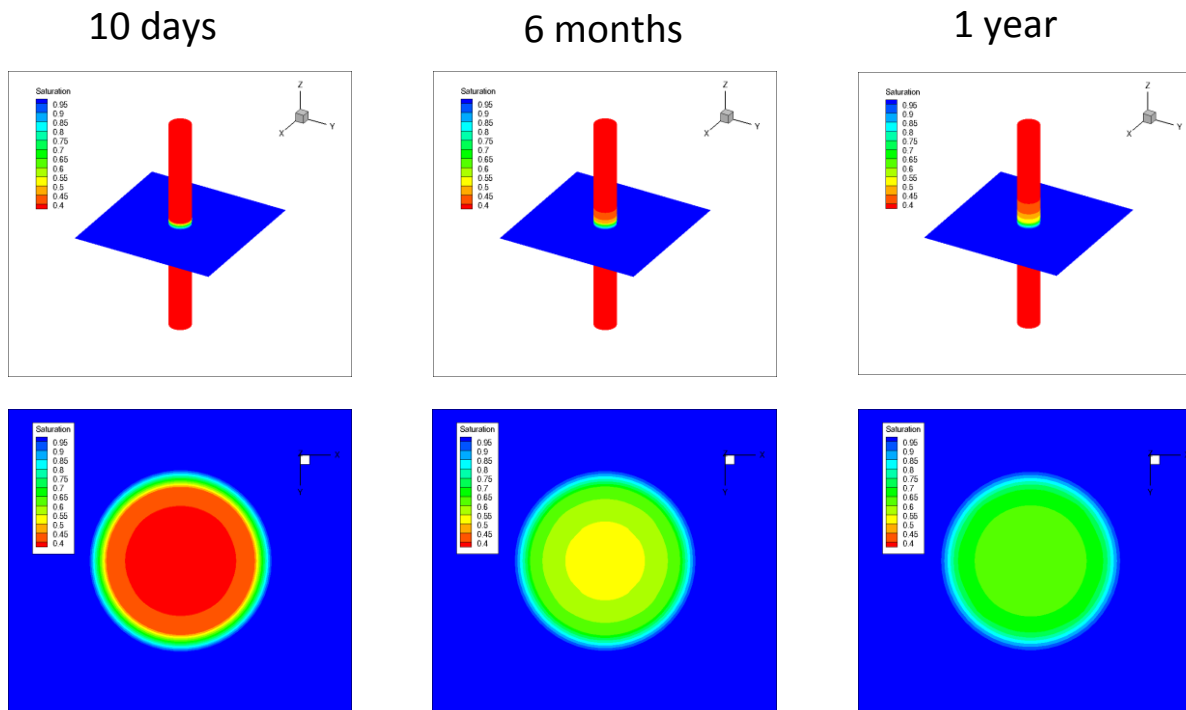


Figure 7-4. Liquid saturation for a scoping calculation using a single fracture and a bentonite cylinder representing one of the BRIE boreholes. The images in the bottom row are at the plane of the fracture.

A comparison between the Richards equation representation, which treats gas as a passive phase and ignores the conservation equation for air, and a more complete representation that solves the two-component system is shown in Figure 7-5. There is no significant difference between the two representations at 1 year, which suggests that the Richards equation representation is adequate for representing the rewetting process. This comparison would need to be revisited for longer simulation times, however.

Liquid saturation at 1 year for the reference case is compared to two variant cases in Figure 7-6. The images on the left show liquid saturation for a variant case in which bentonite permeability is higher by an order of magnitude. The images on the right are for the case with an annular gap at the outer edge of the bentonite cylinder. The effect of the annular gap is represented by increasing vertical permeability in the outermost ring of cells. In both variant cases, the bentonite wetting progresses faster than in the reference case. A variant case with higher fracture permeability was also run. That result was not significantly different from the reference case and is not shown.

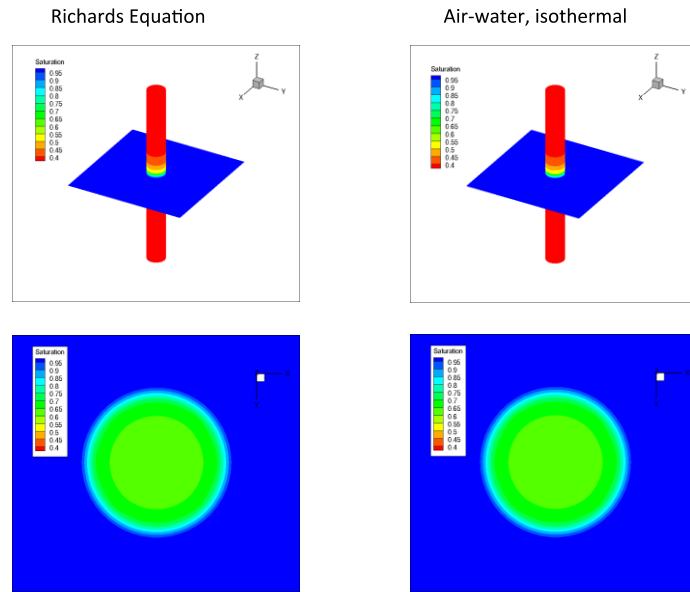


Figure 7-5. Comparison between the Richards equation representation and a more complete two-component representation. Shown is liquid saturation at 1 year.

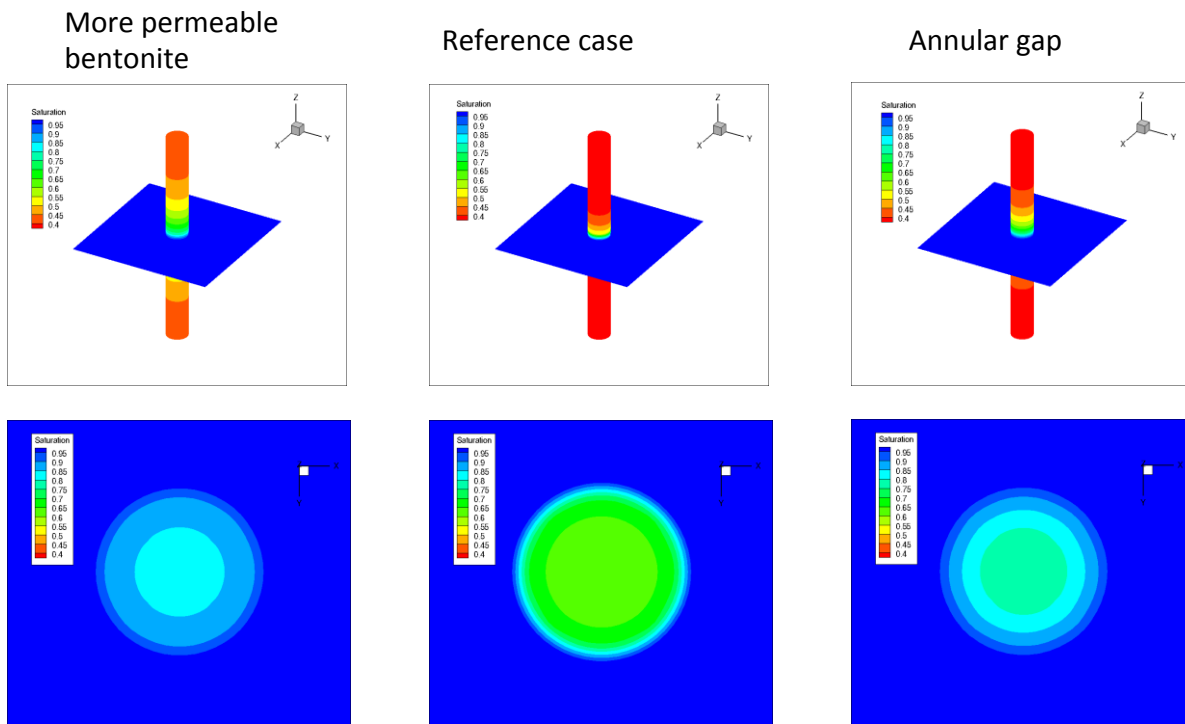


Figure 7-6. Comparison between the reference case scoping run and two variant cases. Shown is liquid saturation at 1 year.

7.4 Model Setup for Hybrid DFN/Bentonite Simulations

A primary goal of this work is to gain experience in applying advanced DFN models in practical applications that involve complicated geometries and boundary conditions. Task 8d of SKB’s Task Force on Groundwater Flow and Transport Modeling is a valuable application for that purpose. In Task 8d, the flows in the fractured granite surrounding the two BRIE boreholes as well as the flows in the boreholes themselves are being modeled. This section describes preliminary model setup for Task 8d.

Model geometry is shown in Figure 7-2. The domain of interest is a 40 m × 40 m × 40 m cube. The model domain contains multiple tunnels, the two BRIE boreholes, and three deterministic fractures. For this work, the task description (Bockgård et al., 2010) specified a DFN model for stochastically simulating unobserved fractures (Table 7-2). This model used the isotropic Fisher distribution (Fisher, 1953) for fracture orientation

$$f(q) = \frac{k \sin q e^{k \cos q}}{e^k - e^{-k}} \quad (2)$$

where t is the deviation of the fracture pole orientation from the mean orientation and the parameter $k > 0$ is the concentration parameter. The concentration parameter quantifies the degree of clustering; values approaching zero represent a uniform distribution on the sphere and large values imply small average deviations from the mean direction.

Table 7-2. DFN Parameters for the Fractured Rock Mass Near the BRIE Boreholes (Bockgård et al., 2010)

Set	Orientation Distribution: Fisher			Size Distribution: Power Law		Fracture Density
	Mean Trend	Mean Plunge	Concentration Parameter	Lower Cutoff r_0	Exponent k_r	Area per Volume P_{32}
1	280°	20°	10	0.25 m	2.6	1.1 m ⁻¹
2	20°	10°	15	0.25 m	2.6	2 m ⁻¹
3	120°	50°	10	0.25 m	2.6	0.75 m ⁻¹

A workflow was developed for modeling the BRIE experiment. The major steps are:

1. A realization of the DFN model is created using stochastic simulation. The stochastically generated fractures are combined with the three deterministic fractures.
2. Two meshes are created. In the first, the DFN model is meshed without the boreholes. In the second, the DFN is meshed in combination with a tetrahedral mesh for the interior of the boreholes using the methods described in Section 7-3. These two meshes do not include tunnels.
3. The tunnel is represented in both meshes by specifying all nodes that fall inside the tunnel as boundary nodes with pressure specified as atmospheric.

4. Boundary conditions are mapped to the faces of the cube in both meshes. Pressure results from a larger simulation were provided for that purpose.
5. A steady-state flow simulation is performed without the boreholes to establish pre-experiment conditions in the fracture network.
6. The result of Step 5 is used as initial condition for a transient flow simulation with the BRIE boreholes represented. The liquid saturation index in the bentonite is initially 36%. Of interest is the rewetting of the bentonite.

The result of Step 2, a meshed realization of the DFN with the three deterministic fractures and the two BRIE boreholes is shown in Figure 7-7. For this preliminary simulation the lower cutoff was increased to 1.0 m to reduce the size of the network, with appropriate adjustments to the fracture density. The network contains approximately 3500 stochastically generated fractures.

The result of Step 3, a computational mesh with tunnel nodes identified is shown in Figure 7-8. The tunnel nodes are blue and green. Non-tunnel nodes are shown in red.

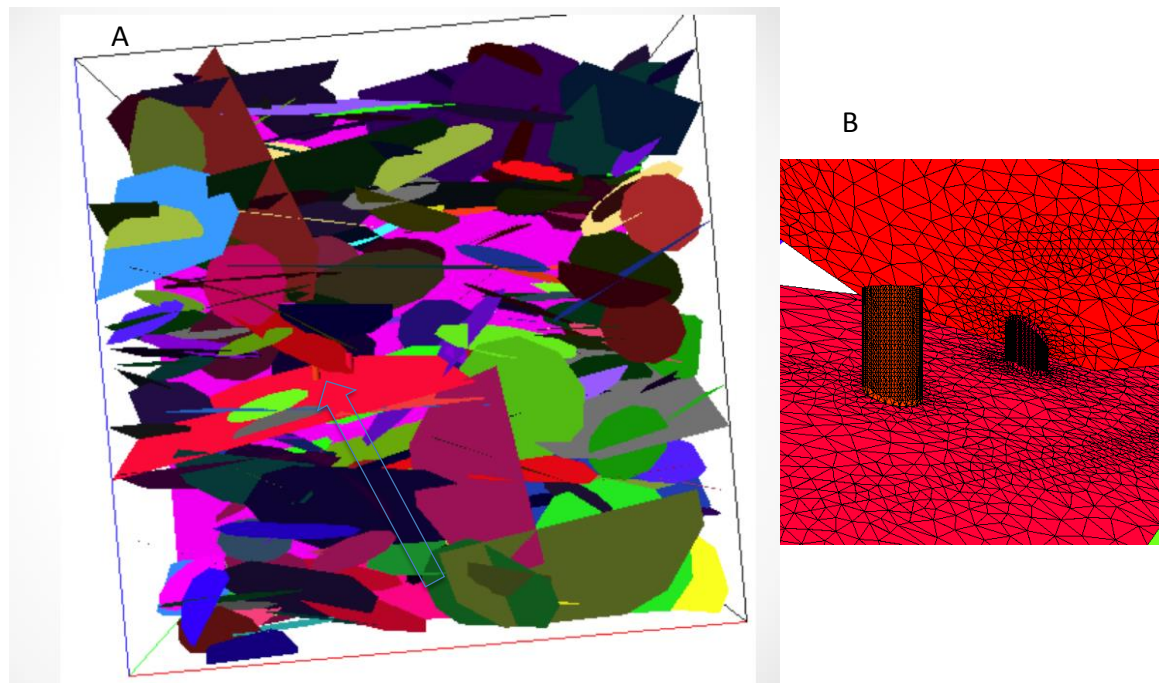


Figure 7-7. Computational mesh for the three-dimensional model of the BRIE experiment. The DFN and boreholes are shown in A. The arrow indicates the position of the boreholes. A detail from the computational mesh showing the merged DFN and tetrahedral mesh is shown in B.

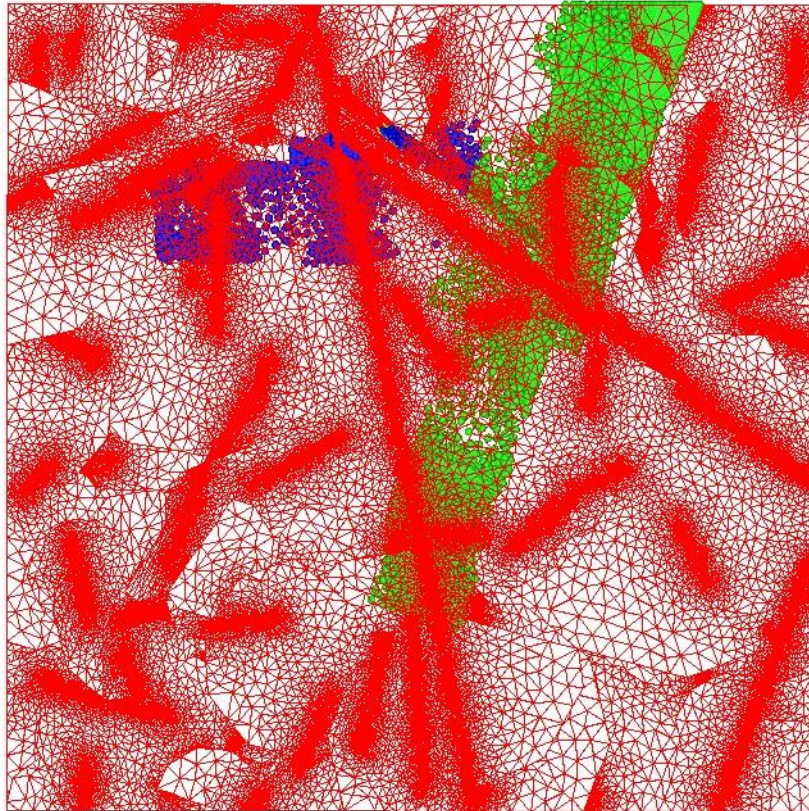


Figure 7-8. Computational mesh with tunnel nodes tagged (blue and green).

7.5 Summary and Status of the Work

Refinement and extension of the DFN modeling capability was undertaken to enable representation of the tetrahedral mesh within the DFN mesh. That development work is largely complete and initial computational meshes for the DFN and BRIE boreholes have been generated. The work is continuing in FY2014. The next steps are to apply boundary conditions and perform the flow simulations (Steps 4-6 in Section 5). Comparisons to data on moisture content in the bentonite will then be undertaken.

7.6 References

- Bockgård, N., Vidstrand, P., Åkesson, M., Fransson, Å. and Stigsson, M. (2010) Task 8: Modelling the Interaction between Engineered and Natural Barriers – an Assessment of a Fractured Bedrock Description in the Wetting Process of Bentonite at Deposition Tunnel Scale. SKB report 2010-04-14. SKB, Stockholm. Revised 10/10/2012.
- Cvetkovic V., Painter S., Outters N., and Selroos J.-O., 2004. Stochastic simulation of radionuclide migration in discretely fractured rock near Aspo hard rock laboratory, Water Resources Research 40, W02404, doi:10.1029/2003WR002655
- Fisher, R.A., 1953. Dispersion on a Sphere. *Proc. Roy. Soc. London Ser. A.*, 217: 295-305
- Hyman, J., Gable, C.W., Painter, S.L. 2013. Conforming Delaunay Triangulation of Stochastically Generated Three Dimensional Discrete Fracture Networks: A Feature Rejection Algorithm for Meshing Strategy. *SIAM Journal on Scientific Computing* (submitted).
- Los Alamos Grid Toolbox, LaGriT (2011) Los Alamos National Laboratory, <<http://lagrit.lanl.gov>>.
- Painter, S., Gable, C., Makedonska, N., Hyman, J., Hsieh, T.-L. Bui, Q., Liu, H.H., Birkholzer, J., 2012. Fluid Flow Model Development for Representative Geologic Media. Los Alamos National Laboratory. LAUR-12-26878. FCRD-UFD-2013-000058.
- Svensk Kärnbränslehantering AB, 2011. Long-term safety for the final repository for spent nuclear fuel at Forsmark, SKB TR-11-01, Svensk Kärnbränslehantering AB
- van Genuchten, M., 1980. A closed-form equation for predicting the hydraulic conductivity of unsaturated soil, *Soil. Sci. Soc. Am. J.*, 44(5), 892-898.
- Zyvoloski G. A., 2007. FEHM: A control volume finite element code for simulating subsurface multi-phase multi-fluid heat and mass transfer. Los Alamos Unclassified Report LA-UR-07-3359

8. Summary

The international collaboration on the natural system evaluation and tool development in FY13 was focused on the following activities: (1) data interpretation of colloid-facilitated transport experiments at Grimsel Test Site, (2) thermal-hydrologic-mechanical (THM) model development and validation for Mont Terri FE-heater test and HG-A test, (3) experimental study of Pu-bentonite interactions, (4) modeling of stable isotope, tritium and CFC-12 transport at the Bedrichov Tunnel site as a part of the DECOVALEX program, (5) KAERI Underground Research Tunnel testing in crystalline rocks, and (6) Swedish Bentonite-Rock Interaction Experiment (BRIE). The major accomplishments include:

- **Colloids Formation and Migration (CFM):** A reactive transport Laplace transform (RELAP) model was developed and used to interpret colloid facilitated transport data collected at the Grimsel Test Site between 2008 and 2012. The model accounts for diffusion between fractures and matrix, as well as linear, first-order reactions in both fractures and matrix. The model was used to fit the conservative tracer extraction breakthrough curves by adjusting the mean residence time and Peclet number in the shear zone as well as the fractional tracer mass participation in each test. The mean residence time, Peclet number and fractional mass participation estimated for the conservative tracers using these matrix diffusion parameters were not significantly different from estimates obtained assuming no matrix diffusion. However, matrix diffusion and sorption were found to be necessary to explain the transport behavior of the reactive solutes that were not strongly associated with colloids, so a small amount of matrix diffusion was allowed. The model was also used to estimate colloid transport parameters (filtration and resuspension rate constants) and reactive solute transport parameters (fracture and matrix adsorption and desorption rate constants for solutes not strongly associated with colloids, and colloid desorption rate constants for solutes strongly associated with colloids). The resulting best-fitting parameters were used as initial parameter estimates in a 2-D numerical model that could account for processes that RELAP does not explicitly account for. The most important of these processes were (1) the variable injection flow rates observed in some of the tests and (2) the simultaneous transport of colloids and reactive solutes (RELAP does not account for interacting species). RELAP can be used to obtain initial estimates for the more robust numerical model.
- **Mont Terri FE Heater Test:** A new suite of simulations related to the FE test at Mont Terri were conducted, including scoping calculations, benchmarking, and some initial predictive modeling of the real heater test. These include model simulations using 1D axisymmetric, 2D plane strain, and full 3D model geometries. A THM analysis involving the BBM in a full 3D field setting was conducted for modeling the geomechanical behavior of the buffer. Compared to our previous 2D model analysis, this 3D analysis provides a much more accurate estimate of the temperature evolution near the heater and thereby should provide a better prediction of the peak temperature. The peak temperature may become as high as 160°C at the inner parts of the buffer. This prediction strongly depends on the thermal and diffusion properties of the buffer, which are parameters that have presently not been well constrained for this buffer material. THM model

simulations were conducted with a simplified buffer mechanical model, whereas a ubiquitous joint model was used for modeling the anisotropic mechanical strength properties of the Opalinus Clay. The analysis shows that some minor failure may occur near the tunnel wall behind the concrete lining after excavation. This failure does not expand much further during the 20-year heating, meaning that the rock mass remains in an elastic mechanical state. Overall, the initial model analyses show that the adopted modeling approach is adequate for modeling the coupled THM processes at the FE heater, including all components of bentonite, concrete lining, and Opalinus Clay.

- **Mont Terri HG-A Test: The Rigid-Body-Spring-Network (RBSN) model** was used to simulate the HG-A test. Two additional model capabilities were developed: (1) a method for computing fracturing under compressive load and (2) a method to treat the anisotropic geomechanical properties of the Opalinus Clay. The use of the Mohr-Coulomb failure criterion led to RBSN model predictions for fracturing under compressive load that roughly follow trends expected for a homogeneous medium. For a layered system, the results were also reasonable in that fracturing followed the stiff layers for high bedding angles but was not controlled by bedding at low bedding angles. Currently, rock failure is modeled using a brittle model in which all strength is lost at failure. However, a more realistic failure response results in a more gradual loss of strength following failure. In addition, contacts along fracture surfaces under compressive loads will lead to friction along fracture planes not currently accounted for in the model. Anisotropic properties for the bulk rock were represented in the RBSN model using layered heterogeneity. While the current approach was successful at producing the desired anisotropic bulk properties and trends for fracture behavior under compressive load, significant differences remain between the RBSN results and observations in the HG-A test, indicating that further model development is needed.
- **Pu-bentonite interactions:** The experiments were designed to develop a mechanistic understanding of Pu interactions with representative mineral substrates under granitic chemical conditions. The sorption/desorption experiments covered a large range of Pu concentrations and were compared to sorption/desorption experiment with montmorillonite. The experiments are being coordinated with the CFM international project. The work to date indicate that adsorption behavior of Pu(V) on bentonite is similar to montmorillonite, suggesting that our understanding of the simple binary Pu-montmorillonite system can provide insight for the more complex multi-component mineralogy of bentonite clay. The Pu(IV) sorption isotherm for bentonite is broadly linear over a large range in Pu concentration ($[Pu]_{\text{initial}}$ ranging from 10^{-7} mol L⁻¹ to 10^{-16} mol L⁻¹), suggesting that the process controlling sorption at extremely low concentrations is the same as at higher concentrations. The desorption behavior of the bentonite and montmorillonite are very similar, indicating that, as with the adsorption experiments, the same processes are responsible for the desorption of Pu from the two materials.
- **DECOVALEX-Bedrichov Tunnel Tests:** Lumped parameter models were developed for stable isotope, tritium and CFC-12 transport at the Bedrichov Tunnel site and modeled results were compared to measured data. To account for matrix diffusion in the fractured system at Bedrichov, the effect of matrix diffusion on travel must be

investigated. The retention time from matrix diffusion was taken into account using a random walk in time methodology. The lumped parameter models consistently predict heavier isotopic values than those observed at the site, indicating preferential recharge of winter precipitation. The variability in isotopic composition of discharge observed at the site is indicative of short travel times – as modeled isotopic composition with mean travel times over 5 years tend to show no temporal variation. These results are consistent with those from CFC and ^3H which indicate travel times of less than 5 years in the Bedrichov tunnel. Using parameters indicative of the Bedrichov Tunnel we show that matrix diffusion is probably not a major process at this site given the very fast transit times. However, this process will have very large effect with longer residence times.

- KAERI Underground Research Tunnel Test: Sandia National Laboratories (SNL) and Korean Atomic Energy Research Institute (KAERI) have developed a multi-year plan for joint field testing and modeling to support the study of high-level nuclear waste disposal in crystalline geologic media. The work currently planned includes three tasks: (1) streaming potential (SP) testing, (2) sharing KURT site characterization data, and (3) technique development for in-situ borehole characterization. For task 1, KAERI has acquired the needed equipment and started experimental setup for laboratory testing. This testing system will be transferred to the underground research laboratory once the new excavation in the KURT is completed. For task 2, KAERI has provided a comprehensive set of geological, hydrological, and geochemical data. These data will be used for the UFD discrete fracture network model development.
- BRIE Project: Refinement and extension of the DFN modeling capability was undertaken to enable representation of the tetrahedral mesh within the DFN mesh. That development work is largely complete and initial computational meshes for the DFN and BRIE boreholes have been generated. The work is continuing in FY2014. The next steps are to apply boundary conditions and perform the flow simulations (Steps 4-6 in Section 7-5). Comparisons to data on moisture content in the bentonite will then be undertaken.